SIMPLIFIED MODELING OF STRATIFIED-CHARGE COMBUSTION IN A CONSTANT VOLUME CHAMBER

DISSERTATION

Presented in Partial Fulfillment of the Requirements for

the Degree Doctor of Philosophy in the Graduate

School of The Ohio State University

By

Nigel Charles Janes, B.S.M.E., M.S.

*****

The Ohio State University

2002

Dissertation Committee:

Dr. Yann Guezennec, Advisor

Dr. Giorgio Rizzoni

Dr. Ahmet Selamet

Approved by

_____

Advisor

Department of Mechanical Engineering

ABSTRACT

The value of combustion models cannot be overstated. As a major component of engine models they are widely used as research tools in the continuing effort to improve existing combustion systems and to develop completely new concepts. Models also find use in the classroom where they allow students to manipulate control parameters and study the effect on performance, efficiency and pollutant formation without ever visiting an engine test cell. Models of varying complexity are available for premixed combustion but there is a lack of published work on simplified modeling of the more complex case of stratified-charge combustion. In this investigation, such a model is developed and validated against experimental data for stratified combustion in a constant volume chamber. This first iteration is intended as an oversimplified foundation to which additional complexity can be added in subsequent iterations after weaknesses are identified. Data are obtained for a range of test cases from a purpose-built test stand. Each of the experimental cases is simulated and the results compared. Simulation results for pressure and flame radius match well with the experimental data. The timing of key events is also predicted with relative accuracy. Significant errors are observed only in the period where the model is predicted to break down. The overall positive result shows that it should be possible to capture the essential characteristics of stratified-charge combustion in a simple model, given adequate development time.

ACKNOWLEDGEMENT

This work would not have been possible without the support of a number of people. The opportunity is taken here to identify them and offer my gratitude for their contributions. My wife and family made financial and personal sacrifices, allowing me the freedom to complete this portion of the degree program. Dr. Yann Guezennec suggested the research topic and secured the funding necessary for its investigation. Dr. Nizar Trigui at the Ford Motor Company Powertrain & Vehicle Research Laboratory saw merit in the proposed work and his efforts led to support from Ford for the purchase of the necessary experimental hardware. Don Williams at the Ohio State Center for Automotive Research offered machining assistance during construction of the test stand. Dr. Woong Chul-Choi provided guidance for proper setup and operation of the high-speed digital imaging system employed. I am deeply appreciative to all who contributed inn one way or another to this effort.

VITA

April 4, 1963	Born – Grimsby, Great Britain
1995	B.S.M.E. – The Ohio State University
1998.....	M.S.M.E. – The Ohio State University
1996 – 1997	Graduate Research Fellow Center for Automotive Research Department of Mechanical Engineering The Ohio State University
1997 – Present	Graduate Research Associate Center for Automotive Research Department of Mechanical Engineering The Ohio State University

Major Field: Mechanical Engineering

Internal Combustion Engines and Alternative Vehicles

Faculty Advisor: Professor Yann G. Guezennec

TABLE OF CONTENTS

LIST OF TABLES

LIST OF FIGURES

Figure Page

Figure Page

Figure Page

Figure Page

NOMENCLATURE LIST

I. Acronyms

AFR	Air-Fuel Ratio	ICE	Internal Combustion Engine
CVCC	Constant Volume Combustion Chamber	PI	Port Injection
DISC	Direct-Injection Stratified-Charge	PWM	Pulse Width Modulation
EGR	Exhaust Gas Recirculation	SI	Spark Ignition
GDI	Gasoline Direct Injection		

II. General Variables

A	Area	Q	Heat Energy
BO	(Diffusion) Boundary Offset	R	Universal Gas Constant
DOS	Degree of Stratification	S_L	Laminar Flame Speed
FA_s	Stoichiometric Fuel-Air Ratio	S_p	Propagation Speed
H	Enthalpy	SG	(Ignition) Spark gap
L	Integral Length Scale	SO	Offset of Ignition Source from Chamber Wall
L_c	Chamber Length	T	Temperature
M	Molecular Weight	U	Internal Energy
P	Pressure	$\forbidden{V}$	Volume

II. General Variables (cont.)

c_p	Specific Heat at Constant Pressure	t	Time
c_v	Specific Heat at Constant Volume	t_c	Chamber Thickness
h	Mass Specific Enthalpy	v	Specific Volume
k	Turbulence Energy	U	Mass Specific Internal Energy
m	Mass	u'	Turbulence Intensity
r	Radius		

III. Greek Variables

χ	Mass Fraction	λ	Taylor Microscale
ϕ	Fuel-Air Equivalence Ratio	ν_i	Moles of i-th Mixture Component
ε	Turbulence Decay Rate	ρ	Density
γ	Ratio of Specific Heats	τ_b	Characteristic Burning Time

IV. Subscripts

avg	Average	*i*	Initial
b	Burned	*ie*	Ignition Electrode
c	Chamber	*ign*	Ignition
cs	Chamber Surface	*nw*	Near Wall
d	Diffuse or Diffusion	*r/l/d*	Rich/Lean/Diffuse
e (entr)	Entrained (Entrainment)	*rd*	Reaction-Diffuse
eb	Entrained and Burned	*ref*	Reference State
eu	Entrained but Not Yet Burned	*sw*	Side Wall
fw	Far Wall	*u*	Unburned
hx	Heat Transfer	*w*	Window

CHAPTER 1

INTRODUCTION

Engine models are invaluable tools for the development and analysis of new engine concepts. They are also teaching tools, helping to elucidate complex physical processes. The object of this investigation is a simplified stratified-charge combustion model to serve these roles. A rudimentary model is formulated and evaluated against experimental data from a constant volume combustion chamber (CVCC). In the following sections, motivation for work is provided, relevant literature is reviewed and a methodology is established for the model formulation and evaluation.

1.1 Physical Motivation for a Stratified-Charge Model

Interest in stratified-charge is strong due to the implementation of this technology in the direct-injection stratified-charge (DISC) engine. This is one of the most promising new technologies in the never-ending search for automotive powerplants with improved efficiency and reduced emissions. Operation of the DISC engine is quite different from the conventional port-injected (PI) engine. In a conventional gasoline-fueled engine, power is controlled by regulating airflow to the engine with the throttle. A fuel quantity, determined by the engine management computer, is injected into the intake airstream and the entire cylinder volume is filled (in most cases) with a homogeneous mixture. Intake throttling is responsible for a considerable portion of the total inefficiency of a conventional engine. In the DISC engine, power is primarily controlled

by regulating the amount of fuel, injected directly into the cylinder. By controlling fluid motion within the cylinder it is possible to stratify the contents into a core region of combustible mixture and a surrounding fuel-lean region. The air-fuel ratio (AFR) within the core region is approximately equal to that of the conventional engine. Overall AFR that is much higher due to the large amount of excess air in the lean region. Typical PI engines run with AFR values in the mid-teens with the current class champion Honda VTEC, able to run at up to 22 [30]. The production DISC engines of Mitsubishi and Toyota effectively double the maximum AFR of the outstanding Honda VTEC with values in excess of 40 [16, 20, 25, 26 and 43]. For the two engine types operating at a given power level, the DISC engine has significantly reduced throttling and a corresponding efficiency gain (~15% or approximately one-half the total improvement of ~30% [43]). The maximum benefit is also realized at part load operation where the vast majority of automotive engines spend most of their operating lives. This translates into sizeable fuel economy improvements over test cycles with a bias on city driving. The best evidence of the improvement is provided by fuel consumption rates measured during actual vehicle operation. Results published by Mitsubishi and Toyota [16, 20, 25 and 26] report fuel savings of up to 30 percent over the Japanese test cycle. As of 1999, Mitsubishi, Nissan and Toyota were the only manufacturers to offer vehicles equipped with DISC engines (only in the home market). A recent review of DISC technologies and trends by Zhao, et al. [43] makes it clear that the automotive industry is deeply committed to these advanced engines. It seems likely that within the next five to ten years, U.S. consumers will have the choice of conventional or DISC engine options when buying a new car, truck or sport utility. As DISC engines become commonplace in the U.S. marketplace in the near future, the need for models as design tools and teaching aids will grow.

1.2 Engine Models – Enablers of New Technologies

There are many challenges during development of new advanced concepts such as the DISC engine. Modeling makes it possible for new technologies like DISC to evolve more efficiently from initial concepts to fully functional systems. From the point of view of research and design engineers, the ability to study many possibilities is a benefit. A variety of "what-if" scenarios can be examined in short order and only those with significant merit, put forth for execution and testing in prototype hardware. Modeling is also a benefit for management and marketing personnel as the cost associated with following blind leads is reduced. Costs of new designs are also reduced, with more of the development and optimization process carried out in the virtual domain. Design cycle times are reduced, allowing products to be brought to market sooner. This means that product lines can be kept up date and better track the changing wants and needs of consumers and with more stringent government regulations.

Engine models also enhance the educational process and in this role are also enabling new technologies by helping engineers to grasp the underlying theories. This is true both for new engineers at the university level and those already at work in industry. The opportunity to conduct practical modeling exercises is often very useful in reinforcing new and complex concepts and systems such as the DISC engine.

1.2.1 Model Detail – An Appropriate Level for Each Task

Models may be constructed with any level of detail subject to the constraints of computing resources and available time. Any increase in resolution, spatial, temporal or other, is accompanied by an increased need for computing power if a fixed execution time is to be maintained. In any case the level of detail must suit the intended purpose(s) the model is to serve. It is sensible to choose the model that provides sufficient accuracy for the task at hand and invest

the savings in time and effort into other aspects of the research or design program of which the modeling is but one part. Today, detailed finite-element models (FEM) have their place but much of the *meat and potatoes* engine simulation work is still accomplished with simplified models. Large-scale parametric studies are one instance where a simple model is often selected. In this case the identification of general trends is more important than the ability to accurately predict performance for specific cases. Lower computational overhead and shorter simulation run times are distinct advantages. As teaching tools, complex models have little value. Complex models often obscure basic concepts where simplified models can convey the essentials with greater clarity. The literature contains a number of works describing detailed modeling of stratified-charge combustion but there is a notable lack of published work on simple alternatives. This motivates the present work.

1.3 Relevant Information from the Literature

The first step, before setting to the modeling task, is to look back over the history of engine and combustion modeling for any literature with information that may help in establishing a starting point. It has already been noted that there is a lack of published work on simplified modeling of stratified-charge combustion. Relevant works dealing specifically with stratified-charge are presented first. The field is then expanded to include simplified modeling of homogeneous combustion and other works that may contain information relevant to this investigation.

1.3.1 Specific Efforts in Stratified Combustion Modeling

The initial search yielded only a small number of papers published over the last thirty years dealing specifically with stratified combustion modeling. Most of those containing details relevant to this investigation are from researchers with strong interest in the automotive field.

These include Butler, et al. [9] from 1980, Baritaud et al. from 1996 [4], Fan from 1999 [12] and Tatschl and Riediger from 1998 [39]. The modeling approach in all cases is FEM and these publications can contribute nothing directly to the development of a simplified model. In 1998 Robeck and Ellzey [34] published their results for one-dimensional simulation of a CVCC (based on the experimental work of Moriyoshi [32]). This also describes a detailed model (45 computational zones) and is not able to contribute anything relevant to the knowledge base.

The poor result of the detailed search is not a surprise. Strong interest in stratified combustion, at least for IC engine application, is relatively new. It is likely that work on less complex stratified combustion models has taken place. Organizations with the strongest motivation are the auto manufacturers. The wealth of internal publications is not, in general, available and those works unavailable must be considered as not existing at all.

1.3.2 General Approaches to Simplified Combustion Modeling

Unlike stratified combustion modeling, premixed combustion modeling is a well-documented field with many published works. There is a vast amount of material available on the topic in textbooks, papers and journal articles. This vast amount of information must be distilled to the subset of general concepts and sub-models appropriate for addition to the knowledge base. Targets include basic building blocks for a combustion model and noteworthy approaches to the formulation of complete combustion models. Basic building blocks may take the form of fully developed sub-models or general concepts that aid in the development of new sub-models. Successful past combustion simulations are of interest even if they include more the than desired level of detail. These are the most likely source for information on the merits and pitfalls of the many possible combinations of available sub-models. Additional content may include simple and efficient methods for solution of numerical systems by computer. Information of all types gleaned from the general literature search serves the goal of accelerating the model

development process. The effort for a fundamental analysis is reduced and common mistakes are avoided thanks to the astute observations of those who have traveled the same path. A literature filter based on the key requirements of any combustion model is employed. These requirements are identified in the following list.

Chamber Description — The chamber contents must be defined at any stage of the combustion. At the start of combustion the chamber contains only unburned mixture and is described by a suitable set of initial conditions. As mixture burns, the total chamber contents must be described in a manner that remains consistent throughout the entire combustion process.

Flame Geometry — The flame propagates through the chamber with a characteristic shape. The position of the flame as it comes into existence at the point of ignition until it ceases to exist must be tracked.

Flame Speed — Flame speed is not constant with changes in equivalence, temperature and pressure. A means to evaluate the flame speed for any combination of these parameters is necessary.

Mass Reaction Rate — Unburned mixture undergoes an exothermic reaction to exhaust products. The influence of chamber conditions on this process must be determined.

Turbulence — Turbulence is known to affect the combustion duration. IC engines operate with differing levels of turbulence so the effect on the flame speed, mass reaction, etc. must be known.

Heat Transfer — Heat transfer affects the combustion as is known from introductory thermodynamics. In an insulated vessel the adiabatic flame temperature is observed. The CVCC is not insulated heat transfer may be significant and the effect non-negligible.

Mixture Composition — It is known that gas mixture composition may not be constant with changes in pressure and temperature. The range over which the change is significant must be determined and the effect included where appropriate.

Thermodynamic Properties — Property values for the constituent gasses in the unburned and burned mixtures are strong functions of temperature. A simple means to evaluate these and the mixture properties is needed.

Ignition — The choice must be made to model ignition in detail, considering the energy of the electric discharge or to simply initiate the model after a small amount of mass has burned. The more detailed approach should be considered and its value weighed against the additional complexity.

Diffusion — The general literature may also be an indirect source of concepts for the stratified model. Simple models for the turbulent transport of heat, momentum, etc. might be used in a simple mixture diffusion sub-model.

1.3.2.1 The Two-Zone, Turbulent Entrainment – Laminar Burn-Out Model

Much published work in the area of simplified combustion modeling is based on original work published by Blizard and Keck (B&K) in 1974 [6]. This two-zone turbulent entrainment model has been modified and improved numerous times since by various authors but the fundamentals are unchanged throughout. Major contributors to the evolution of this model include: Tabaczynski, Ferguson and Radhakrishnan in 1977 [37], Tabaczynski, Trinker, and Shannon in 1980 [38], Keck in 1982 [23], Beretta, Rashidi and Keck (B-R-K) in 1983 [5], Keck, Heywood and Noske in 1987 [24] and Chen and Veshagh in 1992 [10]. Much of the material is also presented in a condensed form in several texts, including Heywood [18]. The basic approach remains the best basis for a simplified combustion model and addresses many of the needs previously identified.

Chamber Description

Two zones are defined, containing unburned reactants and burned products. Each is assumed to be well-mixed, with uniform properties. The amount of mass in the midst of reacting is usually considered as negligible compared to these two zones.

Flame Geometry

The flame is assumed to propagate with an ideal spherical shape until contact is made with the chamber surfaces. The free burning surface continues its spherical expansion until contact with the cool chamber walls. Changes in burn characteristics in the near-wall regime are not accounted for in most model implementations.

Mass Entrainment and Laminar Burn-Out Rates and the Effect of Turbulence

Most important in the B&K model and its derivatives is the treatment of mass reaction in the flame front. This is modeled as a simple two-step turbulent entrainment and laminar burn-out process and eliminates the need to deal explicitly with chemical kinetics.

$$\frac{dm_e}{dt} = \rho_u \cdot A_f \cdot S_P \tag{1.1}$$

$$\frac{dm_b}{dt} = \frac{m_e - m_b}{\tau_b} \tag{1.2}$$

The model assumes that during turbulent combustion, flame packets are passed on by turbulence over distances of the Taylor microscale (l_M). Laminar diffusion over the Taylor microscale is assumed and once entrained, packets of mixture burn-out at the laminar burning velocity. Mass entrainment is proportional to unburned mixture density, flame area and propagation velocity. Burn rate is proportional to the amount of mass contained in the flame front and inversely proportional to the characteristic burning time (τ_b). This is defined as the time for the flame, traveling at the laminar flame speed, to consume an entrained eddy of size l_M.

$$\tau_b = l_M / S_L \tag{1.3}$$

The turbulent propagation speed (flame speed relative to the flame front) is the sum of the laminar burning and turbulence velocities with an exponential multiplier added to approximate the change from ignition until the combustion becomes fully turbulent.

$$S_P = S_L + u' \cdot \left(1 - \exp(-t/\tau_1)\right) \tag{1.4}$$

Initially, the burn is laminar. The symbol τ_1 denotes the length of the initial period of pre-turbulent combustion. This is the time required for the flame to reach the edge of the first eddy.

1.3.2.2 Peripherals and Support

A range of supporting functions is required for both the homogeneous and stratified models. Key components are assembled from a number of sources. The amount of material available varies from a passing comment in one work to several complete monographs of a single topic.

Changes in Turbulence Velocity and Length Scale

Turbulence velocity and the Taylor microscale are not constant through the combustion process as zone densities vary. There are a number of well-documented models to track these changes. The most common models for quasi-dimensional combustion modeling are reviewed in a 1988 paper by Agarwal, et al. [1]. Each turbulence sub-model is exercised in a two-zone engine model and the results compared against experimental data. The conclusion is reached that two-zone k-epsilon model with transport across the flame front is better than other common models at following an experimental pressure trace. This model, suggested by Borgnakke, et al. in 1980 [8], is not excessively complex or difficult to implement.

Laminar Flame Speed

The most widely used laminar flame speed relationship for propane (the current CVCC fuel) was published by Metgalchi and Keck in 1980 [31]. The authors' power law curve-fit of experimental allows evaluation of the flame speed over the typical range of pressure and temperature encountered in combustion. Heywood [18] simplifies matters and provides

coefficient functions in terms of equivalence. This allows evaluation of laminar flame speed for any pressure, temperature and equivalence without the need to interpolate power law coefficients.

Heat Transfer

Woschni [41] has developed what may be the most commonly used heat transfer sub-model in IC engine modeling. Lumley [27] describes another simple approach with a good degree of detail. This sub-model is implemented in the Stanford Engine Simulation (ESP) program and like the Woschni model, has a proven ability to capture the effects of heat transfer without excess and unwarranted detail. The issue of heat transfer to the ignition electrodes is not directly addressed in either of these works. In the work of Anbarasu, et al. [2], it is claimed that a 1-D heat transfer model is valid for use with ignition electrodes where the thermal penetration is less than one millimeter. This combination of sources provides sufficient information to address all heat transfer issues.

Mixture Composition

Heywood [18] is a convenient source for condensed information on the behavior of gaseous air-fuel mixtures at higher pressures and temperatures. The temperature rise of unburned mixture is limited and the mixture is generally assumed to be unaffected. For the exhaust products, a temperature threshold of 1700K is given, below which the composition is effectively frozen. Above this limit, the composition begins to change as the constituent gasses seek new equilibrium. Assuming that chemical kinetics are fast relative to the other processes it is reasonable to take the mixture at chemical equilibrium. The exhaust mixture can be modeled as a combination of any number of constituent gasses. One simple model limits the exhaust to a mixture of six species: carbon dioxide, water, nitrogen, oxygen, carbon monoxide and hydrogen. A larger number of species can be included but the complexity increases substantially.

Thermodynamic Properties

Evaluation of mixture properties is made easier due to work carried out by government researchers. The resulting JANAF tables provide thermodynamic data for all the required chemical species. Polynomial curve fits for the major species are provided in many texts. Heywood [18] provides the polynomial forms and coefficients for various fuels and for the six exhaust mixture species. With these tools, enthalpy and specific heat for reactants and exhaust products can be evaluated quickly at any temperature.

Ignition

Ignition by electrical discharge in a gas medium is complex and entire papers are devoted to modeling the process. The paper by Shen, et al. in 1994 [35] provides a complete description of the process and a model that includes all dominant effects. This is a good choice if a more detailed model is desired but the complexity is not in keeping with the general goal of model simplicity. The simplest model considers ignition as a discontinuity over which a small amount of mass is entrained and burned. The range of initial enflamed mass fractions in the literature varies from one to five percent with the lower value being most common. Lumley [27] describes in detail a convenient method for solution of the post ignition pressure and temperatures using this simple method. Several additional works dealing specifically with ignition and early combustion modeling approaches are also available in the literature [17, 28 and 42].

Diffusion

The general combustion literature contains little in the way of simple diffusion models. Lumley gives a simple form for the turbulent transport of any mixture property through a length *L* over a time *t*. This provides one possibility for modeling mixture diffusion, simply.

$$L \approx \sqrt{\tfrac{2}{3} \cdot u' \cdot l \cdot t} \tag{1.5}$$

The product of the turbulence velocity and the integral length scale is also known as the turbulent transport coefficient.

1.3.3 Additional Combustion Modeling Literature

There are a number of additional publications not referenced directly that provide nothing well worth reading for background material on combustion modeling [7, 8, 22, 29, 36 and 44].

1.4 Goals

The formation of concrete goals is difficult with the lack of information in the public domain and no basis to determine an appropriate level of detail. If the open-ended problem is viewed as merely the first step in a continuing evolution then modest goals may defined.

- Develop a first iteration model in which simplicity of prime importance.
- Maintain clarity in the model structure to maximize value as a teaching tool and to provide a foundation onto additional details can layered in subsequent iterations.
- Show the promise of continued development by validating the baseline model for a simple fixed volume chamber (for which data are available).

1.5 Methodology for Model Development

The model development process is divided into two steps. The first step is to build a homogeneous model for the specific experimental case. The second step is to extend the base model to include stratified-charge operation of the combustion chamber. The extension is made by applying a simplifying logic, similar to that observed in the reduction of the homogeneous complexity by past researchers.

It is not the intent of the present work to recreate existing work and build a model from first principals. The intent is to use existing, proven techniques for modeling premixed combustion and extend the range of cases to include an initially stratified chamber. Published work will be used to streamline the model development, subject to one constraint. Validation by the author(s) or later researchers is required (no completely theoretical studies) and also wide acceptance by other researchers in the field. This eliminates the need to independently validate borrowed material.

CHAPTER 2

EXPERIMENTAL APPARATUS

Hardware is key to this study as it provides data that is not typically available. Stratified combustion data for a simple geometry CVCC is not to be found in the literature. A CVCC capable of stratified-charge operation at elevated pressure was previously designed and constructed at Ohio State University's Center for Automotive Research to study the fundamentals of stratified combustion. Physical layout and functionality of the system are described here without excess detail. The reader is referred to the author's MS Thesis [21] for a detailed design synthesis and more thorough description of the hardware. Additional material on CVCC testing for homogeneous and stratified combustion is available in a number of publications [3, 13, 14, 15 and 33].

Current specifications for the system are listed in Table 2.1. The complete system is shown in Figure 2.1 in simplified block-diagram form.

Chamber Size	76.2 x 76.2 x 25.4 mm
Working Volume	147.5 cm^3
Crevice Volume	~1% (percent of working volume)
Charge Pressure	70 kPa – 0.7 MPa
Fuel / Oxidizer	Research Grade Propane / Zero Air
AFR Control Method	Partial Pressures (using PWM flow control)
AFR Range	0.0 – 2.0 (software limited)
Stratifying Mechanism	0.6 mm Partition (actuation time < 100 msec)
Turbulence Generation	Perforated Paddles
Ignition	Inductive Discharge 0.5 mm Stainless Steel Electrodes
Instrumentation	Initial Pressure of Both Zones Initial Gas and Wall Temperatures Combustion Pressure (10 kHz) Natural Light Imaging (up to 500fps)
Additional Features	Synthetic EGR (CO_2 / N_2 mixture) Variable Mixture Diffusion (after partition opening) Exhaust Sampling

Table 2.1: Current Specifications for CVCC Test System

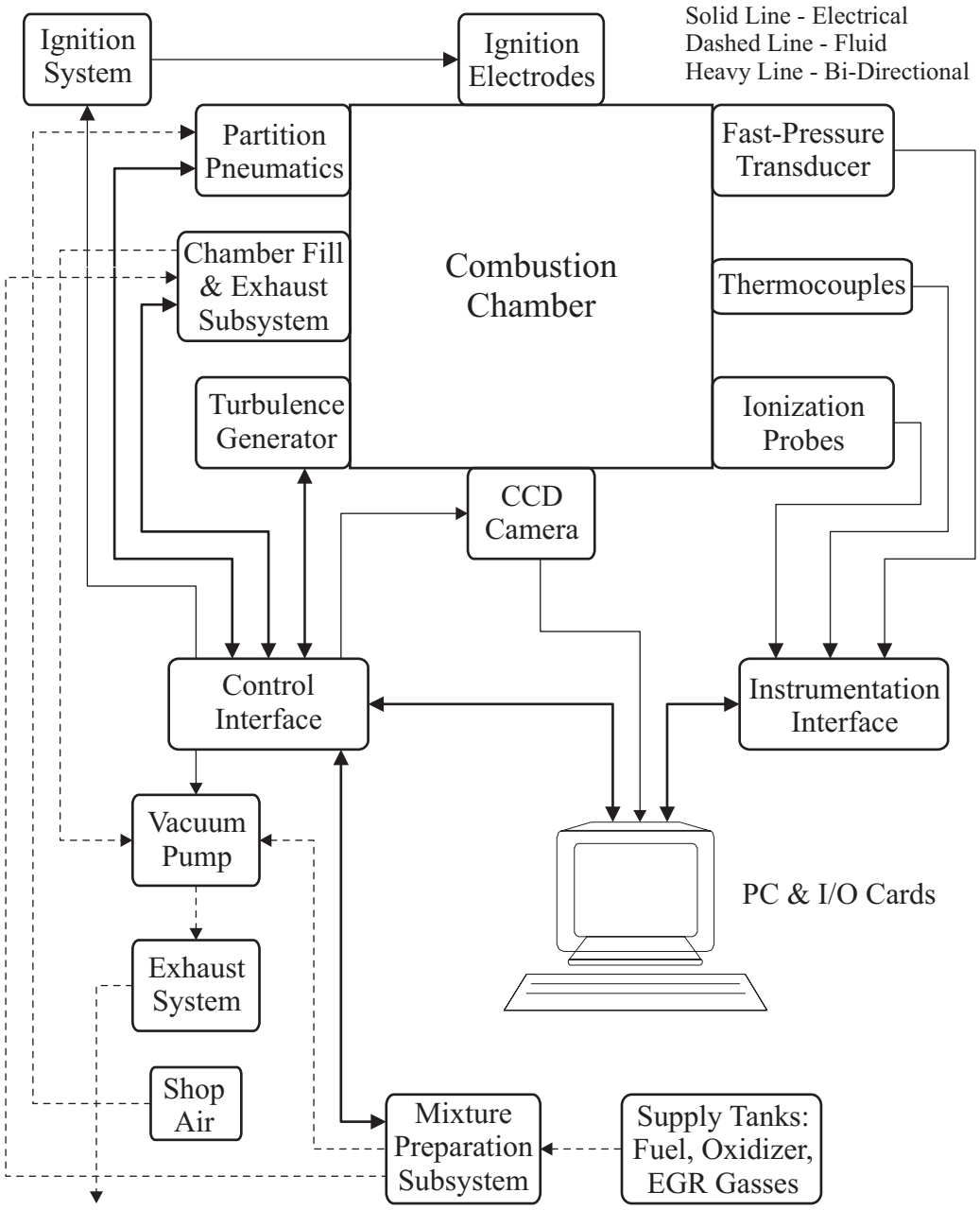

Figure 2.1: Simplified Block Diagram of Complete System

The test system is a safe, user-friendly and robust design. The hardware is designed for trouble-free operation during lengthy test sessions and the highly automated control and acquisition system requires a minimum of effort from the operator to complete each test series.

2.1 Chamber Hardware

The chamber is a robust design and has required only routine maintenance after more than four thousand test cycles.

2.1.1 Basic Construction

The chamber is constructed of 6061 aluminum alloy, several stainless steels and high-performance engineering plastics. A square cross-section with side wall length equal to three times the chamber thickness is used. This provides an abundance of flat surfaces for mounting of instrumentation and the chamber stratifying mechanism. Four interlocking pieces form the main body onto which all remaining components are fastened [Figure 2.2]. This leaves open the possibility for chamber and instrumentation modifications without the need to re-machine the entire frame.

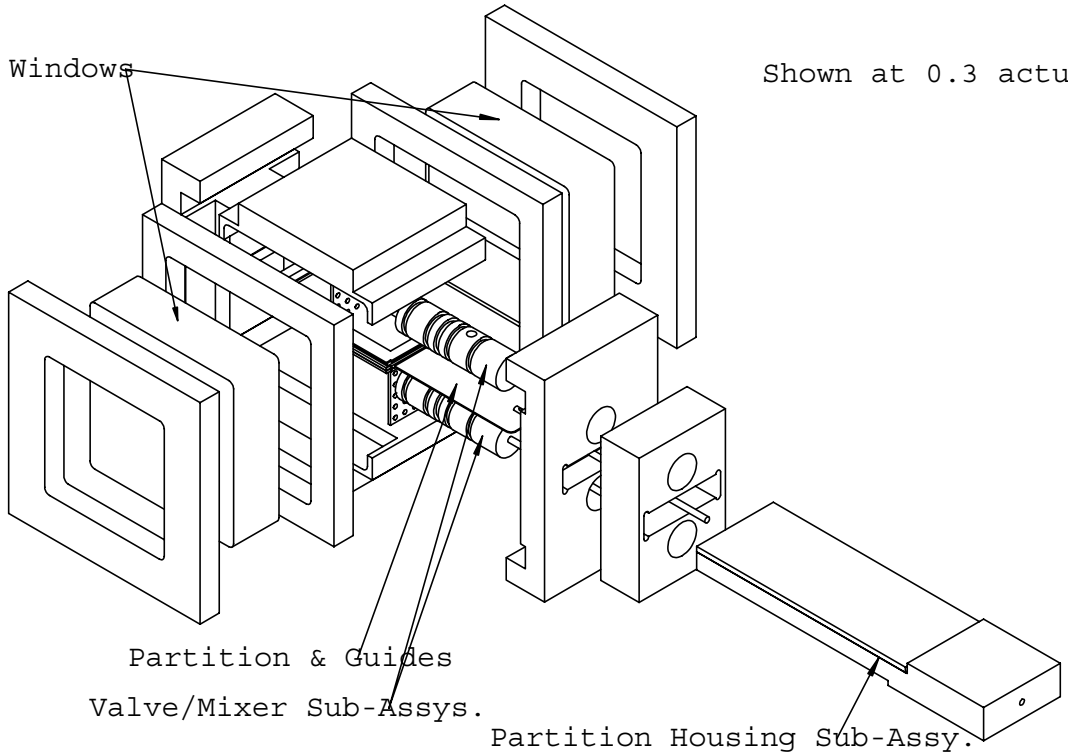

Figure 2.2: Exploded View of Chamber Assembly

Visual access to the chamber is provided by a pair of cell-cast acrylic windows. Crevice volume is minimized at the window/frame junction by close tolerance machining and manual final sizing. The windows, frame and additional components are sealed with a combination of fluorocarbon o-rings and flexible sealants. Fluorocarbon O-rings are used for their compatibility with gaseous and liquid hydrocarbon fuels, their high temperature rating and ability to survive transitions from high vacuum and moderately high pressure. The ability of o-rings to seal with slight dimensional changes at increased temperature also allows the possibility of bomb operation at higher than ambient starting temperature. The upper bound is currently set at 100 C although all tests to date have been from ambient starting temperature.

2.1.2 Chamber Partition – "Stratifier"

Key to successful operation in stratified mode is the chamber partition and its actuating mechanism. The partition is 0.6 mm thick polished stainless steel running in Teflon guides. The line drawing [Figure 2.3b and c] shows the partition, guide and the housing into which the partition retracts. Low mass and a low drag surface finish on the partition reduce the actuator force required to accelerate the partition from rest and also the stopping force to bring it to rest. Disturbance of the chamber contents during partition withdrawal is minimized by the thin cross-section and careful shaping to reduce turbulence at the trailing edge. The housing design minimizes jetting of mixture from the housing and a baffle at the opening serves to break up the small flow.

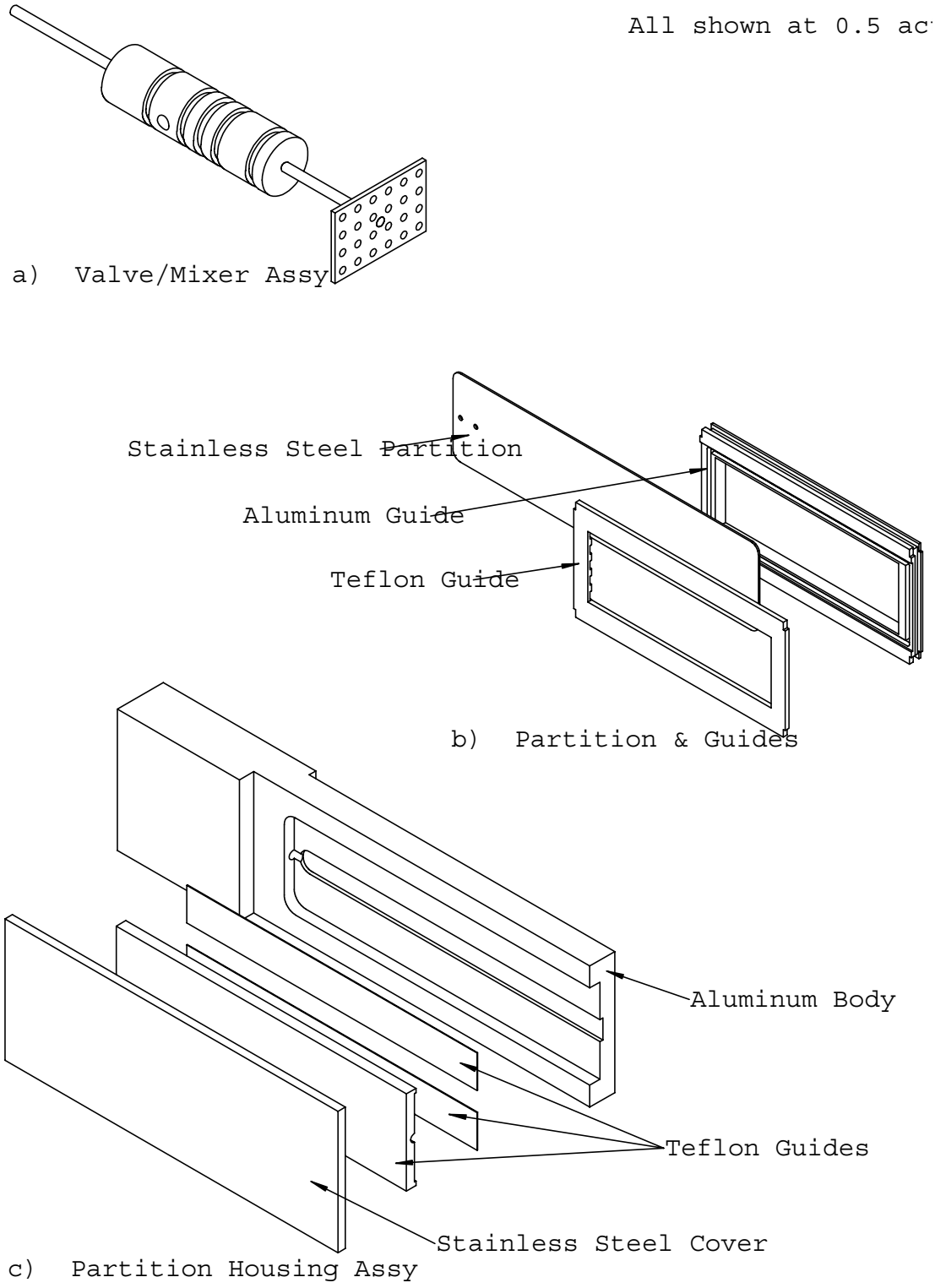

Figure 2.3: Major Chamber Sub-Assemblies

A 19mm pneumatic cylinder is used to drive the partition. The pneumatic circuit [Figure 2.4] allows independent control of the closing (extending into chamber) and withdrawal speeds and the holding force when in the closed position. A surge tank is placed as close to the cylinder as possible to maintain a high average pressure in the cylinder without the need for high supply pressures and/or large diameter supply plumbing. The low moving mass of the partition and actuator requires only a moderate supply pressure of 70 kPa to achieve partition withdrawal times well below 100 milliseconds.

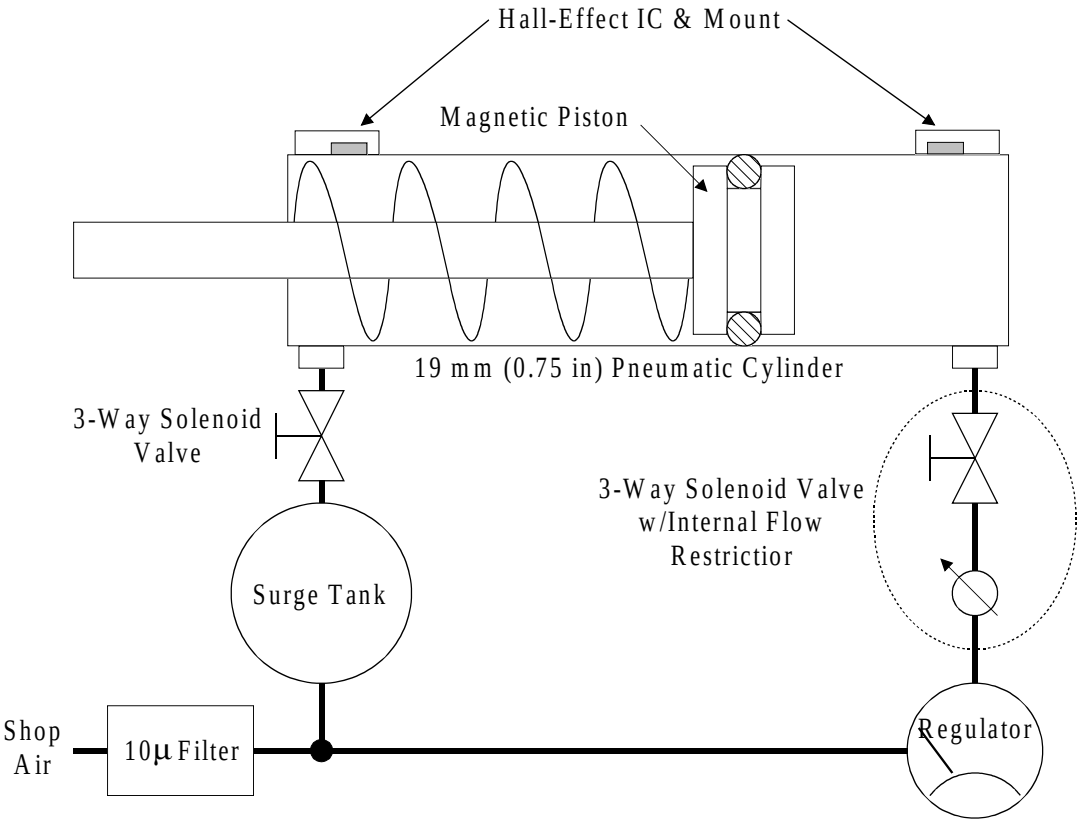

Figure 2.4: Pneumatic Circuit for Fast-Response Partition Actuator

2.1.3 Turbulence Generation

Turbulence is produced by a pair of perforated Teflon paddles [Figure 2.3a]. Integral length scale is determined primarily by the diameter of the perforations (according to Ting, et al. [40]) and turbulence intensity is proportional to the speed at which the paddles are driven. A low cost linear electric actuator is currently used to drive the paddles. Teflon is used for the paddles to allow a tight fit with the frame and windows without causing any appreciable wear. Snug fitting paddles minimize edge leakage and wall flows.

2.1.4 Ignition

The ignition electrodes are 0.5 mm non-reactive stainless steel wire. Small diameter wire is used to minimize heat transfer from the flame kernel during the early stages of its development. Electrodes are mounted on the top wall for normal stratification mode or on the side wall for parallel stratification mode [Figure 2.5].

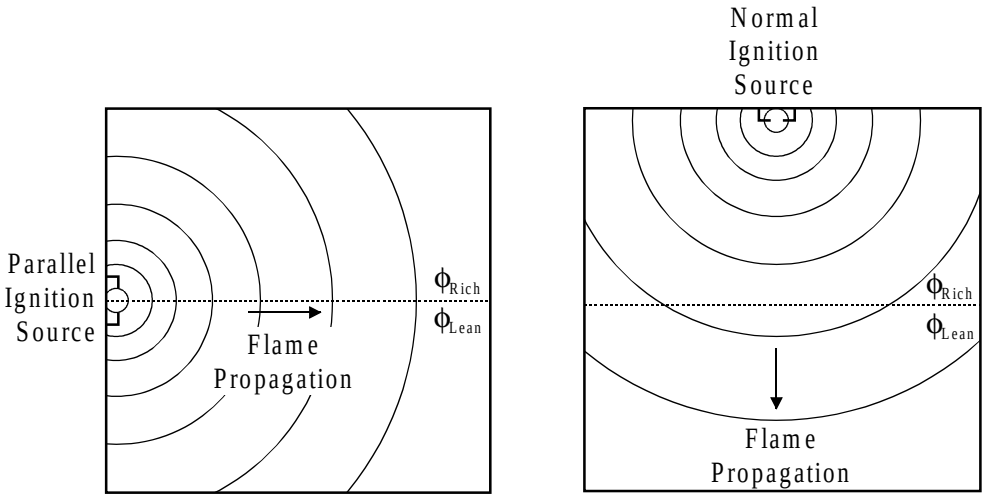

Figure 2.5: Ignition Electrode Location for Parallel and Normal Stratification

In both modes the electrodes are positioned to center the spark gap on the appropriate wall (on the chamber centerline). The electrode mountings [Figure 2.6] provide electrical isolation of approximately 31.4 kV. Isolation of both electrodes reduces voltage surges in the chamber frame and lessens any impact on the instrumentation. Spark gap and wall offset are adjustable and set at 1.0 mm and 6 mm respectively for all runs in the validation data set.

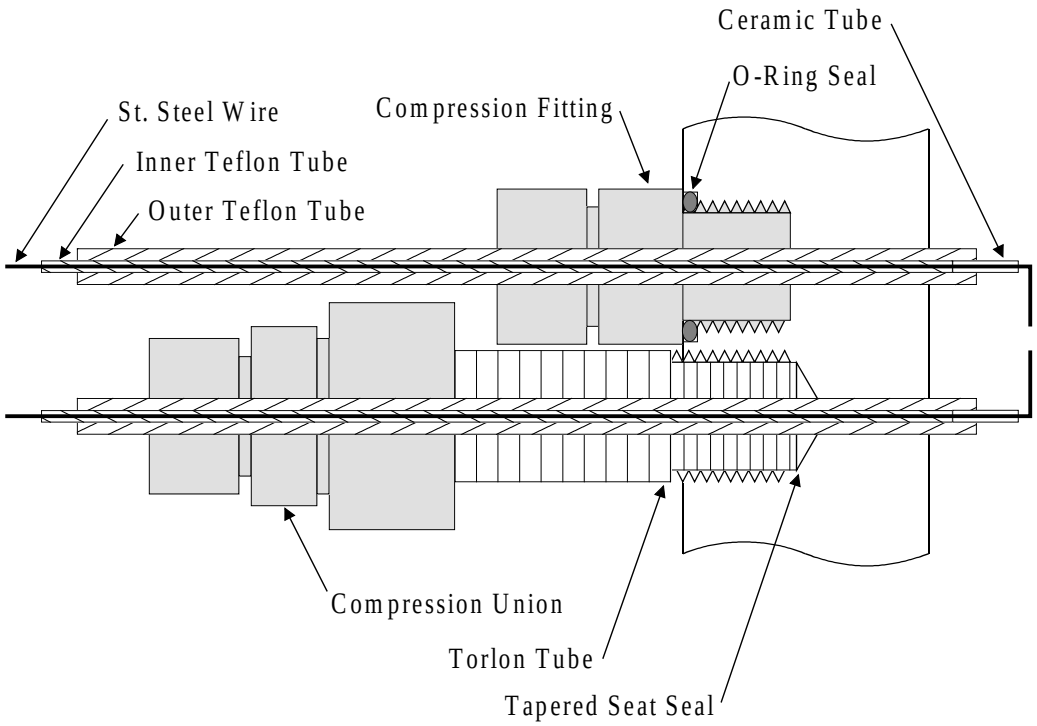

Figure 2.6: Fine-Wire Ignition Electrodes and Isolated Frame Fittings

2.2 Peripheral Hardware

As a safety precaution, the chamber is mounted behind a Lexan shield to reduce the chance of injury to the operator in the event of catastrophic failure. The chamber exhaust and gas purge valve outlets are scavenged by a suction system and safely removed from the lab. All electrical devices, including ten solenoid valves, used to automate the test system are powered by a single power supply that is mounted in a centralized control case. The main power switch controls all these devices and is mounted within easy reach to allow rapid shut down of the entire system if a problem should arise.

2.2.1 Mixture Preparation

The method of partial pressures is used to prepare mixtures of any desired equivalence and EGR dilution. A pair of small mixing tanks (3.8 L) allow preparation of sufficient volumes of rich and lean mixtures to run up to 50 runs at the highest charge pressure. Figure 2.7 shows the mixing system as a simplified fluid schematic. Manual restrictions provide rough adjustment of flow rates with fine control by a PWM flow control scheme [see Section 2.4.4]. A vacuum pump is used to draw the mixing tanks to less than 3 kPa before mixing begins and the control algorithm ensures that supply lines are properly purged after switching between supply tanks.

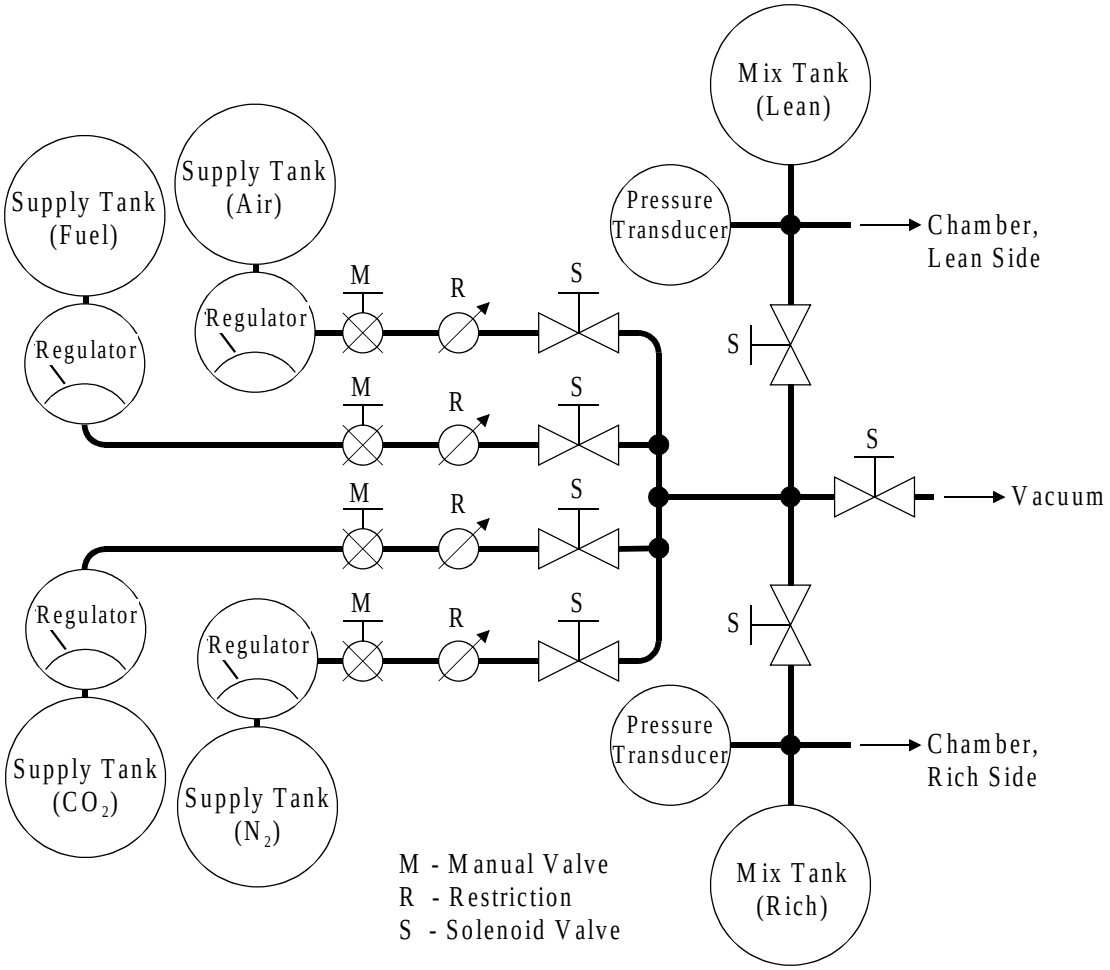

Figure 2.7: Fluid Circuit of Mixture Preparation System

2.2.1.1 Synthetic EGR

Exhaust products are approximated with a blend of carbon dioxide and nitrogen. The mean specific heat of the blend is fixed to correspond to that of the exhaust products over the range of combustion temperatures, assuming complete combustion. The ratio of carbon dioxide and nitrogen is computed for a range of equivalences and a third-order curve fit made to the results. This simple function is used in the control algorithm to determine the proper balance of gasses.

$$CO_2\ Fraction = 0.1582 \cdot \phi^3 + 0.5081 \cdot \phi^2 + 0.6340 \cdot \phi + 0.2331 \qquad (2.1)$$

2.2.2 Chamber Filling, Emptying and Exhaust Sampling

Figure 2.8 shows another simplified fluid schematic for the components involved in filling and emptying the chamber and for sampling the chamber contents after combustion is complete. The vacuum pump is used to evacuate the chamber to less than 6 kPa after combustion is complete. The closed-loop control system [see Section 2.4.4] minimizes the pressure difference between the chamber halves during stratified filling to prevent leakage across the partition. Exhaust sampling hardware is provided for but not currently implemented.

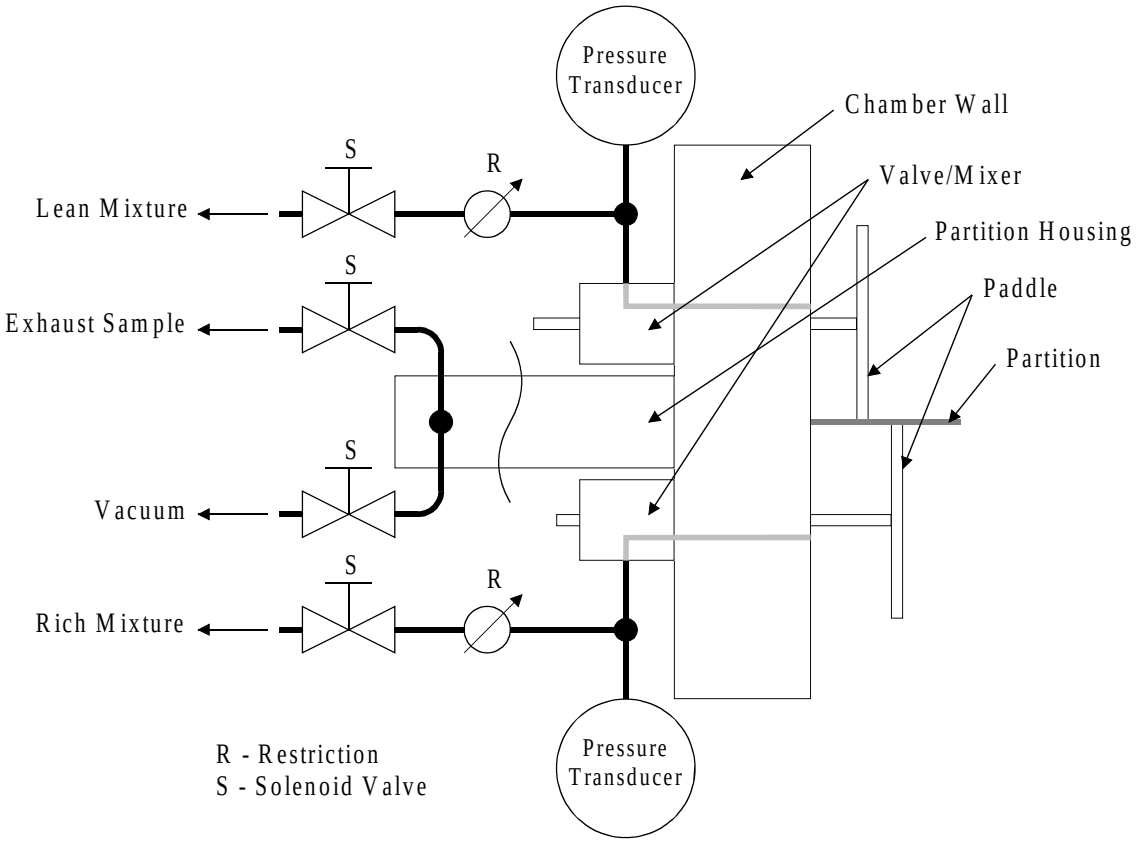

Figure 2.8: Fluid Circuit of Chamber Filling/Emptying System

2.2.3 Ignition System

A self-contained and isolated inductive ignition system is used to ignite the mixture. A separate 12vdc battery powers the ignition and a double buffered interface isolates the computer I/O card from the coil switching circuit. Automotive EMI/RFI suppressed ignition cable completes the system, connecting the module to the chamber mounted electrodes. Attention is paid to ignition isolation to minimize the impact on the highly sensitive instrumentation.

2.2.4 Thermal Management

Temperature rise over a test series is limited by two means. Heated exhaust products are removed quickly from the chamber and a delay between cycles allows heat to pass from the chamber walls to the surrounding air (enhanced by an electric fan).

2.3 Instrumentation

Instrumentation is grouped under two main headings. First is that required for recording initial chamber conditions and the combustion event. Second is that needed for the peripheral support systems and to provide control and automation of chamber operation. Table 2.2 lists the instrumentation used for control, test sequencing and for monitoring/recording the combustion event.

Data Recording	LabVIEW™ Running Under Windows® 95
PC Interface Cards	National Instruments™ AT-MIO-64-E-3 (Multifunction I/O) National Instruments™ PC-DIO-24 (Digital I/O) National Instruments™ DC-AO-2DC (DIO and Analog Output)
Mixing Tank Pressure	SenSym STI-V1-300A Absolute Pressure Transducers
Position Feedback	Custom Hall-Effect Sensors
Starting Pressure	SenSym STI-V1-100A Absolute Pressure Transducers
Starting Temperatures	J-Type Thermocouples
Combustion Pressure	Kistler Piezo-Electric Transducer (sensor from 6117B) Kistler 5010B Charge Amplifier
Natural Light Imaging	Redlake Imaging MotionScope® PCI500 Digital Cameras

Table 2.2: Control & Acquisition Hardware

2.3.1 Computer Based Acquisition Hardware

The National Instruments™ AT-MIO-64-E-3 multifunction I/O card is configured for a 10 kHz acquisition rate (differential inputs) and minimum possible interchannel delay. This small delay is subsequently removed in post-processing to obtain a fully synchronized data set.

2.3.2 Initial Condition and Combustion Event Recording

Five initial conditions are recorded for the chamber. These include gas pressures and temperatures on both sides of the chamber and the chamber wall temperature. Data recorded during the combustion can range from pressure only to pressure, imaging and an array of ionization current probes. The ionization probes are not used during the validation data tests. More information about the probes can be found in Janes [21].

2.3.2.1 Initial Pressure and Temperature

Initial pressures are measured with a pair of absolute pressure transducers. Three J-type thermocouples are fitted to the chamber for temperature measurements. Two protrude slightly beyond the inside surface to record the gas temperature on each side of the partition and the third reads temperature in the wall several millimeters from the inside surface. This provides an average value for the chamber frame. Analog Devices monolithic IC thermocouple amplifiers with 1.0 C accuracy are used to interface the thermocouples with the computer I/O card.

2.3.2.2 Combustion Pressure

A Kistler piezo-electric pressure transducer is used to record pressure during the combustion event. The transducer is positioned to be nearly equidistant from the ignition source in both stratification directions to lessen dependency of results on the ignition location. Thermal shock is lessened by mounting the transducer with a slight recess from the chamber wall. The only cost of this option is a slight increase in crevice volume.

2.3.2.3 Combustion Imaging

Natural light imaging is provided by a pair of Redlake Imaging MotionScope® PCI500 charge-coupled-discharge (CCD) digital cameras. A pair of cameras offers greater freedom in how the combustion event is captured. One camera is positioned to capture the local area around the ignition electrodes in order to provide greater detail of early flame kernel development. The second camera is optimally positioned to capture the entire chamber area with the greatest spatial resolution. The detail camera records an area of 40x40 cm at 500 fps and 320x280 pixel image size. The overall camera area is 76x76 cm with the same rate and pixel size.

2.3.3 Peripheral Support and Control/Automation

Instrumentation of the second type, for control and chamber automation, includes pressure transducers and several feedback devices. Pressure in the mixing tanks is measured with a pair of absolute pressure transducers. Position of the partition is sensed with a pair of conditioned Hall-Effect ICs. These are mounted to the pneumatic cylinder and provide a clear signal that the partition is in the open or closed position. Position of the turbulence generating paddles is measured with a linear potentiometer and a simple interface circuit.

2.4 Control

Most aspects of the testing process are automated and controlled by the user, interacting with the system through an intuitive graphical interface. This increases testing efficiency by eliminating several sources of human error.

2.4.1 User-System Interaction (Software)

All programming tasks are accomplished with LabVIEW™ (National Instruments™ graphical programming language). The range of functions under the control and acquisition program is shown in Figure 2.9.

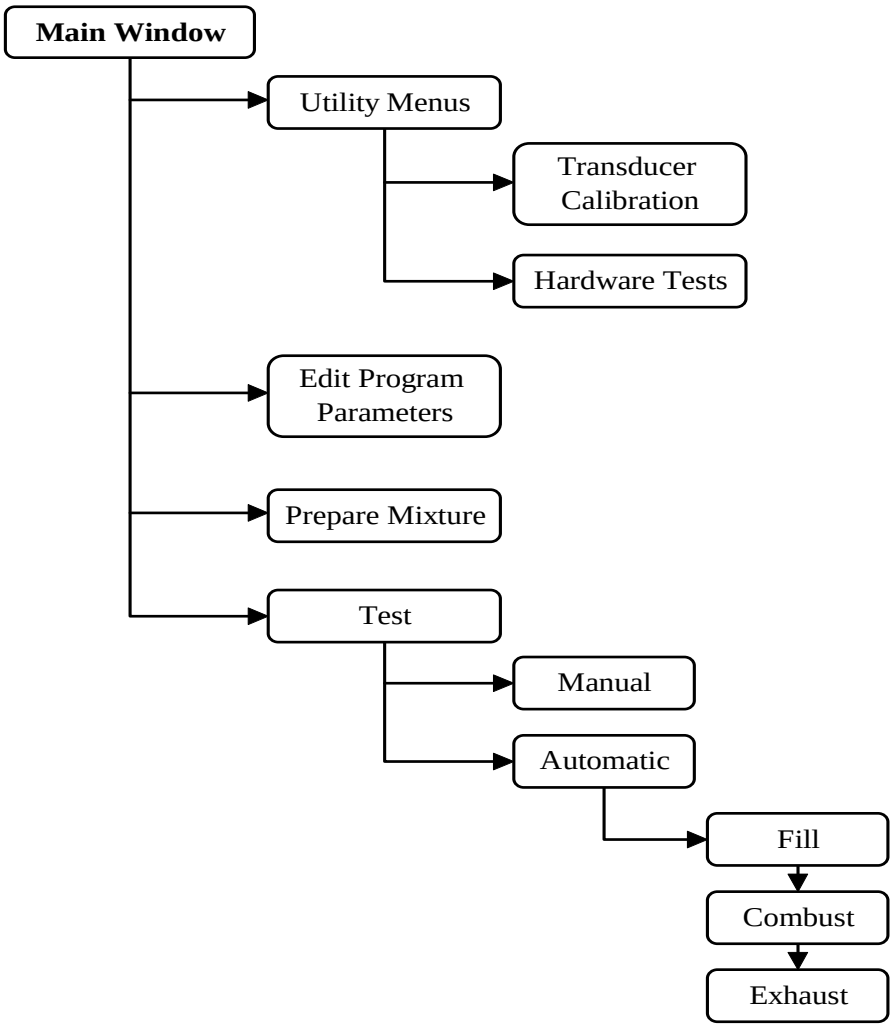

Figure 2.9: Control and Acquisition Program Hierarchy

The main interface window is shown in Figure 2.10. The user has only to set several options and click to start the desired operation. Dialogs and warning dialog boxes are displayed at appropriate times when user intervention is required (opening supply tank valves, etc.). Real-time monitoring of the chamber condition is also provided in another window.

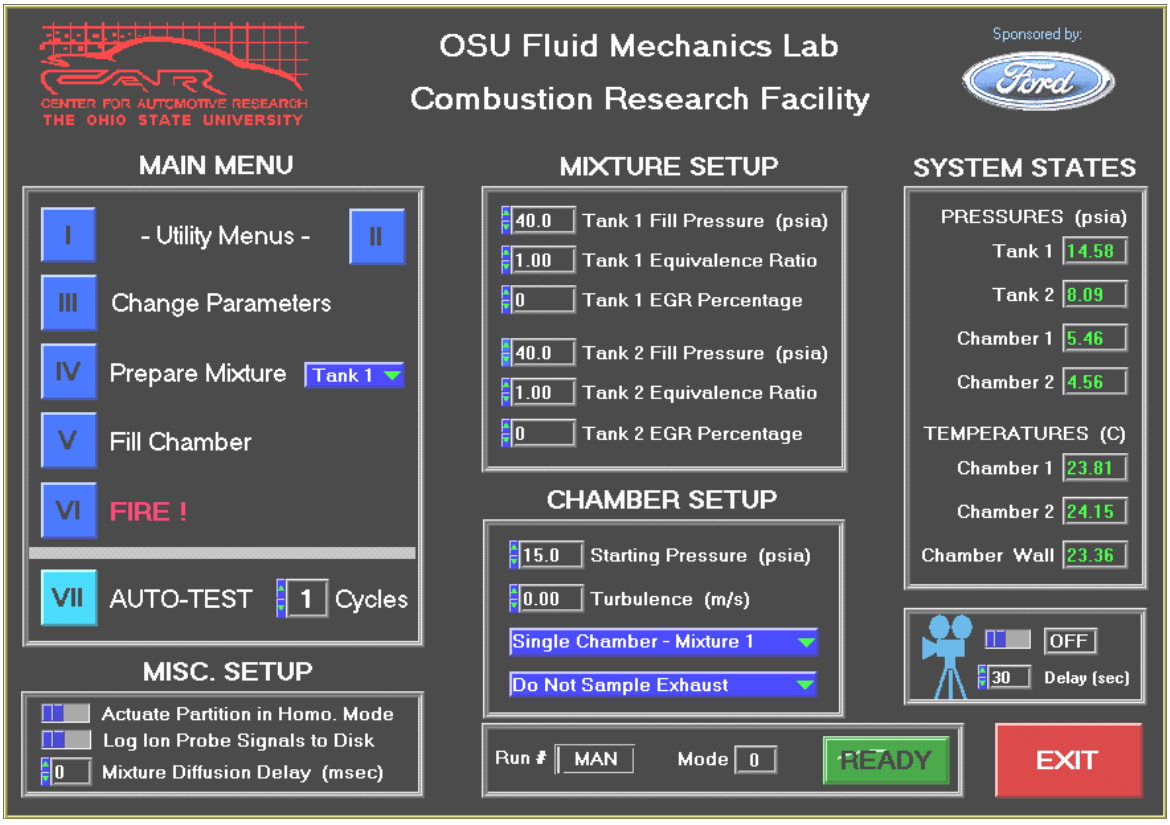

Figure 2.10: Graphical User Interface (Screen Capture)

2.4.2 Error Control

The substantial quantity of combustible mixture under computer control requires the control system be free of operating glitches that might cause unintended release into the lab. Several steps are taken to minimize this risk. On-screen dialogs are used to instruct the user when to open and close manual supply valves. Software time limits are also imposed so that if any process does complete within the expected time an error code is generated. In the event of an error an error message is displayed, all hardware is set to a default safe state and program execution ceases.

2.4.3 Automated Test Sequencing

Up to 50 test cycles can be run without user input. The user specifies initial conditions of pressure and turbulence intensity and then the requested number of combustion cycles is automatically executed and the data logged. Dated directories are automatically created and files are time stamped and sequentially numbered. Automatic file control eliminates the chance of accidental overwrites and simplifies file handling in post-processing routines. Operation in automated mode is truly hands-off.

2.4.4 PWM Flow Regulation Scheme

Fine flow rate adjustment is obtained by effectively transforming the simple solenoid valves into computer-controlled variable orifice devices. The AT-MIO-64-E-3 multifunction I/O card has counter/timer functions that can be used to generate a variable frequency and duty cycle (PWM) signal. This feature is used to drive the solenoid valves in pulsed mode and vary the time averaged solenoid valve orifice. Flow rates can be reduced to less than 20 percent of the maximum with this control system.

2.4.5 Operating Procedures

Key operating procedures of mixture preparation and chamber firing are outlined in this section.

2.4.5.1 Mixture Preparation

Closed-loop control is used to prepare mixture in either the rich or lean mixing tank up to software limited pressures of 1.4 MPa (equivalent to 50 runs at maximum initial pressure) and equivalence ratios of 2.0.

The mixing tank is first evacuated, short-filled with air (to 70 kPa) and then evacuated a second time. This ensures a known content at the start of mixing and is necessary since an

absolute vacuum cannot be attained. Fuel is added to the tank followed by EGR (if this option is selected) and then zero air. The PWM flow regulation scheme provides rapid filling and accurate final pressure control by filling in several stages. A high flow rate is used during the initial fill up to 85-90 percent of the target pressure. Tank temperature is then allowed to equilibrate. Duty cycle is reduced and filling continues at a lower flow rate up to the final pressure. Measured fuel pressure, which differs slightly from target pressure in most cases, is used to revise the target air pressure for improved equivalence accuracy. This method of mixture preparation provides typical error of less than 0.3 kPa and equivalence error less than 0.01.

2.4.5.2 Fire-Acquire Sequence

Manual control over chamber filling and firing is available but in most cases it is desirable to use the auto-test sequencer option. A complete automated test cycle consists of several steps.

Chamber Filling

The chamber is filled using a procedure similar to that described for mixture preparation. A partial fill is made to purge the mixing tank lines and ensure the chamber has no holdover from the previous cycle. The chamber is then evacuated a second time before filling to the desired pressure in two stages.

Filling in stratified mode is more complex as the pressure differential across the partition must be minimized to prevent mixture crossover. The mixture tank pressures are first equalized to better balance flow rates to each side of the divided chamber. The control system monitors pressure on both sides of the partition and interrupts flow so the pressure differential is minimized.

Turbulence Generation

Turbulence is generated by sweeping the perforated paddles across the full length of the chamber. Paddle speed is controlled by PWM control that provides a continuous range from zero to the maximum unregulated speed.

Partition Movement

The partition is synchronized to withdraw from the chamber after the mixing paddles have completed their sweep.

Mixture Diffusion

If a mixture diffusion delay is specified the system pauses after the partition moves for the required period.

Start of Acquisition

Data acquisition is digitally triggered after the partition has moved and any diffusion delay has elapsed. The trigger pulse is also used to synchronize external instrumentation such as the digital camera(s).

Ignition and Combustion

The ignition is triggered and data are recorded for a specified period that depends on mixture strength and chamber configuration. The usual period for homogeneous combustion is 250 msec.

Exhaust

The products of combustion are removed from the chamber as soon as possible to minimize exposure of the acrylic windows and minimize the chamber temperature rise. In the case that the exhaust sampling option is, the exhaust opens to purge any unburned mixture from the partition housing and then the exhaust sample valve opens to direct flow to an instrument or sample container.

Cycle Control

A fixed delay is used between cycles to allow temperature of the chamber frame to stabilize. This reduces the rise in heat transfer surface temperature from the first cycle to the last. A delay of 120 seconds is used for a total cycle time of approximately three minutes.

CHAPTER 3

HOMOGENEOUS-CHARGE MODEL

A homogeneous model is developed in this chapter for combustion in the CVCC. Substantial sub-model detail is provided since the stratified model can share the same basic structure. A reverse model is also developed in order to determine constants for relationships that require tuning for the specific CVCC geometry, material, etc. (one example is the heat transfer coefficient).

3.1 Model Detail and Appropriate Assumptions

Simplifying assumptions are made to reduce the complexity of the modeling problem without deviating significantly from reality.

3.1.1 Chamber Geometry

Surfaces of the chamber are rigid so the chamber volume is assumed to be constant throughout the combustion process. The effect of crevice volumes is neglected since the total crevice volume is approximately one percent of the working chamber volume. Slight imperfections in the basic chamber shape (a rectangular box) are neglected.

3.1.2 Multiple, Distinct Chamber Zones

Two zones are defined following common modeling practice [Figure 3.1].

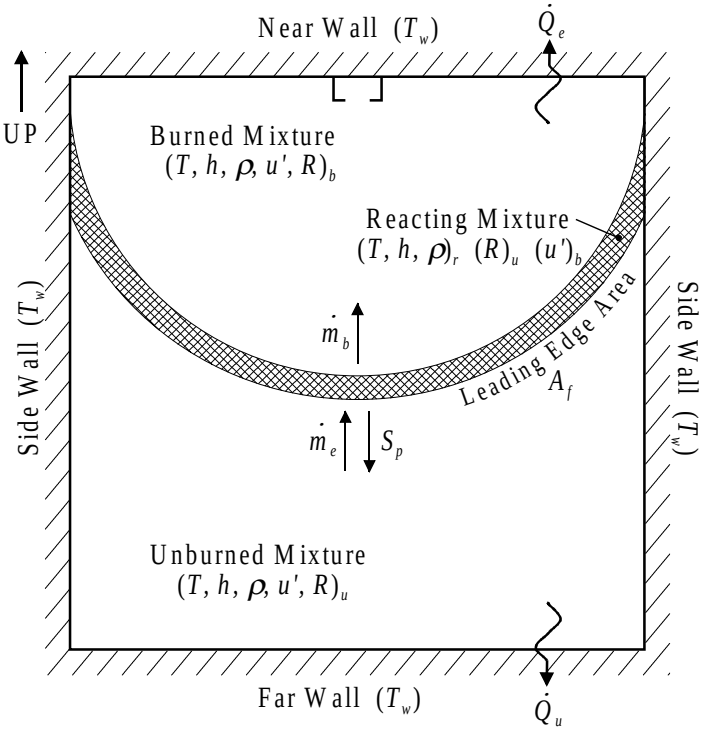

Figure 3.1: Idealized Combustion in a CVCC

The unburned zone is defined as the region ahead of the flame front and contains only reactants. The entrained zone is defined as the region behind the leading edge of the flame front and is comprised of two sub-zones. First is the reaction zone where reactants undergo the thermochemical process to products. The reaction zone contains only reactants since products are immediately transferred to the burned sub-zone after reaction is complete. The burned sub-zone

contains only exhaust products. Each of the three zones is taken at a uniform (bulk) temperature, specific density (mixture equivalence) and turbulence intensity.

Model equations are developed using three zone masses and unique zone properties. This allows a choice in the treatment of the reaction zone. The equations can be left in original form and the reaction zone treated as having a non-negligible mass. A thin reaction zone can also be assumed in which case masses in the entrained sub-zones are combined and the model collapses along the lines of the common two-zone formulation. A difference between the two formulations should be evident in the early stage of combustion. During this period, the fraction of the total entrained mass within the reaction sub-zone is greatest. As the combustion progresses, the ratio of the burned and reacting masses continues to increase and the contribution of the reacting mass to the (entrained) zone-averaged property values becomes less significant.

3.1.3 Flame Geometry

Ignition occurs at the center of the ignition electrode gap and the flame initially propagates as a sphere until contact is made with the first chamber surface. After wall contact the free-burning (propagating) surface continues as a sphere with the constraints imposed by the chamber geometry. The ignition location is centered on the chamber wall and there is no large-scale directionality in the flow field (isotropic turbulence is assumed). The center of the spherical expansion is therefore constant and is not displaced during the process. Change in the shape of the flame front in the near wall region is neglected and constant curvature is assumed throughout combustion. This is not the actual case since lower temperatures and reduced fluid motion in the near wall region both cause a slowing of the front. This assumption greatly reduces the complexity of the flame geometry. With centered ignition and the other assumptions it is clear that flame front geometry is symmetric and this allows a simplification in the analysis by considering only one-quarter of the chamber.

3.1.4 Flame Speed

The flame speed correlation of Metgalchi and Keck [31] as presented in Heywood [18] is used. This allows flame speed to be written as a function of temperature, pressure and turbulence velocity.

3.1.5 Mass Entrainment and Reaction Rates

A modified form of the Blizard and Keck turbulent entrainment model is used. The chemical reaction rate is assumed to be sufficiently fast that turbulent transport dominates the entrainment rate after an initial pre-turbulent period. Laminar diffusion is assumed over a distance of the Taylor length scale so that mass within an entrained eddy burns in a characteristic time, equal to the ratio of the Taylor length scale and laminar flame speed.

3.1.6 Flame Extinction / Completion of Burn

The end of the burn phase is determined by mixture strength, pressure and temperature (significant wall heat transfer effect). All mixture in the chamber may not react before conditions become unsuitable for flame propagation. It is not likely for the range of homogeneous mixtures planned that a significant amount of unburned mass will result so a simple maximum entrained mass fraction of 99.9 percent determines completion of the burn.

3.1.7 Turbulence

Turbulence at ignition is assumed to isotropic. After ignition, turbulence increases in the unburned zone as it is compressed by the expanding burned zone. Turbulence energy is also transferred between zones as unburned mass enters the reaction zone. Any attenuation during the boundary crossing is neglected. Turbulence energy in both zones is allowed to decay at a rate based on a simple turbulence model. For simplicity, the initial integral length scale is computed as a function of the turbulence generating paddle hole size as suggested by Ting [40].

3.1.8 Heat Transfer

Convective heat transfer from the unburned and entrained zones to chamber surfaces (including the ignition electrodes) is included. The thermal boundary layer is neglected and wall temperature is taken as constant throughout the combustion. The fine-wire ignition electrodes thermal mass is far smaller and the temperature is allowed to vary according to a simple lumped parameter model. Mixtures are near stoichiometric and any heat transfer due to banded radiation is neglected since insignificant amounts of soot particles are formed. Simple heat transfer between the burned and unburned zones is included in the later stages when the effect becomes more pronounced.

3.1.9 Gas Mixtures

Combustion reactants and products are mixtures of gasses that obey the ideal gas law and do not dissociate at high temperature. Reactants are taken as a mixture of propane fuel, nitrogen and oxygen. Water and trace gasses are neglected since Zero contains only negligible amounts of both. Combustion products are modeled with the common six species mixture model (carbon dioxide, carbon monoxide, water vapor, diatomic hydrogen, oxygen and nitrogen). The equilibrium reaction is valid for evaluation of mixture composition since chemical kinetics are assumed to be significantly faster than the simulation time scale.

Water can exist in the chamber in three different forms: vapor, suspended liquid droplets and droplets condensed on the surfaces. During the burn period when mean temperature and turbulence are high, the vapor pressure is sufficiently high that droplet formation is not likely. Condensation is therefore neglected during the burn period.

3.2 Forward Model

The basic function of the forward model is represented graphically in Figure 3.2. Inputs to the model are the initial conditions: temperature, pressure, turbulence intensity and length scale. For a specific set of initial conditions the time histories of pressure and flame front position are predicted.

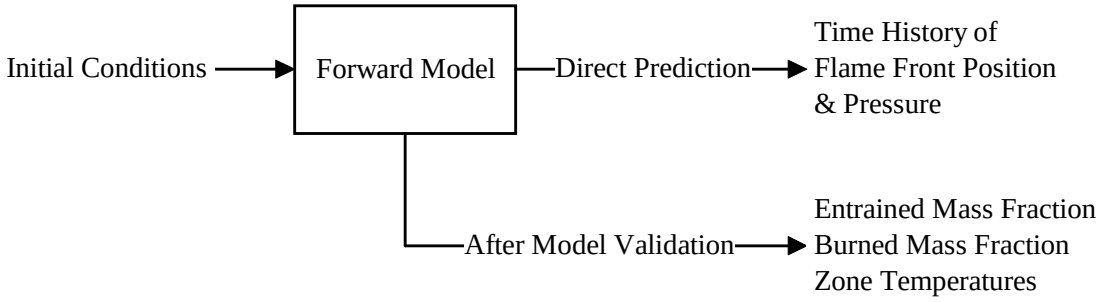

Figure 3.2: Functional Form of Homogeneous-Charge Forward Model

These results allow direct comparison of the model output against experimental data generated in the CVCC facility. Model parameters can be tuned with a small data set for improved performance and the result validated against additional experimental cases. Once validated it is possible to use the model for extraction of additional information about the combustion such as the time histories of entrained and burned mass fractions and temperatures in the unburned and entrained zones.

In the sections that follow a system of equations is developed without any simplifying grouping of terms. Additional supporting relationships, property evaluation methods, etc. are also described. Each equation is manipulated into a standard form with progress variables of pressure, unburned and burned temperature, entrained and burned mass fractions.

3.2.1 Chamber Co-Ordinate System

Before defining necessary geometric parameters a co-ordinate system must be established. The co-ordinate system shown in Figure 3.3 is established to take advantage of the chamber shape, ignition electrode location (centered on the top wall) and symmetry of the flame front.

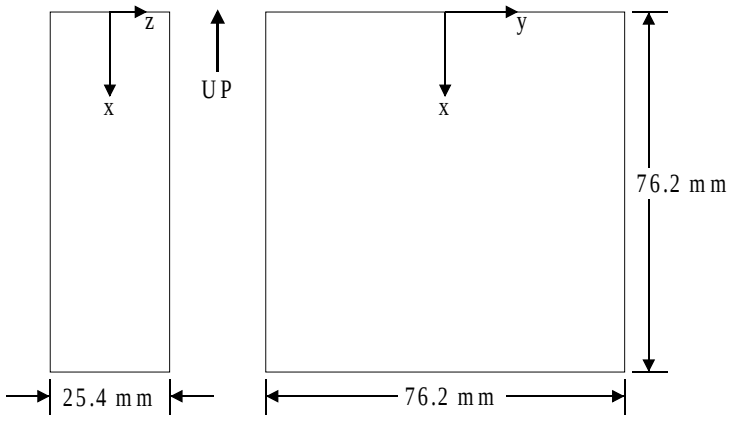

Figure 3.3: Chamber Co-Ordinate System

3.2.1.1 Basic Geometric Parameters

Basic geometric values for the chamber include total volume and wall areas. Equations 3.1 through 3.5 define these values in terms of the chamber length and thickness.

Volume of chamber $$V_c = t_c \cdot L_c^2 \tag{3.1}$$

Area of far wall $$A_{fw} = t_c \cdot L_c \tag{3.2}$$

Area of near wall $$A_{nw} = t_c \cdot L_c \tag{3.3}$$

Area of side walls $$A_{sw} = 2 \cdot t_c \cdot L_c \tag{3.4}$$

Area of windows $$A_w = 2 \cdot L_c^2 \tag{3.5}$$

Surface names are assigned with reference to the ignition source. The near wall is that on which the ignition electrodes are located. Similar logic is used in naming the side walls and far wall [see Figure 3.1].

3.2.2 Flame Geometry

The flame front shape is idealized as a sphere expanding in and constrained by the walls of a flattened box. Geometric parameters of interest are entrainment area, entrained volume and contact areas of each zone with the walls and ignition electrodes. The process is first characterized from ignition until maximum entrainment. A method is then formulated to generate the required parameters through the entire combustion process.

3.2.2.1 Phases of Flame Front Development from Ignition to Extinction

The front spends a short time expanding in free space before coming into contact with the first chamber surface. Contact is then made with additional surfaces until finally, any subsequent burning takes place at the walls. With an ignition source close to the wall, there are eleven phases of development during which the flame comes into contact with an increasing number of surfaces. These phases are defined by a range of flame front radius values in equations 3.6 through 3.16. Values are given in terms of chamber length, thickness and ignition offset from the wall. Equation 3.17 gives the terminating criterion for flame front radius. After the front reaches this distance, burning takes place only at the chamber surfaces.

During Phase 1, the flame front expands as a sphere in free space.

$$0 \le r_e < SO \tag{3.6}$$

Phase 2 begins after the flame front has contacted the near wall. The shape is a sphere less a spherical cap at the wall. The first two phases as presented are valid only for the case where the offset of the ignition gap is less than one-half of the chamber thickness. This is the case for all planned tests.

$$SO \le r_e < \tfrac{1}{2} \cdot t_c \tag{3.7}$$

Phase 3 begins after the flame front has contacted the windows. There are now two additional spherical caps at the windows.

$$\tfrac{1}{2} \cdot t_c \le r_e < \sqrt{\left(\tfrac{1}{2} \cdot t_c\right)^2 + SO^2} \tag{3.8}$$

Phase 4 begins after the front has contacted the edges at the junctions of the near wall and windows. The shape now becomes too complex to provide a simple description.

$$\sqrt{\left(\tfrac{1}{2}\cdot t_c\right)^2 + SO^2} \le r_e < \tfrac{1}{2}\cdot L_c \tag{3.9}$$

Phase 5 begins after the front has contacted the side walls.

$$\tfrac{1}{2}\cdot L_c \le r_e < \sqrt{\left(\tfrac{1}{2}\cdot L_c\right)^2 + SO^2} \tag{3.10}$$

Phase 6 begins after the front has contacted the edges at the junctions of the near and side walls.

$$\sqrt{\left(\tfrac{1}{2}\cdot L_c\right)^2 + SO^2} \le r_e < \sqrt{\left(\tfrac{1}{2}\cdot t_c\right)^2 + \left(\tfrac{1}{2}\cdot L_c\right)^2} \tag{3.11}$$

Phase 7 begins after the front has contacted the edges at the junctions of the side walls and windows.

$$\sqrt{\left(\tfrac{1}{2}\cdot t_c\right)^2 + \left(\tfrac{1}{2}\cdot L_c\right)^2} \le r_e < \sqrt{\left(\tfrac{1}{2}\cdot L_c\right)^2 + SO^2 + \left(\tfrac{1}{2}\cdot t_c\right)^2} \tag{3.12}$$

Phase 8 begins after the front has contacted the corners at the junction of the near wall, side walls and windows.

$$\sqrt{\left(\tfrac{1}{2}\cdot L_c\right)^2 + SO^2 + \left(\tfrac{1}{2}\cdot t_c\right)^2} \le r_e < L_c - SO \tag{3.13}$$

Phase 9 begins after the front has contacted the far wall.

$$L_c - SO \le r_e < \sqrt{\left(L_c - SO\right)^2 + \left(\tfrac{1}{2}\cdot t_c\right)^2} \tag{3.14}$$

Phase 10 begins after the front has contacted the edges at the junctions of the far wall and windows.

$$\sqrt{\left(L_c - SO\right)^2 + \left(\tfrac{1}{2}\cdot t_c\right)^2} \le r_e < \sqrt{\left(L_c - SO\right)^2 + \left(\tfrac{1}{2}\cdot L_c\right)^2} \tag{3.15}$$

Phase 11 begins after the front has contacted the edges at the junctions of the side walls and windows.

$$\sqrt{\left(L_c - SO\right)^2 + \left(\tfrac{1}{2}\cdot L_c\right)^2} \le r_e < \sqrt{\left(L_c - SO\right)^2 + \left(\tfrac{1}{2}\cdot L_c\right)^2 + \left(\tfrac{1}{2}\cdot t_c\right)^2} \tag{3.16}$$

Phase 12 (final phase) begins after the front has contacted the corners at the junctions of the far wall, side walls and windows. Burning in this phase takes place only at the walls and windows.

$$r_e = \sqrt{\left(L_c - SO\right)^2 + \left(\tfrac{1}{2}\cdot L_c\right)^2 + \left(\tfrac{1}{2}\cdot t_c\right)^2} \tag{3.17}$$

3.2.2.2 Burned and Unburned Heat Transfer Areas at Walls

At each flame front radius, the locus of points on each surface formed by the intersections of all differential slices and the specific surface form a bounding curve for the entrained/burned zone heat transfer area. Unburned heat transfer area for each surface is the difference of the total surface area and the entrained zone area for the surface.

Unburned area at far wall $$A_{hx,u,fw} = A_{fw} - A_{hx,e,fw} \tag{3.18}$$

Unburned area at near wall $$A_{hx,u,nw} = A_{nw} - A_{hx,e,nw} \tag{3.19}$$

Unburned area at side walls $$A_{hx,u,sw} = A_{sw} - A_{hx,e,sw} \tag{3.20}$$

Unburned area at windows $$A_{hx,u,w} = A_w - A_{hx,e,w} \quad (3.21)$$

3.2.2.3 Ignition Electrode Heat Transfer Area

Heat transfer areas for the ignition electrode, exposed to the flame kernel are also required if the characteristics of early kernel development are to be accurately captured. The wire diameter is only 0.5 mm but if initial flame kernel diameters are on the order of several millimeters, early heat transfer to the electrodes can still have a significant impact.

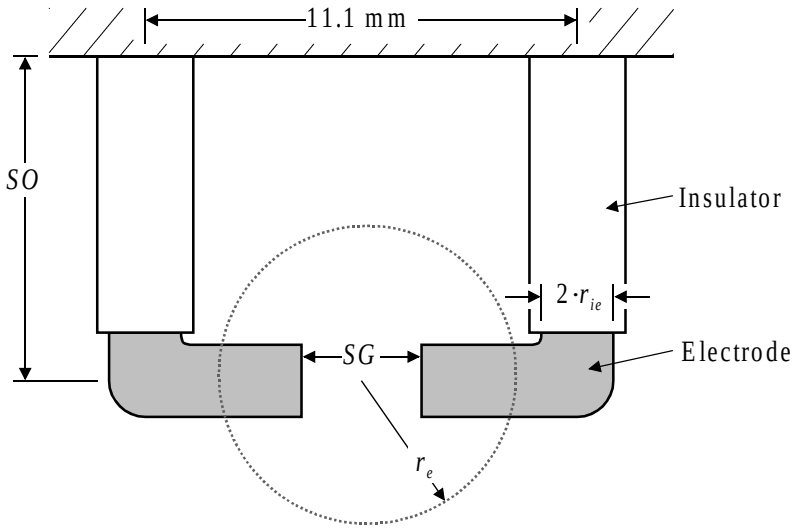

Figure 3.4: Early Flame Front Detail at Ignition Electrodes

As Figure 3.4 illustrates, each electrode is insulated from the chamber wall until the 90 degree bend. The electrode area varies when the flame radius has a value in the range

$$SG \le 2 \cdot r_e < 11.1\,mm \ . \quad (3.22)$$

This maximum value corresponds to the centerline of the insulator and the slight increase beyond is ignored. Total area is twice the sum a circular disc and short cylinder and is defined in terms of the wire radius, spark gap and flame radius.

$$A_{hx,ie} = 2 \cdot \pi \cdot r_{ie} \cdot \left(r_{ie} + 2 \cdot r_e - SG \right) \tag{3.23}$$

The area takes a constant value after flame contact with the insulators.

$$A_{hx,ie} = 2 \cdot \pi \cdot r_{ie} \cdot \left(r_{ie} + 11.1\, mm - SG \right) \tag{3.24}$$

3.2.2.4 Method for Generating Flame Front Geometry

Expressions in closed form may be derived for most if not all of the phases but is it easier to approximate the values using a general algorithm. This leaves open the possibility of changing chamber parameters and recomputing areas and volumes for other cases, with minimal effort. Geometry is generated using spherical co-ordinates. This is sensible given the assumed spherical flame front. A differential disc approach used is shown in Figure 3.5. The slice (bounded disc) is intersected with all appropriate bounding surfaces at the given level (z co-ordinate) and the areas and volumes computed. Individual areas and volumes for each slice are summed to give the quadrant values (one-quarter of the total chamber values). Volumes, flame front area and heat transfer areas are tabulated for the full range of flame radius values and written to a look-up table for implementation in the simulation.

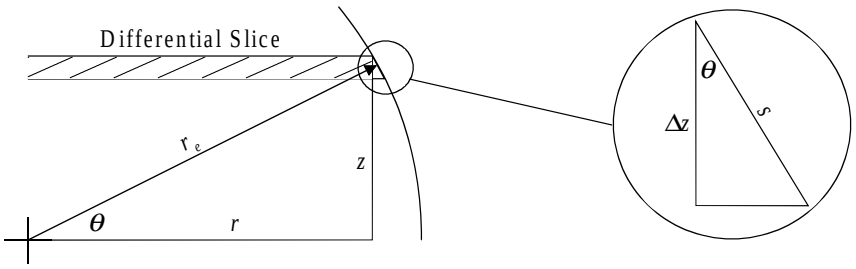

Figure 3.5: Flame Front Geometry Approximation Method

The effect of curvature (of the spherical front) is also accounted for in order to reduce error in area and volume approximations. Values for the error in area due to the curvature are obvious when the equation for the arc length (Equation 3.26) is considered. As the angle θ (Equation 3.25) nears a value of 90 degrees in the topmost slices, the error can be significant for early phases where the front radius is small. The correction is less important in later phases as the front radius increases and the angle θ approaches zero.

Inclined angle of disc face $$\theta = \sin^{-1}\left(z/r_e\right) \tag{3.25}$$

Arc length of disc face $$s = \Delta z/\cos\left(\theta\right) \tag{3.26}$$

3.2.2.5 Validation of Geometry Generation Method

Geometry data are generated using 125 differential slices and 500 radial steps in order to obtain satisfactory resolution in each geometry parameter. Ignition offset obviously affects the result and here the test configuration value of 6 mm is used. Figure 3.6 shows all the geometrical parameters plotted against entrainment radius. Some breaks between phases are easy to identify and other less so. Vertical lines are added to clearly indicate the breaks and show the span of radius values over which each phase is valid.

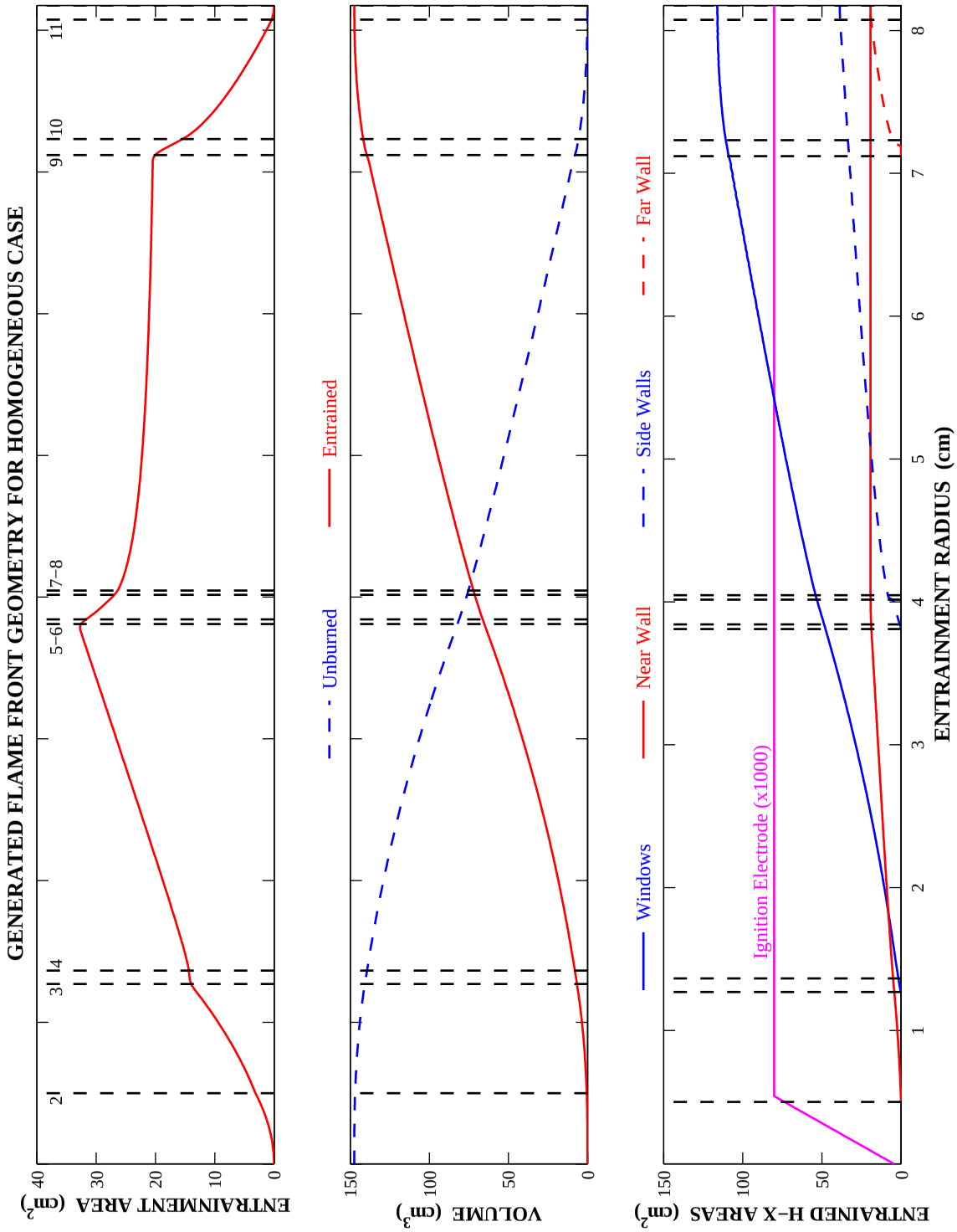

Figure 3.6: Flame Front & H-X Parameters, Generated with General Algorithm

The geometry generation routine is validated for three cases. These cases are selected for easy calculation of the true front and heat transfer areas and the entrainment volume. In all cases, approximation errors are negligible and the general algorithm functions satisfactorily.

Case I

In Phase 1, the front forms a sphere with easily computed surface area and volume. In this case, all the heat transfer areas are all zero. Values generated by the approximation are compared with the actual values (calculated with Equations 3.27 and 3.28) of the entrainment area and volume in Table 3.1. The errors for Case I are insignificant.

Actual flame front area during Phase 1 $$A_e = 2 \cdot \pi \cdot r_e^2 \tag{3.27}$$

Actual entrained volume during Phase 1 $$V_e = \tfrac{4}{3} \cdot \pi \cdot r_e^3 \tag{3.28}$$

Parameter	Approximation	Actual Value
Entrainment Area (mm^2)	434.21	434.21
Entrained Volume (mm^3)	850.78	850.79

Table 3.1: Test of Geometry Parameter Generation – Case I

Case II

The second test case is that of termination, when the flame front has reached its maximum radius. This is a simple test to verify that entrainment area goes to zero, volume approaches the total chamber volume and heat transfer areas, the total surface areas. The results in Table 3.3 show errors for Case II are also negligible.

Parameter	Approximation	Actual Value
Entrainment Area (cm^2)	0.70	0.00
Entrained Volume (cm^3)	147.48	147.48
H-X Area at Near Wall (cm^2)	19.36	19.36
H-X Area at Side Walls (cm^2)	38.70	38.71
H-X Area at Windows (cm^2)	116.02	116.13
H-X Area at Far Wall (cm^2)	19.28	19.36

Table 3.2: Test of Geometry Parameter Generation – Case II

Case III

A third case with simple areas and volumes is possible if a chamber with extended length (x-axis) is considered. In an infinitely long box, the flame front becomes a rectangle with area equal to that of the near wall. The algorithm is used to compute values for an imaginary chamber with a length of 100 cm (Phase 8). Comparing the results to the values calculated for simple rectangles (Table 3.3) shows again that the algorithm approximations are very accurate.

Parameter	Approximation	Actual Value
Entrainment Area (cm^2)	19.35	19.36
Entrained Volume x1000 (cm^3)	193.99	193.98
H-X Area at Side Walls x10 (cm^2)	109.42	109.12
H-X Area at Windows x100 (cm^2)	152.83	152.83

Table 3.3: Test of Geometry Parameter Generation – Case II

3.2.3 Ideal Gas Equation

The ideal gas law is used repeatedly in manipulation of other equations into alternate more desirable forms.

$$P \cdot \cancel{V} = m \cdot R \cdot T \tag{3.29}$$

This relationship is used to compute zone volumes at specific temperature and pressure. The equation for the unburned zone is simple since only reactants are involved.

$$\upsilon_u = \frac{R_u \cdot T_u}{P} \tag{3.30}$$

The entrained zone contains both reactants and products so the specific volume is a function of the both properties.

$$\upsilon_e = \frac{\left(\chi_e - \chi_b\right) \cdot R_u \cdot T_u + \chi_b \cdot R_b \cdot T_b}{\chi_e \cdot P} \tag{3.31}$$

3.2.4 Energy Balance for the Unburned Zone

An energy rate balance is written for the unburned zone.

$$\frac{dU_u}{dt} = -\underbrace{h_u \cdot \frac{dm_e}{dt}}_{Mass\ Transfer} - \underbrace{P \cdot \frac{d\cancel{V}_u}{dt}}_{Zone\ Compression} - \underbrace{\frac{dQ_u}{dt}}_{Heat\ Transfer} \tag{3.32}$$

The first term results from the transfer of mass from the unburned zone to the entrained zone as the flame front progresses. The unburned mass derivative is negative so this is a loss. The second term is due to compression of the unburned zone. As temperature in the entrained zone increases more rapidly than the unburned temperature, the entrained zone expands and compresses the unburned zone by a significant amount. The unburned volume rate is negative so

this term is a gain. The last term is the result of heat transfer from unburned zone. This term may be a loss or gain since it is the net of heat loss to the chamber surfaces and gain from the entrained zone.

The defining equation of absolute enthalpy is differentiated and the result used to eliminate the energy balance volume rate in favor of the desired pressure rate. Absolute internal energy terms drop during simplification.

$$H_u = U_u + P \cdot \cancel{V_u} \qquad \Rightarrow \qquad P \cdot \frac{\cancel{V_u}}{dt} = \frac{d\left(m_u h_u\right)}{dt} - \frac{dU_u}{dt} - \cancel{V_u} \cdot \frac{dP}{dt} \tag{3.33}$$

$$0 = -h_u \cdot \frac{dm_e}{dt} - \frac{d\left(\left(m_c - m_e\right) \cdot h_u\right)}{dt} + \cancel{V_u} \cdot \frac{dP}{dt} - \frac{dQ_u}{dt} \tag{3.34}$$

The enthalpy derivative is expanded and specific enthalpy is expressed in terms of specific heat and the unburned temperature derivative.

$$\left(m_c - m_e\right) \cdot \frac{dh_u}{dt} - \cancel{V_u} \cdot \frac{dP}{dt} = -\frac{dQ_u}{dt} \tag{3.35}$$

$$\frac{dh_u}{dt} = \frac{dh_u}{dT_u} \cdot \frac{dT_u}{dt} = c_{p,u} \cdot \frac{dT_u}{dt} \quad \Rightarrow \quad \left(m_c - m_e\right) \cdot c_{p,u} \cdot \frac{dT_u}{dt} - \cancel{V_u} \cdot \frac{dP}{dt} = -\frac{dQ_u}{dt} \tag{3.36}$$

The desired form of the energy balance is obtained after expressing entrained mass as mass fraction and dividing through by the total chamber mass (m_c).

$$\boxed{\left(1 - \chi_e\right) \cdot c_{p,u} \cdot \frac{dT_u}{dt} - \frac{\cancel{V_c} - \cancel{V_e}}{m_c} \frac{dP}{dt} = -\frac{1}{m_c} \cdot \frac{dQ_u}{dt}} \tag{3.37}$$

3.2.5 Energy Balance for the Entrained Zone (Reaction and Burned Zones)

The same steps are now applied to the entrained zone energy balance. The starting equation has similar form with one sign change.

$$\frac{dU_e}{dt} = \underbrace{h_u \cdot \frac{dm_e}{dt}}_{\text{Mass Transfer}} - \underbrace{P \cdot \frac{d\cancel{V_e}}{dt}}_{\text{Zone Expansion}} - \underbrace{\frac{dQ_e}{dt}}_{\text{Heat Transfer}} \tag{3.38}$$

The first term is the same as the unburned balance with opposite sign since the flow is reversed relative to the entrained zone. This term is now a gain. The second term is also a gain since the entrained zone is expanding (doing work on the unburned zone). The heat transfer term is a loss through the entire combustion since the entrained temperature is higher than either the unburned zone or the surroundings.

The absolute enthalpy substitution is applied and common terms are cancelled.

$$0 = h_u \cdot \frac{dm_e}{dt} - \frac{d\left(\left(m_e - m_b\right) \cdot h_u + m_b \cdot h_b\right)}{dt} + \cancel{V_e} \cdot \frac{dP}{dt} - \frac{dQ_e}{dt} \tag{3.39}$$

In this case the enthalpy derivative expansion and substitution of specific heats involves both reactants and products.

$$\left(h_u - h_b\right) \cdot \frac{dm_b}{dt} + \left(m_e - m_b\right) \cdot \frac{dh_u}{dt} + m_b \cdot \frac{dh_b}{dt} - \cancel{V_e} \cdot \frac{dP}{dt} = -\frac{dQ_e}{dt} \tag{3.40}$$

$$\left(h_b - h_u\right) \cdot \frac{dm_b}{dt} + \left(m_e - m_b\right) \cdot c_{p,u} \cdot \frac{dT_u}{dt} + m_b \cdot c_{p,b} \cdot \frac{dT_b}{dt} - \cancel{V_e} \cdot \frac{dP}{dt} = -\frac{dQ_e}{dt} \tag{3.41}$$

The balance is finally rendered in the same form as the unburned balance. The major difference is the term accounting for heat release as the unburned mixture reacts.

$$\left.\begin{array}{r}\left(\chi_e-\chi_b\right)\cdot c_{p,u}\cdot\dfrac{dT_u}{dt}\cdots\\ +\chi_b\cdot c_{p,b}\cdot\dfrac{dT_b}{dt}\cdots\\ -\dfrac{\forall_e}{m_c}\cdot\dfrac{dP}{dt}\end{array}\right\}=\left\{\begin{array}{l}-\dfrac{1}{m_c}\cdot\dfrac{dQ_e}{dt}\cdots\\ +\left(h_u-h_b\right)\cdot\dfrac{d\chi_b}{dt}\end{array}\right. \tag{3.42}$$

3.2.6 Constant Volume Constraint

Chamber volume does not vary so three zone volumes must sum to this constant value.

$$\forall_u+\forall_r+\forall_b=\forall_c \tag{3.43}$$

Volumes are written in terms of the appropriate zone mass and specific volume. Masses are written in terms of mass fractions and both sides of the resulting equation are divided by total chamber mass.

$$\left(m_c-m_b\right)\cdot\upsilon_u+m_b\cdot\upsilon_b=\forall_c \tag{3.44}$$

$$\left(1-\chi_b\right)\cdot\upsilon_u+\chi_b\cdot\upsilon_b=\frac{\forall_c}{m_c} \tag{3.45}$$

Specific volumes are eliminated using the ideal gas law and the resulting denominators cleared by multiplying through by pressure. The derivative is taken and the result arranged into a form similar to the energy balances.

$$\left(1-\chi_b\right)\cdot R_u\cdot T_u+\chi_b\cdot R_b\cdot T_b=\frac{P\cdot\forall_c}{m_c} \tag{3.46}$$

$$-R_u \cdot T_u \cdot \frac{d\chi_b}{dt} + (1-\chi_b) \cdot \frac{d(R_u \cdot T_u)}{dT_u} \cdot \frac{dT_u}{dt} + R_b \cdot T_b \cdot \frac{d\chi_b}{dt} + \chi_b \cdot \frac{d(R_b \cdot T_b)}{dT_b} \cdot \frac{dT_b}{dt} = \frac{\forall_c}{m_c} \cdot \frac{dP}{dt} \tag{3.47}$$

$$\left.\begin{aligned} &(1-\chi_b) \cdot \frac{d(R_u \cdot T_u)}{dT_u} \cdot \frac{dT_u}{dt} \cdots \\ &+\chi_b \cdot \frac{d(R_b \cdot T_b)}{dT_b} \cdot \frac{dT_b}{dt} \cdots \\ &-\frac{\forall_c}{m_c} \cdot \frac{dP}{dt} \end{aligned}\right\} = (R_u \cdot T_u - R_b \cdot T_b) \cdot \frac{d\chi_b}{dt} \tag{3.48}$$

At a given temperature, the derivatives of the gas constant and temperature products are evaluated using the result of a chain rule expansion.

$$\frac{d(R_u \cdot T_u)}{dT_u} = R_u + T_u \cdot \frac{dR_u}{dT_u} \qquad \frac{d(R_b \cdot T_b)}{dT_b} = R_b + T_b \cdot \frac{dR_b}{dT_b} \tag{3.49}$$

The gas constant and temperature products can be replaced by the gas constant alone in the case that its change with temperature is negligible.

3.2.7 Mass Entrainment Rate (Leaving Unburned & Entering Reaction Zone)

Mass is entrained by the flame front as it advances through the unburned zone. The mass entrainment rate is the product of the unburned mixture density, flame front area and propagation velocity.

$$\frac{dm_e}{dt} = \rho_u \cdot A_e \cdot S_P \tag{3.50}$$

The transformation is made from mass to mass fraction and both sides are divided by the total chamber mass.

$$\boxed{\frac{d\chi_e}{dt} = \frac{\rho_u \cdot A_e \cdot S_P}{m_c} = \frac{A_e \cdot P \cdot S_P}{m_c \cdot R_u \cdot T_u}} \tag{3.51}$$

Area in this case is the idealized area of the smooth flame front without the wrinkles associated with turbulent combustion. The true turbulent flame front is easily pictured as a human brain with its many convolutions. An analogy for the smooth area is then the inside of the skullcap surrounding the convoluted brain. The two areas are obviously not equal but it is far is simpler to model the smooth area than the actual wrinkled flame front area.

The propagation velocity (S_p) is the sum of laminar flame speed and turbulence intensity with exponential term to improve behavior during the early burn period.

$$S_P = S_L + u_u' \cdot \left(1 - \exp\left(-t/\tau_1\right)\right) \tag{3.52}$$

At the start of combustion, before the flame reaches the edge of the first eddy, there is a period during which the combustion is not fully turbulent. The constant (τ_1) here is the time required for the first eddy to burn completely.

3.2.8 Mass Reaction Rate (Leaving Reaction & Entering Burned Zone)

Mass reacts at a rate proportional to the amount of mass present in the reaction zone (enflamed mass) and inversely proportional to the characteristic burning time (τ_b).

$$\frac{dm_b}{dt} = \frac{m_e - m_b}{\tau_b} \tag{3.53}$$

The only manipulation is a change to mass fractions.

$$\frac{d\left(\chi_b \cdot m_c\right)}{dt} = \frac{\left(\chi_e - \chi_b\right) \cdot m_c}{\tau_b} \tag{3.54}$$

$$\boxed{\frac{d\chi_b}{dt} = \frac{\chi_e - \chi_b}{\tau_b}} \tag{3.55}$$

The characteristic burning (τ_b) time is the time required for the flame to travel a distance equal to the Taylor microscale (completely burn one eddy) at the laminar flame speed.

$$\tau_b = \frac{\lambda}{S_L} \tag{3.56}$$

The changing value of the Taylor microscale is computed from a relationship given in Tabaczynski, et al. [37]. The integral length scale (L) is assumed as constant and viscosity values for air are used to further simplify the calculation.

$$\lambda = \left(\frac{15 \cdot \nu \cdot L}{u_u'}\right)^{1/2} \tag{3.57}$$

3.2.9 Laminar Flame Speed

Laminar flame speed is computed as a function of pressure, temperature and mixture equivalence. Heywood [18] gives a more convenient form of the power law originally derived by Metgalchi and Keck [31].

$$\boxed{S_L = S_{L,ref} \cdot \left(\frac{T_u}{T_{ref}}\right)^{\alpha} \cdot \left(\frac{P}{P_{ref}}\right)^{\beta}} \tag{3.58}$$

The three coefficients ($S_{L,ref}$, α and β) are functions of equivalence and simplify the calculation of flame speed for a specific mixture equivalence.

$$\alpha = 2.18 - 0.80 \cdot (\phi - 1) \tag{3.59}$$

$$\beta = -0.16 + 0.22 \cdot (\phi - 1) \tag{3.60}$$

$$S_{L,ref} = B_m + B_\phi \cdot (\phi - \phi_m)^2 . \tag{3.61}$$

B_m is the maximum laminar flame speed at a specified reference temperature and pressure and ϕ_m is the equivalence at which this maximum laminar flame speed occurs (the reference state is 1 atm and 298 K). Constants valid over a range of pressure from 1-8 atm and temperature from 300-700 K are provided for several fuel types. Values for propane are of interest here.

$$\phi_m = 1.08 \tag{3.62}$$

$$B_m = 34.2 \text{ cm/sec} \tag{3.63}$$

$$B_\phi = -138.7 \text{ cm/sec} \tag{3.64}$$

3.2.10 Turbulence

A two-zone k-epsilon model is used to track the turbulence energy separately in the unburned and entrained zones. This model includes turbulence energy production due to compression, decay due to viscous dissipation and transport with mass flux across the flame front.

Total turbulence energy change in the unburned zone is the sum of a production and decay term.

$$\frac{dk_u}{dt} = \underbrace{\frac{2}{3}\cdot\frac{k_u}{\rho_u}\cdot\frac{d\rho_u}{dt}}_{Production} - \underbrace{\varepsilon_u}_{Decay} \tag{3.65}$$

The expression for the entrained zone includes an additional term for the flux of turbulence energy across the flame front.

$$\frac{dk_b}{dt} = \underbrace{\frac{2}{3}\cdot\frac{k_b}{\rho_b}\cdot\frac{d\rho_b}{dt}}_{Production} - \underbrace{\varepsilon_b}_{Decay} + \underbrace{F_{k,b}}_{Flux} \tag{3.66}$$

Changes in rates of decay for each zone are given in similar terms.

$$\frac{d\varepsilon_u}{dt} = \frac{4}{3}\cdot\frac{\varepsilon_u}{\rho_u}\cdot\frac{d\rho_u}{dt} - \frac{2\cdot\varepsilon_u^2}{k_u} \tag{3.67}$$

$$\frac{d\varepsilon_b}{dt} = \frac{4}{3}\cdot\frac{\varepsilon_b}{\rho_b}\cdot\frac{d\rho_b}{dt} - \frac{2\cdot\varepsilon_b^2}{k_b} + F_{\varepsilon,b} \tag{3.68}$$

Flux terms across the flame front include the ratio of the burned and unburned densities to account for the crossing between regions with different densities.

$$F_{k,b} = \frac{1}{m_b}\cdot\frac{dm_b}{dt}\cdot\left(k_b^* - k_b\right) = \frac{1}{\chi_b}\cdot\frac{d\chi_b}{dt}\cdot\left(k_b^* - k_b\right) \tag{3.69}$$

$$F_{\varepsilon,b} = \frac{1}{m_b}\cdot\frac{dm_b}{dt}\cdot\left(\varepsilon_b^* - \varepsilon_b\right) = \frac{1}{\chi_b}\cdot\frac{d\chi_b}{dt}\cdot\left(\varepsilon_b^* - \varepsilon_b\right) \tag{3.70}$$

$$k_b^* = \left(\frac{\rho_b}{\rho_u}\right)^{2/3} \cdot k_u = \left(\frac{R_u \cdot T_u}{R_b \cdot T_b}\right)^{2/3} \cdot k_u \tag{3.71}$$

$$\varepsilon_b^* = \left(\frac{\rho_b}{\rho_u}\right)^{4/3} \cdot \varepsilon_u = \left(\frac{R_u \cdot T_u}{R_b \cdot T_b}\right)^{4/3} \cdot \varepsilon_u \tag{3.72}$$

The density rates are expanded in terms of pressure and temperature rates to remain consistent with previously developed expressions.

$$\frac{d\rho_u}{dt} = \frac{1}{R_u \cdot T_u} \cdot \left(\frac{dP}{dt} - \frac{P}{T_u} \cdot \frac{dT_u}{dt}\right) \tag{3.73}$$

$$\frac{d\rho_b}{dt} = \frac{1}{R_b \cdot T_b} \cdot \left(\frac{dP}{dt} - \frac{P}{T_b} \cdot \frac{dT_b}{dt}\right) \tag{3.74}$$

Initial turbulence energy is computed from the known intensity and an initial value for epsilon in the unburned zone is computed from the initial energy and the integral length scale.

$$k = \tfrac{1}{2} \cdot \left(u'\right)^2 \tag{3.75}$$

$$\varepsilon_u = \frac{C_\varepsilon \cdot m_c \cdot \left(u_u'\right)^3}{L} = C_\varepsilon \cdot \frac{m_c}{L} \cdot \left(\frac{2 \cdot k_u}{3 \cdot m_c}\right)^{3/2} \tag{3.76}$$

Agarwal [1] gives a value of 0.43 for the constant C_ε, for an idling engine. This is closest to the CVCC case in terms of pressure and turbulence and provides a reasonable starting point. The integral length scale (L) is assigned a value based on the diameter of the mixing paddle perforations. Ting, et al. [40] have performed CVCC experiments with a perforated plate turbulence generator and claim hole size controls integral length scale. For an entire range of hole sizes (2.5-20 mm), the ratio of integral length scale to hole diameter is 0.25.

3.2.10.1 Net Rate Between Paddle Movement and Ignition (Delay)

There is a short delay after the turbulence generating paddles come to rest and before the ignition fires. There is no entrained zone during this period and no need to evaluate the production term for the unburned zone. The turbulence equations in this case can be simplified.

$$\frac{dk_u}{dt} = -\varepsilon_u \tag{3.77}$$

$$\frac{d\varepsilon_u}{dt} = -\frac{2 \cdot \varepsilon_u^2}{k_u} \tag{3.78}$$

3.2.11 Heat Transfer & Thermal Models

As noted by Lumley [27], the primary convective heat transfer mechanism is turbulence and not molecular transport. The heat transfer rate is written with an effective coefficient for turbulent heat transfer.

$$\frac{dQ_{conv}}{dt} = A_{conv} \cdot \gamma_{conv} \cdot \frac{\partial T}{\partial x} \tag{3.79}$$

$$\gamma_{conv} = \frac{c_p \cdot u' \cdot l}{\upsilon} \tag{3.80}$$

The temperature gradient is approximated as the difference between the appropriate zone and surface temperatures contact over a distance *l*.

$$\frac{\partial T}{\partial x} \approx \frac{T_{gas} - T_{surface}}{l} \tag{3.81}$$

Substituting the heat transfer coefficient and temperature terms into the original equation yields a usable equation form. A constant (C_{hx}) is included to allow matching of heat transfer rates with the experimental data.

$$\frac{dQ_{conv}}{dt} = \frac{C_{hx} \cdot A_{conv} \cdot c_p \cdot u'}{\upsilon} \cdot \left(T_{gas} - T_{surface}\right) \tag{3.82}$$

3.2.11.1 Heat Transfer to Chamber Surfaces

Heat transfer rates from the unburned and entrained zones to the chamber surfaces are written the appropriate zone temperatures and heat transfer areas.

$$\boxed{\frac{dQ_{cs,u}}{dt} = \frac{C_{hx} \cdot A_{hx,u} \cdot c_{p,u} \cdot u_u' \cdot P}{R_u \cdot T_u} \cdot \left(T_u - T_{surface}\right)} \tag{3.83}$$

$$\boxed{\frac{dQ_{cs,e}}{dt} = \frac{C_{hx} \cdot A_{hx,e} \cdot c_{p,b} \cdot u_e' \cdot P}{R_b \cdot T_b} \cdot \left(T_b - T_{surface}\right)} \tag{3.84}$$

The total entrained heat transfer area excludes the ignition electrodes since this is accounted for separately. Chamber surface temperature is assumed constant for all surfaces.

3.2.11.2 Ignition Electrode Heat Transfer & Thermal Model

The heat transfer rate from the entrained zone to the ignition electrodes is written to account for a fine-wire electrode temperature that is not constant. Temperature of the electrode is taken as uniform and any conduction from the chamber along the path provided by the electrodes is neglected.

$$\frac{dQ_{ie,e}}{dt} = \frac{C_{hx} \cdot A_{hx,ie} \cdot c_{p,b} \cdot u_e' \cdot P}{R_b \cdot T_b} \cdot \left(T_b - T_{ie}\right) \tag{3.85}$$

A simple lumped energy rate balance for the ignition electrode thermal mass is written and combined with the heat transfer rate to obtain an expression for the change in electrode temperature.

$$\frac{dQ_{ie}}{dt} = c_{p,ie} \cdot m_{ie} \cdot \frac{dT_{ie}}{dt} \tag{3.86}$$

$$\frac{dT_{ie}}{dt} = \frac{1}{c_{p,ie} \cdot m_{ie}} \cdot \frac{dQ_{ie}}{dt} = \frac{C_{hx} \cdot A_{hx,ie} \cdot c_{p,b} \cdot u_e' \cdot P}{c_{p,ie} \cdot m_{ie} \cdot R_b \cdot T_b} \cdot \left(T_b - T_{ie}\right) \tag{3.87}$$

3.2.12 Ignition

Ignition models of varying complexity are described in the literature but this sub-model is not critical in proving or disproving the possibility of a simplified stratified-charge combustion model. With this in mind a simple ignition sub-model is selected. Ignition is treated as a discontinuity over which a small mass fraction is entrained. Only 99 percent of the mass is burned in order to enter the model burn phase with a non-zero reaction zone mass. This treatment of ignition as a discontinuity is fair since the major transfer of ignition energy to the mixture is complete within several tenths of a millisecond [18]. Since the event is rapid it is also assumed to take place isentropically.

Energy Balance Across the Ignition Discontinuity

An energy balance is written over the discontinuity, including a term for electrical energy delivered to the ignition electrodes.

$$\left(1 - m_b\right) \cdot \tilde{u}_u + m_b \cdot \tilde{u}_b = m_c \cdot u_i + W_{elec} \tag{3.88}$$

$$\left(1 - \chi_b\right) \cdot \tilde{u}_u + \chi_b \cdot \tilde{u}_b = u_i + \frac{W_{elec}}{m_c} \tag{3.89}$$

Isentropic Pressure-Temperature Relationship

The unburned volume is compressed very little during the ignition and specific heat for the isentropic process is assumed to be constant. This provides a relationship between the post-ignition pressure and temperature.

$$\frac{\tilde{P}_{isentropic}}{P_i} = \left(\frac{\tilde{T}_u}{T_i} \right)^{\frac{\gamma}{\gamma-1}} \tag{3.90}$$

Constant Volume Constraint and Ideal Gas Law

A second expression for the post-ignition pressure is derived from the constant volume constraint and the ideal gas law.

$$\frac{\tilde{V}_u}{V_c} = \frac{\left(1-\chi_e\right) \cdot \tilde{R}_u \cdot \tilde{T}_u}{\left(1-\chi_b\right) \cdot \tilde{R}_u \cdot \tilde{T}_u + \chi_b \cdot \tilde{R}_b \cdot \tilde{T}_b} \tag{3.91}$$

$$\tilde{P}_{ideal} = \frac{\left(1-\chi_e\right) \cdot m_c \cdot \tilde{R}_u \cdot \tilde{T}_u}{\tilde{V}_u} = \frac{\left(1-\chi_b\right) \cdot \tilde{R}_u \cdot \tilde{T}_u + \chi_b \cdot \tilde{R}_b \cdot \tilde{T}_b}{V_c} \cdot m_c \tag{3.92}$$

Solution Method

A system error is defined from the conservation of energy and volume constraints and the assumed isentropic compression of the unburned volume.

$$Error = Err_{energy} + Err_{pres} = \left| 1 - \frac{(1-\chi_b)\cdot \tilde{u}_u + \chi_b \cdot \tilde{u}_b}{u_i - \frac{W_{ign}}{m_c}} \right| + \left| 1 - \frac{\tilde{P}_{ideal}}{\tilde{P}_{isentropic}} \right| \qquad (3.93)$$

A multivariable optimization routine is used to solve the post-ignition temperatures by minimizing the given error function. The routine FMINSEARCH[1] is a built-in *Matlab®* function and provides a fast and efficient means to solve the post-ignition temperatures. Convergence criteria for the optimization are 0.1 K on the input vector of unburned and burned temperatures and 1.0e-3 on the error function.

Lookup tables for post-ignition pressures and temperatures are compiled for a reasonable range of initial conditions (pressure, temperature, equivalence and enflamed mass fraction) to allow a simple lookup for post-ignition conditions during simulation [Figure 3.7]. This effectively shortens run times since linear interpolation from the lookup tables takes substantially less time than the post-ignition solver routine.

[1] FMINSEARCH is an implementation of the simplex method described in Lagarias, J.C., J.A. Reeds, M.H. Wright, P.E. Wright, "Convergence Properties of the Nelder-Mead Simplex Algorithm in Low Dimensions," *SIAM Journal of Optimization*.

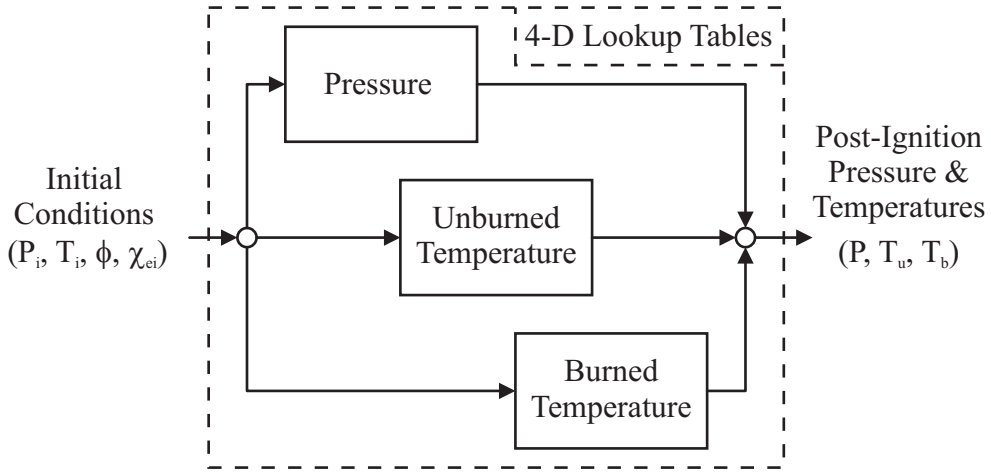

Figure 3.7: Post-Ignition Conditions Solution Method Employing Lookup Table

3.2.13 Mixture Composition

Chemical kinetics are assumed to be much faster than the combustion time scale and a six species equilibrium reaction is used to establish the chemical composition of the burned mixture for temperature.

A one-step reaction is written for the reaction of a pure hydrocarbon fuel with one mole of idealized air (79% Nitrogen and 21% Oxygen). This is reasonable since ZERO air is used and the small percentage of trace gasses is assumed negligible.

$$\phi \cdot FA_s \cdot C_\alpha H_\beta + \begin{pmatrix} 0.21 \cdot O_2 \cdots \\ +0.79 \cdot N_2 \end{pmatrix} \rightarrow \nu_1 \cdot CO_2 + \nu_2 \cdot H_2O + \nu_3 \cdot N_2 + \nu_4 \cdot O_2 + \nu_5 \cdot CO + \nu_6 \cdot H_2 \qquad (3.94)$$

Elemental balances for the four species gives a like number of equations.

Carbon (*C*) balance $$\alpha \cdot \phi \cdot FA_s = \nu_1 + \nu_5 \tag{3.95}$$

Hydrogen (*H*) balance $$\beta \cdot \phi \cdot FA_s = 2 \cdot (\nu_2 + \nu_6) \tag{3.96}$$

Oxygen (*O*) balance $$0.42 = 2 \cdot (\nu_1 + \nu_4) + \nu_2 + \nu_5 \tag{3.97}$$

Nitrogen (N_2) balance $$0.79 = \nu_3 \tag{3.98}$$

The stoichiometric fuel-air ratio is a function of the carbon-hydrogen ratio of a specific fuel. The balance is solved for $\phi = 1.0$ to obtain an expression for FA_s.

$$FA_s = \frac{0.84}{4 \cdot \alpha + \beta} \tag{3.99}$$

3.2.13.1 Lean/Stoichiometric Case ($\phi \leq 1$)

For lean and stoichiometric combustion there is sufficient oxygen for complete oxidation of the fuel and no carbon monoxide or free hydrogen result. For these cases the four elemental balance equations are sufficient to solve the product composition.

Carbon dioxide (CO_2) moles $$\nu_1 = \alpha \cdot \phi \cdot FA_s \tag{3.100}$$

Water (H_2O) moles $$\nu_2 = \tfrac{1}{2} \cdot \beta \cdot \phi \cdot FA_s \tag{3.101}$$

Nitrogen (N_2) moles $$\nu_3 = 0.79 \tag{3.102}$$

Oxygen (O_2) moles $$\nu_4 = 0.21 \cdot (1 - \phi) \tag{3.103}$$

Carbon monoxide (*CO*) moles $\nu_5 = 0$ (3.104)

Hydrogen (H_2) moles $\nu_6 = 0$ (3.105)

3.2.13.2 Rich Combustion ($\phi > 1$)

For the case of rich combustion there is insufficient oxygen for complete oxidization of the fuel. The oxygen balance is no longer trivial.

Oxygen (*O*) balance $0.42 = 2 \cdot \nu_1 + \nu_2 + \nu_5$ (3.106)

There are more unknowns than equations and an additional relationship is needed in order to solve the right-side mixture composition. For the temperature range encountered during combustion, the "*water gas reaction*" may be used.

$$CO_2 + H_2 \xrightarrow{K} CO + H_2O \qquad where\ K = \frac{\nu_2 \cdot \nu_5}{\nu_1 \cdot \nu_6} \tag{3.107}$$

$$K(T) = \exp\left(2.743 - \frac{1.761 \cdot 10^3}{T} - \frac{1.611 \cdot 10^6}{T^2} + \frac{0.2803 \cdot 10^9}{T^3}\right) \qquad \begin{matrix} Temperature\ in \\ Degrees\ Kelvin \end{matrix} \tag{3.108}$$

The forward reaction rate (*K*) provides an additional relationship in the form of a molar ratio. In conjunction with the elemental balances this allows a solution of the composition. Solving for one of the unknowns results in a quadratic function involving the reactant mixture parameters. The lesser of the two roots of the quadratic is retained and used to solve for the remaining coefficients. One of the coefficients must initially be selected and solved for in quadratic form as the first step. Here, the carbon monoxide (ν_5) coefficient is selected.

Carbon dioxide (CO_2) moles $$\nu_1 = \alpha \cdot \phi \cdot FA_s - \nu_5 \quad (3.109)$$

Water (H_2O) moles $$\nu_2 = 0.42 - 2 \cdot \alpha \cdot \phi \cdot FA_s + \nu_5$$

or $$\nu_2 = 0.42 - 2 \cdot \nu_1 - \nu_5 \quad (3.110)$$

Nitrogen (N_2) moles $$\nu_3 = 0.79 \quad (3.111)$$

Oxygen (O_2) moles $$\nu_4 = 0 \quad (3.112)$$

Carbon monoxide (CO) moles $$\nu_5 = \left(-b + \left(b^2 - 4 \cdot a \cdot c \right)^{\frac{1}{2}} \right) \Big/ 2 \cdot a \quad (3.113)$$

Hydrogen (H_2) moles $$\nu_6 = 0.42 \cdot (\phi - 1) - \nu_5 \quad (3.114)$$

The quadratic coefficients (a, b, and c) are expressed in terms of the stoichiometric fuel-air ratio, equivalence ratio, forward reaction rate and fuel properties.

$$a = K - 1 \quad (3.115)$$

$$b = -\left(0.42 \cdot (\phi - 1) \cdot (K - 1) + \phi \cdot FA_s \cdot \left(\alpha \cdot K + \tfrac{1}{2} \cdot \beta \right) \right) \quad (3.116)$$

$$c = 0.42 \cdot \alpha \cdot \phi \cdot FA_s \cdot K \cdot (\phi - 1) \quad (3.117)$$

3.2.13.3 Molecular Weights of Reactant and Product Mixtures

The molecular weight of the reactants is a function of the stoichiometric fuel-air and equivalence ratios and the fuel type. It is not a function of temperature since the reactant composition does not vary in the unburned and reaction zones (assuming no dissociation).

$$M_u = \frac{0.21 \cdot M_{O2} + 0.79 \cdot M_{N2} + \phi \cdot FA_s \cdot M_{fuel}}{1 + \phi \cdot FA_s} \tag{3.118}$$

Reactant molecular weight is similar for lean and stoichiometric mixtures with four terms in the numerator (ν_1, ν_2, ν_3 and ν_4).

$$M_b = \frac{\sum [\nu_i \cdot M_i]}{\sum \nu_i} \tag{3.119}$$

Rich mixtures have a temperature dependent composition so the molecular weight may also be a function of temperature. The numerator contains one net additional term for rich mixtures since carbon monoxide and hydrogen are present added but oxygen is absent.

3.2.14 Evaluation of Thermodynamic Properties

Thermodynamic properties are evaluated for a particular exhaust species or fuel type at any temperature using curve fits of JANAF table data given in Heywood [18] and described in detail in Appendix A. The resulting values are molar specific, indicated here by the addition of a tilde.

Since the reactant molecular weight is constant with temperature (fixed composition is assumed) so is the gas constant. For the homogeneous case, it is also true that the unburned and reaction zone gas constants are equal.

$$R_u(\phi) = \frac{\tilde{R}}{M_u(\phi)} \tag{3.120}$$

Specific heat and enthalpy for the reactants and all values for the products are temperature dependent. Product values first require evaluation of the mixture composition at a specific temperature using the six species equilibrium model.

$$c_{p,u}\left(\phi,T_u\right)=\frac{0.21\cdot\tilde{c}_{p,O2}\left(T_u\right)+0.79\cdot\tilde{c}_{p,N2}\left(T_u\right)+\phi\cdot FA_s\cdot\tilde{c}_{p,\,fuel}\left(T_u\right)}{\left(1+\phi\cdot FA_s\right)\cdot M_u\left(\phi\right)} \tag{3.121}$$

$$h_u\left(\phi,T_u\right)=\frac{0.21\cdot\tilde{h}_{O2}\left(T_u\right)+0.79\cdot\tilde{h}_{N2}\left(T_u\right)+\phi\cdot FA_s\cdot\tilde{h}_{fuel}\left(T_u\right)}{\left(1+\phi\cdot FA_s\right)\cdot M_u\left(\phi\right)} \tag{3.122}$$

$$R_b\left(\phi,T_b\right)=\frac{\tilde{R}}{M_b\left(\phi,T_b\right)} \tag{3.123}$$

$$c_{p,b}\left(\phi,T_b\right)=\frac{\sum\left[\nu_i\cdot\tilde{c}_{p,i}\left(T_b\right)\right]}{\sum\left[\nu_i\right]\cdot M_b\left(\phi,T_b\right)}=\frac{\sum\left[\nu_i\cdot\tilde{c}_{p,i}\left(T_b\right)\right]}{\sum\left[\nu_i\cdot M_i\right]} \tag{3.124}$$

$$h_b\left(\phi,T_b\right)=\frac{\sum\left[\nu_i\cdot\tilde{h}_i\right]}{\sum\left[\nu_i\right]\cdot M_b\left(\phi,T_b\right)}=\frac{\sum\left[\nu_i\cdot\tilde{h}_i\right]}{\sum\left[\nu_i\cdot M_{b,i}\right]} \tag{3.125}$$

Specific heat of the stainless steel ignition electrodes is evaluated as the temperature increases using a fifth-order polynomial curve-fit of data over 200-1500 K. A higher order is required to fit a break in the curve over the 300-400 K range.

$$c_{p,ie}=a_{ie1}+a_{ie2}\cdot T_{ie}+a_{ie3}\cdot T_{ie}^2+a_{ie4}\cdot T_{ie}^3+a_{ie5}\cdot T_{ie}^4+a_{ie6}\cdot T_{ie}^5 \tag{3.126}$$

The dynamic viscosity of air is used to simplify calculation of the Taylor microscale. Data for viscosity at the standard pressure of 1.0 atm are fit with a polynomial. In this case a third-order polynomial is sufficient over a temperature range of 300-3000 K.

$$\nu_0 = a_{vis1} + a_{vis2} \cdot T_u + a_{vis3} \cdot T_u^2 + a_{vis4} \cdot T_u^3 \tag{3.127}$$

Dynamic viscosity at other than the standard pressure is computed using the empirical correlation suggested by Stone (from Collis and Williams, 1959).

$$\nu = \nu_0 \cdot \frac{\rho_0}{\rho_u} \cdot \left(\frac{T_u}{T_0} \right)^{0.76} \tag{3.128}$$

Coefficients for all curve-fits in this section (a_i , A_f , a_{ie} and a_{vis}) and original data are included in Appendix A.

3.2.15 Complete System of Equations Describing the Combustion Process

The combustion process is broken into three phases: pre-ignition, ignition and combustion.

3.2.15.1 Common to All Simulation Phases

Mixture composition is solved using the six species model described in Section 3.2.13. Properties for the reactant and product mixtures are evaluated using the JANAF and ignition electrode data curve-fits of Section 3.2.14.

3.2.15.2 Pre-Ignition

The simulation begins a single zone in which the only modeled process is decay of the turbulence energy according to the equations of Section 3.2.10.1.

3.2.15.3 Ignition

Post-ignition temperatures and pressure are computed directly using the solver or found from the lookup table (Section 3.2.12). With this method an initial burned mass fraction is specified.

3.2.15.4 Combustion

The unburned energy balance (Equation 3.37), entrained energy balance (Equation 3.42) and constant volume (Equation 3.49) form a system of equations that describes the physics of the combustion process using first principles.

$$\begin{bmatrix} a_{11} & 0 & a_{13} \\ a_{21} & a_{22} & a_{23} \\ a_{31} & a_{32} & a_{33} \end{bmatrix} \cdot \frac{d}{dt}\begin{pmatrix} T_u \\ T_b \\ P \end{pmatrix} = \begin{bmatrix} b_{11} & 0 & 0 \\ 0 & b_{22} & b_{23} \\ 0 & 0 & b_{33} \end{bmatrix} \cdot \frac{d}{dt}\begin{pmatrix} Q_u \\ Q_e \\ \chi_b \end{pmatrix} \tag{3.129}$$

Non-zero elements in the coefficient matrices have the following values.

$$a_{11} = \left(1-\chi_e\right)\cdot c_{p,u} \qquad a_{23} = -\frac{\cancel{V_e}}{m_c}$$

$$a_{13} = -\frac{\cancel{V_u} - \cancel{V_e}}{m_c} \qquad a_{31} = \left(1-\chi_b\right)\cdot \frac{d\left(R_u \cdot T_u\right)}{dT_u}$$

$$a_{21} = \left(\chi_e - \chi_b\right)\cdot c_{p,u} \qquad a_{32} = \chi_b \cdot \frac{d\left(R_b \cdot T_b\right)}{dT_b}$$

$$a_{22} = \chi_b \cdot c_{p,b} \qquad a_{33} = -\frac{\cancel{V_c}}{m_c}$$

$$b_{11} = -\frac{1}{m_c} \qquad b_{23} = h_u - h_b$$

$$b_{22} = -\frac{1}{m_c} \qquad b_{33} = R_u \cdot T_u - R_b \cdot T_b$$

The coefficient matrix A is always invertible since the entrained and burned mass fractions are never zero. Multiplying through by the inverse of A gives the solution for temperature and pressure rates in terms of the two matrices and the rates for heat transfer (Equations 3.83 through 3.86), mass entrainment (Equation 3.51) and mass reaction (Equation 3.55).

$$\frac{d}{dt}\begin{pmatrix} T_u \\ T_b \\ P \end{pmatrix} = \begin{bmatrix} a_{11} & 0 & a_{13} \\ a_{21} & a_{22} & a_{23} \\ a_{31} & a_{32} & a_{33} \end{bmatrix}^{-1} \cdot \begin{bmatrix} b_{11} & 0 & 0 \\ 0 & b_{22} & b_{23} \\ 0 & 0 & b_{33} \end{bmatrix} \cdot \frac{d}{dt}\begin{pmatrix} Q_u \\ Q_e \\ \chi_b \end{pmatrix} \tag{3.130}$$

Other equations and relationships required for the solution are turbulence (Section 3.2.10), flame propagation speed (Equation 3.58) and flame geometry (using a lookup table, Section 3.2.2.4).

3.2.16 Solution Method

The solution method is shown graphically in Figure 3.8. The physical system is defined at any instant by pressure, zone temperatures, entrained and burned mass fractions and zone turbulence intensities. Each time-varying parameter is represented in the figure as a function of other time-varying parameters (time-invariant parameters are not shown). The order of parameter evaluation and progression of key parameters to the next time step are clearly identified. This solution method is implemented in *Matlab® v6.0* to simulate the homogeneous combustion process for any set of initial conditions.

Several key points of the solution process are:

i) The decay of turbulence after paddle movement before the ignition fires is small for the homogeneous case but inclusion of the feature allows also for the stratified case where the delay is larger due to the time required for opening of the partition.

ii) Entrained volume is computed from the ideal gas law. This is then used to obtain the heat transfer area from the geometry lookup table.

iii) Three termination criteria are specified for the simulation. First is a maximum entrained mass fraction of 99.9%. Second is a maximum burned mass fraction of 99.5%. All equations are valid over the burn period specified by these two criteria. A third criterion is specified to terminate the simulation if the burned mass stagnates and the rate of change falls below 0.001% of the maximum rate. This provides for possible stratified cases where entrainment may cease well short of the maximum specified values.

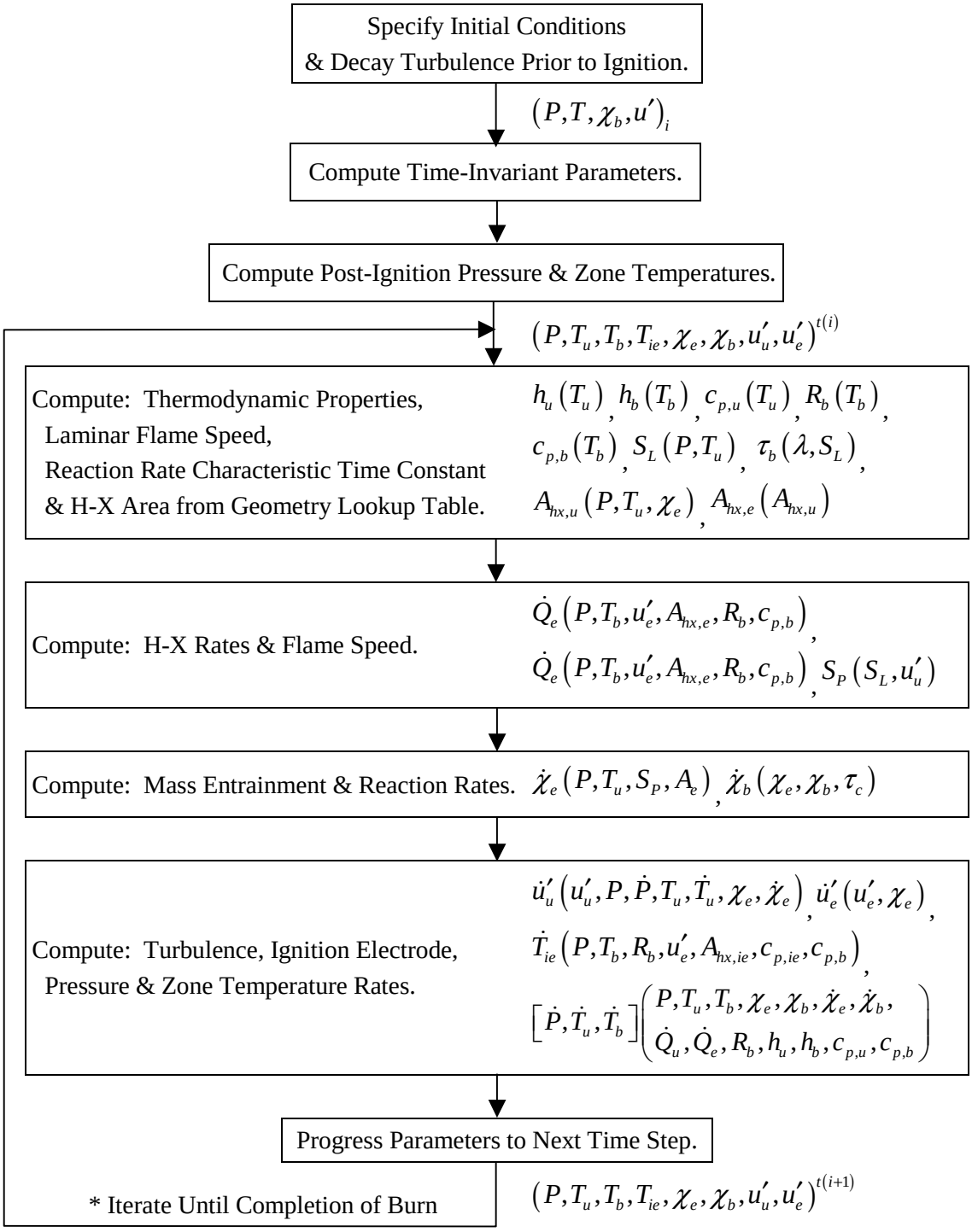

Figure 3.8: Graphical Representation of Solution Process (Parameter Flow)

3.3 Reverse Model

The purpose of the reverse model is to determine model parameters for the CVCC that are not available in the literature and are difficult or impossible to determine experimentally. Figure 3.9 shows the general logic of the reverse model. The forward model is used along with the *Matlab®* built-in optimization function "FMINSEARCH" to obtain optimal values for one or more simulation input parameters of interest.

Inputs to the reverse model are a vector of the parameters to be optimized and experimental histories of pressure and flame radius. A scalar error function is defined from the average instantaneous differences in experimental and simulation pressure and entrainment radius histories.

$$Error = \frac{1}{w_p + w_r} \cdot \left(\frac{w_p \cdot \sum_{j=j_1}^{j=m+j_1} \left[\left| P_{sim} - P_{\exp} \right| \right]_j}{m \cdot \left(P_{\exp,\max} - P_{\exp,\min} \right)} + \frac{w_r \cdot \sum_{k=k_1}^{k=n+k_1} \left[\left| r_{sim} - r_{\exp} \right| \right]_k}{n \cdot \left(r_{\exp,\max} - r_{\exp,\min} \right)} \right) \tag{3.131}$$

Independent summation ranges are used, based on the nature of the experimental data. Pressure data is valid for the entire recording period but is limited here from ignition until the peak value is reached. Radius is only available until the flame nears the far wall and the front loses its characteristic circular shape. The function includes weights to allow a bias on the more certain pressure data. Flame radius accuracy is a less certain since the value is based on visible light emission, which may not correspond to the actual leading edge. The weights are initially fixed at 2.0 for pressure and 1.0 for flame radius.

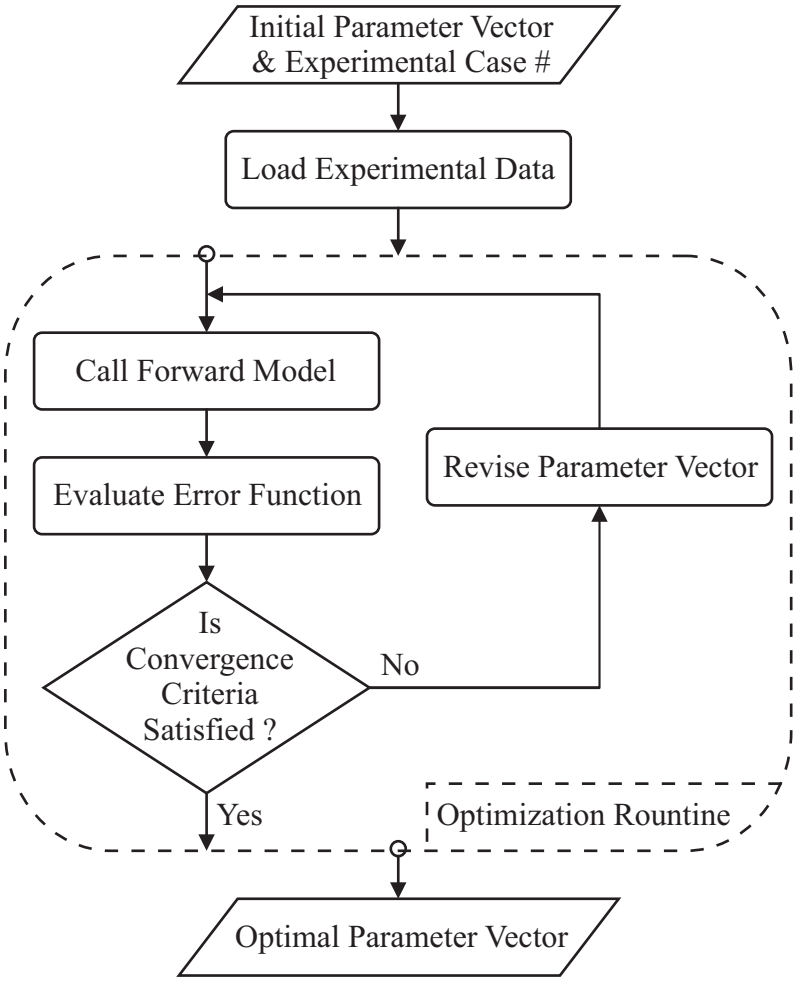

Figure 3.9: General Logic Flow of Reverse Model

CHAPTER 4

STRATIFIED-CHARGE MODEL

In this chapter, the homogeneous model is extended to include the case of an initially stratified chamber with two distinct mixture zones. This introduces significant complexities beyond those of the homogeneous case. Key differences of stratified combustion are first identified. Appropriate modifications of and additions to the homogeneous model are then formulated following the procedure of the Chapter 3 development. The goal is to a stratified model with the same level of detail, simplification, etc. as the two-zone homogeneous model.

4.1 Complexities of Stratified Combustion

In order to capture the essential nature of stratified combustion in a simplified model it is first necessary to identify the dominant issues. One obvious issue is the boundary that separates the mixture zones. Initially the boundary is clearly defined by the partition but it becomes less well defined as time progresses and evolves into a third zone that may contain a non-negligible fraction of the total chamber volume. The process by which the boundary zone evolves must be reduced to a manageable mathematical form for inclusion in the model. A second issue is the variance of flame propagation rates in regions of different equivalence since laminar flame speed is a function of pressure, temperature and equivalence. The homogeneous model includes the effect of varying equivalence on laminar flame speed but it is clear that the effect of entrainment from multiple mixture zones must be carefully considered. An attempt is made in the following sections to address these issues and develop a model that is a balance between sufficient detail and excess complexity.

4.2 Model Detail and Appropriate Assumptions

Several terms with specific meaning are used from this point. *Region* is used to describe and differentiate mass/volume sub-zones of mixture within the unburned zone. In this way the term zone is associated with the combustion process and the term region with mixture strength. *Stage* is used to identify periods in the combustion event during which the mixture regions undergo similar processes. *Phase* continues to identify the various cases of flame geometry that occur from ignition to extinction.

Issues of zone definition, mixture diffusion (mass exchange between regions) and flame geometry are so closely coupled that it is most sensible to address them jointly. The combustion process is broken into four stages based on significant changes in the interaction of the flame front and multiple mixture regions. Suitable levels of model detail and simplifying assumptions are then formulated for each of these stages.

4.2.1 Stages of Idealized Stratified Combustion

4.2.1.1 Stage 1

Stage 1 is the trivial case prior to the conjoining of the two chamber halves. The chamber contents are described by two mixture regions with a static boundary [Figure 4.1].

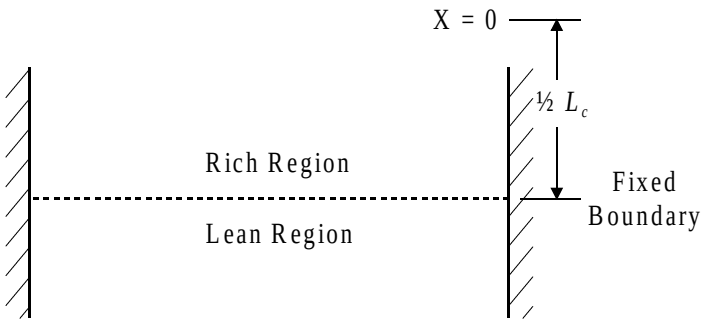

Figure 4.1: Idealized Stratified Combustion – Stage 1

4.2.1.2 Stage 2

Once the partition opens and mixing between the two distinct mixtures begins, the boundary is no longer static. Three regions [Figure 4.2] are needed to describe the system during this period.

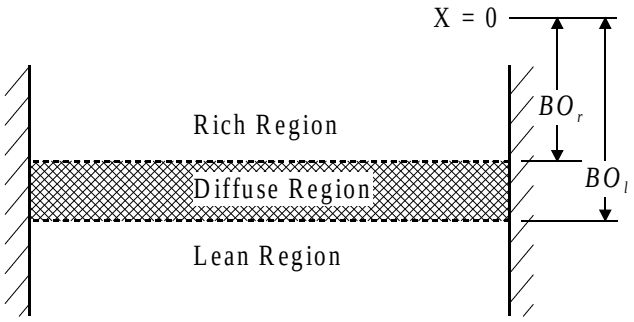

Figure 4.2: Idealized Stratified Combustion – Stage 2

A third region forms at the previously static boundary location. The volume of this region is initially zero and increases as mixture enters from the rich and lean regions. The dominant mechanism controlling diffusion is assumed to be turbulent transport. This is based on the observation in the literature that turbulent transport is the dominant mechanism for property transport during turbulent combustion. With this assumption, the rate of mixture influx is a function of the turbulence level, integral length scale and boundary surface area. As a first approximation, uniform equivalence is assumed within the diffuse region following the simple analysis of the two-zone homogeneous model. The boundary areas on the rich and lean side are equal so the amount of mass entering the diffuse region from each side is also equal. As long as this is the case, the overall diffuse equivalence is equal to the overall chamber equivalence. This is true until Stage 4 when the rich and lean boundary areas are no longer equal. Diffusion does

not begin across the chamber at one instant but evolves over a finite time as the partition opens. This is handled simply by initiating diffusion across the entire chamber after the partition has opened halfway.

4.2.1.3 Stage 3

The third stage begins after ignition and continues until the flame front reaches the diffuse region. Ignition can take place in either of two locations for normal or parallel stratification. The normal case (top mounted electrodes) is selected to simplify the complexity as described in the following sidebar.

Sidebar – Varied Complexity of Normal and Parallel Stratification

The CVCC hardware allows for either normal or parallel stratification by changing the location of the ignition electrodes. The simplest stratified charge case to model is normal stratification. This is clear in the following comparison between both cases. Figure 4.3 shows flame front development at three times for a typical parallel-stratified case. Initial conditions are: 103 kPa initial pressure, upper equivalence 1.2, lower equivalence 0.4 and quiescent flow.

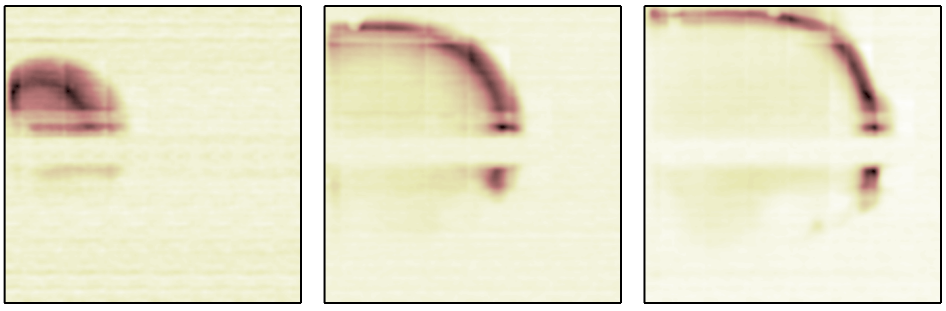

Figure 4.3: Complex Flame Geometry of Parallel-Stratified Case

In this instance the flame geometry is not symmetric and distorts due to uneven front expansion rates in the zones with differing equivalence. Figure 4.4 shows flame front development at three times for a normal-stratified case with the same initial conditions.

Figure 4.4: Simple Flame Geometry of Normal-Stratified Case

Symmetry of the flame front along the vertical centerline of the chamber is clear. This symmetry makes the normal-stratified flame front evolution far simpler to model (continuing to use one-quarter of the front as in the homogeneous case). It makes most sense in studying the viability of a simplified model to begin with the simplest stratified case and the normal case is clearly the best choice.

In Stage 3 the diffuse region is no longer stationary and moves along with the lean region as the entire unburned zone is compressed ahead of the flame front. The three zones of the homogeneous case must be modified to account for the multiple mixture regions in the unburned

zone. The entrained and burned zones remain unchanged but the unburned zone now has three sub-zones defined by the two surfaces bounding the diffuse region [Figure 4.5].

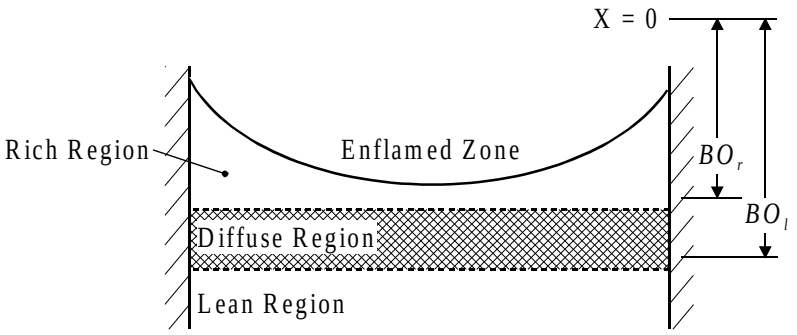

Figure 4.5: Idealized Stratified Combustion – Stage 3

Compression of the unburned zone results in both longitudinal and lateral movement of mixture. This is required for the uniform pressure assumption to hold in the unburned zone as the flame front expands and curvature increases. The less significant lateral displacement is ignored and as a first approximation, the boundaries are assumed to retain their planar shape as the unburned zone is compressed.

Early flame geometry is identical to that of the homogeneous case. Since the stratification is initially at the chamber mid-distance, the flame front cannot reach the diffuse region before flame geometry Phase 7 [see Section 3.2.2.1]. The fact that the diffuse boundaries undergo a displacement means that contact with the first boundary is most likely made during flame geometry Phase 8. Since contact with the diffuse region occurs after the flame reaches a distant position in the chamber where the front is relatively flat, the assumption of planar diffuse region boundaries seems reasonable.

4.2.1.4 Stage 4

The fourth and final stage of the idealized stratified combustion begins when the flame front crosses the first diffuse zone boundary [Figure 4.6]. Early in this stage, only mass from the rich and diffuse regions is entrained and burned.

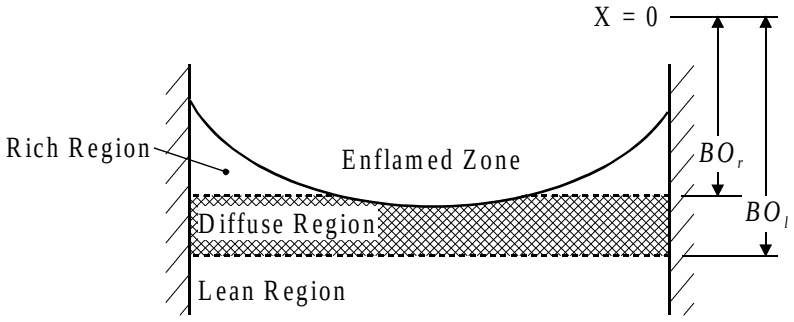

Figure 4.6: Idealized Stratified Combustion – Stage 4 (Early)

In Stage 4, mass contributions from all three regions are possible [Figure 4.7]. It is also possible that the entire rich region may be consumed, leaving only the diffuse and lean regions.

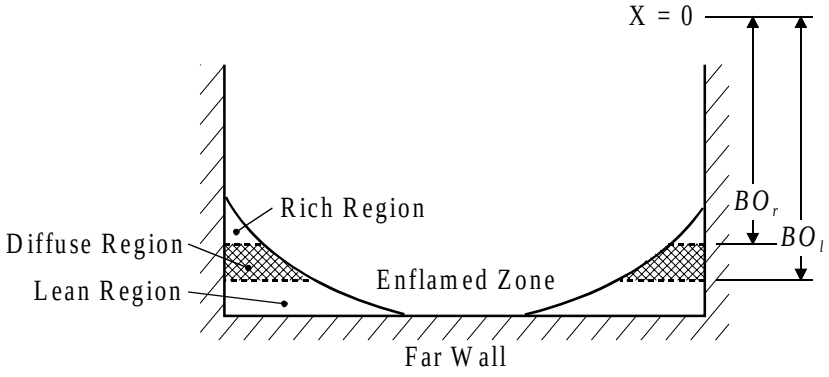

Figure 4.7: Idealized Stratified Combustion – Stage 4 (Late)

Flame front curvature theoretically increases in the leaner regions, resulting in a flattening at the chamber center (assuming the rich region flame speed is higher). The difference in curvature is small since the front is relatively flat by the time the front has reached the diffuse region. The difference is neglected and a constant curvature is assumed to allow use of the existing flame geometry lookup tables. The constant curvature front is assumed to advance at a weighted propagation velocity with weights determined by the front's exposure in each region.

Once entrained, it is assumed that mixture from each region reacts before it has sufficient time to mix with mass from the other regions. This is reasonable since the reaction of a small amount of mass in the zone is quick in comparison to the time required the zone to become well-mixed along the greatest dimension (reaction rate >> turbulent mixing rate). The mass reaction rates for each mass stream may vary since no assumption requires a uniform reaction zone thickness.

4.3 Forward Model

Rich, lean and diffuse mixture regions in the unburned zone are denoted by the symbols $\chi_{u,r}$, $\chi_{u,l}$ and χ_d. Each of these is defined as the fraction of total chamber mass contained within the given region.

4.3.1 New Definitions for the Stratified Model

Degree of stratification (*DOS*) is a new term, defined to have values of zero when the rich and lean region equivalences are equal (homogeneous case) and unity for the case of maximum stratification where the lean zone contains no fuel.

$$DOS = \frac{\phi_l - \phi_r}{\phi_l + \phi_r} \tag{4.1}$$

The equivalence of the rich and lean mixtures is written in terms of the overall equivalence and *DOS*.

$$\phi = \frac{\phi_l + \phi_r}{2} \tag{4.2}$$

$$\phi_l = \phi \cdot (1 + DOS) \tag{4.3}$$

$$\phi_r = \phi \cdot (1 - DOS) \tag{4.4}$$

4.3.2 General Diffusion and Geometry Issues

The unburned zone is comprised of three mixture regions, each with a distinct and uniform equivalence. The diffuse region has zero initial mass. Turbulent transport brings mass into the diffuse region from the rich and lean regions after the partition is opened [Figure 4.8].

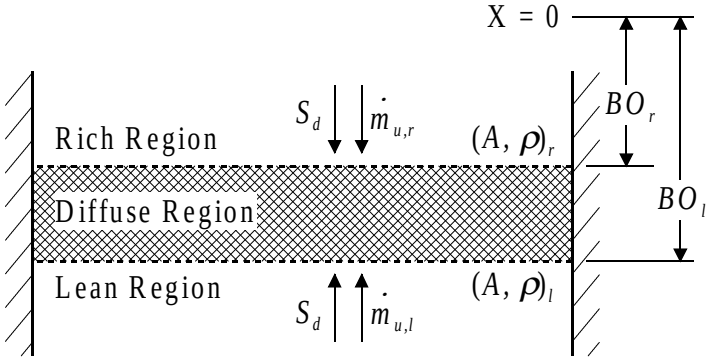

Figure 4.8: Diffuse Region Mass Flows

Diffusion speed S_d is some function of turbulence velocity and integral length scale. The turbulent transport relationship from Lumley [27] allows displacement of the boundaries over a time Δt (the simulation time step) to be written without need for an explicit expression of the diffusion speed. These are approximations and not the target differential forms of Chapter 3 but once implemented for computer solution this distinction disappears.

$$\Delta BO = K_d \cdot \sqrt{\tfrac{2}{3} \cdot u_u' \cdot L \cdot \Delta t} \tag{4.5}$$

A diffusion rate constant K_d is added to allow scaling of the diffusion effect and matching with experimental data. The incremental change of the mass fraction in each region over the same time t is written in terms of the boundary offset.

$$\Delta \chi_{u,l}\big|_{diff} = -\frac{K_d \cdot A_{d,l} \cdot \Delta BO}{m_c \cdot \upsilon_{u,l}} \tag{4.6}$$

$$\Delta \chi_{u,r}\big|_{diff} = -\frac{A_{d,r} \cdot \Delta BO}{m_c \cdot \upsilon_{u,r}} \tag{4.7}$$

$$\Delta \chi_{d}\big|_{diff} = \frac{\Delta BO}{m_c} \cdot \left(\frac{A_{d,l}}{\upsilon_{u,l}} + \frac{A_{d,r}}{\upsilon_{u,r}} \right) \tag{4.8}$$

In this expression, the areas are not necessarily constant. Once the flame front has crossed the rich boundary (Stage 4), the rich area is less than the lean area. It is also possible for the front to cross the lean boundary before the entire rich region is consumed.

4.3.3 Specific Governing Equations After Stage 1

During Stage 1, nothing more than the existing turbulence decay model is required to provide an initial intensity value at the time of partition opening. With the start of Stage 2, additional equations are necessary to model the diffusion process and extend the homogeneous model to handle the of multiple unburned mixture regions.

4.3.3.1 Stage 2 – Prior to Ignition

Both planar boundaries are initially located at the chamber midpoint. The locations at the time ignition can be computed easily if the turbulence decay time history is known and the simulation time step is constant.

$$BO_l\big|_{ign} = \tfrac{1}{2}\cdot L_C + \sum \Delta BO \tag{4.9}$$

$$BO_r\big|_{ign} = \tfrac{1}{2}\cdot L_C - \sum \Delta BO \tag{4.10}$$

The summation is taken of all turbulence intensity values from partition opening until the time step prior to ignition. Mass fractions at ignition are written in terms of the initial mass fractions and the initial and final locations of the lean and rich boundaries.

$$\chi_{u,l}\big|_{ign} = \left(\frac{BO_l\big|_{ign}}{L_c/2} - 1\right)\cdot \chi_{u,l}\big|_{init} \tag{4.11}$$

$$\chi_{u,r}\big|_{ign} = \left(1 - \frac{BO_r\big|_{ign}}{L_c/2}\right)\cdot \chi_{u,r}\big|_{init} \tag{4.12}$$

$$\chi_{d}\big|_{ign} = 1 - \left(\frac{BO_l\big|_{ign}}{L_c/2} - 1\right)\cdot \chi_{u,l}\big|_{init} - \left(1 - \frac{BO_r\big|_{ign}}{L_c/2}\right)\cdot \chi_{u,r}\big|_{init} \tag{4.13}$$

4.3.3.2 Stage 3 – After Ignition, Before Contact with the Diffuse Region

Stage 3 continues until the flame front reaches the rich boundary of the diffuse region.

$$r_e \begin{cases} < BO_r - SO & Stage\ 3 \\ \geq BO_r - SO & Stage\ 4 \end{cases} \tag{4.14}$$

Three separate effects to consider are diffusion, entrainment and compression. Diffusion results in a change in the three unburned mass fractions and movement of the diffuse region boundaries. Entrainment in this period involves only the rich region and no special consideration is required. Compression of the unburned zone results in an easily computed shift of the planar boundaries.

Diffusion

At each time-step, boundary locations and region mass fractions are updated prior to mass entrainment and reaction.

$$\Delta\chi_{u,l}\Big|_{diff} = -\frac{A_{d,l} \cdot \Delta BO \cdot P}{m_c \cdot R_{u,l} \cdot T_u} \tag{4.15}$$

$$\Delta\chi_{u,r}\Big|_{diff} = -\frac{A_{d,r} \cdot \Delta BO \cdot P}{m_c \cdot R_{u,r} \cdot T_u} \tag{4.16}$$

The diffuse mass fraction rate is the sum of the previous two rates with appropriate change of sign.

$$\Delta\chi_d\Big|_{diff} = \frac{\Delta BO \cdot P}{m_c} \cdot \left(\frac{A_{d,l}}{R_{u,l} \cdot T_u} + \frac{A_{d,r}}{R_{u,r} \cdot T_u} \right) \tag{4.17}$$

In Stage 3, this is a simple matter since the diffusion areas are constant and equal.

$$A_{d,l} = A_{d,r} = L_c \cdot t_c \tag{4.18}$$

Mass Entrainment

An expression for the mass fraction entrainment from the rich region is obtained from the homogeneous expression for the reaction zone mass fraction entrainment rate [Equation 3.51]. The only changes required are in variable subscripts and overall sign.

$$\frac{d\chi_e}{dt} = -\left.\frac{d\chi_{u,r}}{dt}\right|_{entr} = \frac{A_{e,r} \cdot P \cdot S_P}{m_c \cdot R_{u,r} \cdot T_u} \tag{4.19}$$

The rich region entrainment area is equal to the total entrainment area since only the rich region is in contact with the reaction zone.

Zone/Region Compression

A new issue is compression of the unburned zone and the resulting displacement of the diffusion boundaries. The use of planar diffusion boundaries and constant areas makes this a relatively simple task in Stage 3. Updated region volumes are found for the new mass fractions and thermodynamic properties. New boundary locations are then computed easily since both lean and rich boundary areas are simple rectangles.

$$BO_l = L_c - \frac{\forall_{u,l}}{\mathrm{A_{d,l}}} \tag{4.20}$$

$$BO_r = BO_l - \frac{\forall_{u,d}}{\mathrm{A_{d,r}}} \tag{4.21}$$

4.3.3.3 Stage 4 – After Contact with the Diffuse Region

Modeling of all processes in Stage 4 is considerably more complicated than Stage 3. The diffusion model requires tracking of the varying diffusion areas as the flame front is in contact with one or both of the boundaries. The actual diffusion boundaries are complex curves but the planar assumption and the assumed constant curvature of the flame front reduces the geometry to a manageable level. Entrainment now involves one, two or all three regions. Compression driven boundary shift is also more complex since the boundary areas are no longer constant.

Flame Front and Mixture Region Geometry

Figure 4.9 shows the most complex case where the front is in contact with both boundaries and the far wall.

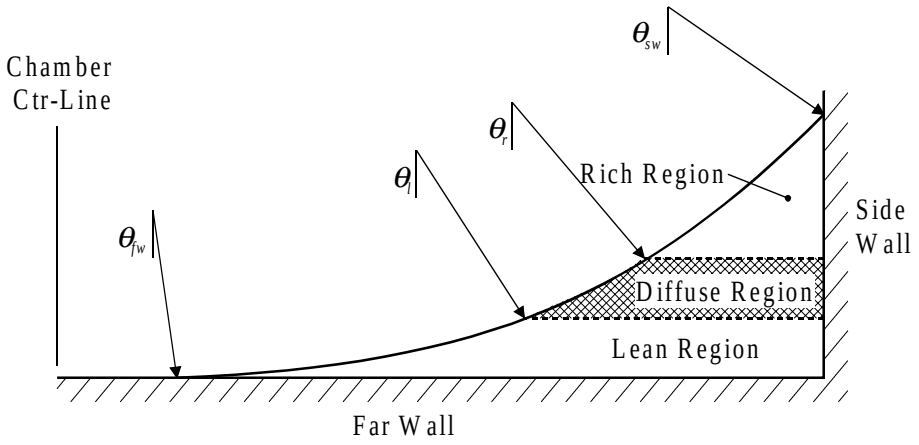

Figure 4.9: Flame Front Contact with Multiple Regions

Several simplifications beyond those already noted are used here to ease the task of computing required areas and volumes. Out-of-plane curvature of the front is neglected. To minimize associated error, distances to the front at the center plane and the window are averaged. This average planar radius is used to compute the required angles.

$$r_{avg} = \frac{r_e + \sqrt{r_e^2 - \frac{1}{4} \cdot t_c^2}}{2} \tag{4.22}$$

Flame Front Areas

Flame front areas in each region are needed to compute the entrainment rates. The lookup table contains the total area and this must be split into the region areas. With the assumed constant curvature of the front, the ratio of areas is equivalent to the ratio of arc lengths or swept angles. Using this approach, only four angles are necessary at each time step to provide the ratio of flame front area in each region to the total flame front area. Three swept angles are those in the rich, lean and diffuse regions.

$$\frac{\theta_{e,r}}{2} = \theta_{sw} - \theta_r = \sin^{-1}\left(\frac{L_c}{2 \cdot r_{avg}}\right) - \cos^{-1}\left(\frac{BO_r - SO}{r_{avg}}\right) \tag{4.23}$$

$$\frac{\theta_{e,l}}{2} = \theta_l - \theta_{fw} = \cos^{-1}\left(\frac{BO_l - SO}{r_{avg}}\right) - \cos^{-1}\left(\frac{L_c - SO}{r_{avg}}\right) \tag{4.24}$$

$$\frac{\theta_{e,d}}{2} = \theta_r - \theta_l = \cos^{-1}\left(\frac{BO_r - SO}{r_{avg}}\right) - \cos^{-1}\left(\frac{BO_l - SO}{r_{avg}}\right) \tag{4.25}$$

The ratio of each is taken with the total free angle of the flame front ($\theta_{e,t}$) to obtain the ratio of flame front area in each region.

$$\frac{\theta_{e,t}}{2} = \theta_{sw} - \theta_{fw} = \sin^{-1}\left(\frac{L_c}{2 \cdot r_{avg}}\right) - \sin^{-1}\left(\frac{L_c - SO}{r_{avg}}\right) \tag{4.26}$$

Diffusion

The Stage 3 expressions for diffusion are unchanged. Diffusion areas are now time varying and written in terms of the boundary locations and average planar radius.

$$A_{d,l} = t_c \cdot \left(L_c - 2 \cdot \sqrt{r_{avg}^2 - \left(BO_l - SO\right)^2}\right) \tag{4.27}$$

$$A_{d,r} = t_c \cdot \left(L_c - 2 \cdot \sqrt{r_{avg}^2 - \left(BO_r - SO\right)^2}\right) \tag{4.28}$$

Mass Entrainment

Multiple regions are in contact with the flame front and the amount of mass entrained from each varies depending on the flame front location. The mass entrainment rate for each region is computed using a weighted propagation velocity, local flame front areas and property values.

$$\left.\frac{d\chi_{u,r}}{dt}\right|_{entr} = -\frac{\theta_{e,r}}{\theta_{e,t}} \cdot \frac{A_e \cdot P \cdot S_P}{m_c \cdot R_{u,r} \cdot T_u} \tag{4.29}$$

$$\left.\frac{d\chi_{u,l}}{dt}\right|_{entr} = -\frac{\theta_{e,l}}{\theta_{e,t}} \cdot \frac{A_e \cdot P \cdot S_P}{m_c \cdot R_{u,l} \cdot T_u} \tag{4.30}$$

$$\left.\frac{d\chi_d}{dt}\right|_{entr} = -\frac{\theta_{e,d}}{\theta_{e,t}} \cdot \frac{A_e \cdot P \cdot S_P}{m_c \cdot R_d \cdot T_u} \tag{4.31}$$

$$S_P = \frac{\theta_{e,r} \cdot S_{P,r} + \theta_{e,d} \cdot S_{P,d} + \theta_{e,l} \cdot S_{P,l}}{\theta_{e,t}} \tag{4.32}$$

The rates in each region are summed for the total entrainment rate.

$$\left.\frac{d\chi_e}{dt}\right|_{entr} = \left(\frac{\theta_{e,r}}{R_{u,r}} + \frac{\theta_{e,l}}{R_{u,l}} + \frac{\theta_{e,d}}{R_d}\right) \cdot \frac{A_e \cdot P \cdot S_P}{m_c \cdot \theta_t \cdot T_u} \tag{4.33}$$

Entrainment of mass continues from all regions as long as the weighted speed is nonzero. This is true even if any local speed is zero, as required for the assumed simple flame front geometry sub-model.

Zone/Region Compression

Simple alternatives to closed-form boundary displacement rates are developed. Neglecting the out-of-plane curvature allows the use of area and volume ratios interchangeably. This fact is used to compute the four defined tracking angles ($\theta_{u,r}$, $\theta_{u,l}$, θ_d and $\theta_{e,t}$). A differential element for the planar area integral is defined in Figure 4.10 (based on one half of the symmetric chamber).

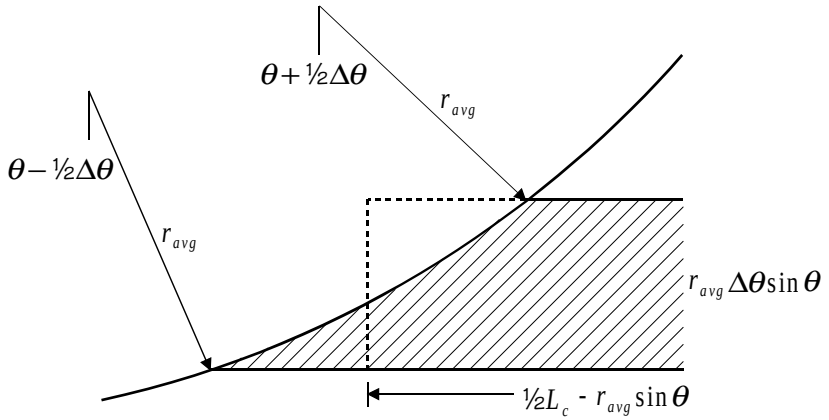

Figure 4.10: Planar Area Integral for Unburned Regions

The differential element area is integrated over the appropriate range of θ to obtain the planar area in each region.

$$\frac{A^*}{2} = \int_{\theta_1}^{\theta_2} \left(\tfrac{1}{2} \cdot L_c \cdot r_{avg} \cdot \sin(\alpha) - r_{avg}^2 \cdot \sin^2(\alpha) \right) d\alpha \tag{4.34}$$

$$\frac{A^*}{2} = \tfrac{1}{2} \cdot r_{avg} \cdot \left[L_c \cdot \left(\cos(\theta_1) - \cos(\theta_2) \right) + r_{avg} \cdot \left((\theta_1 - \theta_2) + \tfrac{1}{2} \cdot \left(\sin(2 \cdot \theta_2) - \sin(2 \cdot \theta_1) \right) \right) \right] \tag{4.35}$$

If the lower limit of integration is zero (chamber centerline) there is an additional rectangular area ahead of the flame front and this is added to the integrated area. The total unburned area is obtained if the sweep extends from the far wall (or centerline if the front is not yet in contact) to the side wall [see Figure 4.9].

$$\frac{A_u^*}{2} = \tfrac{1}{2} \cdot r_{avg} \cdot \left[L_c \cdot \left(\cos(\theta_{fw}) - \cos(\theta_{sw}) \right) + r_{avg} \cdot \left((\theta_{fw} - \theta_{sw}) + \tfrac{1}{2} \cdot \left(\sin(2 \cdot \theta_{sw}) - \sin(2 \cdot \theta_{fw}) \right) \right) \right] \tag{4.36}$$

The lean and diffuse areas are obtained similarly.

$$\frac{A_l^*}{2} = \tfrac{1}{2} \cdot r_{avg} \cdot \left[L_c \cdot \left(\cos\left(\theta_{fw}\right) - \cos\left(\theta_l\right) \right) + r_{avg} \cdot \left(\left(\theta_{fw} - \theta_l\right) + \tfrac{1}{2} \cdot \left(\sin\left(2 \cdot \theta_l\right) - \sin\left(2 \cdot \theta_{fw}\right) \right) \right) \right] \qquad (4.37)$$

$$\frac{A_d^*}{2} = \tfrac{1}{2} \cdot r_{avg} \cdot \left[L_c \cdot \left(\cos\left(\theta_l\right) - \cos\left(\theta_r\right) \right) + r_{avg} \cdot \left(\left(\theta_l - \theta_r\right) + \tfrac{1}{2} \cdot \left(\sin\left(2 \cdot \theta_r\right) - \sin\left(2 \cdot \theta_l\right) \right) \right) \right] \qquad (4.38)$$

With the out-of-plane curvature neglected, the ratio of region volumes and planar areas is equal. Error functions are defined using the known region volumes, total planar areas and the unknown region planar areas.

$$\varepsilon_l = \left| A_l^* - \frac{V_l}{V_u} \cdot A_u^* \right| \qquad \varepsilon_d = \left| A_d^* - \frac{V_d}{V_u} \cdot A_u^* \right| \qquad (4.39a/b)$$

Volumes are functions of the region mass fractions and thermodynamic properties. Total planar areas are functions of the entrainment radius. Region areas are the only unknown terms and these can be computed using the following steps:

i) Compute region and total volumes from mass fractions and zone properties.

ii) Provide an initial seed for the new lean region angle.

iii) Use the built-in *Matlab*® function FMINBND (bounded optimization routine) to minimize each error function and obtain values for the rich and lean contact angles.

4.3.4 Modifications of and Additions to the Homogeneous Model

The structure of the model allows the stratified model to share much of the existing homogeneous development. Modifications and new modules necessary to handle stratified system complexities are presented in this chapter.

4.3.4.1 Mass Tracking

A split-mass method of accounting is used to ease tracking of time-varying equivalences and to ensure mass conservation. Total mass flows between the unburned regions and between the unburned, reaction and burned zones are split into rich and lean components. Variables carry single or double subscripts to denote the overall zone/region value or the value for the rich/lean mass component. A new double subscript is defined to denote properties associated with the entire unburned zone (rich, lean and diffuse regions). As an example of the subscripting system, consider the total unburned mass fraction. This is the sum of the rich and lean mass fractions from the rich, lean and diffuse regions and can be expressed in several equivalent forms.

$$\chi_{uu} = \chi_u + \chi_d = \left(\chi_{u,r} + \chi_{u,l}\right) + \left(\chi_{d,r} + \chi_{d,l}\right) = 1 - \chi_e = 1 - \left(\chi_{e,r} + \chi_{e,l}\right) \tag{4.40}$$

4.3.4.2 Time Varying Equivalence Ratio

Mean equivalence in the diffuse region, reaction and burned zones varies throughout the combustion process unless the initial unburned mixtures are identical (this is equivalent to the homogeneous case). The mean equivalence is required for a zone only if property values are evaluated under the assumption of uniform mixture within that zone. At any time step, the equivalence is a function of the rich and lean mixture equivalences and the current ratio of rich/lean mass in the region/zone. The burned zone expression is given as an example.

$$\left[\phi_b\right]_i = \frac{\left[\chi_{b,r}\right]_i \cdot \phi_{u,r} + \left[\chi_{b,l}\right]_i \cdot \phi_{u,l}}{\left[\chi_b\right]_i} \tag{4.41}$$

4.3.4.3 Ideal Gas Equation

The homogeneous unburned specific volume is not valid since the amount of rich and lean mass is not constant. The newly defined double-u subscript is used to define the overall unburned zone specific volume (rich, lean and diffuse regions).

$$\upsilon_{uu} = \frac{\left(\chi_{u,r} + \chi_{d,r}\right) \cdot R_{u,r} + \left(\chi_{u,l} + \chi_{d,l}\right) \cdot R_{u,l}}{\chi_{uu}} \cdot \frac{T_u}{P} \tag{4.42}$$

The entrained zone expression is also modified to account for the fact that the unburned and reaction zone equivalences and gas constants are no longer equal.

$$\upsilon_e = \frac{\left(\chi_e - \chi_b\right) \cdot R_r \cdot T_u + \chi_b \cdot R_b \cdot T_b}{\chi_e \cdot P} \tag{4.43}$$

4.3.4.4 Energy Balance for the Unburned Zone

The homogeneous energy balance [Equation 3.37] is valid also for the stratified case.

$$\left(1-\chi_e\right) \cdot c_{p,u} \cdot \frac{dT_u}{dt} - \frac{\forall_c - \forall_e}{m_c} \frac{dP}{dt} = -\frac{1}{m_c} \cdot \frac{dQ_u}{dt} \tag{3.37}$$

The unburned specific heat for the overall unburned zone ($C_{p,uu}$) is used to differentiate this from the homogeneous case (see Section 4.3.4.10).

$$\boxed{\left(1-\chi_e\right) \cdot c_{p,uu} \cdot \frac{dT_u}{dt} - \frac{\forall_c - \forall_e}{m_c} \frac{dP}{dt} = -\frac{1}{m_c} \cdot \frac{dQ_u}{dt}} \tag{4.44}$$

4.3.4.5 Energy Balance for the Entrained Zone

The homogeneous energy balance [Equation 3.42] is valid with changes to account for the different zone mixture equivalences.

$$\left.\begin{array}{r}\left(\chi_e-\chi_b\right)\cdot c_{p,u}\cdot\dfrac{dT_u}{dt}\cdots\\ +\chi_b\cdot c_{p,b}\cdot\dfrac{dT_b}{dt}\cdots\\ -\dfrac{\cancel{V_e}}{m_c}\cdot\dfrac{dP}{dt}\end{array}\right\}=\left\{\begin{array}{l}-\dfrac{1}{m_c}\cdot\dfrac{dQ_e}{dt}\cdots\\ +\left(h_u-h_b\right)\cdot\dfrac{d\chi_b}{dt}\end{array}\right. \qquad [3.42]$$

Properties $C_{p,u}$ and h_u become $C_{p,r}$ and h_r respectively.

$$\boxed{\left.\begin{array}{r}\left(\chi_e-\chi_b\right)\cdot c_{p,r}\cdot\dfrac{dT_u}{dt}\cdots\\ +\chi_b\cdot c_{p,b}\cdot\dfrac{dT_b}{dt}\cdots\\ -\dfrac{\cancel{V_e}}{m_c}\cdot\dfrac{dP}{dt}\end{array}\right\}=\left\{\begin{array}{l}-\dfrac{1}{m_c}\cdot\dfrac{dQ_e}{dt}\\ +\left(h_r-h_b\right)\cdot\dfrac{d\chi_b}{dt}\end{array}\right.} \qquad (4.45)$$

In the homogeneous case, the enthalpy difference represents the change of reactants to products. In the stratified case this represents the net for conversion of reactants to products for the multiple reacting streams and subsequent mixing of the new volume into the existing burned zone.

4.3.4.6 Constant Volume Constraint

The homogeneous constant volume constraint [Equation 3.49] is valid with changes, similar to those necessary for the energy balances.

$$\left.\begin{aligned}\left(1-\chi_b\right)\cdot\frac{d\left(R_u\cdot T_u\right)}{dT_u}\cdot\frac{dT_u}{dt}\cdots\\ +\chi_b\cdot\frac{d\left(R_b\cdot T_b\right)}{dT_b}\cdot\frac{dT_b}{dt}\cdots\\ -\frac{\cancel{V_c}}{m_c}\cdot\frac{dP}{dt}\end{aligned}\right\}=\left(R_u\cdot T_u-R_b\cdot T_b\right)\cdot\frac{d\chi_b}{dt} \qquad [3.49]$$

The left side unburned gas constant is replaced with a new subscripted variable (R_{uur}) specifying the property for all unburned mass contained in the unburned and reaction zones. The right side change is from the unburned to the reaction gas constant since the terms are involved with the mass rate and not the mass fraction.

$$\boxed{\left.\begin{aligned}\left(1-\chi_b\right)\cdot\frac{d\left(R_{uur}\cdot T_u\right)}{dT_u}\cdot\frac{dT_u}{dt}\cdots\\ +\chi_b\cdot\frac{d\left(R_b\cdot T_b\right)}{dT_b}\cdot\frac{dT_b}{dt}\cdots\\ -\frac{\cancel{V_c}}{m_c}\cdot\frac{dP}{dt}\end{aligned}\right\}=\left(R_r\cdot T_u-R_b\cdot T_b\right)\cdot\frac{d\chi_b}{dt}} \qquad (4.46)$$

The R-T product derivatives are evaluated for the overall unburned and burned zone properties.

$$\left(1-\chi_b\right)\cdot\frac{d\left(R_{uur}\cdot T_u\right)}{dT_u}=\left(\chi_{ini,r}-\chi_{b,r}\right)\cdot\frac{d\left(R_{u,r}\cdot T_u\right)}{dT_u}+\left(\chi_{ini,l}-\chi_{b,l}\right)\cdot\frac{d\left(R_{u,l}\cdot T_u\right)}{dT_u} \qquad (4.47)$$

$$\chi_b \cdot \frac{d\left(R_b \cdot T_b\right)}{dT_b} = \chi_{b,r} \cdot \frac{d\left(R_{b,r} \cdot T_b\right)}{dT_b} + \chi_{b,l} \cdot \frac{d\left(R_{b,l} \cdot T_b\right)}{dT_b} \tag{4.48}$$

4.3.4.7 Mass Reaction Rate

No assumption thus far requires the reaction zone be a uniform thickness so the reaction rate of each mixture stream can be independent. There are three streams, each with a unique equivalence, reacting at three different rates (not considering the trivial case). A new variable is defined for the ratio of rich and lean reaction mass attributable to entrainment from the diffuse region. The Greek variables $\chi\chi_{rd,r}$ and $\chi\chi_{rd,l}$ are used since these values are in fact fractions of fractions.

The rates are written for mixture streams from the unburned rich and lean regions and for the total rate of the mixture stream from the diffuse region.

$$\left.\frac{d\chi_{b,r}}{dt}\right|_{u,r} = \frac{\left(1-\chi\chi_{rd,r}\right)\cdot\left(\chi_{e,r}-\chi_{b,r}\right)}{\tau_{b,r}} \tag{4.49}$$

$$\left.\frac{d\chi_{b,l}}{dt}\right|_{u,l} = \frac{\left(1-\chi\chi_{rd,l}\right)\cdot\left(\chi_{e,l}-\chi_{b,l}\right)}{\tau_{b,l}} \tag{4.50}$$

$$\left.\frac{d\chi_{b,r}}{dt}\right|_{d} + \left.\frac{d\chi_{b,l}}{dt}\right|_{d} = \frac{\chi\chi_{rd,r}\cdot\left(\chi_{e,r}-\chi_{b,r}\right)+\chi\chi_{rd,l}\cdot\left(\chi_{e,l}-\chi_{b,l}\right)}{\tau_{b,d}} \tag{4.51}$$

For mass tracking purposes, the total rate of transfer of rich and lean mass from the reaction to the burned zone is the sum of the contributions from the pure rich/lean and diffuse regions.

$$\frac{d\chi_{b,r}}{dt} = \left.\frac{d\chi_{b,r}}{dt}\right|_{u,r} + \left.\frac{d\chi_{b,r}}{dt}\right|_{d} = \left(\frac{1-\chi\chi_{rd,r}}{\tau_{b,r}} + \frac{\chi\chi_{rd,r}}{\tau_{b,d}}\right)\cdot\left(\chi_{e,r} - \chi_{b,r}\right) \tag{4.52}$$

$$\frac{d\chi_{b,l}}{dt} = \left.\frac{d\chi_{b,l}}{dt}\right|_{u,l} + \left.\frac{d\chi_{b,l}}{dt}\right|_{d} = \left(\frac{1-\chi\chi_{rd,l}}{\tau_{b,l}} + \frac{\chi\chi_{rd,l}}{\tau_{b,d}}\right)\cdot\left(\chi_{e,l} - \chi_{b,l}\right) \tag{4.53}$$

The total burn rate is then the sum of the rich and lean component sums.

$$\frac{d\chi_{b}}{dt} = \frac{d\chi_{b,r}}{dt} + \frac{d\chi_{b,l}}{dt} = \left(\frac{1-\chi\chi_{rd,r}}{\tau_{b,r}} + \frac{\chi\chi_{rd,r}}{\tau_{b,d}}\right)\cdot\left(\chi_{e,r} - \chi_{b,r}\right) + \left(\frac{1-\chi\chi_{rd,l}}{\tau_{b,l}} + \frac{\chi\chi_{rd,l}}{\tau_{b,d}}\right)\cdot\left(\chi_{e,l} - \chi_{b,l}\right) \tag{4.54}$$

The characteristic burning times are evaluated for each local flame speed. One or more of the region speeds may be non-sensible (no-burn condition). A zero rate is assigned in cases where any local speed is nominally zero (an offset is included to allow tuning). The reaction rates cannot change instantaneously and a moving average filter is employed to prevent problems due to abrupt changes (a four-step average is currently used). After all mass in a given region is entrained, the last nonzero speed is retained while the reaction zone clears of the corresponding mass. In lean cases where the flame propagation stops short of full entrainment, the local speed is decayed linearly with time until it reaches zero. This is a simple means to terminate the reaction for cases where the flame stalls in mixture that is too lean to allow continued propagation.

4.3.4.8 Early Burn Termination Due to Unsuitable Conditions

It is possible for some cases that chamber conditions will not support combustion. This is not an issue for the homogeneous model but now a simple means to handle the possibility of extinction before maximum entrainment is required. This is true since the simple flame geometry sub-model does not allow for local stagnation in one mixture region and continued propagation in another. There are multiple situations that may arise. The most simple is consumption of the rich and/or diffuse regions, leaving a non-combustible lean region. A more interesting case is simultaneous entrainment from regions of combustible and non-combustible mixtures (at a specific pressure and temperature). To provide for this case, the requirement is imposed that at least 50 percent of the total mixture entrained must be combustible.

$$\frac{\frac{d\chi_{u,r}}{dt}\left(S_{L,r} \geq S_{L,\min}\right) + \frac{d\chi_{u,l}}{dt}\left(S_{L,l} \geq S_{L,\min}\right) + \frac{d\chi_{d}}{dt}\left(S_{L,d} \geq S_{L,\min}\right)}{\frac{d\chi_{u,r}}{dt} + \frac{d\chi_{u,l}}{dt} + \frac{d\chi_{d}}{dt}} < 0.5 \quad \rightarrow \quad \textit{Extinction} \qquad (4.55)$$

The contribution from any region is zero if the local flame is nominally zero. If the global criterion is not satisfied then the simulation is terminated and a flag set to indicate extinction occurred due to unsuitable conditions. As mentioned in the previous section, mass currently in the reaction zone continues to react while the burn rates decay.

4.3.4.9 Ignition

The homogeneous energy balance and isentropic pressure equations are valid without modification. Post-ignition unburned volume and pressure based on the ideal gas law are modified to account for the fact that ignition takes place in the rich unburned region.

$$\frac{\tilde{V}_{uu}}{V_c} = \frac{\left(\left(\chi_{ini,r} - \chi_{e,ign}\right)\cdot \tilde{R}_{u,r} + \chi_{ini,l}\cdot \tilde{R}_{u,l}\right)\cdot \tilde{T}_u}{\left(\left(\chi_{ini,r} - \chi_{b,ign}\right)\cdot \tilde{R}_{u,r} + \chi_{ini,l}\cdot \tilde{R}_{u,l}\right)\cdot \tilde{T}_u + \chi_{b,ign}\cdot \tilde{R}_b \cdot \tilde{T}_b} \tag{4.56}$$

$$\tilde{P}_{ideal} = \frac{\left(\left(\chi_{ini,r} - \chi_{b,ign}\right)\cdot \tilde{R}_{u,r} + \chi_{ini,l}\cdot \tilde{R}_{u,l}\right)\cdot \tilde{T}_u + \chi_{b,ign}\cdot \tilde{R}_b \cdot \tilde{T}_b}{V_c}\cdot m_c \tag{4.57}$$

4.3.4.10 Evaluation of Thermodynamic Properties

Specific heat, enthalpy and gas constant property values are required for the reaction and burned zones.

$$c_{p,r} = \frac{\left(\chi_{e,r} - \chi_{b,r}\right)\cdot c_{p,reac}\left(\phi_{u,r}, T_u\right) + \left(\chi_{e,l} - \chi_{b,l}\right)\cdot c_{p,reac}\left(\phi_{u,l}, T_u\right)}{\chi_e - \chi_b} \tag{4.58}$$

$$h_r = \frac{\left(\chi_{e,r} - \chi_{b,r}\right)\cdot h_{reac}\left(\phi_{u,r}, T_u\right) + \left(\chi_{e,l} - \chi_{b,l}\right)\cdot h_{reac}\left(\phi_{u,l}, T_u\right)}{\chi_e - \chi_b} \tag{4.59}$$

$$R_r = \frac{\left(\chi_{e,r} - \chi_{b,r}\right)\cdot R_{reac}\left(\phi_{u,r}, T_u\right) + \left(\chi_{e,l} - \chi_{b,l}\right)\cdot R_{reac}\left(\phi_{u,l}, T_u\right)}{\chi_e - \chi_b} \tag{4.60}$$

$$c_{p,b} = \frac{\chi_{b,r}\cdot c_{p,prod}\left(\phi_{u,r}, T_b\right) + \chi_{b,l}\cdot c_{p,prod}\left(\phi_{u,l}, T_b\right)}{\chi_b} \tag{4.61}$$

$$h_b = \frac{\chi_{b,r} \cdot h_{prod}\left(\phi_{u,r}, T_b\right) + \chi_{b,l} \cdot h_{prod}\left(\phi_{u,l}, T_b\right)}{\chi_b} \tag{4.62}$$

$$R_b = \frac{\chi_{b,r} \cdot R_{prod}\left(\phi_{u,r}, T_b\right) + \chi_{b,l} \cdot R_{prod}\left(\phi_{u,l}, T_b\right)}{\chi_b} \tag{4.63}$$

Implicit in the burned mixture expressions is the assumption that the zone is comprised of a mixture of rich and lean products. This is selected over the case of a single well-mixed burn zone in which the equivalence varies as a function of the three mass stream burn rates and equivalences. The second case leaves open the possibility for a secondary reaction of partially oxidized over-rich products if lean products are added with excess oxidizer. Reality lies somewhere between these two cases but a high degree of complexity is not warranted in the first iteration of the model. For this reason, the simple rich/lean mixture method is chosen.

The only overall (rich, lean and diffuse regions) unburned zone property (double-u subscript) required is specific heat.

$$c_{p,uu} = \frac{\left(\chi_{ini,r} - \chi_{e,r}\right) \cdot c_{p,reac}\left(\phi_{u,r}, T_u\right) + \left(\chi_{ini,l} - \chi_{e,l}\right) \cdot c_{p,reac}\left(\phi_{u,l}, T_u\right)}{1 - \chi_e} \tag{4.64}$$

The gas constant for all unburned mass present in the unburned and reaction zones is also required.

$$R_{uur} = \frac{\left(\chi_{ini,r} - \chi_{b,r}\right) \cdot R_{reac}\left(\phi_{u,r}, T_u\right) + \left(\chi_{ini,l} - \chi_{b,l}\right) \cdot R_{reac}\left(\phi_{u,l}, T_u\right)}{1 - \chi_b} \tag{4.65}$$

4.3.4.11 Complete System of Equations

Several coefficients in the system matrix of Section 3.2.15.4 are revised, matching the changes described in the previous sections. The stratified coefficients are given here along with the original homogeneous form.

Homogeneous	Stratified
$a_{11} = (1-\chi_e)\cdot c_{p,u}$	$a_{11} = (1-\chi_e)\cdot c_{p,uu}$
$a_{21} = (\chi_e - \chi_b)\cdot c_{p,u}$	$a_{21} = (\chi_e - \chi_b)\cdot c_{p,r}$
$a_{31} = (1-\chi_b)\cdot \frac{d(R_u \cdot T_u)}{dT_u}$	$a_{31} = (1-\chi_b)\cdot \frac{d(R_{uur} \cdot T_u)}{dT_u}$
$b_{23} = h_u - h_b$	$b_{23} = h_r - h_b$
$b_{33} = R_u \cdot T_u - R_b \cdot T_b$	$b_{33} = R_r \cdot T_u - R_b \cdot T_b$

4.3.4.12 Solution method

The homogeneous termination criteria are modified for the stratified case to account for the fact that a maximum entrained mass does not serve the same purpose. In high *DOS* cases it is possible that a large portion of the chamber mass is not combustible. A maximum entrained/burned fuel mass is specified in place of the maximum entrained mass of the homogeneous case. The remaining fuel mass is evaluated at each time step for the total unburned rich and lean masses.

$$\chi_{fuel} = \frac{\chi_{uu,r} \cdot \phi_r + \chi_{uu,r} \cdot \phi_l}{\phi} \tag{4.66}$$

The solution process in Figure 3.8 requires several additional steps to account for diffusion and tracking of the diffuse region boundaries. One step for diffusion and boundary displacement is added prior to entrainment and reaction. Another step is added after solution of the complete system of equations to compute the boundary locations after mixture reaction. The modified solution method is given in Figure 4.11.

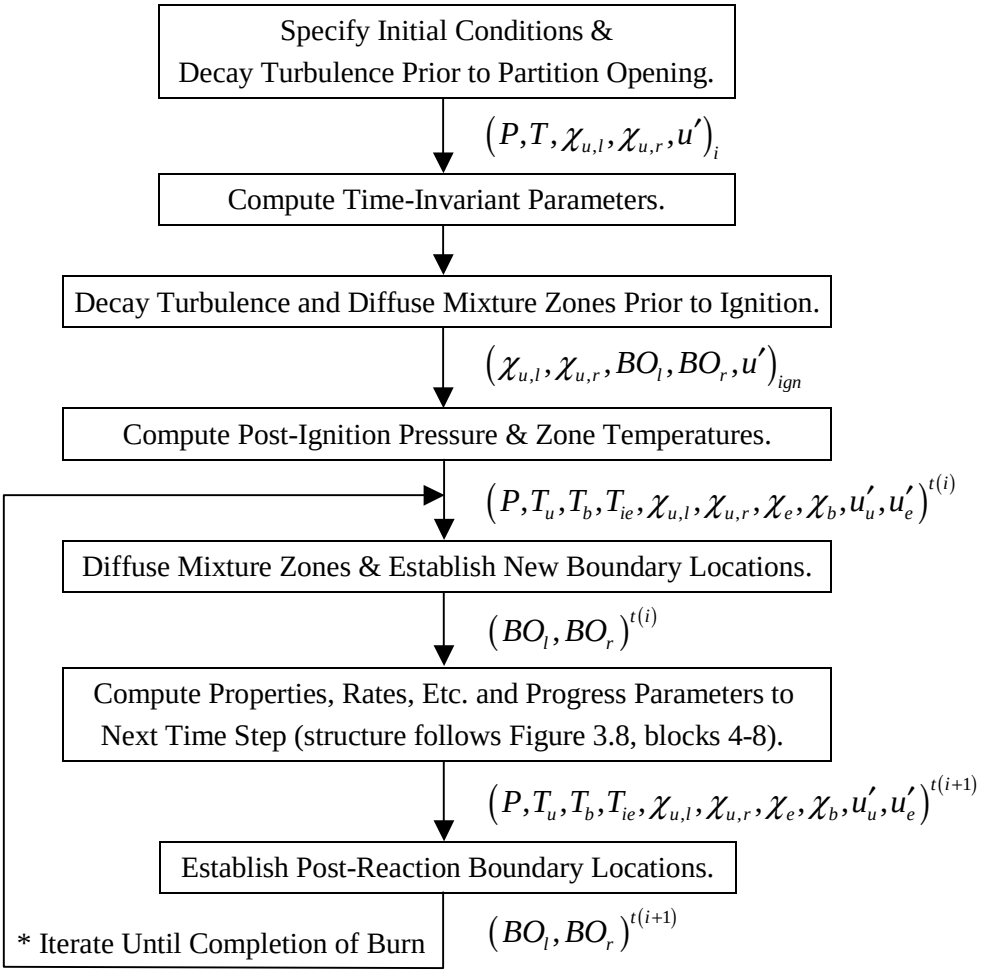

Figure 4.11: Graphical Representation of Modified (Stratified) Solution Process

CHAPTER 5

EXPERIMENTAL DATA AND ANALYSIS TOOLS

Experimental data necessary to evaluate the model are generated with the purpose-built apparatus described in Chapter 2. Details of the experimental procedure are described in this chapter along with data processing and analysis tools developed to aid interpretation of the results.

5.1 Data Collection

The goal is to compile a database of homogeneous and stratified cases that is sufficient to evaluate the simple models' ability to predict the pressure history for a range of initial conditions. A minimal matrix of test cases is first formed to meet this goal and allow completion within a reasonable time. Supplemental tests are added to address several important hardware issues and characterize possible sources of error.

5.1.1 Validation Test Matrix

A base homogeneous case is established and equivalence perturbations are made in both the rich and lean directions. The base stratified case specifies the same common parameters and a light degree of stratification. Perturbations are first made in *DOS*. Rich equivalence is then held constant while the lean value is varied. The range of stratified cases is selected to include those that are certain to burn quickly and completely and those that are less certain to do so. Those

cases in which the flame fails to reach the far wall provide a test for the model's ability to predict early flame extinction.

Case	$\phi_{Overall}$	*DOS*	ϕ_{Lean}	ϕ_{Rich}	Test Description	
H1	1.0	---	---	---	Base Case	Homo.
H3	0.9	---	---	---	Equivalence Perturbation	
H4	1.1	---	---	---		
S1	1.0	0.10	0.9	1.1	Base Case	Strat.
S3	1.0	0.20	0.8	1.2	*DOS* Perturbation	
S4	1.0	0.30	0.7	1.3		
S5	0.7	0.57	0.3	1.1	Equiv./*DOS* Perturbation	
S6	0.8	0.38	0.5	1.1		
S7	0.9	0.22	0.7	1.1		
S8	0.5	1.00	0.0	1.0		
Initial pressure for all cases is 100 kPa.						

Table 5.1: Matrix of (Homogeneous and Stratified) Experimental Test Cases

To improve the consistency of data, a single batch of mixture is prepared for each case. The partition is also actuated in the homogeneous cases to eliminate this as a source of variation. A closing series is run the same parameters as case H1. If the initial and final cases are consistent then the integrity of each intermediate case is more certain.

5.1.2 Supplemental Tests

Supplemental tests verify that the hardware functions properly and that data generated is valid over the test series length of 30 cycles.

5.1.2.1 Calibration of Dynamic Pressure Transducer

A Kistler piezo-electric pressure transducer is used to record the rapid pressure rise during combustion. The transducer element is fit to the chamber with a custom mount and as a result, the manufacturer-supplied calibration data may no longer be valid. The effect of the alternate mounting on the transducer sensitivity must be determined.

One simple means to verify the transducer scale factor is to simultaneously read the dynamic transducer and the calibrated static transducers. The pressure rate of change for such a test must be sufficiently fast to be within the dynamic transducer's operational bandwidth but not so fast to stray outside that of the static transducer. The Kistler signal-conditioning unit time constant is set to the maximum value to slow its response for this test. A temporary supply system is added to provide air at higher flow rates than the normal supply and valving system. Temporary software provides control for the fast-fill hardware and allows for both rapid filling and emptying of the chamber while recording output from the multiple transducers. The test sequence consists of a series of five 140 kPa step inputs starting at 100 kPa and ending at 800 kPa. A smaller step size is used to maintain a higher flow rate and remain within the bandwidth of the dynamic transducer. Pressure data for both transducers are shown in the upper plot of Figure 5.1 (data taken after adjustment of the manufacturer supplied scale factor).

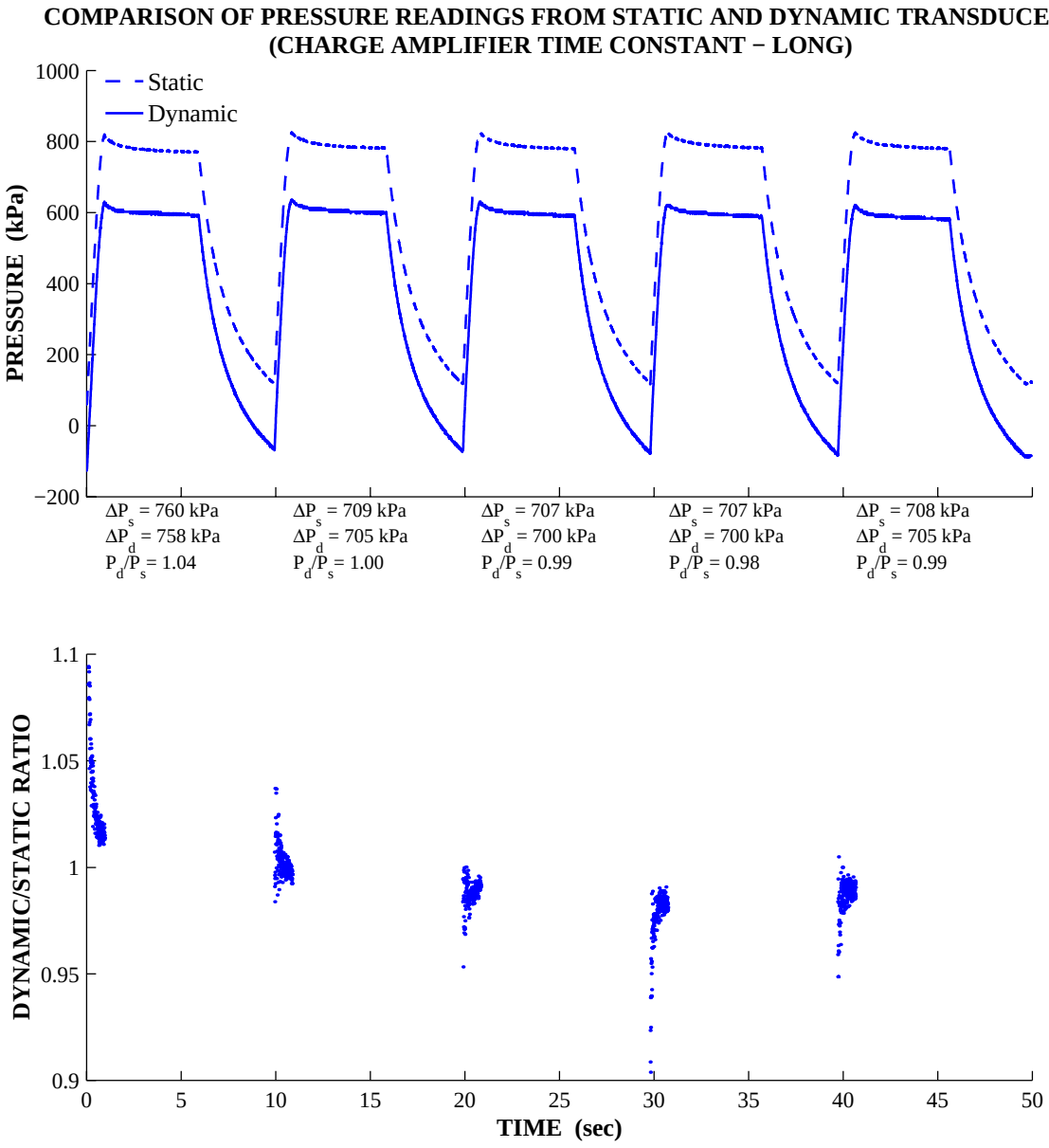

Figure 5.1: Simultaneous Pressure Readings from Static and Dynamic Transducers

Each period of rapid pressure increase is extracted from the dynamic data and referenced to the appropriate starting pressure. The ratio of indicated pressures in each valid region is then computed for each recorded value. A ratio of near unity indicates that the sensitivity of the transducer is properly adjusted for the modified mounting.

5.1.2.2 Verification of Chamber Seal Integrity

Chamber sealing is verified periodically by measuring the change in static pressure over a period of 60 to 300 seconds. There is some concern that the static test may not be capable of detecting small leaks resulting from the rapid rise in pressure during combustion. For this reason a new test is conducted using a alternate procedure, specifically designed to allow a chamber leak of static or dynamic nature to be detected. The chamber is dismounted from its normal fixture and submerged in a water tank, leaving only the ignition electrode connections above the waterline. A positive outcome in this test and the dynamic transducer test allows a high degree of confidence in pressure data recorded during combustion.

5.1.2.3 Quantification of Several Issues Affecting Extended Series Test Results

There are two issues of concern when running 30 cycle long test series. First is the unavoidable increase in temperature. Thermal control is limited to rapid exhausting/purging of the chamber contents, fan-forced cooling with ambient temperature air and an inter-cycle delay. Also of concern is the accumulation of liquid water on chamber surfaces. Some fraction of the water vapor in the combustion products may change phase and condense. A series of 30 cycles is completed and several statistics are extracted for analysis [Figure 5.2]. No significant water deposits were observed during this test and the temperature rise is negligible at less than one degree Celsius. Peak pressure and pressure rise (peak less initial) show no correlation with temperature or cycle number. Cycle-to-cycle variations in peak pressure and pressure rise loosely follow those of the initial charge pressure, as expected. This result shows that existing provisions are adequate.

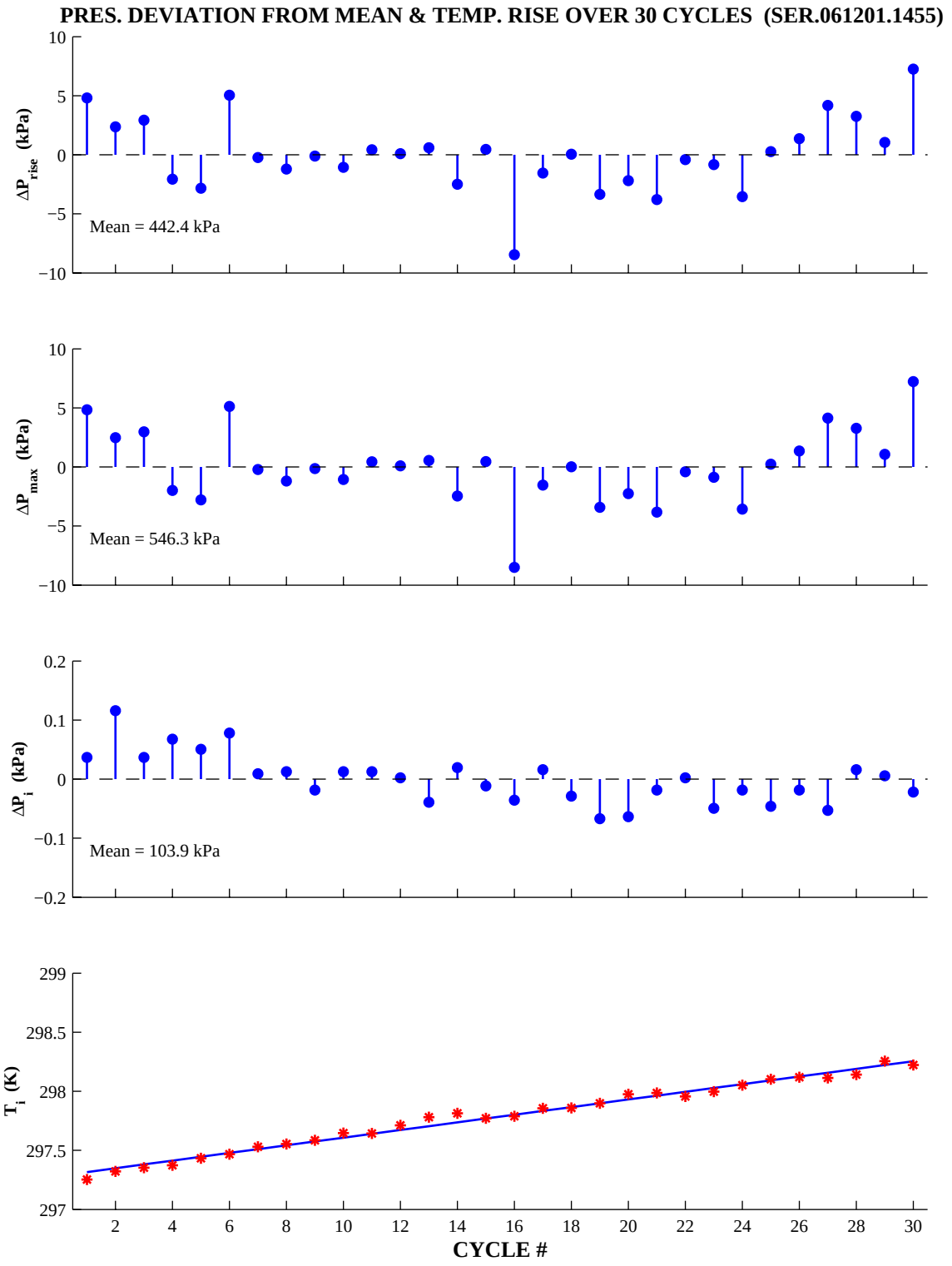

Figure 5.2: Statistics for Extended Test Series of 30 Cycles

5.2 Analysis Tools

The raw data contain a wealth of useful information but post-processing is required before any analysis is possible. Several software tools are developed to allow rapid extraction of the desired information and render the results into easily interpreted graphical forms.

5.2.1 General Points

Post-processing routines are written for *Matlab® v6.0* to be compatible with the simulation program. This commercial package is a wise choice as it contains an extensive library of built-in functions to effectively shorten development time.

The data are reduced as series where the desired outputs are series-averaged pressure and flame radius histories and a measure of the radius error. In batch reductions, details about the individual cycles are also retained for later use since there are cases where output from a single cycle may be desired. One example is a single cycle with imaging in which case the desired output is an appropriate combination of the cycle pressure and flame front histories and a range of processed images.

5.2.2 Real-Time Data Inspection

During the delay period between cycles, pressure and image data are inspected to ensure there are no acquisition errors. Pressure data are displayed in a simple plot [Figure 5.3]. The upper plot contains all runs and the lower plot is percent deviation of each individual run from the series mean. Data sets are accepted if the pressure trace shapes are consistent and peak pressure deviation is not excessive. The series mean value is computed and the series is passed as long as no more than three cycles deviate by more than five percent from the mean. This quick and simple check ensures that any problem during a test is identified before a significant amount of corrupt data is collected.

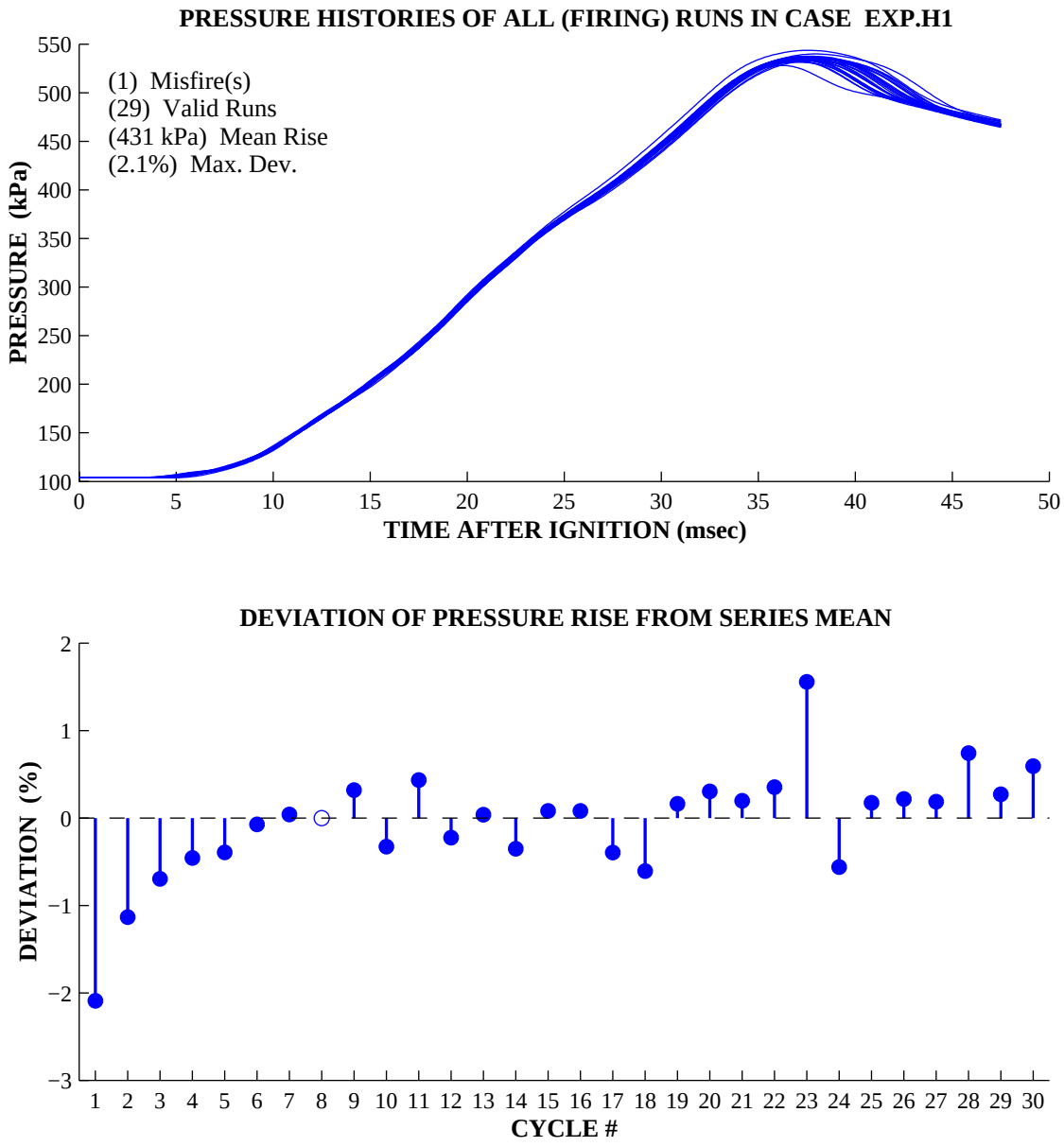

Figure 5.3: Series Statistics for Experimental Case H1

The result for Case H1 is representative of all test cases. Data validation figures for the remaining cases are included in Appendix B.

5.2.3 Pressure Signal Processing

There is a normal amount of background noise in the CVCC environment. This translates, in some cases, into an objectionable level of noise, especially at the start of combustion when the pressure rise is nominally zero and the signal-to-noise ratio is low. The data are subjected to a multi-step noise cleaning process. Any anomalies from acquisition initialization or ignition feedback are first eliminated, locally in the first several milliseconds. The ignition delay period is identified and the data flattened. A zero-phase Butterworth low-pass filter is then applied to the entire pressure history. The dynamic pressure data is then shifted to the actual starting pressure, recorded by the static transducer. Finally, the center of the pressure peak and peak time are identified by taking a mean of all values above 95 percent of the filtered peak. Figure 5.4 shows two critical time ranges for a typical data set. This result illustrates that the majority of signal noise is effectively removed while maintaining the original signal shape and phase.

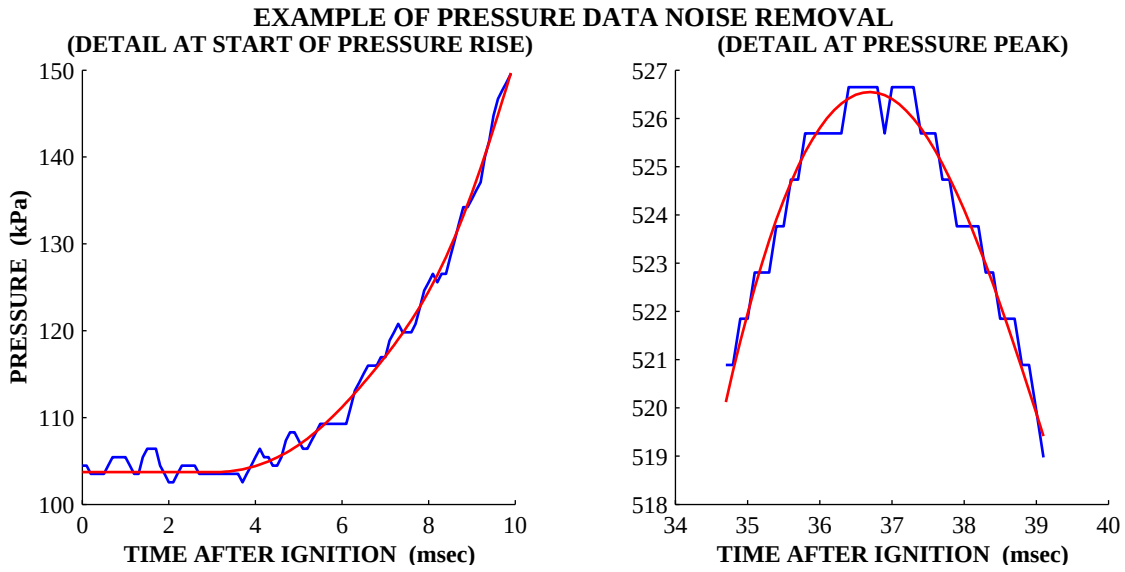

Figure 5.4: Pressure Signal Before and After Noise Removal

5.2.4 Image Processing

The flame front radius at each time step must be extracted for comparison with model output. Any lag of the visible flame front behind the non-visible flame front is neglected. The area covered by the camera extends beyond the limits of the chamber and the first step in processing is to trim the excess. A graphical interface, constructed for the purpose of identifying the valid pixel range (chamber walls) is employed with several images. The mean value of each chamber wall location is retained and used to crop the valid chamber region from each raw image. The region is reduced further to include only 75 percent of the chamber width and eliminate the regions in which the flame front shape is affected strongly by interaction with the wall. Next, small-scale irregularities are reduced in the cropped image with a spatial filter. The first image in each cycle with a discernable kernel size is then identified. A luminosity threshold is imposed locally, in the vicinity of the ignition electrodes, and globally. The local and global threshold areas are used to determine whether the kernel is centered horizontally in the chamber and its size has reached the specified minimum area (corresponding to a flame radius of 6.0 mm). If the kernel is displaced significantly (more than 5.0 mm) from the chamber centerline, the cycle is marked as invalid and processing of the next cycle begins. For each subsequent image in a valid cycle, points along the leading edge of the visible flame front are identified, based on pixel luminosity. A flame radius value is computed for each point and any value varying more than one standard deviation from the mean is discarded. The reduced set is fit, in a least squares sense, with a constant radius curve (centered at the mid-point of the ignition electrode gap) to obtain the mean experimental flame radius. A typical raw image is shown in Figure 5.5 with the processed result shown alongside in Figure 5.6.

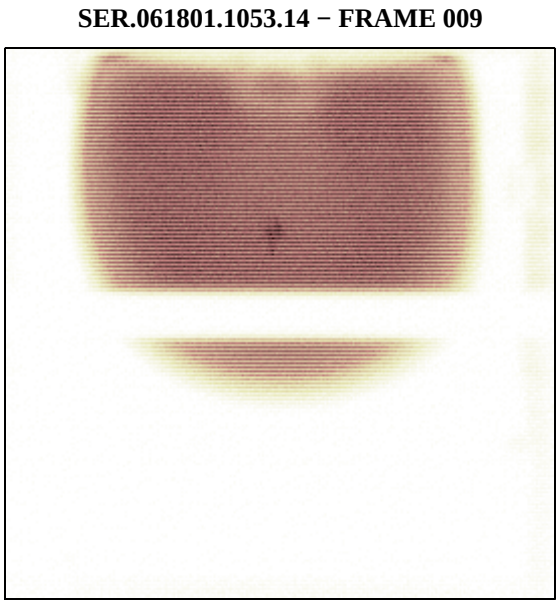

Figure 5.5: Typical Raw Image

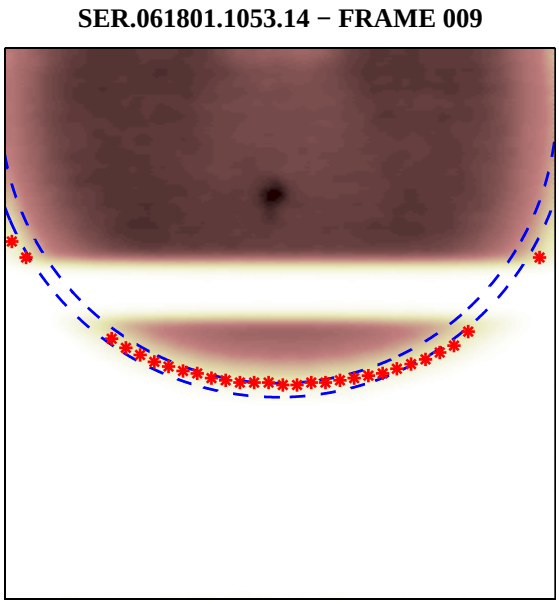

Figure 5.6: Processed Image

Individual points identified on the leading edge of the flame front are shown on the image in addition to a band representing the mean deviation of individual points about the mean experimental flame radius. For improved paper output, the image colormaps are inverted and the histograms modified.

Processing for a cycle is continued until the flame reaches a distance equal to 92 percent of the chamber length. This avoids problems with false edge detection due to reflections on the far wall. The resulting flame front evolution for one cycle is shown in Figure 5.7.

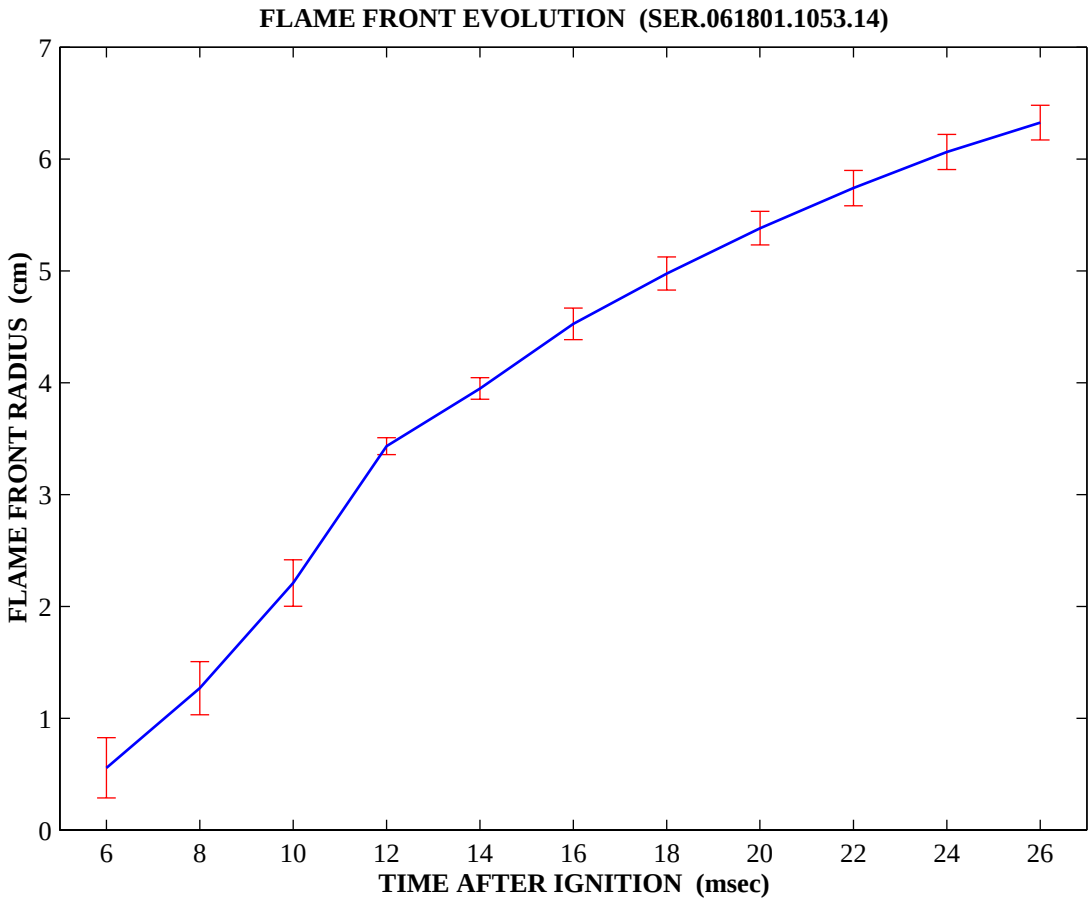

Figure 5.7: Flame Front History Derived from Combustion Images

5.2.5 Series Data Reduction

Descriptions of processing in the previous sections applied to individual cycles. All valid cycles for the entire test matrix (those not identified as misfires or containing invalid image data) are reduced to three matrices (pressure, flame radius and radius error values) and passed for on for series reduction. The mean of each is taken, excluding any cycle with a pressure rise deviating more than five percent from the series mean. This reduces each series to a four column matrix of time, pressure, flame radius and radius error.

Additional routines are created to present the results in simple, intuitive forms. These combine image and pressure data in various graphical forms to aid interpretation.

5.3 Reduced Experimental Data

The first reduced data considered are the opening and closing data consistency test series [Figure 5.8]. These two series of 30 cycles each show no discernible difference in their pressure histories and provide evidence of hardware consistency during the test matrix execution.

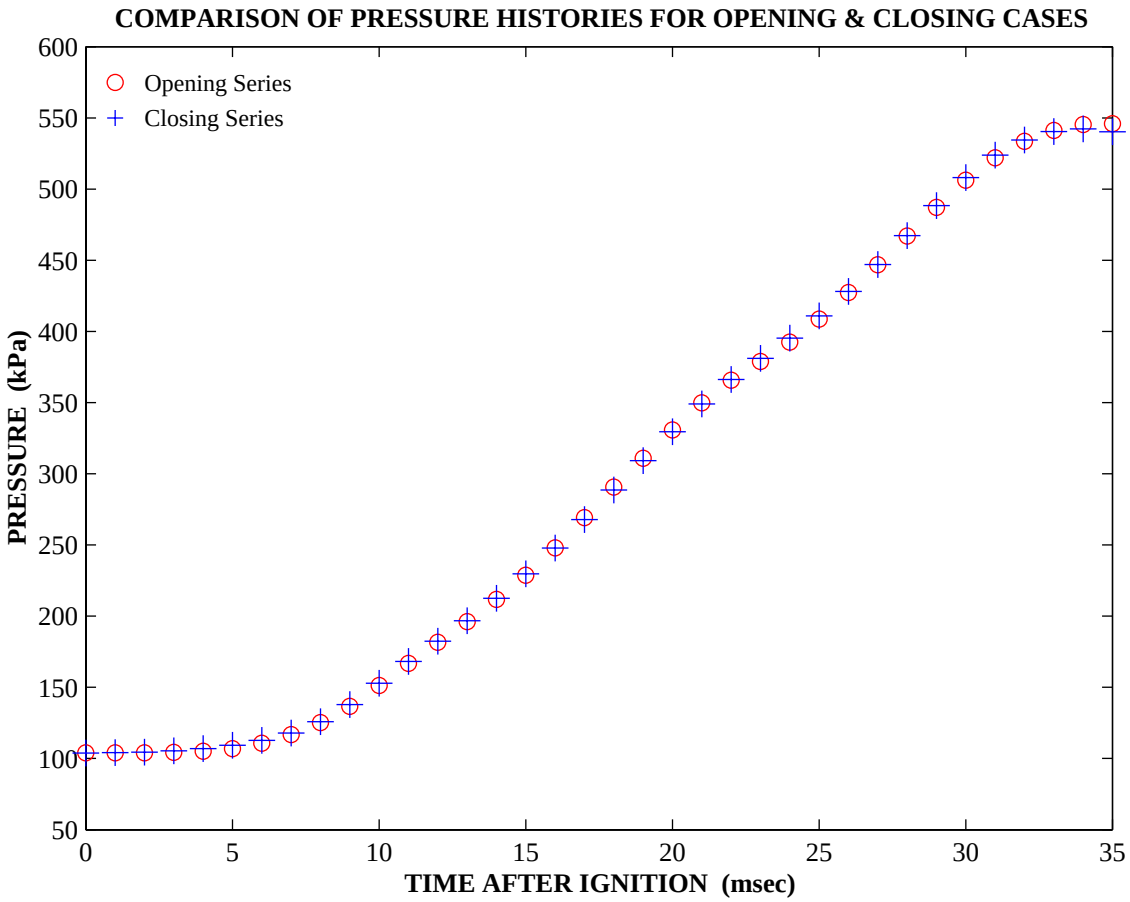

Figure 5.8: Matrix Consistency Check Using Initial-Final Series

Statistics for the complete matrix are compiled in Table 5.2. Information includes the series mean value for pressure rise, maximum deviation in pressure rise and the number of cycles deviating by less than five percent from the series mean (deviation for all cycles is well below the five percent threshold).

Case	Series Mean P_{rise} (kPa)	Max. Deviation (%)	Cycles < 5.0% Deviation
H1	431	2.1	29 (1 misfire)
H3	405	1.5	30
H4	441	1.7	30
S1	421	1.6	29 (1 misfire)
S3	395	1.4	30
S4	365	1.3	30
S5	251	1.4	30
S6	262	1.5	30
S7	358	0.9	30
S8	236	1.3	30

Table 5.2: Series Statistics for Experimental Data

Pressure and flame radius data for each case are presented in the following series of figures [Figure 5.9 through Figure 5.18] as time histories and a series of images, covering the flame evolution. Pressure is displayed from the time of kernel detection until the pressure crests. It should be noted that these images are actually temporal integrations of natural light emission over the camera exposure time of approximately two milliseconds.

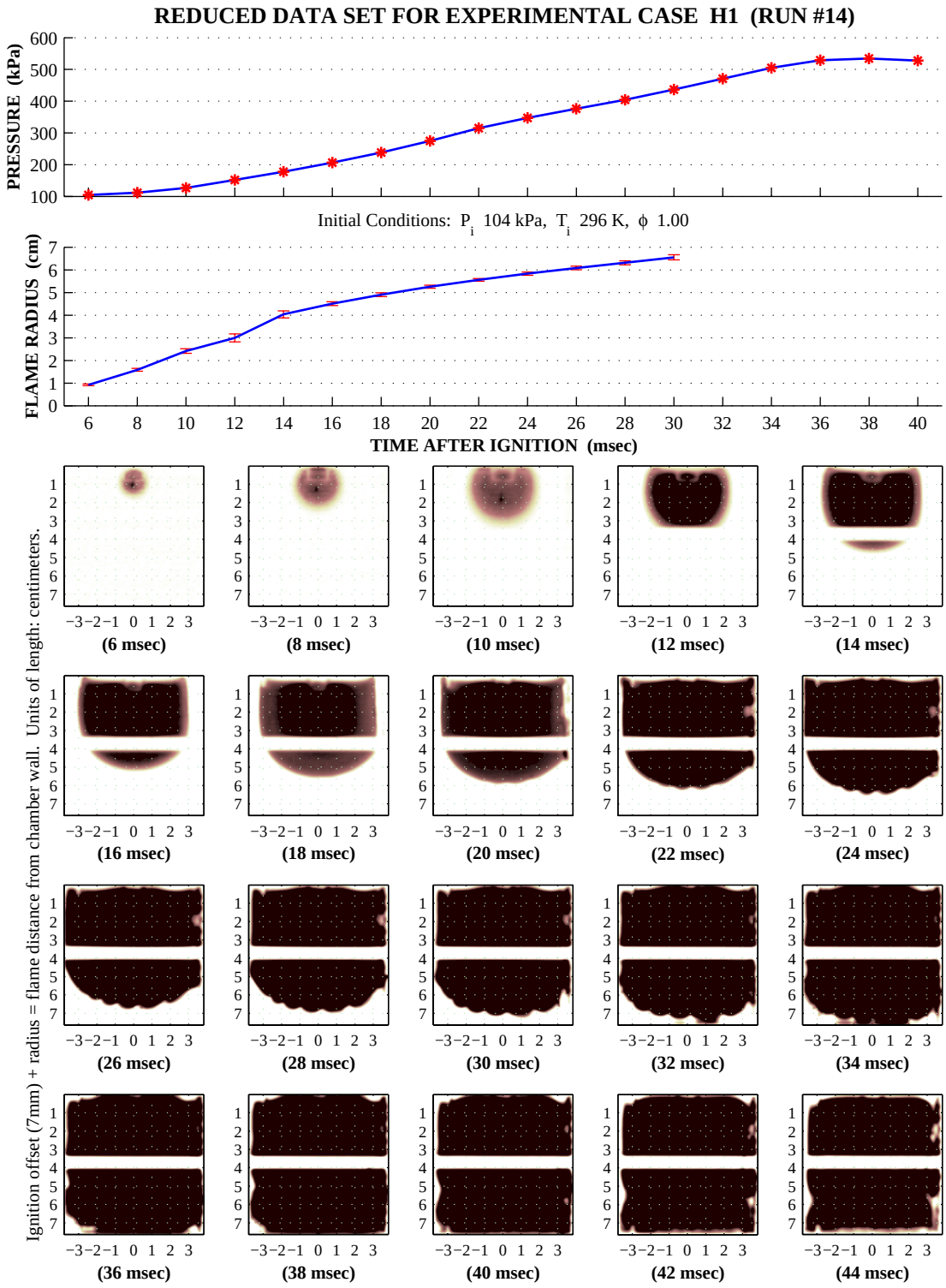

Figure 5.9: Reduced Data for Experimental Case H1

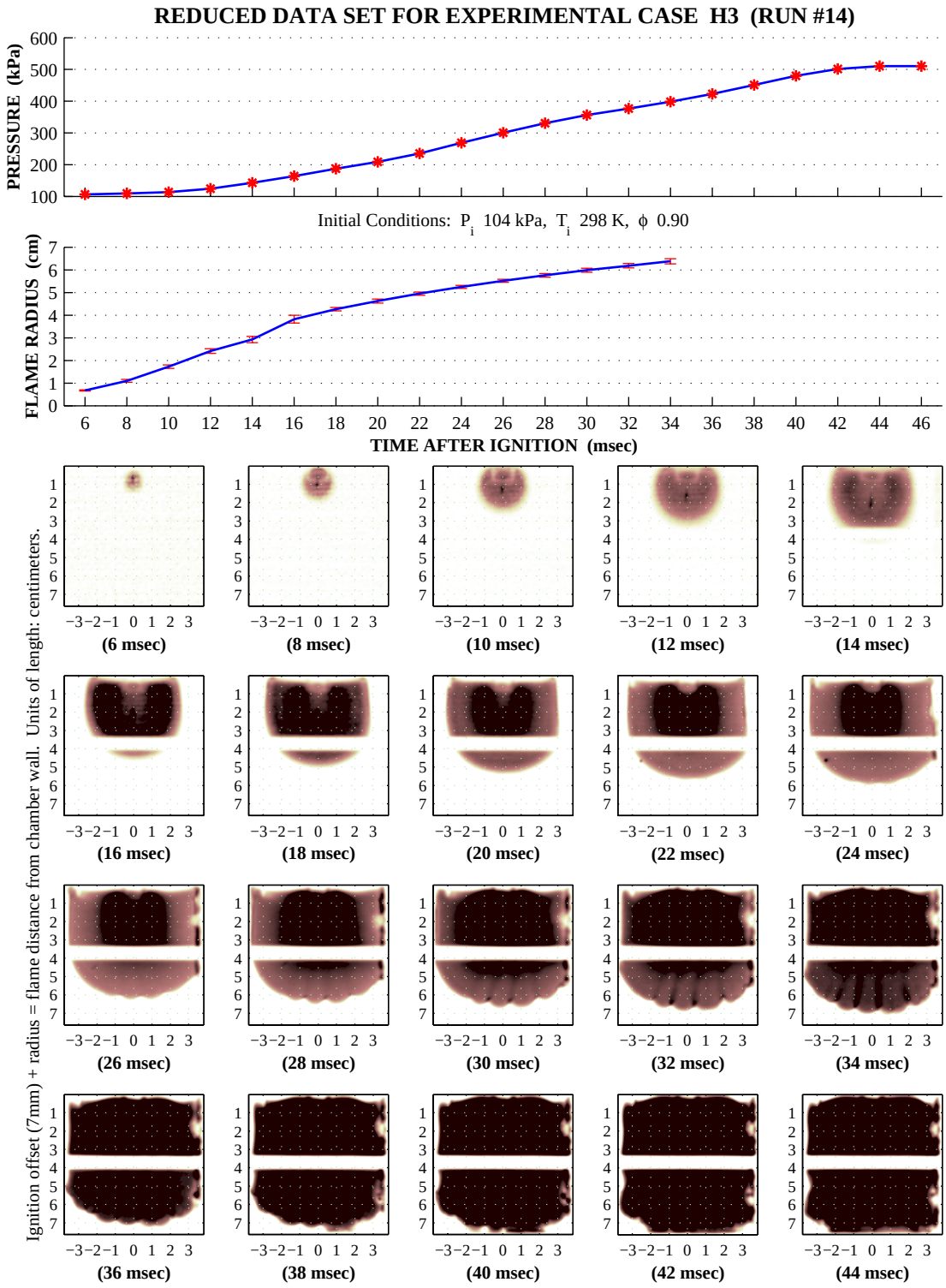

Figure 5.10: Reduced Data for Experimental Case H3

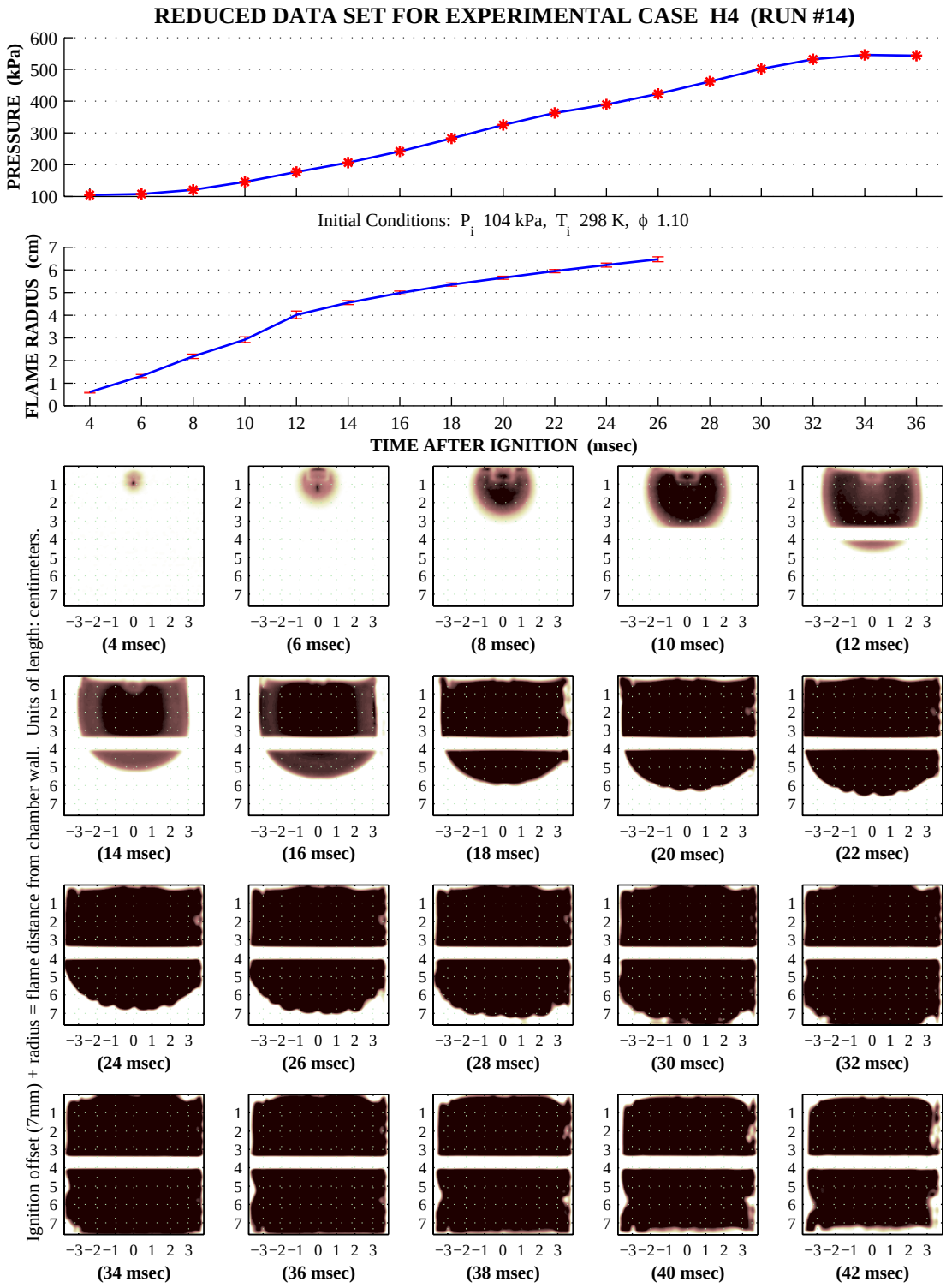

Figure 5.11: Reduced Data for Experimental Case H4

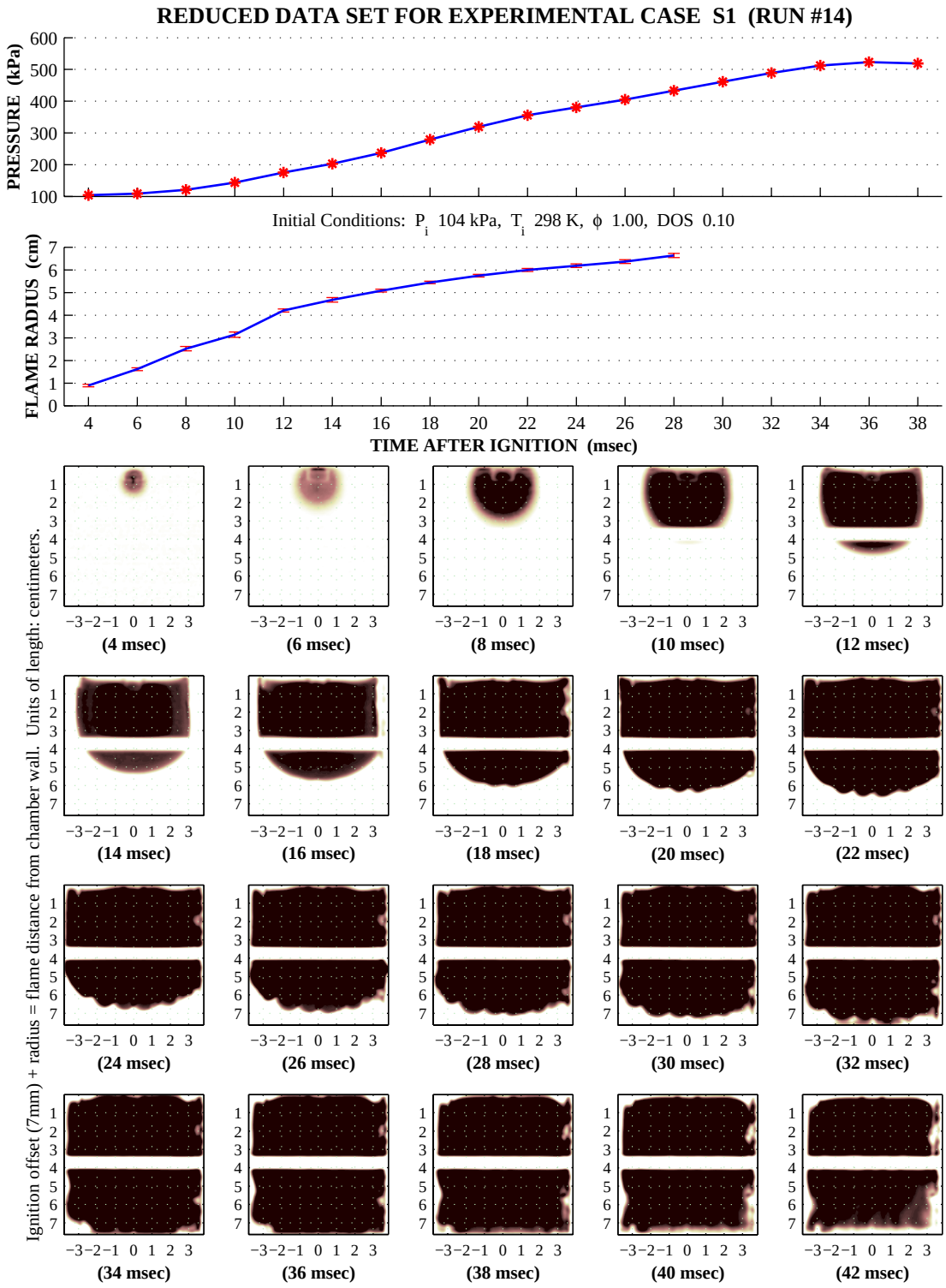

Figure 5.12: Reduced Data for Experimental Case S1

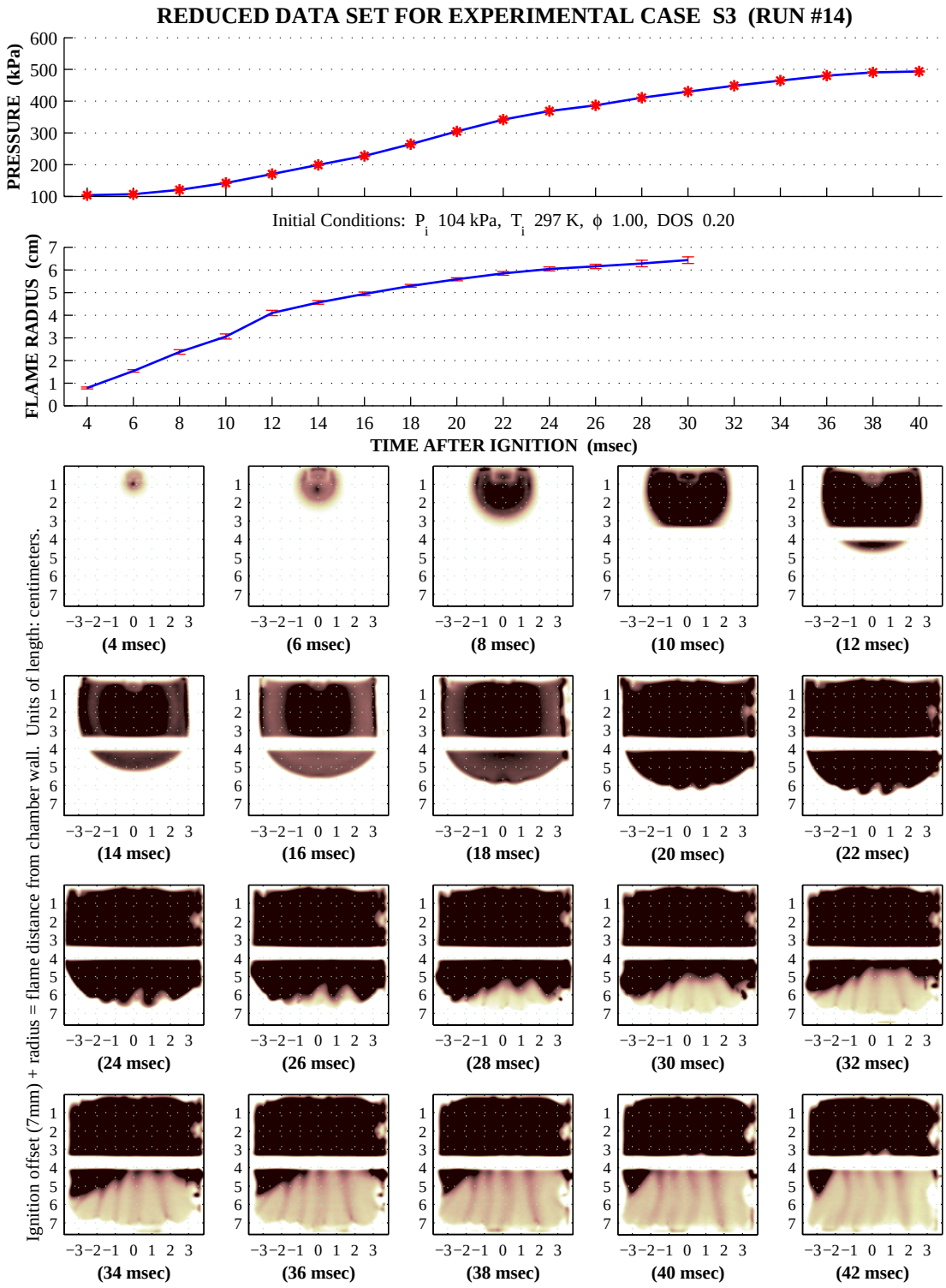

Figure 5.13: Reduced Data for Experimental Case S3

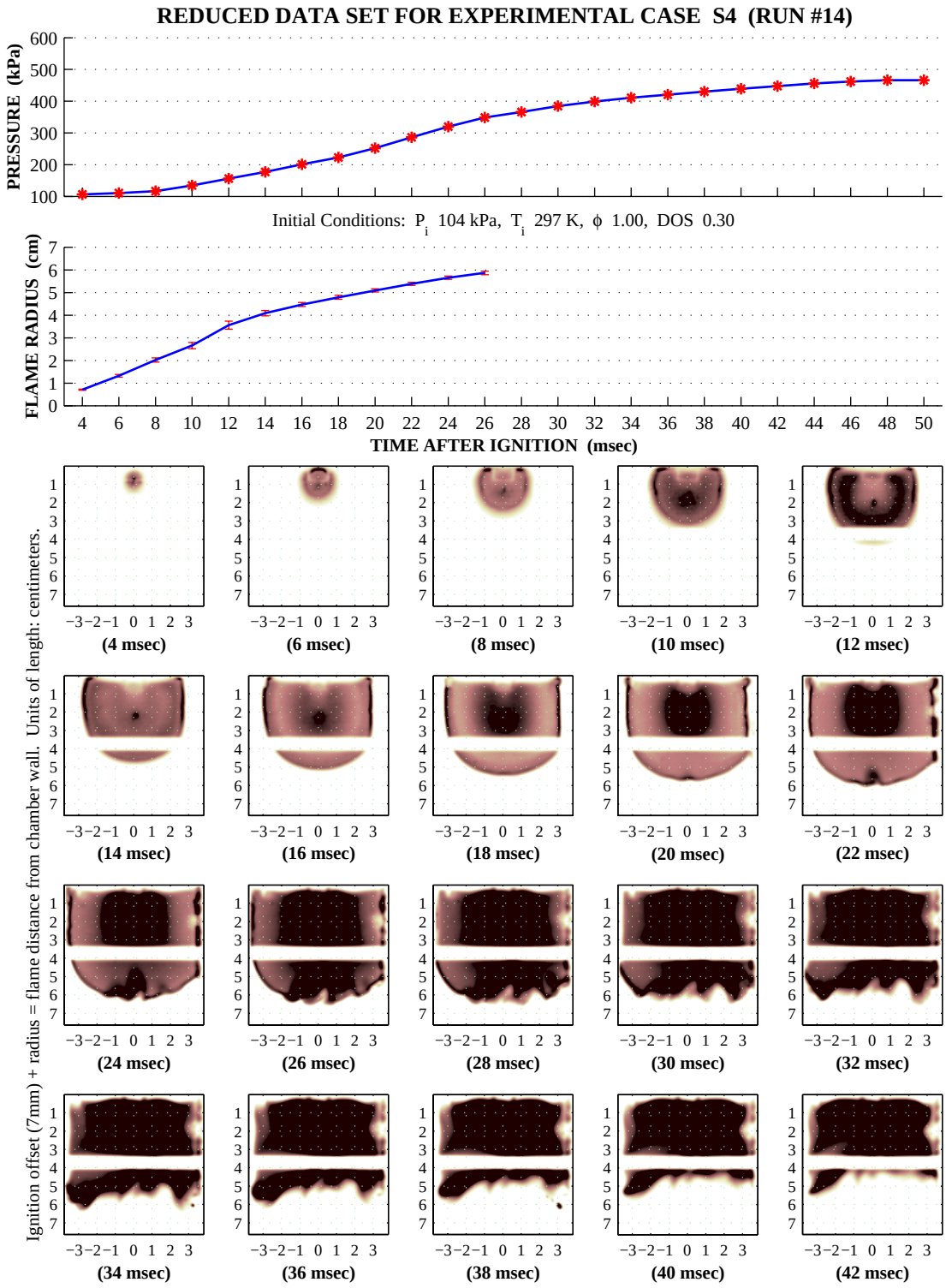

Figure 5.14: Reduced Data for Experimental Case S4

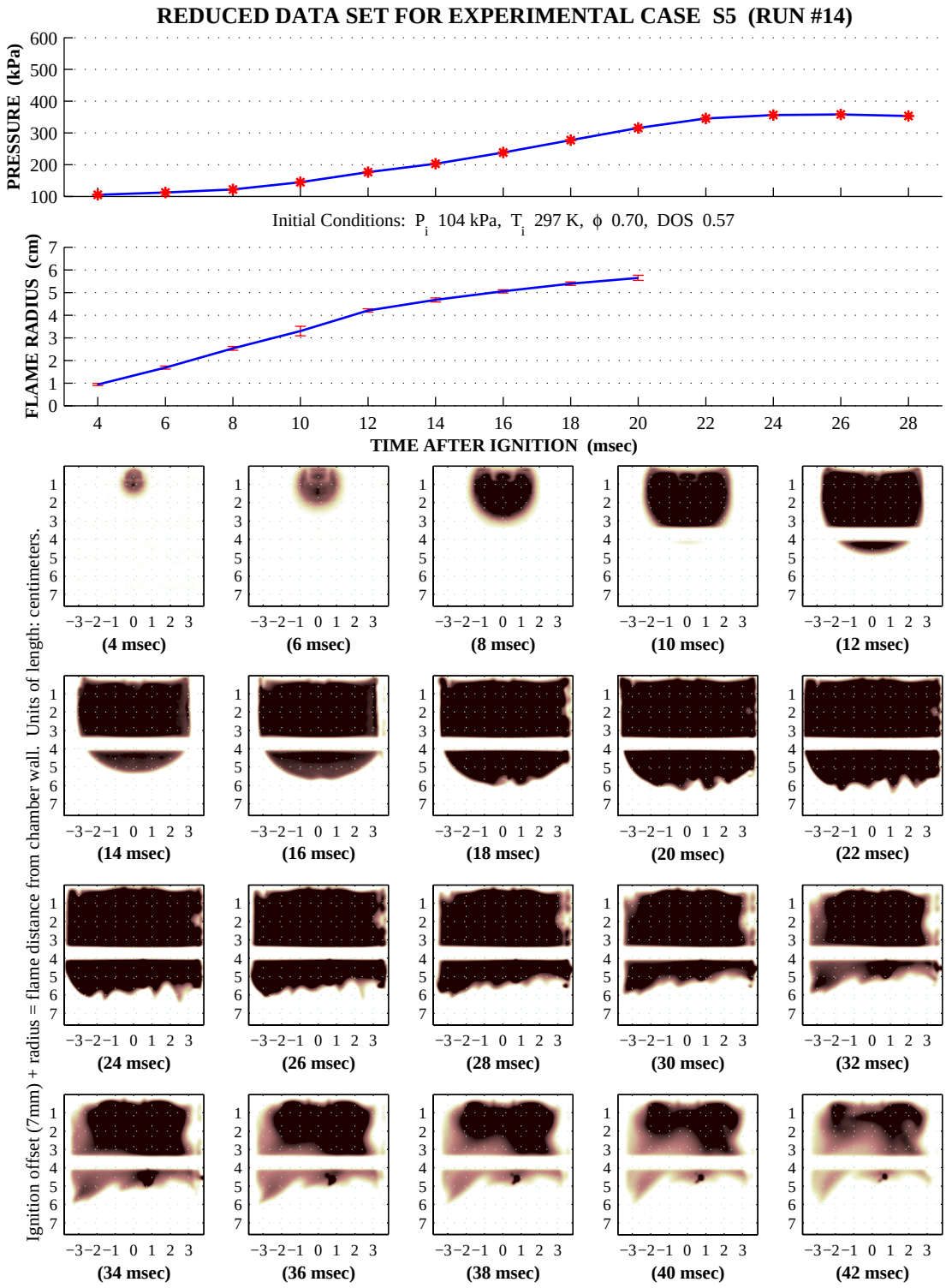

Figure 5.15: Reduced Data for Experimental Case S5

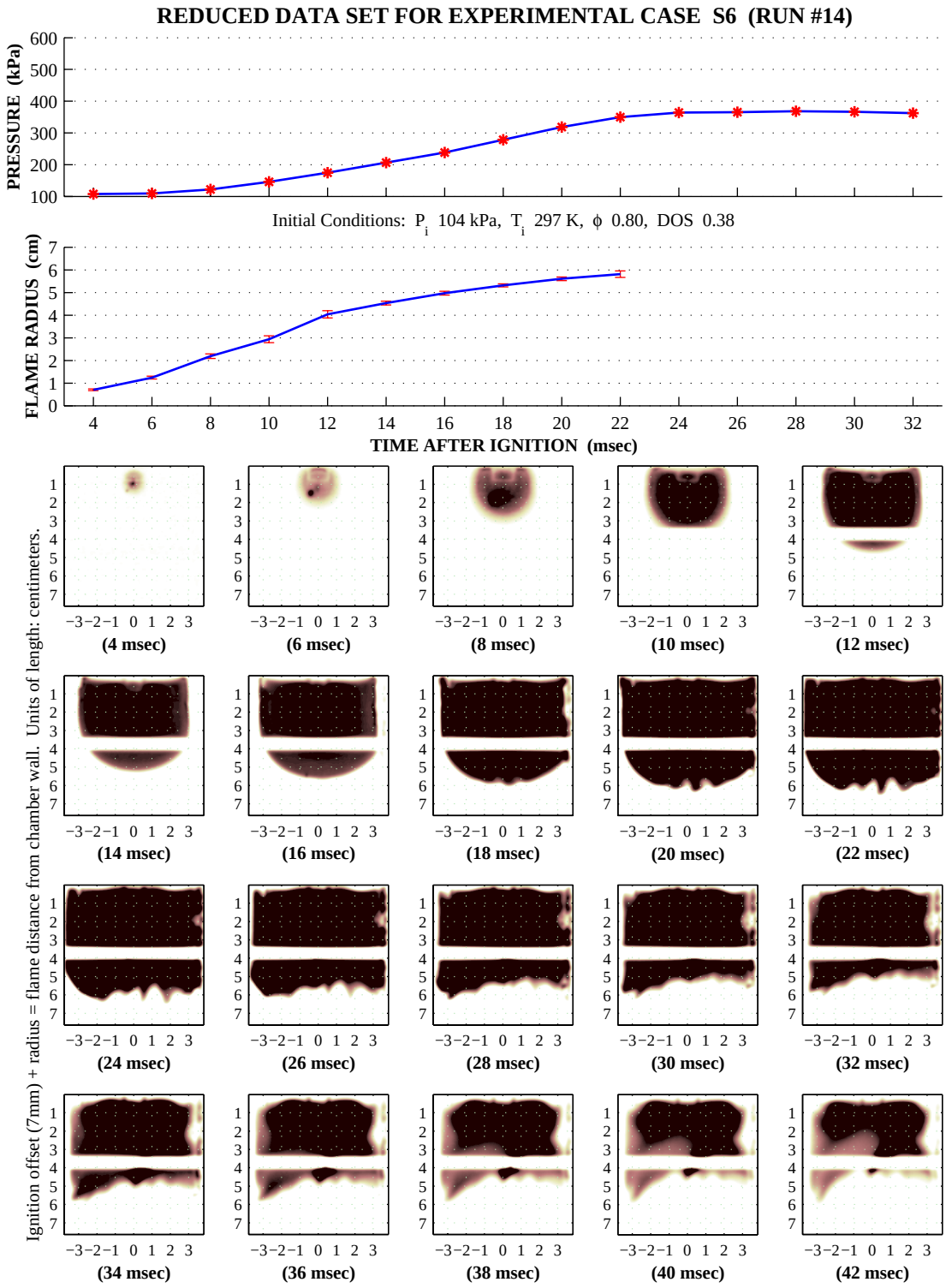

Figure 5.16: Reduced Data for Experimental Case S6

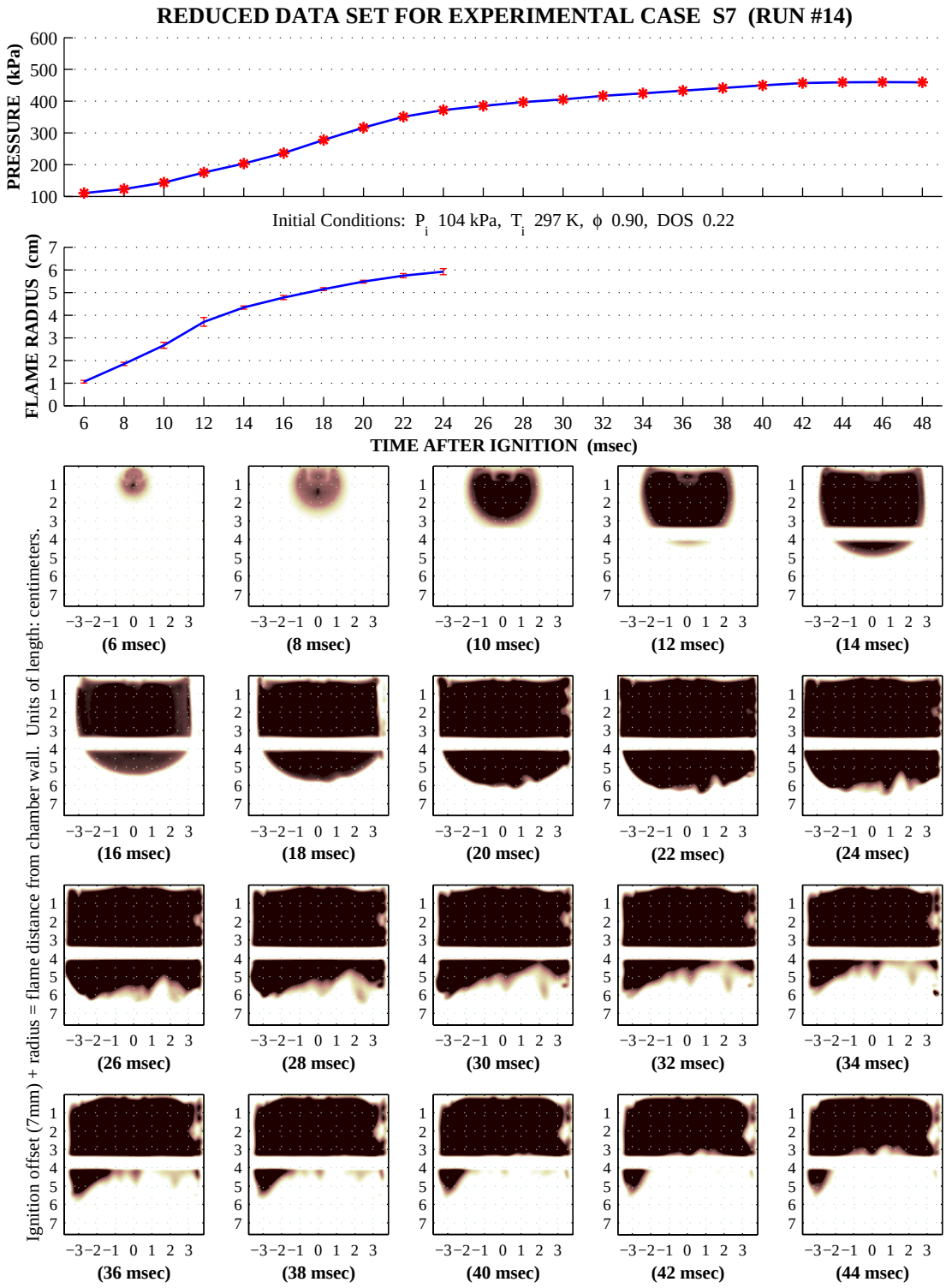

Figure 5.17: Reduced Data for Experimental Case S7

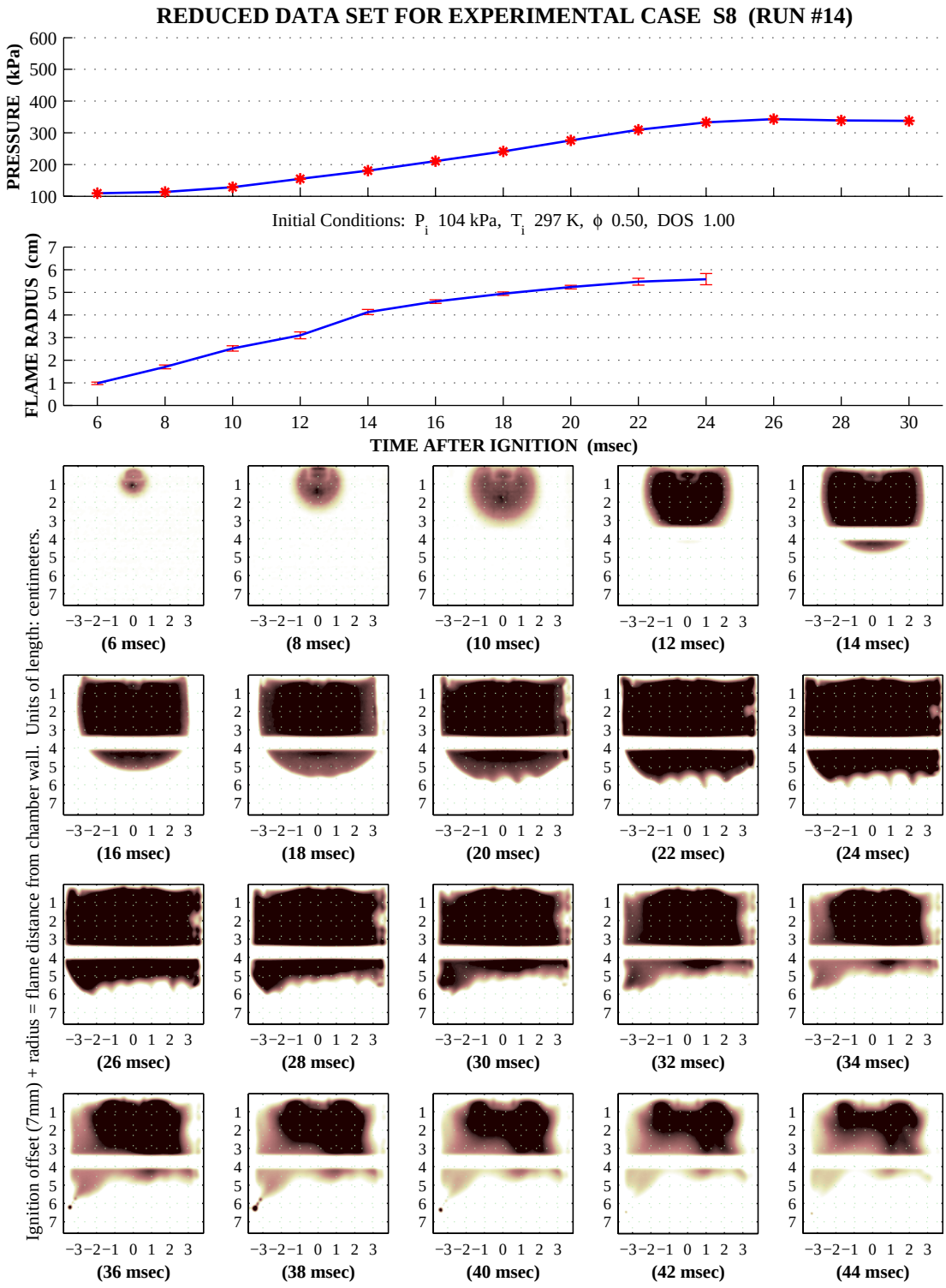

Figure 5.18: Reduced Data for Experimental Case S8

There is little to note in the homogeneous cases other than the processing routines reduce pressure and image data as desired. The range of stratified cases is far more interesting and shows several of the model assumptions are reasonable. Mildly stratified cases S1 and S3 show the flame front does not flatten appreciably when transitioning from the rich to the diffuse/lean mixture. Case S8 with a fuel deplete lean region validates the assumptions about late contact and boundary shape. Contact occurs late so neglecting the out-of-plane flame curvature is valid. The flame runs into a virtual wall and the contact is a relatively straight line so the assumption of flat boundaries during compression of the lean zone is also reasonable.

In cases S1 and S3, the flame travels the full chamber distance (S3 paper output makes this slightly unclear). The same is not true for cases S4, S5, S6, S7 and S8 where the flame apparently stalls in the diffuse/lean mixture. Pressure and radius data are consistent for cases S5, S6 and S8 in which maxima for both pressure and radius occur at approximately the same time. The distance traveled in these cases increases with lean side equivalence since combustibility in the diffuse region is a function of overall equivalence and the rich side equivalence is constant. Cases S4 and S7 (equal lean equivalence, 0.7) are unique and exhibit an inconsistency in pressure and flame radius histories. The pressure peak occurs significantly after the flame appears to stall. This indicates that the active flame front advances in the lean region and may not be visible to the camera.

Simultaneous comparison of several cases can help to make subtle differences more obvious. This is significantly more convenient than reading values from multiple figures spread over several pages. Cases here are compared in three logical grouping: a comparison of homogeneous cases at three different equivalences [Figure 5.19], a comparison of three stratified cases at fixed overall equivalence and varying DOS [Figure 5.20] and a comparison of four stratified cases with fixed rich side equivalence and varying overall equivalence and DOS [Figure 5.21].

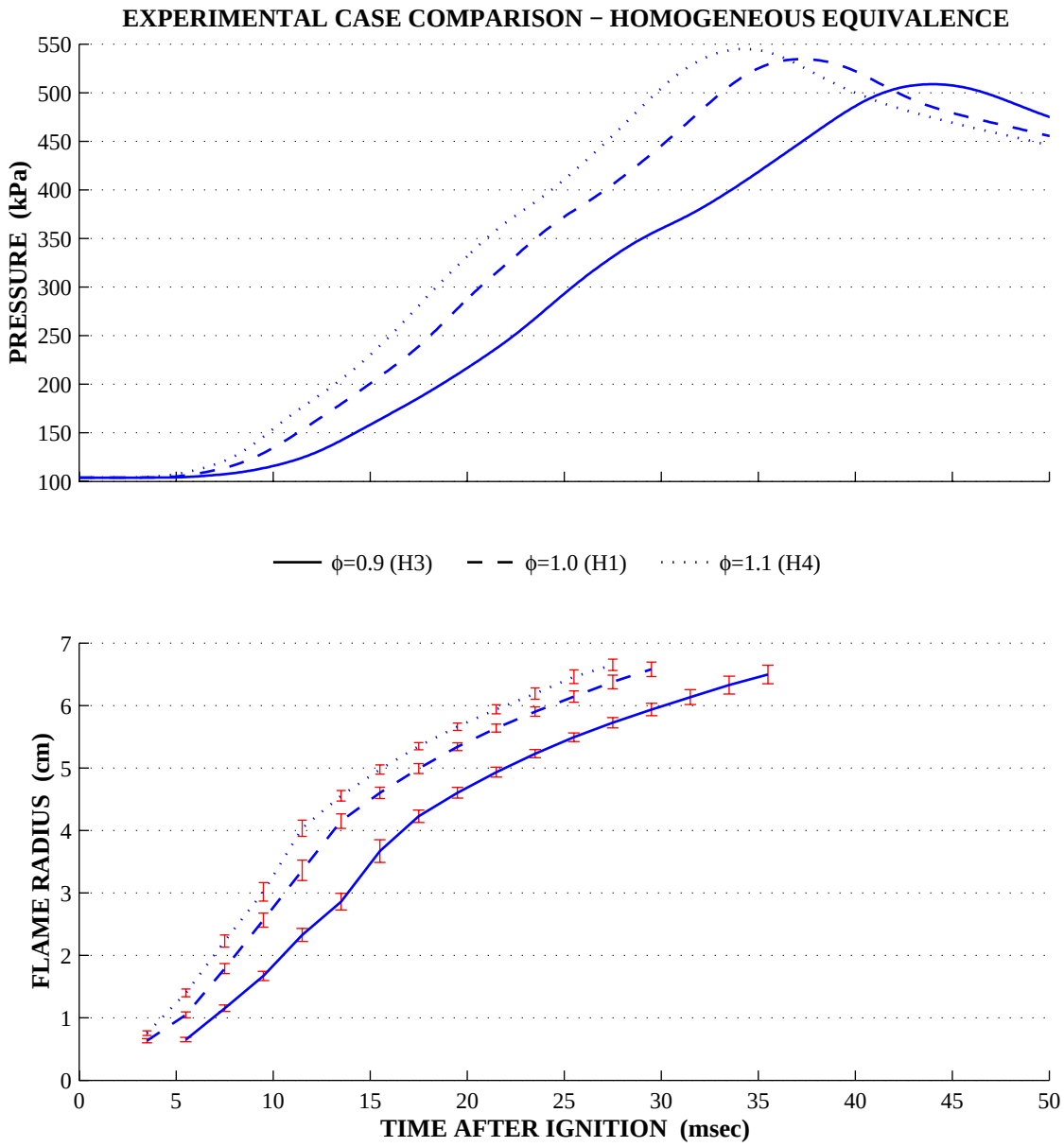

Figure 5.19: Comparison of Three Homogeneous Cases with Varying Equivalence

This shows the significant increase in burn duration from the minimum at equivalence 1.1 (near optimum for a fast burn) to the slightly lean case of 0.9. As mixtures lean, the retardation will be ever more pronounced until the mixture is unable to burn.

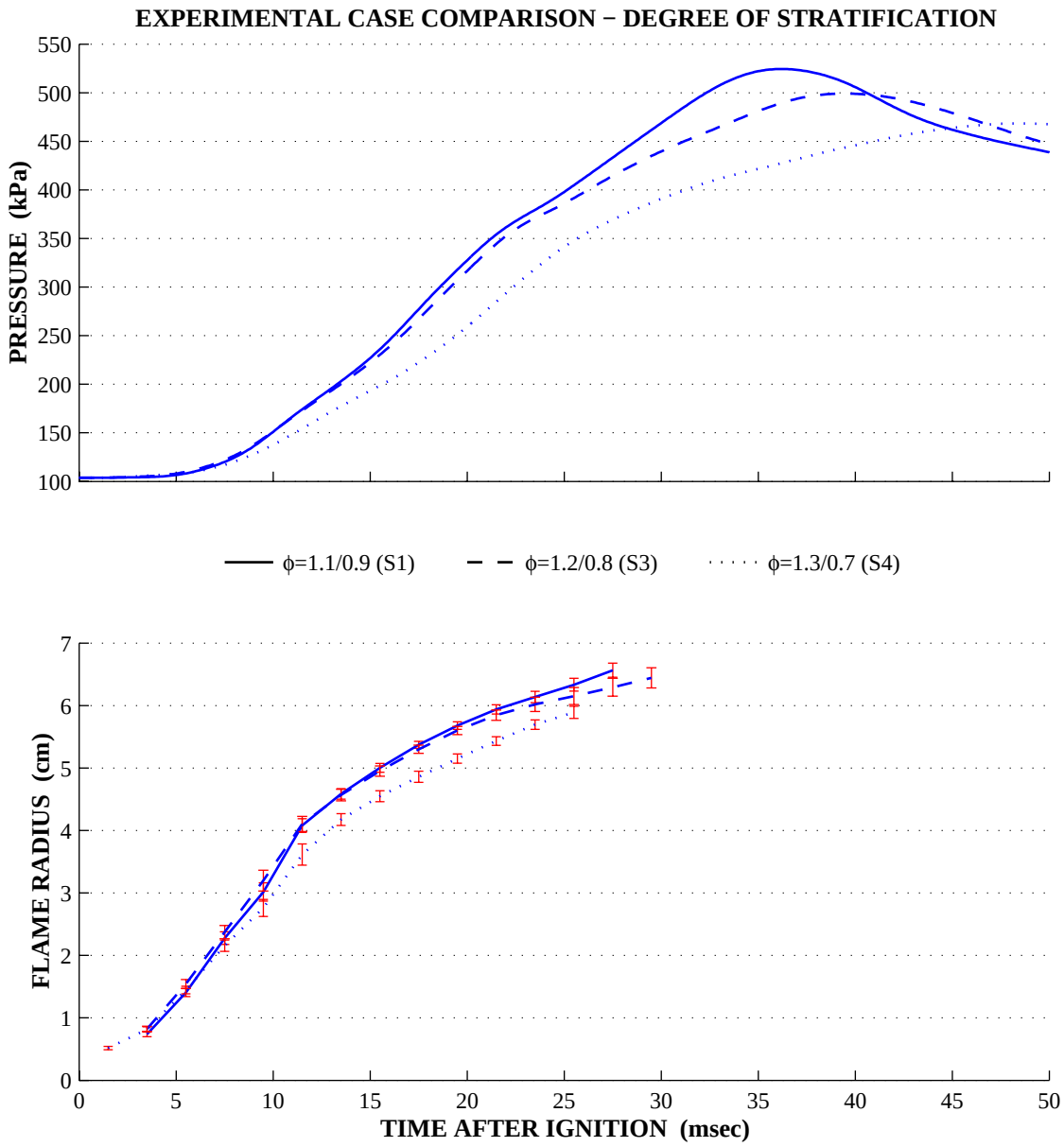

Figure 5.20: Comparison of Three Stratified Cases with Varying DOS

One question is whether the chamber burns completely in case S4. This comparison includes case S4 and two others with the same overall equivalence. Progress in case S4 is slow throughout the entire burn. The rich and lean mixtures are on opposite sides of the optimal range,

resulting in a much slower burn than a slightly lean homogeneous mixture (H3). However, the pressure history does indicate a complete burn for case S4 unlike the images.

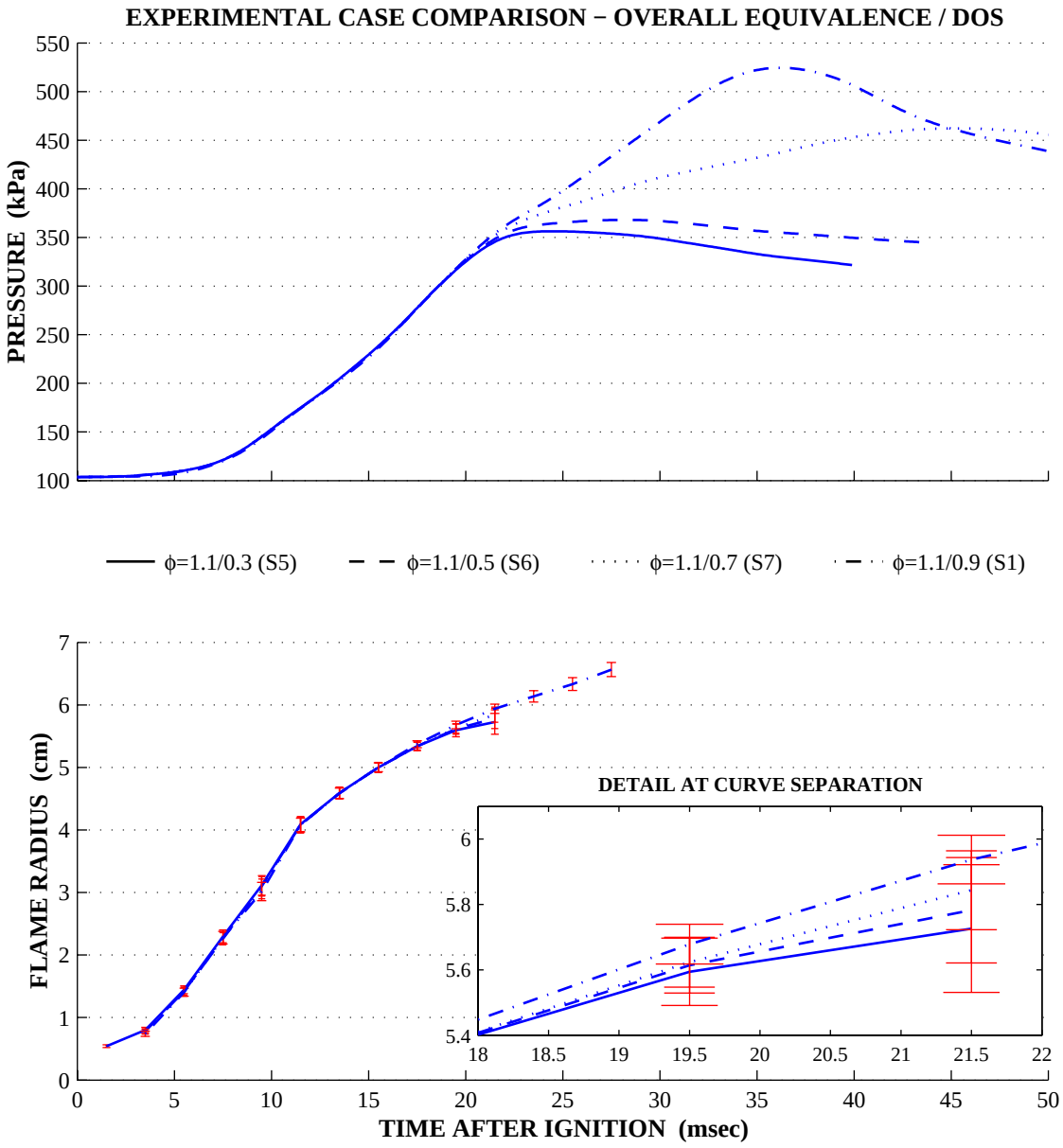

Figure 5.21: Comparison of Four Stratified Cases with Varying Equivalence/DOS

The correlation between increasing lean side equivalence and distance traveled before flame extinction is verified by the small increase from case S5 to case S6. All pressure and radius curves have a distinct knee that separates the early rich burn period from the late diffuse/lean burn period. The late period history for case S7 shows a slow burn but as with case S4, indicates a complete burn and contradicts the images. After additional consideration, it seems more certain that the camera is unable to "see" the active burning region in a very lean mixture. This may be true for all cases. The apparent leading edge may in fact be a secondary, lagging, zone in which visible emission is strong. In lean mixtures, emission from this zone may be greatly reduced and explain the observed inconsistency between pressure and image data (apparent flame stall). This issue need not be resolved here since the distance between the actual and apparent leading edges must be quite small. Cases S4 and S7 require careful consideration in light of the possible image data inconsistency when comparing the experimental data with output from the model.

CHAPTER 6

HOMOGENEOUS-CHARGE RESULTS

The homogeneous model is evaluated against the experimental data in this chapter. A baseline case is run to verify proper basic model function and satisfaction of the conservative constraints. The effect of time step size is studied and a reasonable value fixed for all subsequent model runs. Input parameter sweeps are then made to verify that output trends are predicted. Test matrix cases are simulated and a baseline comparison is made with the experimental data. The experimental data are then used with the reverse model to obtain experimental estimates for the internal parameters of initial enflamed mass and turbulence intensity and for the heat transfer scaling constant. Simulation of each test case is then repeated with the tuned model and the result compared against the simulation baseline and experimental data.

The work in this chapter feeds forward to aid in the stratified model evaluation. Core structures are shared between the two models. The homogeneous result provides a basis by which to judge the extent of total model error that may be attributed to the basic structure and to stratified extensions.

6.1 Verification of Model Functionality

The standard case for initial model runs is defined in Table 6.1.

Mixture Equivalence	1.0 (stoichiometric)
Initial Pressure	100 kPa (ambient)
Initial Temperature	298 K
Initial Enflamed Mass	1.0 % of total chamber mass
Turbulence	0.3 m/s
H-X Scaling Constant	1.0
Time Step	0.1 msec

Table 6.1: Parameters for Base Homogeneous Case

A single simulation run is made for the base case to ensure that model output is not unrealistic. The standard output function for model results includes the primary variables of pressure and flame radius in large scale [Figure 6.1]. Simulation parameters and basic statistics for the run are also displayed. A subset of additional variables from the simulation output is given with less detail in a second figure [Figure 6.2].

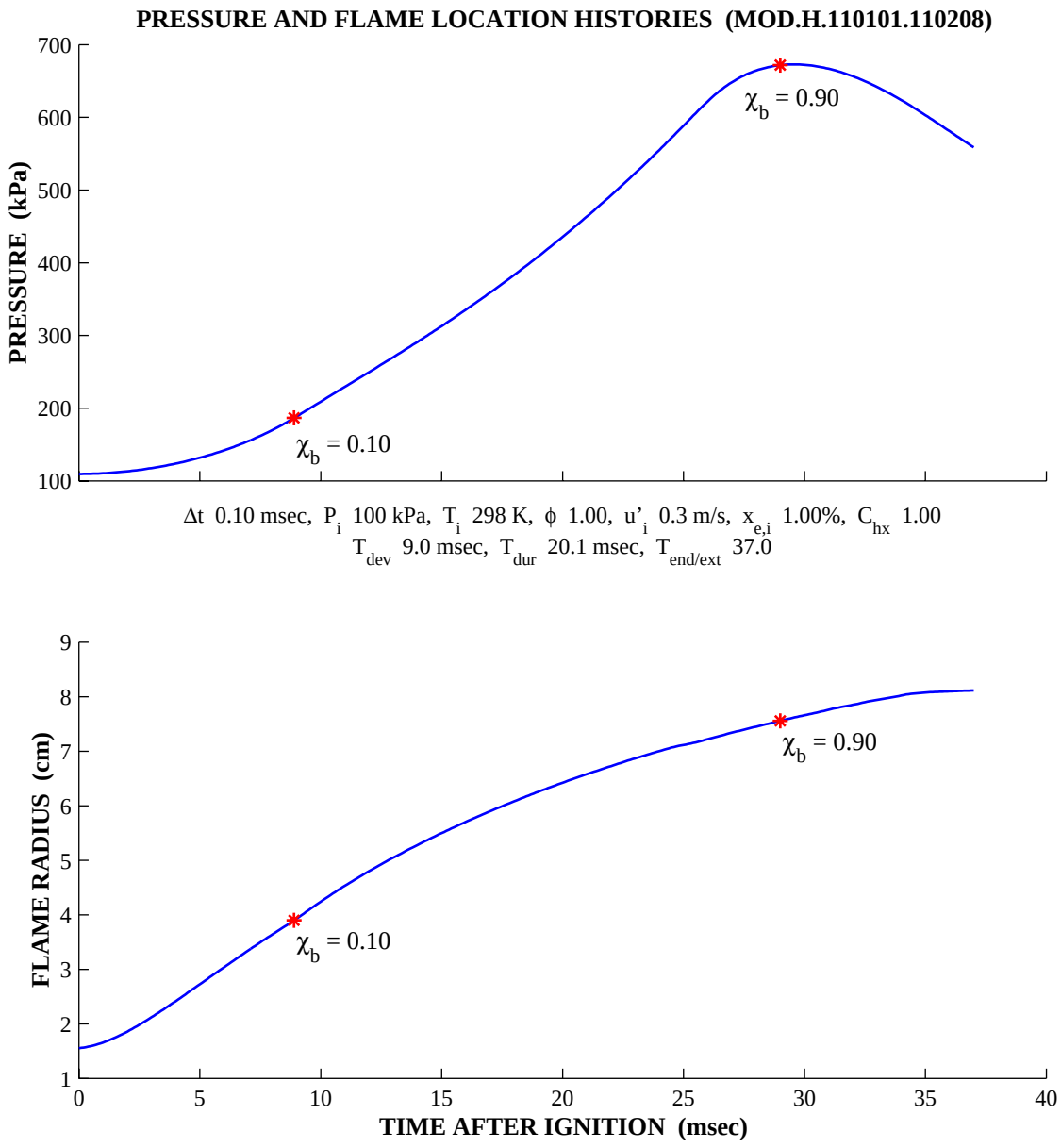

Figure 6.1: Baseline Homogeneous Case – Time Histories of Primary Variables

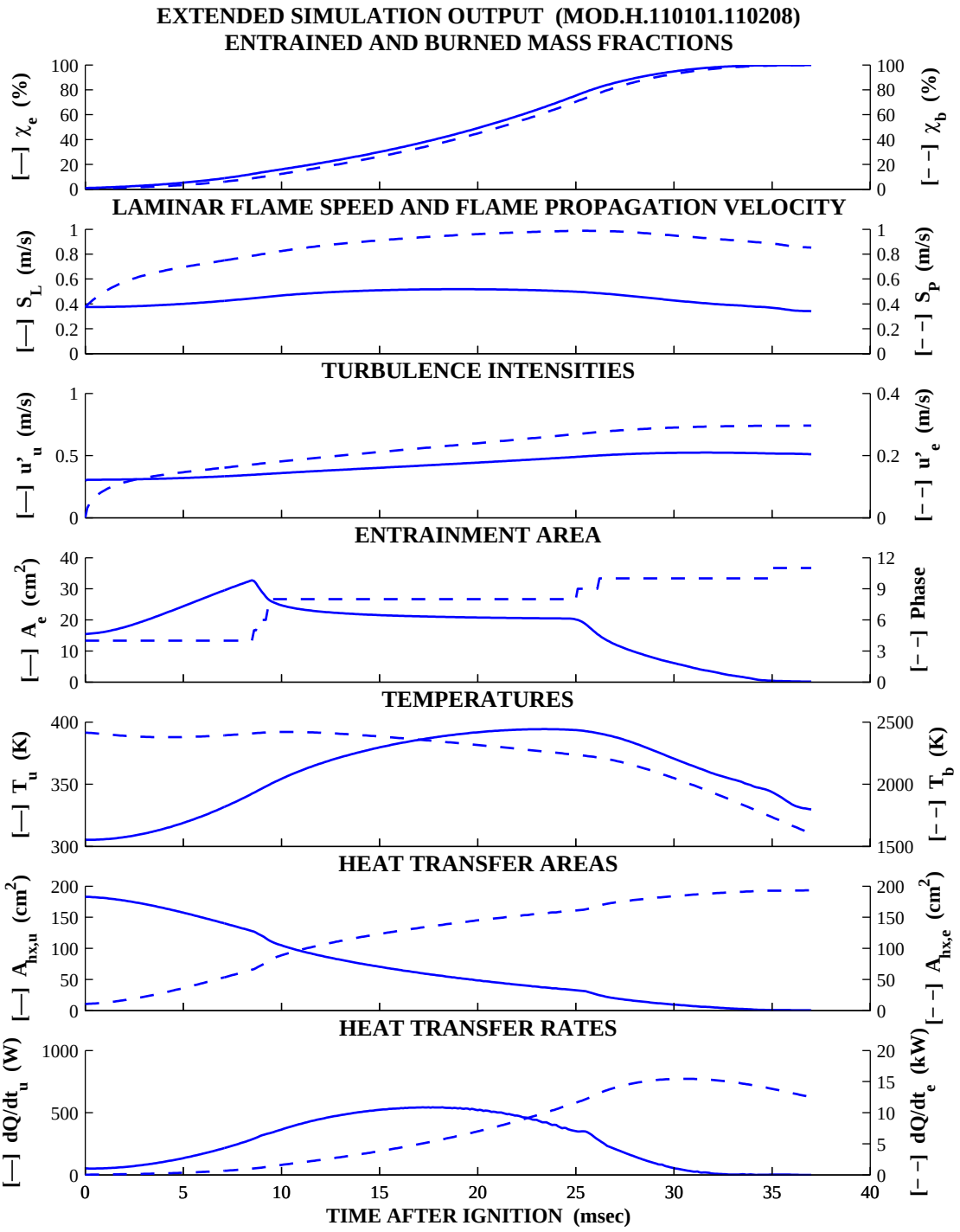

Figure 6.2: Baseline Homogeneous Case – Time Histories of Additional Variables

There is nothing in this baseline result to indicate major structural problems with the current program code and no reason to delay the parameters sweeps and continued development. The magnitude of all values is correct and the behavior of each tracked variable is reasonable.

6.1.1 Fundamental Consistency Test

The baseline run output is examined to determine how well the model satisfies the conservation of energy constraint. Chamber energy and cumulative energy lost to the surroundings are displayed in Figure 6.3. Deviation of the system energy (chamber + heat loss) from the initial energy is shown as a percentage of energy lost to the surroundings. Volume error at each step is evaluated and found to be negligible (much less than one percent). A compromise must be reached between the desire for minimal error and short simulation run times. Increased accuracy in property evaluations, interpolations of flame geometry, etc. can reduce the energy error at the expense of increased run times. An energy deviation of less than one percent and the baseline output show that the current model structure is acceptable for the current investigation.

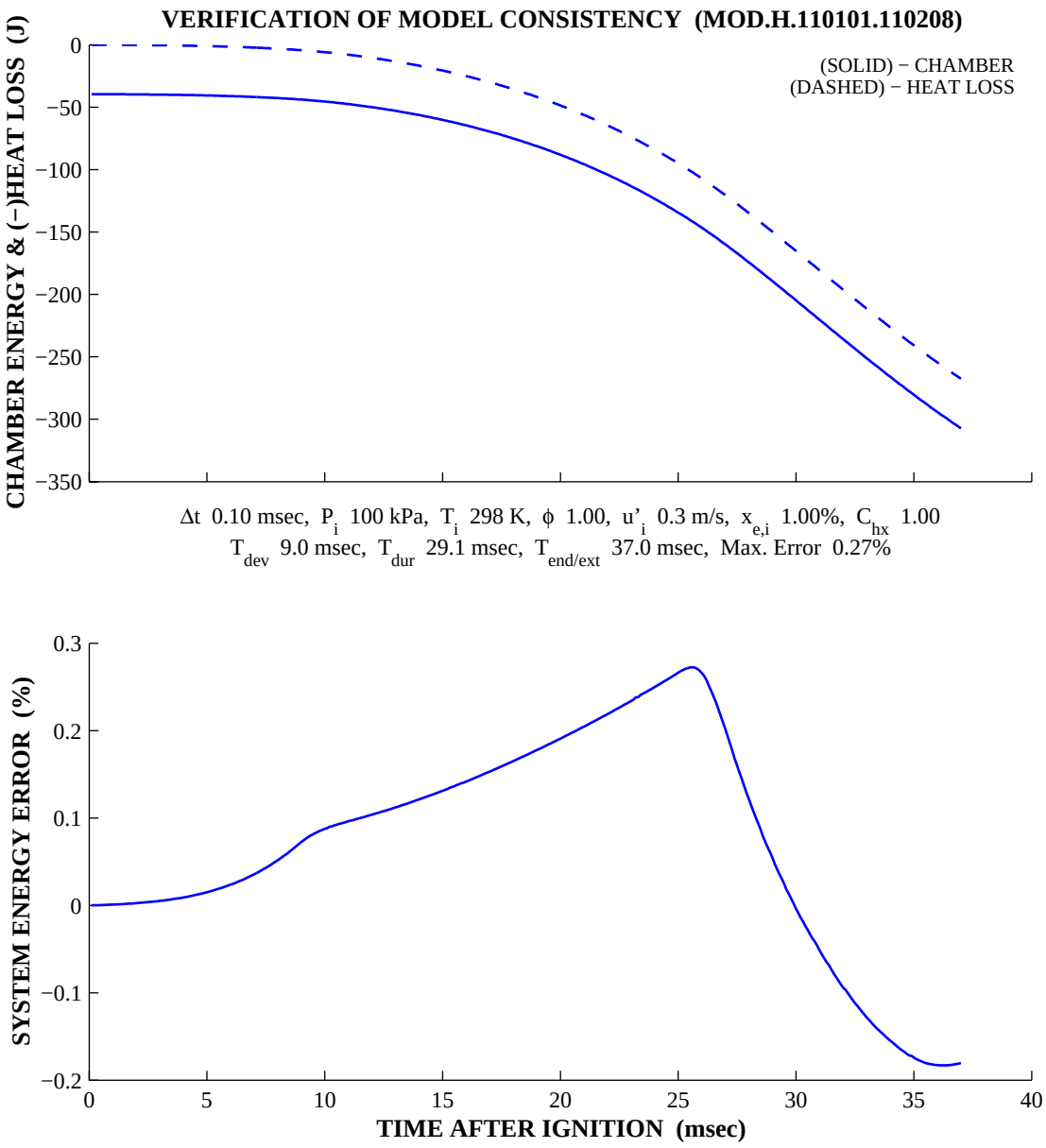

Figure 6.3: Deviation from Initial Internal Energy Through Burn Period

6.1.2 Time Step

Combustion is a continuous event and the simulation is merely an approximation with an accuracy that is a function of the time step size. Smaller step sizes better approximate the continuous process at the cost of increased simulation run times. To study the effect on accuracy and execution time, several step sizes are tested. The expected duration of the physical event is 20 to 60 milliseconds. A time-step of 0.5 millisecond yields a minimum of 40 data points and is taken as the upper limit. The lower limit is chosen to be two orders of magnitude less at 0.005 millisecond. Three intermediate values are selected at 0.05, 0.1 and 0.25 millisecond.

Results using the smallest time-step are taken as the most accurate and average instantaneous errors are computed for the pressure and flame radius.

$$Pressure\ Error = \frac{1}{n} \cdot \sum_{i=1}^{i=n} \left| P - P_{base} \right|_i \tag{6.1}$$

$$Flame\ Radius\ Error = \frac{1}{n} \cdot \sum_{i=1}^{i=n} \left| r_e - r_{e,base} \right|_i \tag{6.2}$$

Burn duration varies with step size so the summations are taken over a limited range from ignition until 90 percent of the mass is burned. Comparison values are interpolated from the base pressure and flame radius vectors for each case to obtain equal length vectors for the summation. The number of expressions that must be evaluated in each case varies inversely with time-step size. A simple curve-fit is for the following function where C is an unknown constant.

$$Simulation\ Time \approx \frac{Calculations}{Step} \cdot \frac{CPU\ Time}{Calculation} \cdot Total\ Steps = \frac{C}{\Delta t} \tag{6.3}$$

Run times and errors are plotted as functions of the time step size in Figure 6.4.

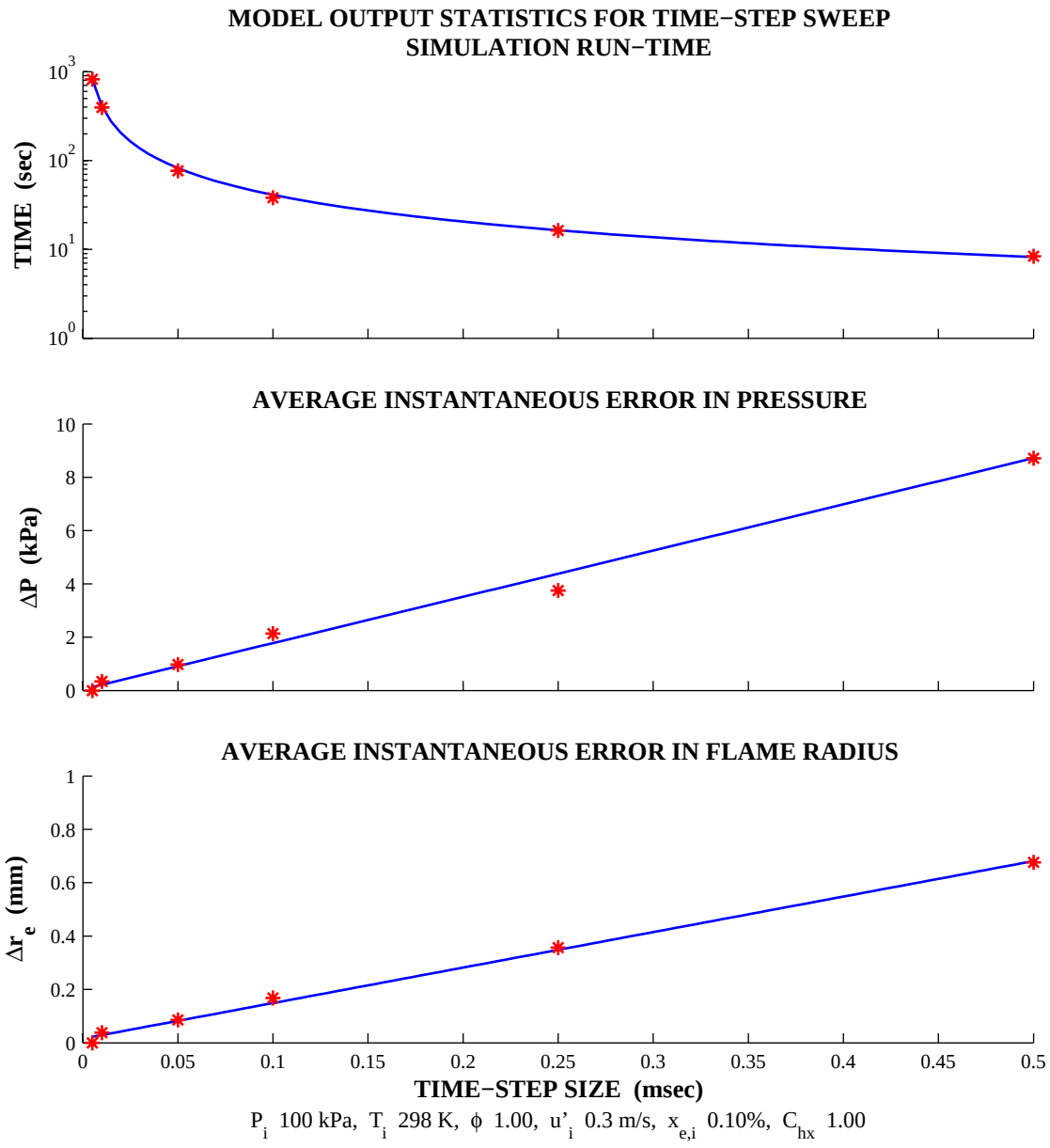

Figure 6.4: Effect of Time Step on Simulation Time and Error

Simulation time follows the expected reciprocal form and both average instantaneous errors exhibit a nearly linear increase with step size. A step size of 0.1 millisecond is selected. This should result in simulation run-times of approximately 30 seconds and time histories for pressure and flame radius not significantly different from the smallest time step case.

6.1.3 Parameter Sweeps and Sensitivity Analysis

Sweeps are made of initial conditions and internal model parameters to verify that trends in the model output are reasonable. The outputs tracked are two commonly used benchmarks for combustion. The early flame development period is defined as the time after ignition at which 10 percent of the mass is burned. Burn duration is similarly defined as the time required for the burned mass fraction to rise from 10 to 90 percent.

Sweeps are made for the initial conditions of mixture equivalence, pressure and turbulence intensity. Internal parameters include initial enflamed mass fraction and the heat transfer scaling constant. Initial enflamed mass is considered an internal parameter and not an initial condition since it is a function of ignition energy, mixture equivalence and turbulence. Perturbations are made in each parameter from a common case defined in Table 6.2.

Mixture Equivalence	1.0 (stoichiometric)
Initial Pressure	400 kPa
Initial Enflamed Mass	1.0 % of total chamber mass
Turbulence	0.3 m/s
H-X Scaling Constant	1.0

Table 6.2: Base Case Values for Parameter Sweeps

The resulting times for each sweep are plotted as a function of the sweep parameter and fit with a second-order polynomial. The polynomial coefficients provide simple first-order sensitivities for each parameter.

$$\frac{\partial T_{dev}}{\partial \phi} = \frac{\partial}{\partial \phi}\left(a_2 \cdot \phi^2 + a_1 \cdot \phi + a_0\right) = 2 \cdot a_2 \cdot \phi + a_1 \tag{6.4}$$

$$\frac{\partial T_{dur}}{\partial \phi} = \frac{\partial}{\partial \phi}\left(b_2 \cdot \phi^2 + b_1 \cdot \phi + b_0\right) = 2 \cdot b_2 \cdot \phi + b_1 \tag{6.5}$$

Mixture equivalence is swept from 0.7 to 1.3 [Figure 6.5]. Minimum times are generated in the 1.0-1.1 range where the laminar flame speeds are greatest.

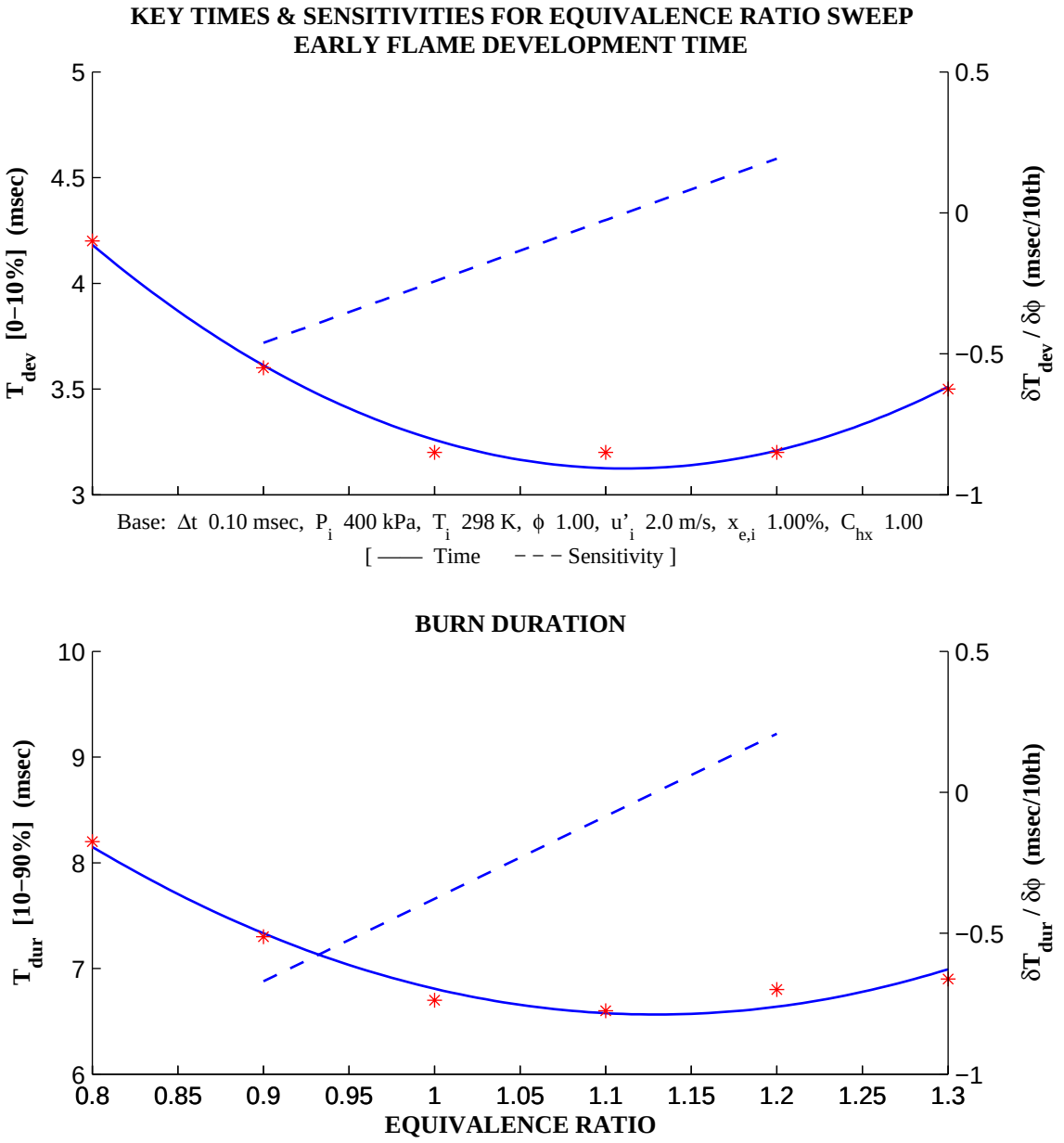

Figure 6.5: Parameter Sweep – Mixture Equivalence

Initial pressure is swept from 100 to 700 kPa [Figure 6.6]. Both times increase slightly as the combustible mass increases proportionally with pressure.

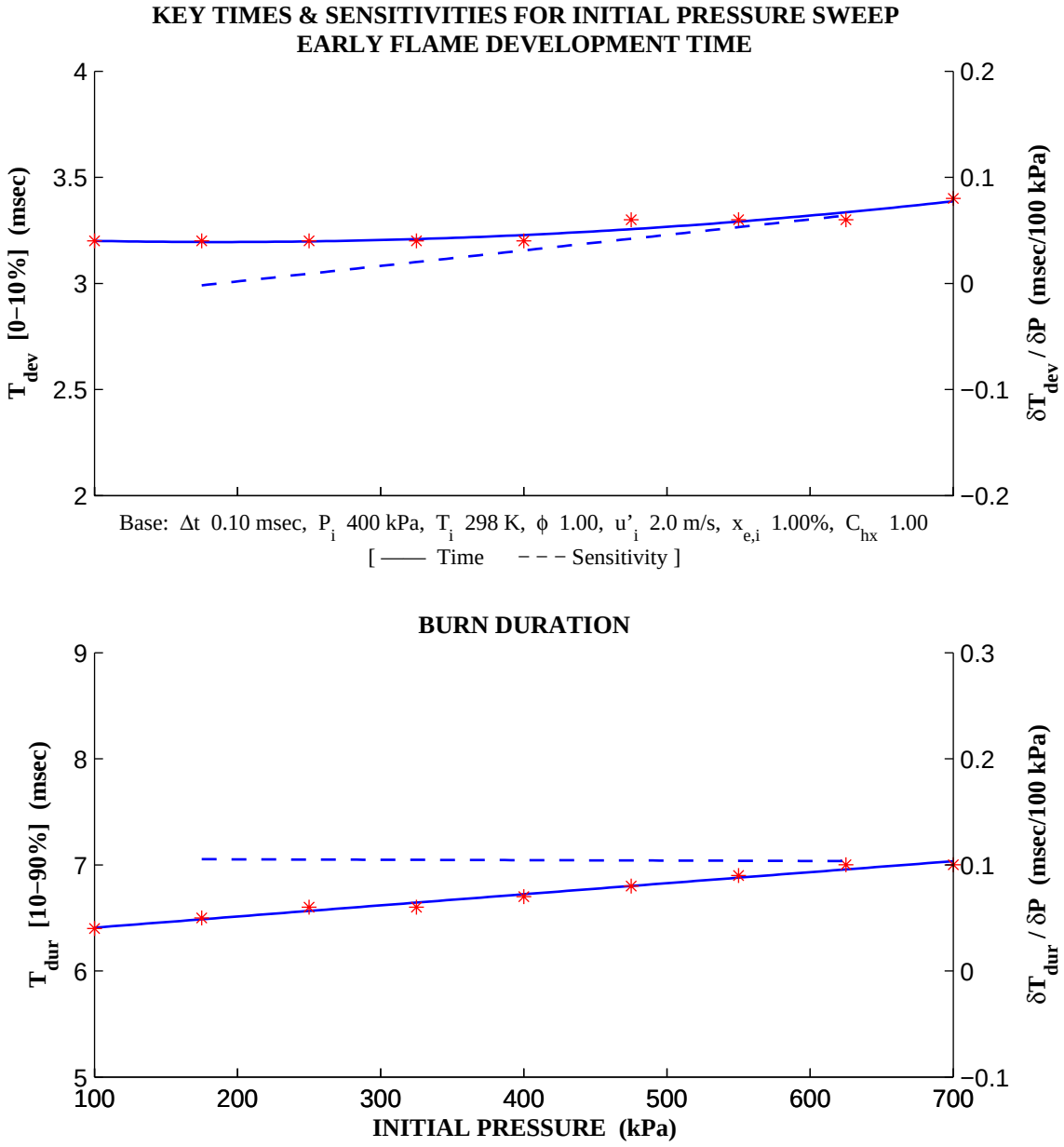

Figure 6.6: Parameter Sweep – Charge Pressure

Turbulence intensity is swept from 0.5 to 4.0 m/s [Figure 6.7]. Both times decrease significantly since mass entrainment rates are directly related to turbulence.

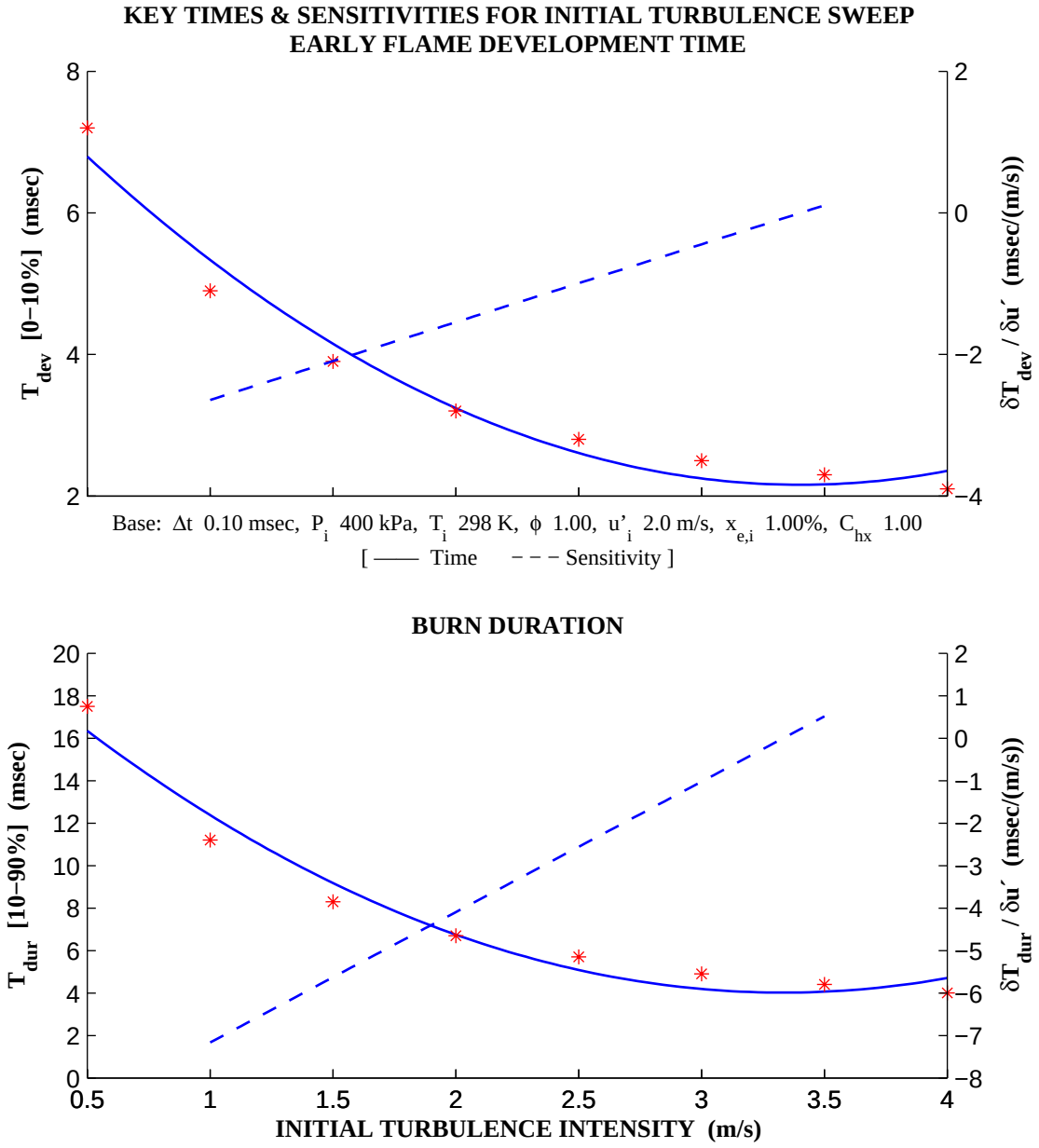

Figure 6.7: Parameter Sweep – Turbulence

Initial enflamed mass is swept from 0.3 to 2.0 percent [Figure 6.8]. Flame development times drop as expected. Only ignition is affected so burn duration remains constant.

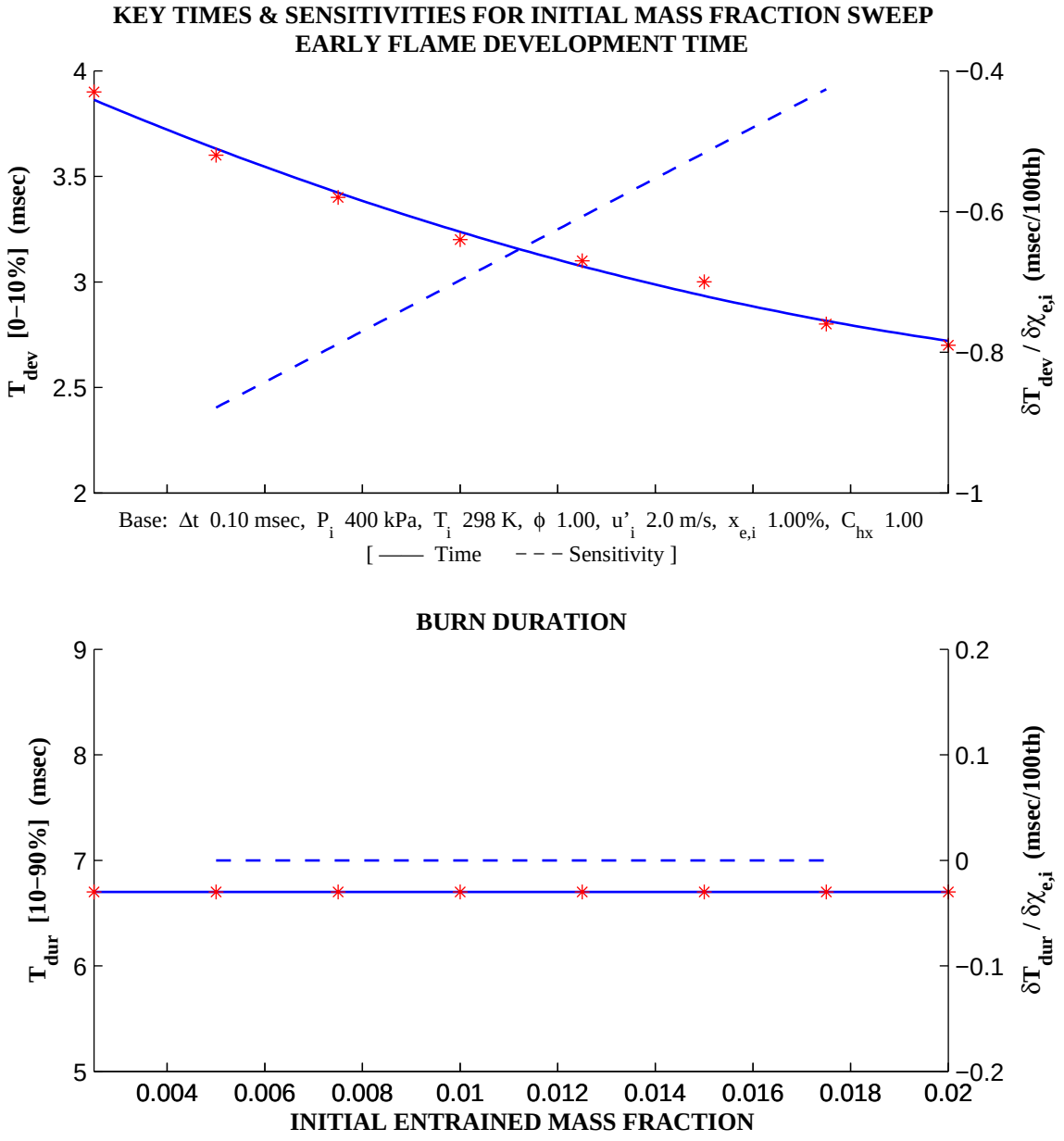

Figure 6.8: Parameter Sweep – Initial Enflamed Mass Fraction

The heat transfer scaling constant is swept from 0.6 to 1.4 [Figure 6.9]. Times increase since higher heat transfer rates result in lower temperatures and flames speeds.

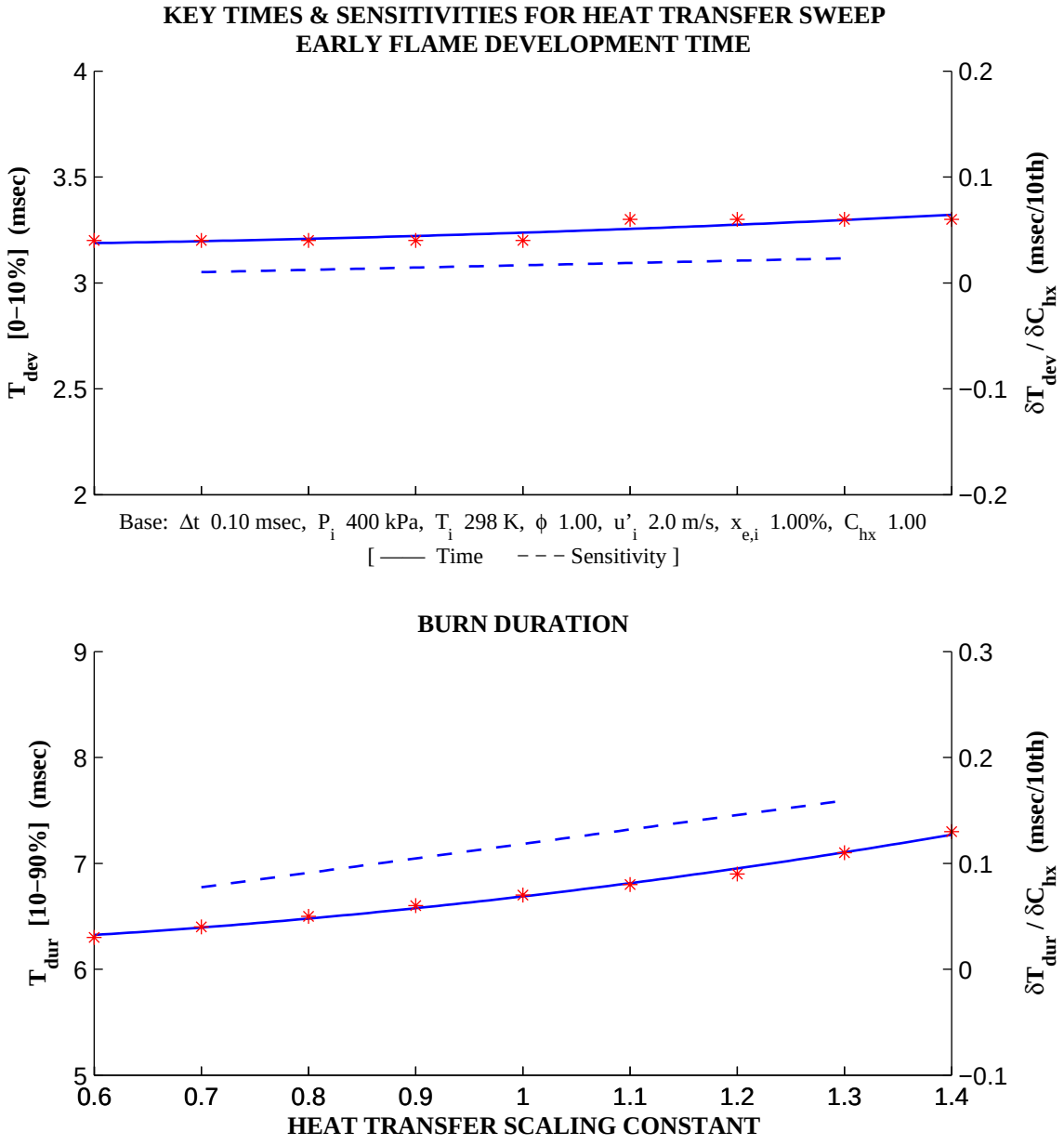

Figure 6.9: Parameter Sweep – Heat Transfer Scaling Constant

For each parameter sweep, the trends in flame development time and burn duration exhibit the expected behavior. These results show the model to be well behaved for typical parameter ranges. All initial tests indicate the simplified homogeneous model functions properly and succeeds in capturing the essential nature of the combustion process.

6.2 Baseline Simulation Results

Each homogeneous test case of Table 5.1 is simulated and the output compared against reduced experimental data. Initial conditions (pressure, temperature and equivalence) in each case are the recorded experimental values. Parameters not measured (initial turbulence, enflamed mass fraction and heat transfer constant) are taken from the baseline homogeneous case [Table 6.1]. The logical comparison is made between pressure and flame front histories. Simulation histories are re-sampled to obtain vector lengths equal to those of the reduced experimental data matrices (2.0 millisecond temporal resolution). Average instantaneous errors are then computed for both parameters.

$$Err_{pres} = \frac{1}{m} \cdot \sum_{j=1}^{j=m} \left| P_{sim} - P_{\exp} \right|_j \tag{6.6}$$

$$Err_{rad} = \frac{1}{n} \cdot \sum_{i=1}^{i=n} \left| r_{e,sim} - r_{e,\exp} \right|_i \tag{6.7}$$

These error definitions differ slightly from those of the time step sweep. Here the range of each summation is independent since the period of valid reduced data is greater for pressure than flame radius. The upper limit for the pressure error is the time corresponding to flame contact with the far wall (end of Phase 8). Experimental images indicate the flame shape deviates significantly from the simple geometry sub-model and the model is expected to break down at

this point. The upper limit for the radius error is determined by the experimental data as described in Chapter 5.

Simulation and experimental results are compared in Table 6.3 for each of the three homogeneous cases.

Case	Average Instantaneous Difference	
	Pressure (kPa)	Flame Radius (mm)
H1	69.9	5.8
H3	65.9	9.3
H4	36.3	2.9

Table 6.3: Comparison of Homogeneous Simulation and Experimental Results

Simulation and experimental results are compared graphically for each case [Figure 6.10 through Figure 6.18]. Simulation outputs are displayed as continuous histories. Markers indicate reduced experimental at two millisecond intervals data and error bars show deviation of the experimental flame radius from the idealized constant curvature front geometry. Simplified flame front development histories and extended simulation output are also provided for each case.

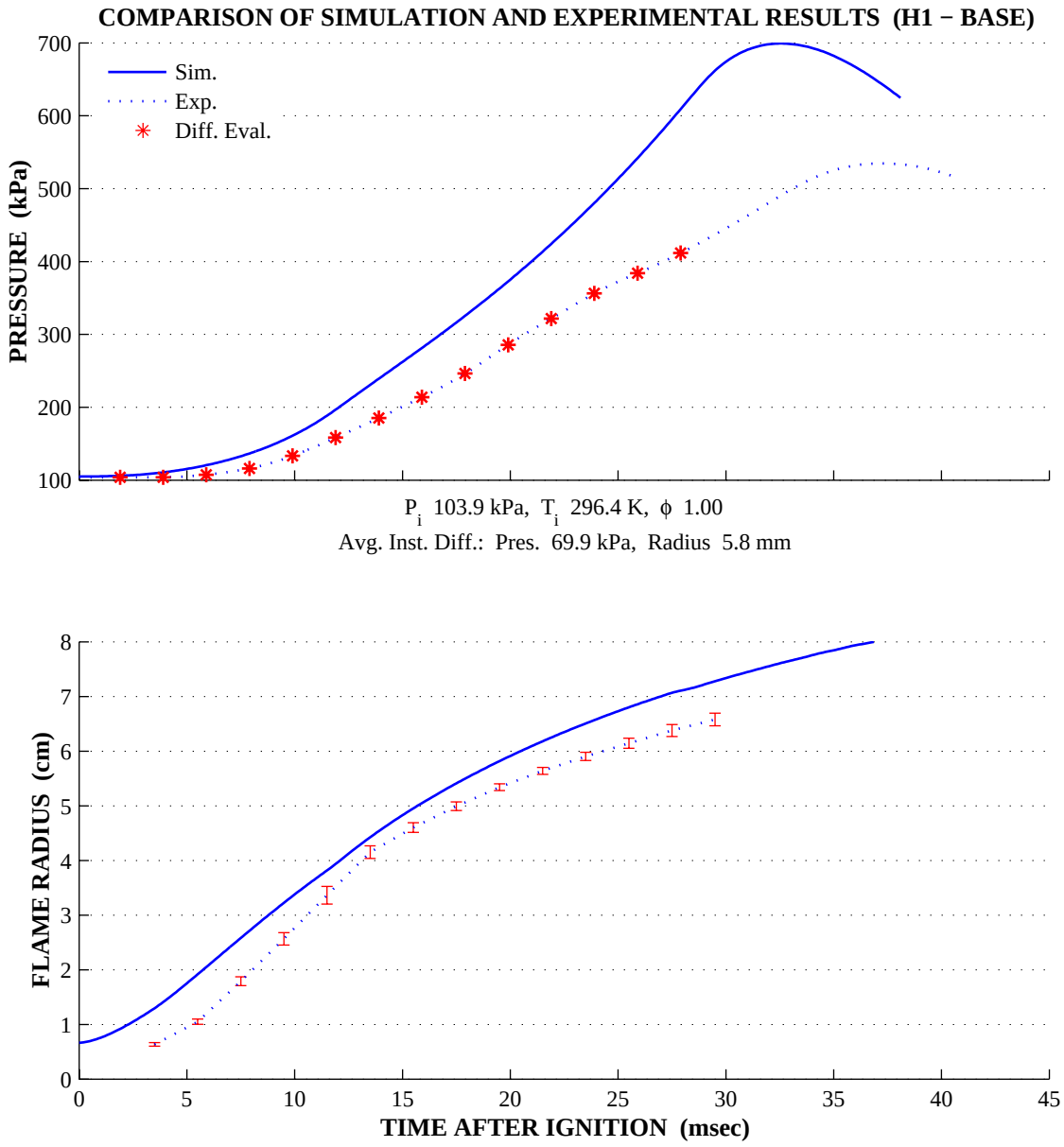

Figure 6.10: Base Homogeneous Simulation Results (Case H1)

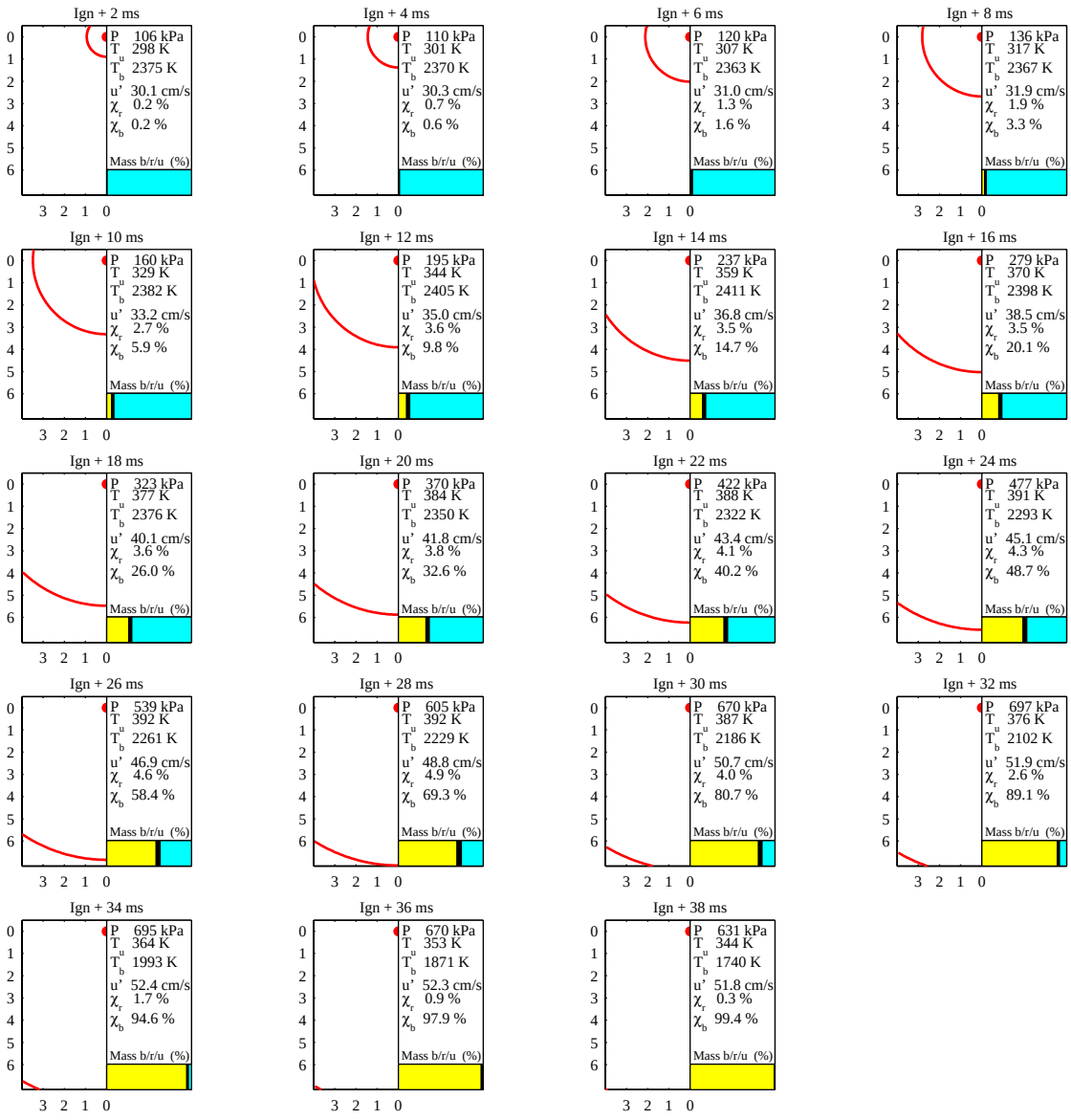

Figure 6.11: Base Homogeneous Simulation, Flame Development (Case H1)

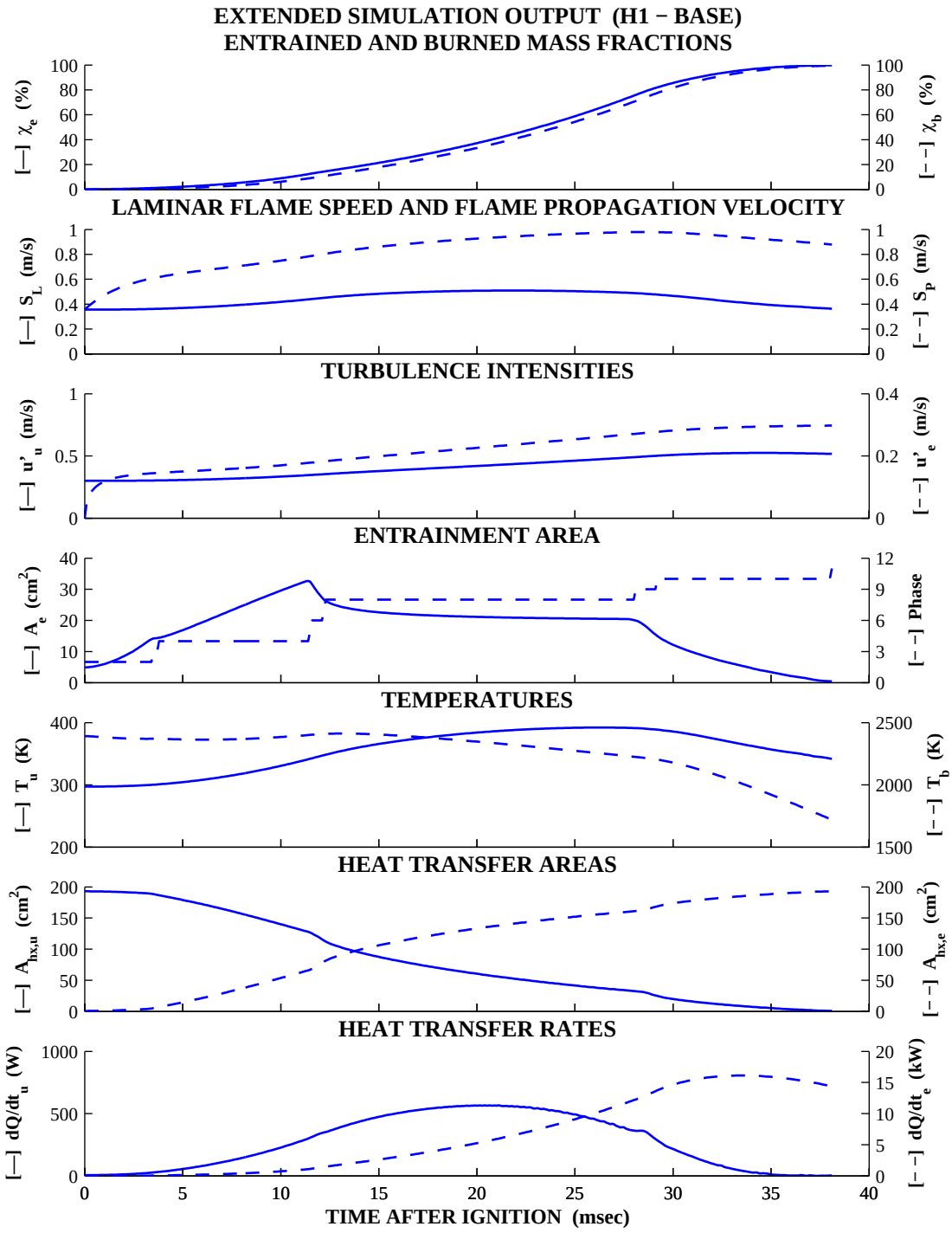

Figure 6.12: Base Homogeneous Simulation, Extended Output (Case H1)

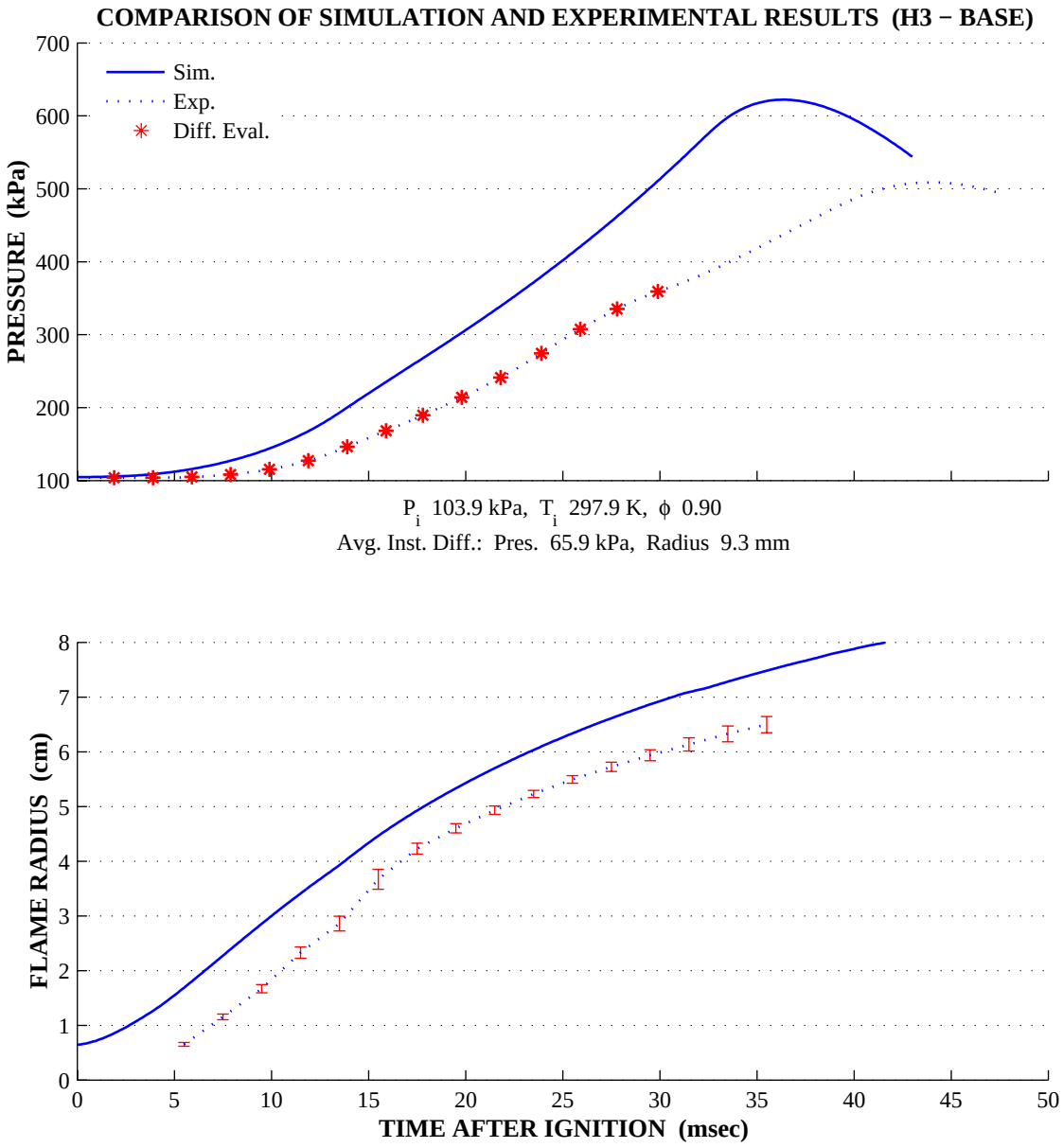

Figure 6.13: Base Homogeneous Simulation Results (Case H3)

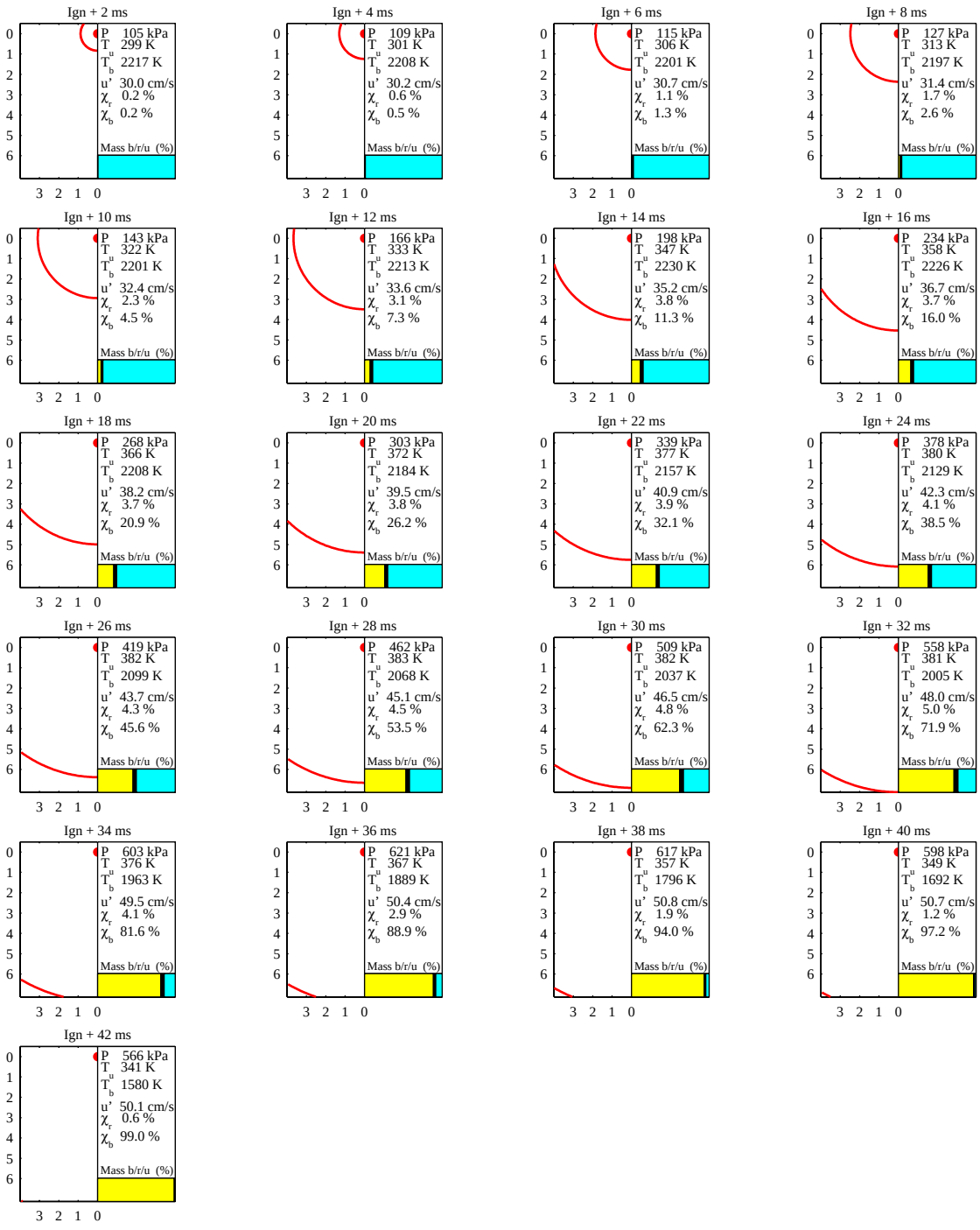

Figure 6.14: Base Homogeneous Simulation, Flame Development (Case H3)

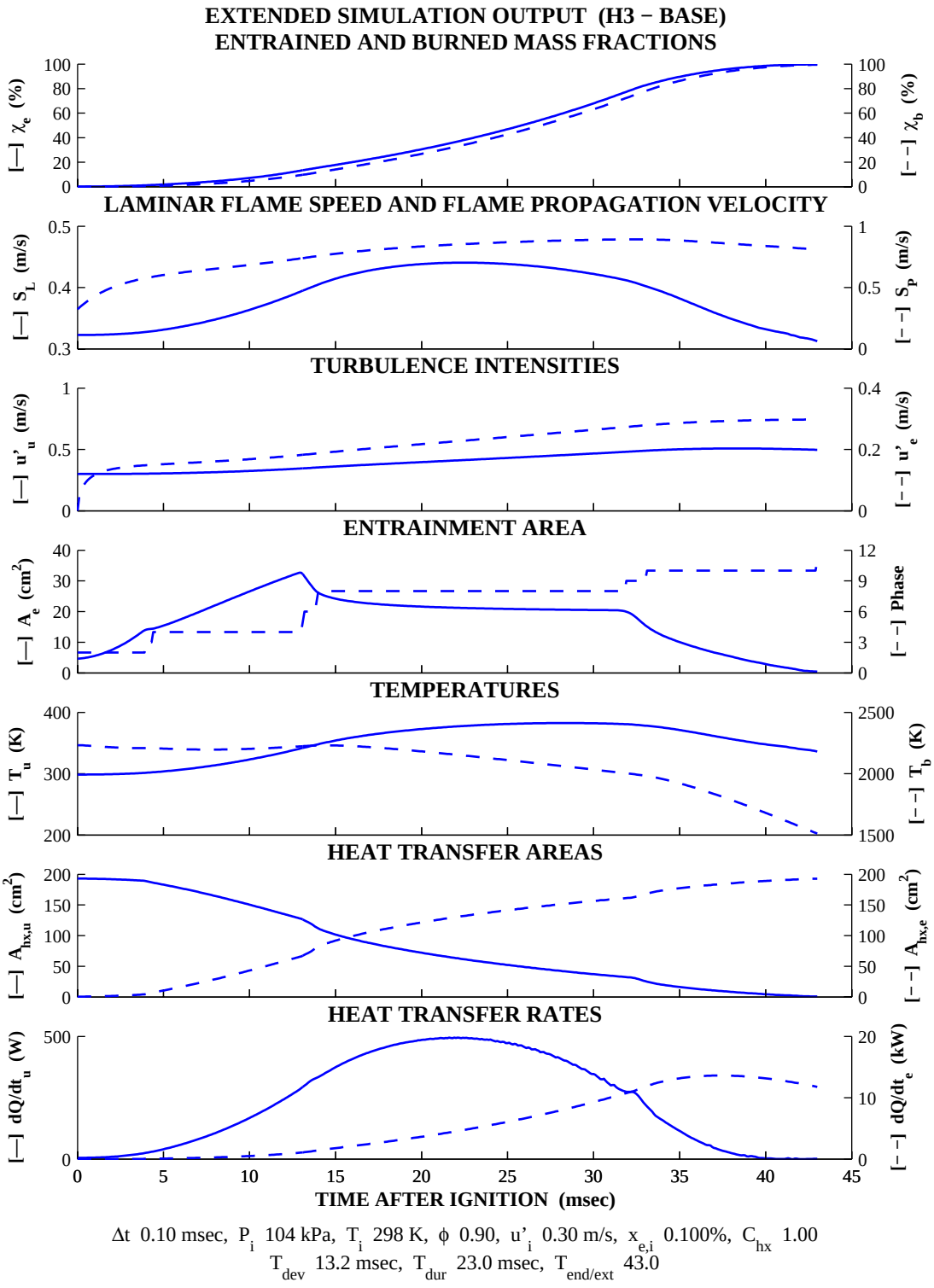

Figure 6.15: Base Homogeneous Simulation, Extended Output (Case H3)

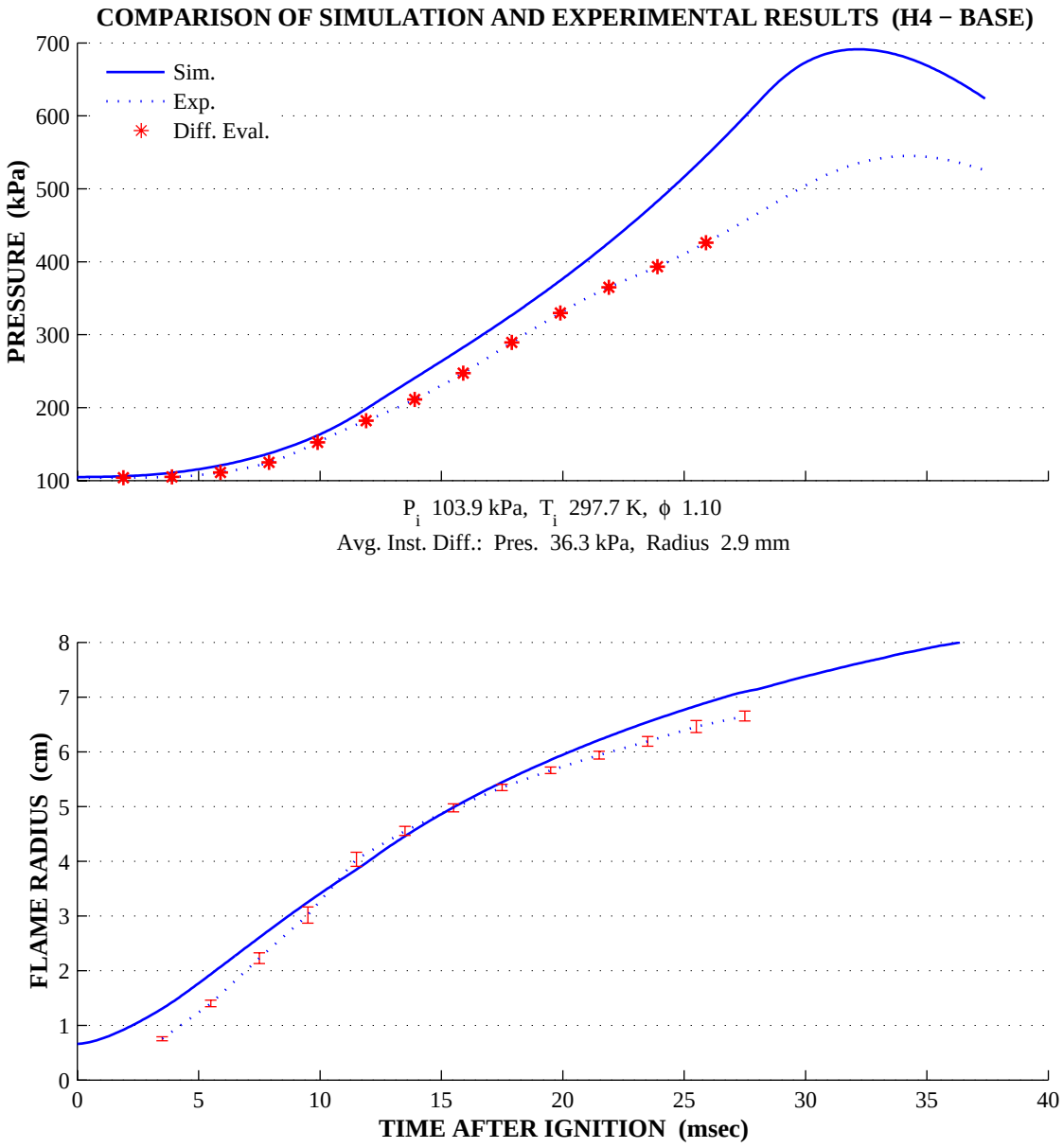

Figure 6.16: Base Homogeneous Simulation Results (Case H4)

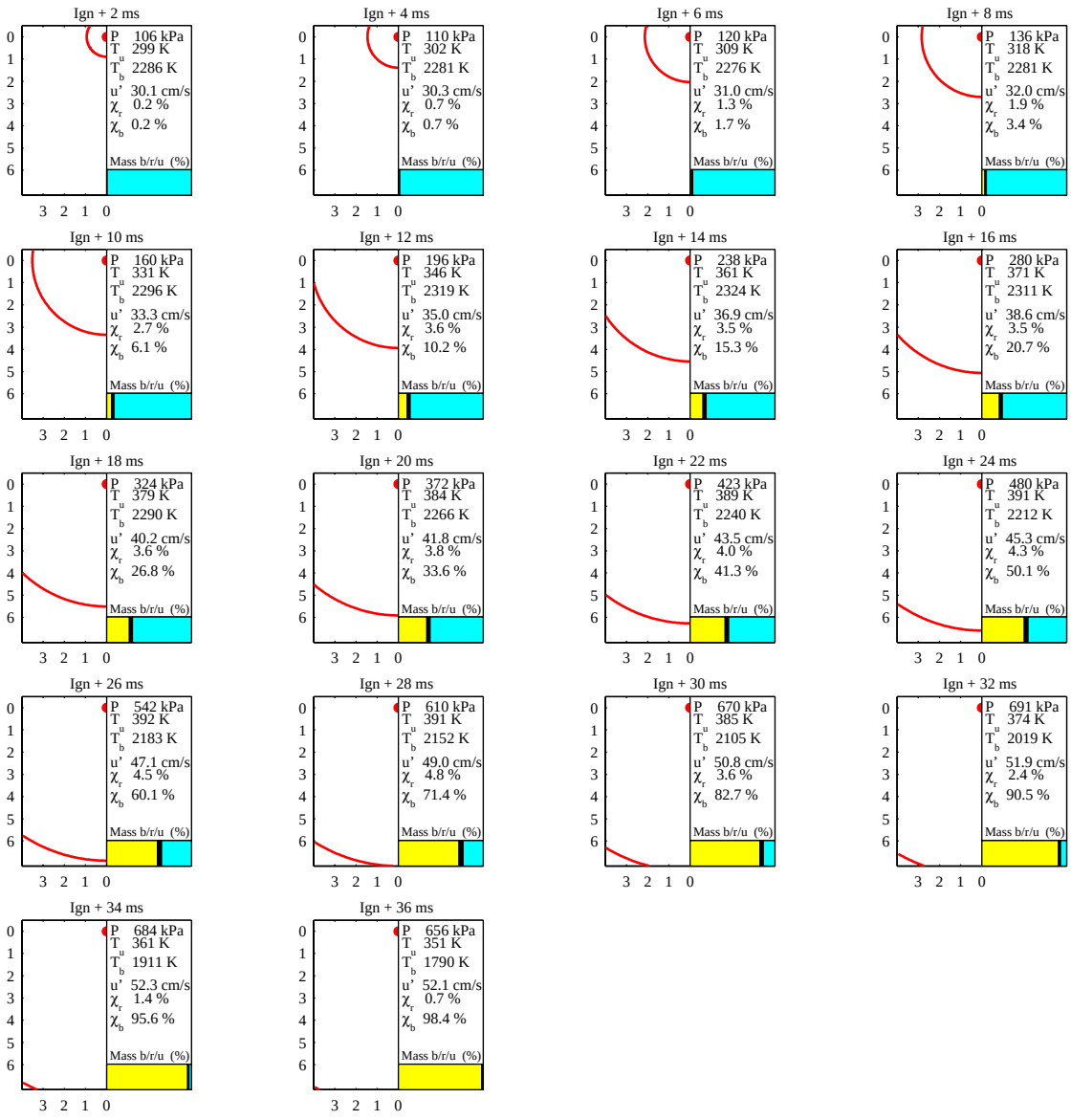

Figure 6.17: Base Homogeneous Simulation, Flame Development (Case H4)

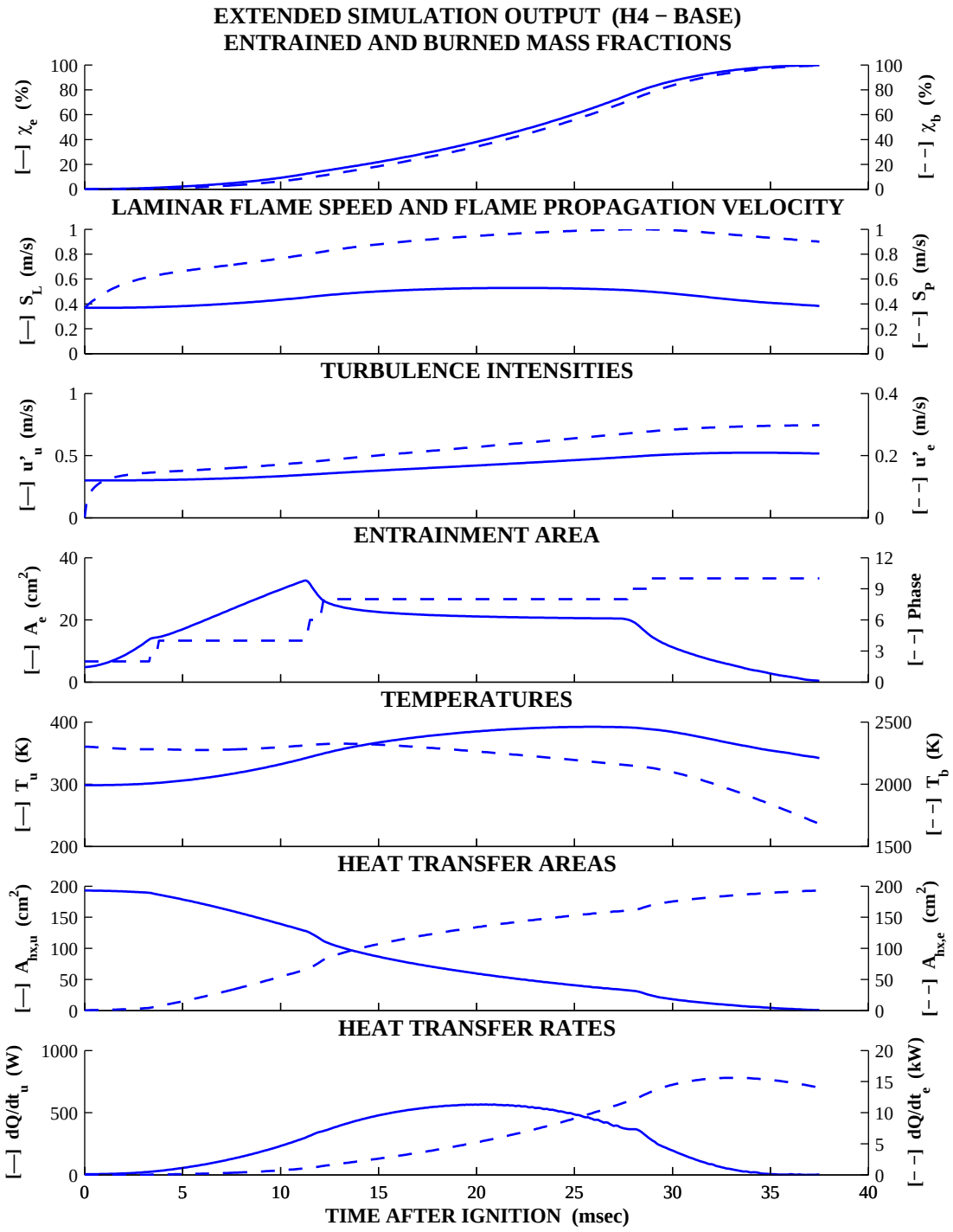

Figure 6.18: Base Homogeneous Simulation, Extended Output (Case H4)

6.3 Tuned Simulation Results

The baseline simulation results are not a close match but this is expected with estimates used for several parameters. Tuning with experimental data is intended to reduce the simulation error. The reverse model is used to obtain estimates for three experimental parameters: initial enflamed mass fraction, initial turbulence and the heat transfer scaling constant. The complete pressure and flame radius time-histories can be controlled with these three parameters. Initial enflamed mass fraction dominates early on while turbulence and heat transfer determine the overall curve shapes and peak pressure. Turbulence tuning is limited here to the initial intensity but can be extended to include internal parameters of the turbulence sub-model. Heat transfer effects are tailored by varying the heat transfer scaling constant.

6.3.1 Tuning – Initial Enflamed Mass Fraction

It is apparent that the fixed initial enflamed mass fraction of one percent exceeds the actual amount for all test cases and that the enflamed mass is not constant. The reverse model is first used to obtain an estimate of the initial mass fraction for each test case. Simulation time is limited to 10 milliseconds where the initial mass fraction dominates. Error function weights (see Section 3.3) are specified as 2.0 for pressure and 1.0 for flame radius based on confidence in the experimental data. Optimization results are presented in Figure 6.19 where the initial enflamed mass fraction and kernel diameter are plotted against equivalence.

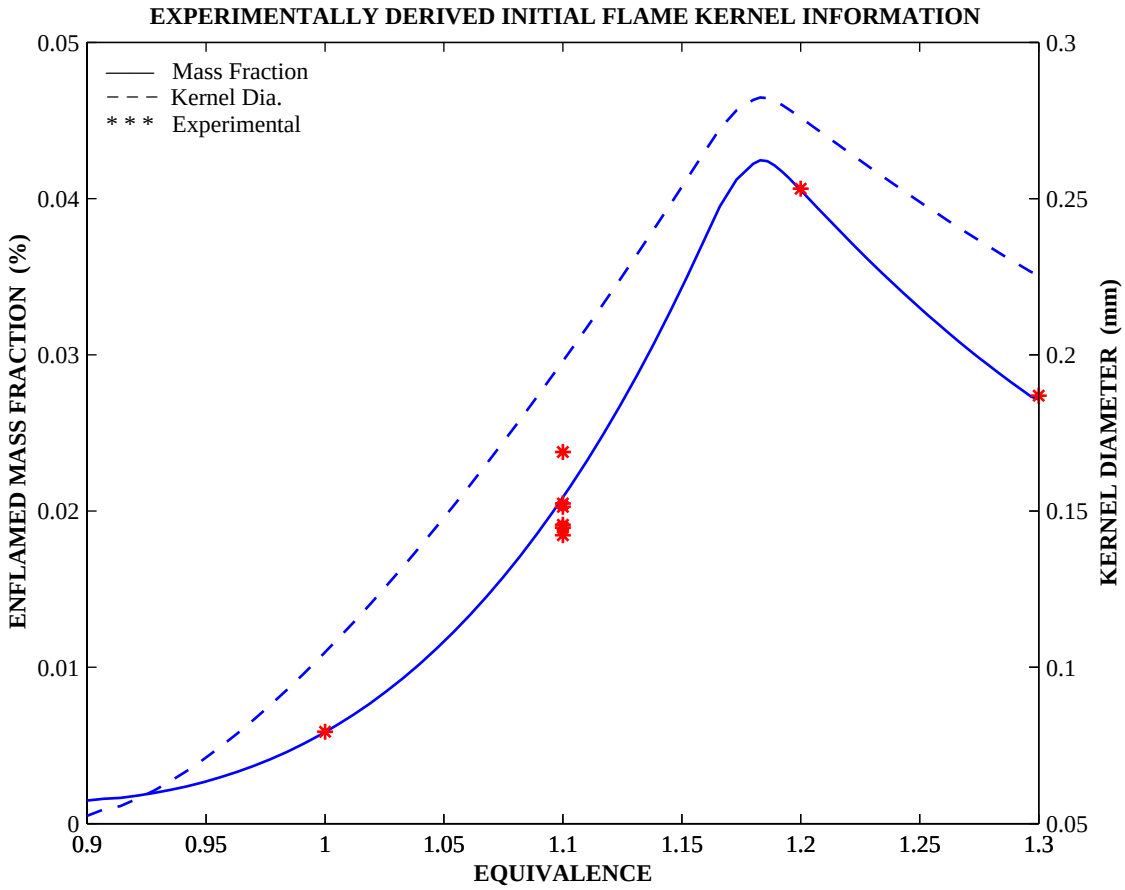

Figure 6.19: Initial Enflamed Mass Fraction Dependence on Equivalence

Regardless of the early experimental pressure and radius histories accuracy, a clear trend exists. Estimated initial kernel sizes are reasonable for the electrode diameter of 0.5 mm and gap of 1.0 mm. Improved estimates of initial enflamed mass fraction are now possible for any equivalence by simple interpolation (with the current ignition system and initial turbulence and at a test pressure of 100 kPa).

6.3.2 Tuning – Initial Turbulence & Heat Transfer Effect

Estimates for the initial turbulence intensity and heat transfer scaling constant are obtained from a multivariable mode run of the reverse model. The simulation is terminated after the experimental peak pressure time. Wall burning is not modeled so comparison in the limited period is more reasonable. Error function weights are unchanged from the initial mass fraction tuning run. Initial and tuned values for the initial turbulence and heat transfer scaling constant are compared in Table 6.4. These are values that minimize the error across all homogeneous cases.

	Initial Turbulence (m/s)	H-X Scaling Constant
Initial Value	0.30	1.00
Tuned Value	0.27	1.54

Table 6.4: Initial and Tuned Parameter Values for Homogeneous Model

After tuning, a mean effective convective heat transfer coefficient of ~200 W/m^2-K is obtained. This falls is in the range of 25-250 W/m^2-K given for forced convection by Incropera & Dewitt [19]. Only convective heat loss is modeled so the estimated convective heat loss is inflated by any loss that is not explicitly modeled (i.e. radiation).

6.3.3 Tuning – Late Burn (Near-Wall Regime) Compensation

Late burn divergence is relatively unaffected as the average pressure error is reduced. A common break in the pressure traces is present, corresponding to mass fractions of 80-90 percent and flame-to-wall distances of approximately ten millimeters. During this period, the simple free surface entrainment-burnout and/or heat transfer models break down. The simple solution is to force the unburned temperature to approach the surface temperature as the unburned volume approaches zero. This is a physical reality that the simple heat transfer sub-model does not require. A simple modification is made that requires no assumptions about the thermal boundary layer.

$$T_{u,\mathrm{mod}} = T_u - \left(T_u - T_{surf}\right) \cdot \left(1 - \frac{\bar{V}_u}{\bar{V}_{u,transition}}\right) \tag{6.8}$$

The modified temperature is computed using the unburned volume. Late in the burn, the volume ratio is approximately equal to the flame-wall distance since the front is relatively flat (until wall contact). After the experimentally derived transition distance is reached, flame speeds are evaluated using this temperature. This simple modification improves pressure prediction in the late burn period for all experimental cases.

Each of the four homogeneous test cases is simulated again using the parameter estimates and enflamed mass fraction function. Average instantaneous errors and the change in each are presented in Table 6.5.

Case	Average Instantaneous Diff.					
	Pressure (kPa)			Flame Radius (mm)		
	Base	Opt.	Chg.	Base	Opt.	Chg.
H1	69.9	6.8	-90.3%	5.8	1.6	-72.4%
H3	65.9	6.1	-90.7%	9.3	1.8	-80.6%
H4	36.3	9.0	-75.2%	2.9	2.2	-24.1%
Avg.	57.4	7.3	-85.4%	6.0	1.9	-59.0%

Table 6.5: Comparison of Homogeneous Simulation Error Before and After Tuning

Results are also given graphically in Figure 6.20 through Figure 6.28. Simulation histories before and after tuning are displayed along with experimental data using the previous format.

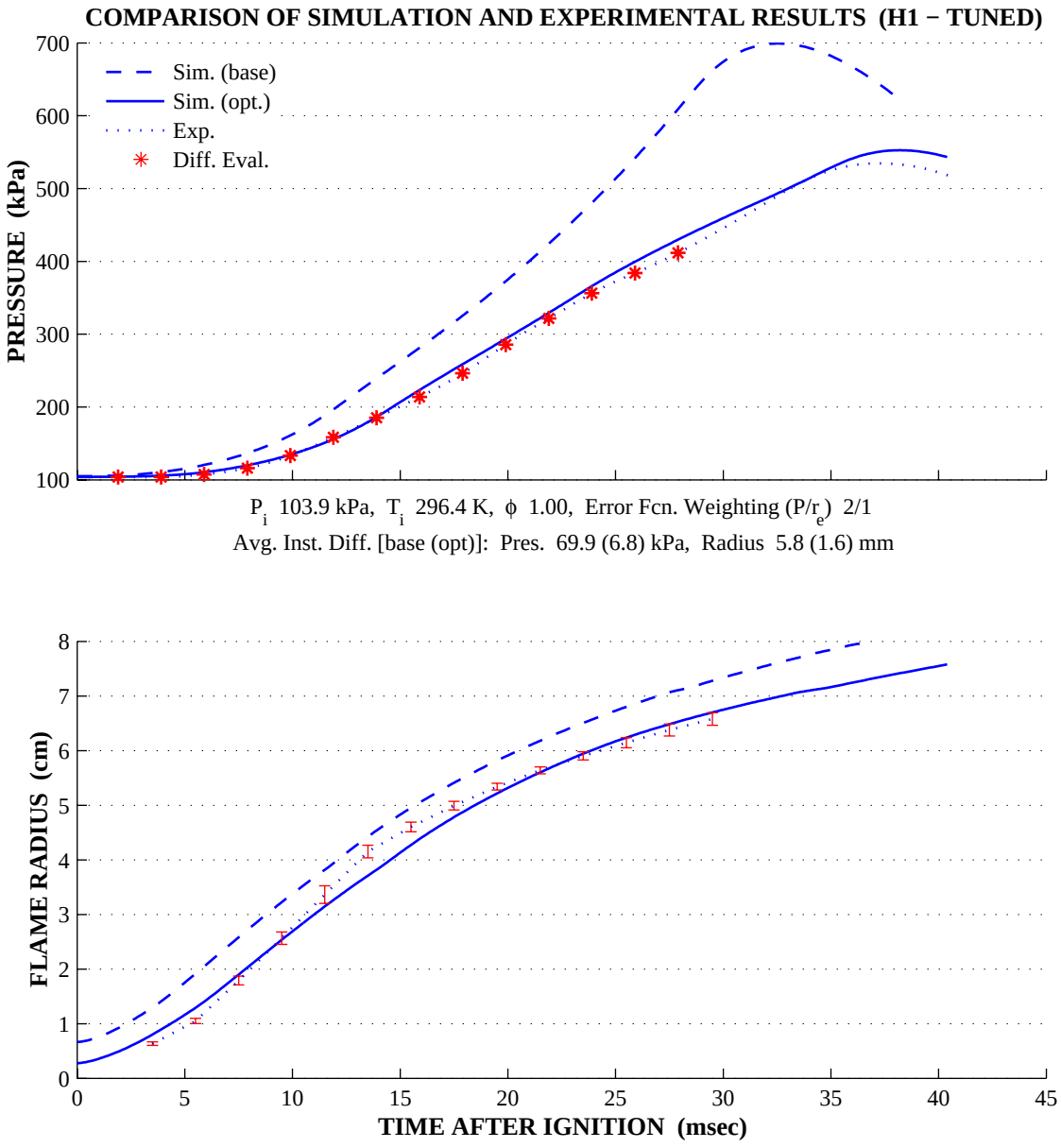

Figure 6.20: Tuned Homogeneous Simulation Results (Case H1)

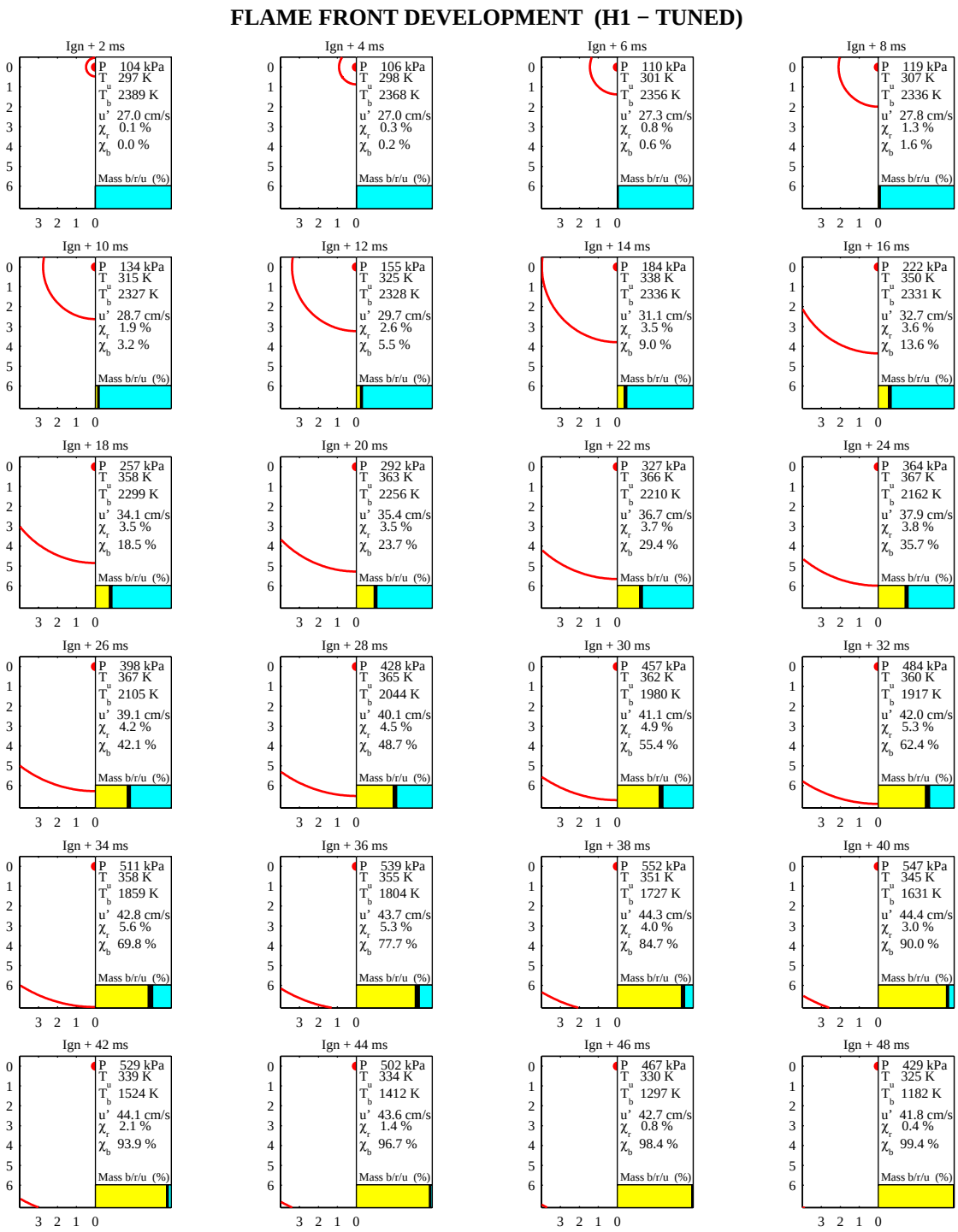

Figure 6.21: Tuned Homogeneous Simulation, Flame Development (Case H1)

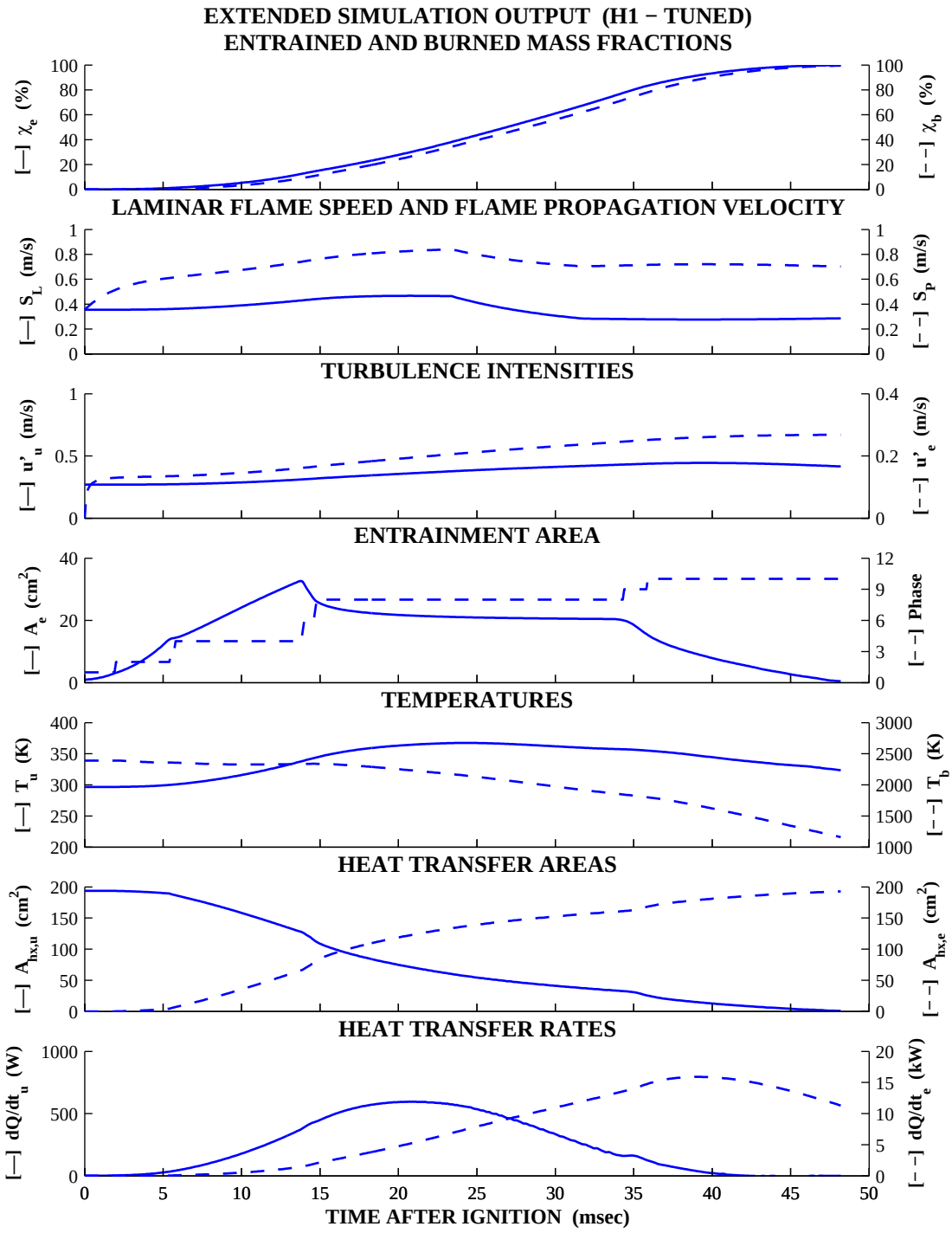

Δt 0.10 msec, P_i 104 kPa, T_i 296 K, ϕ 1.00, u'_i 0.27 m/s, $x_{e,i}$ 0.007%, C_{hx} 1.54
T_{dev} 14.2 msec, T_{dur} 25.6 msec, $T_{end/ext}$ 48.2

Figure 6.22: Tuned Homogeneous Simulation, Extended Output (Case H1)

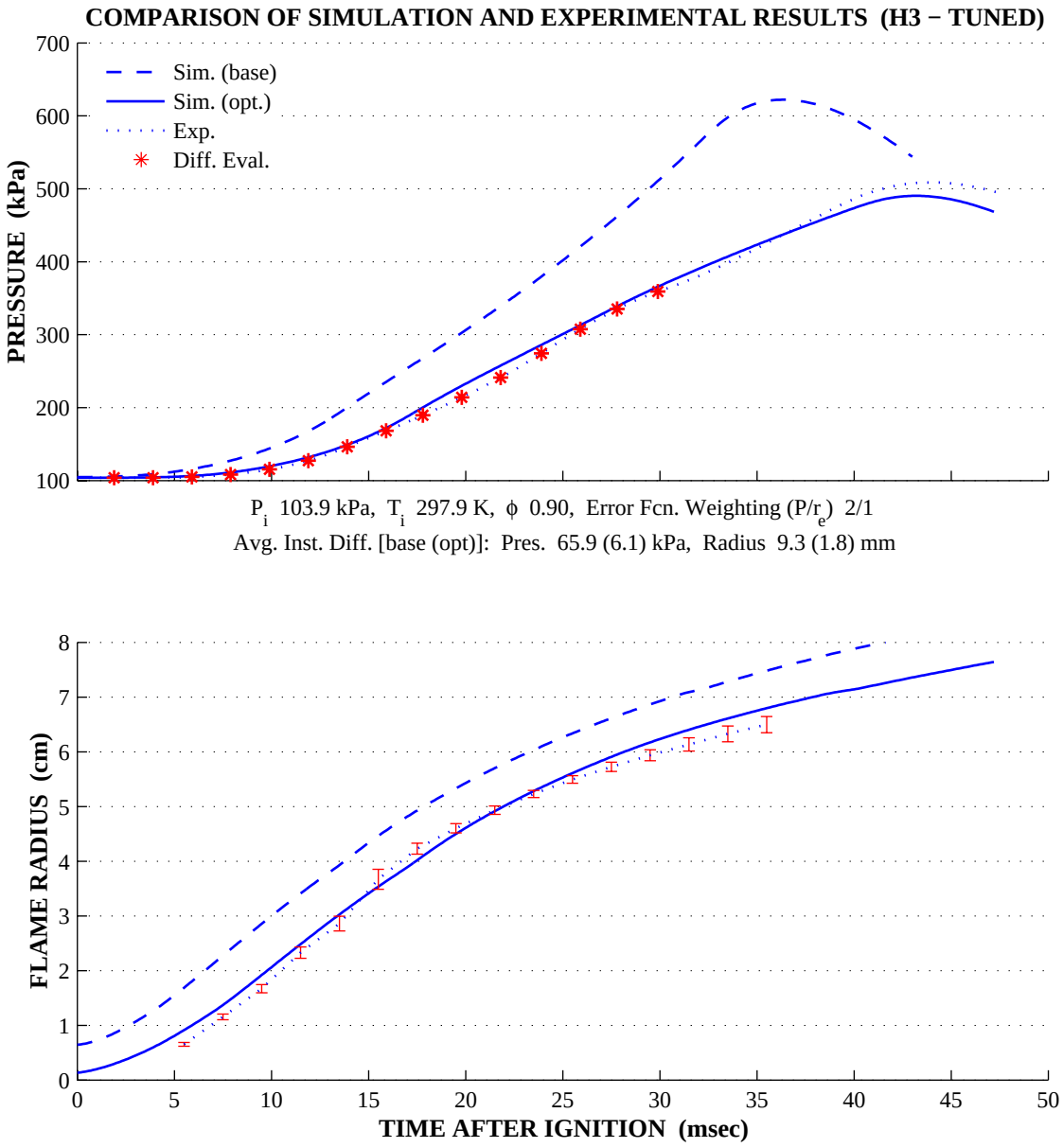

Figure 6.23: Tuned Homogeneous Simulation Results (Case H3)

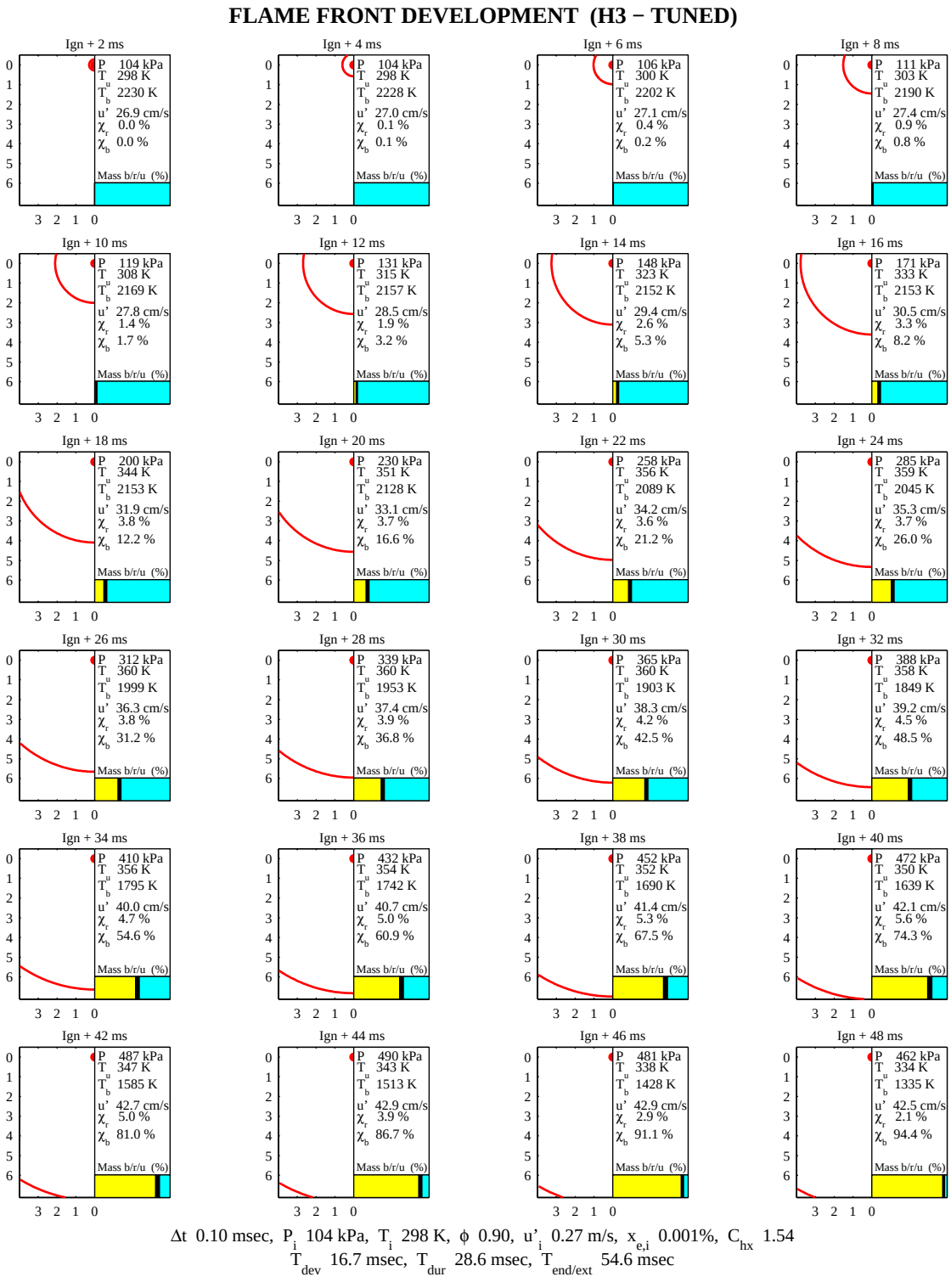

Figure 6.24: Tuned Homogeneous Simulation, Flame Development (Case H3)

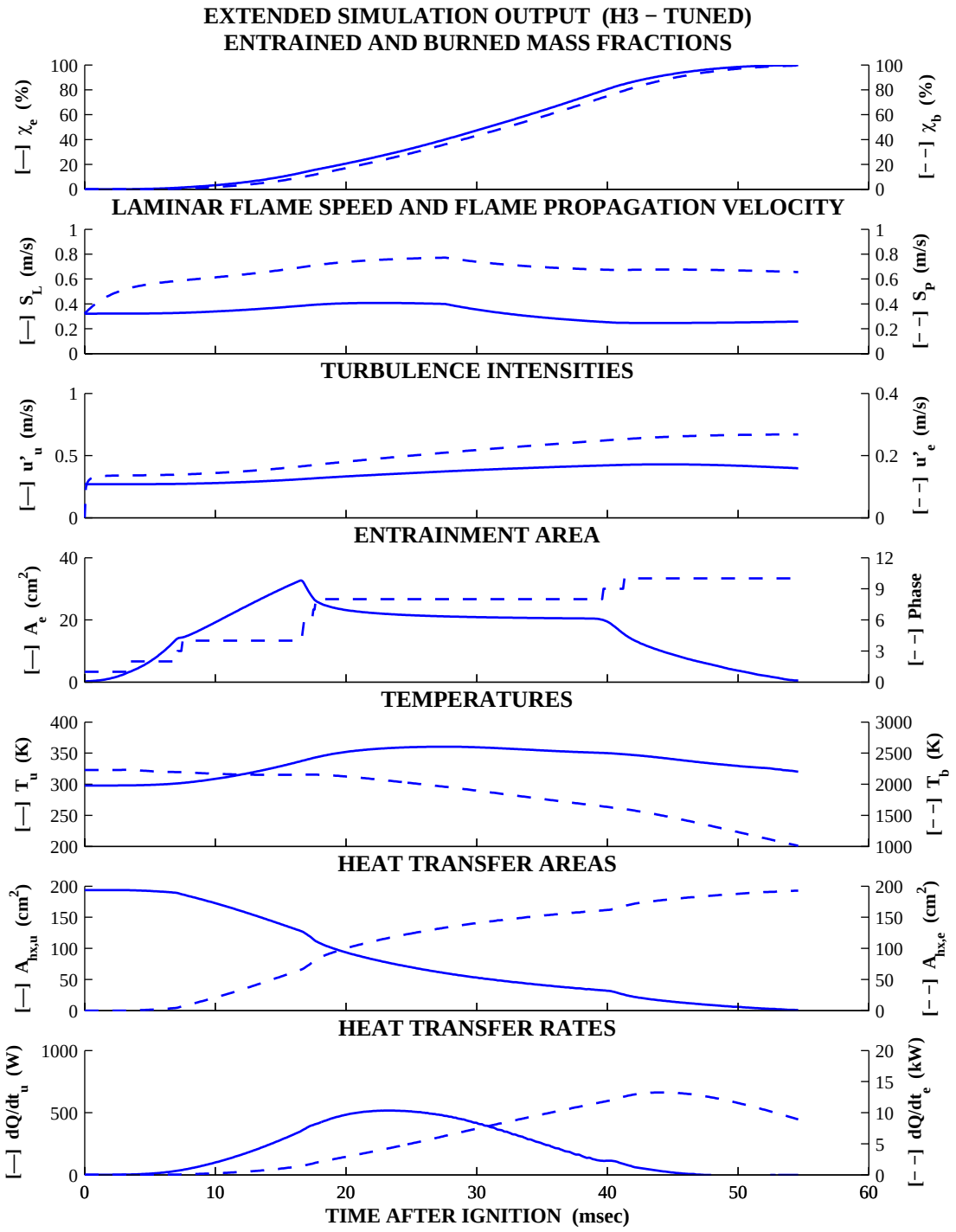

Figure 6.25: Tuned Homogeneous Simulation, Extended Output (Case H3)

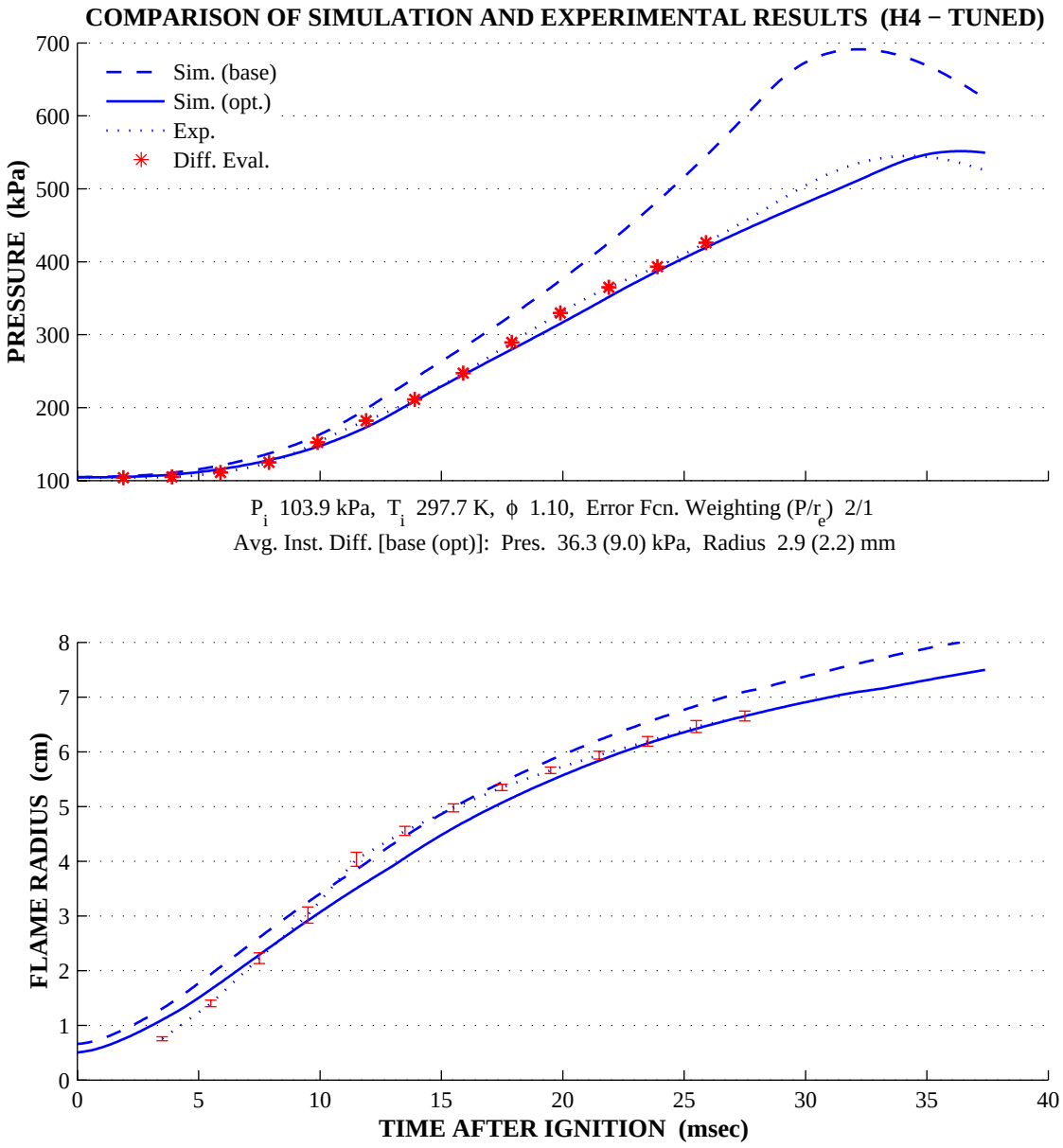

Figure 6.26: Tuned Homogeneous Simulation Results (Case H4)

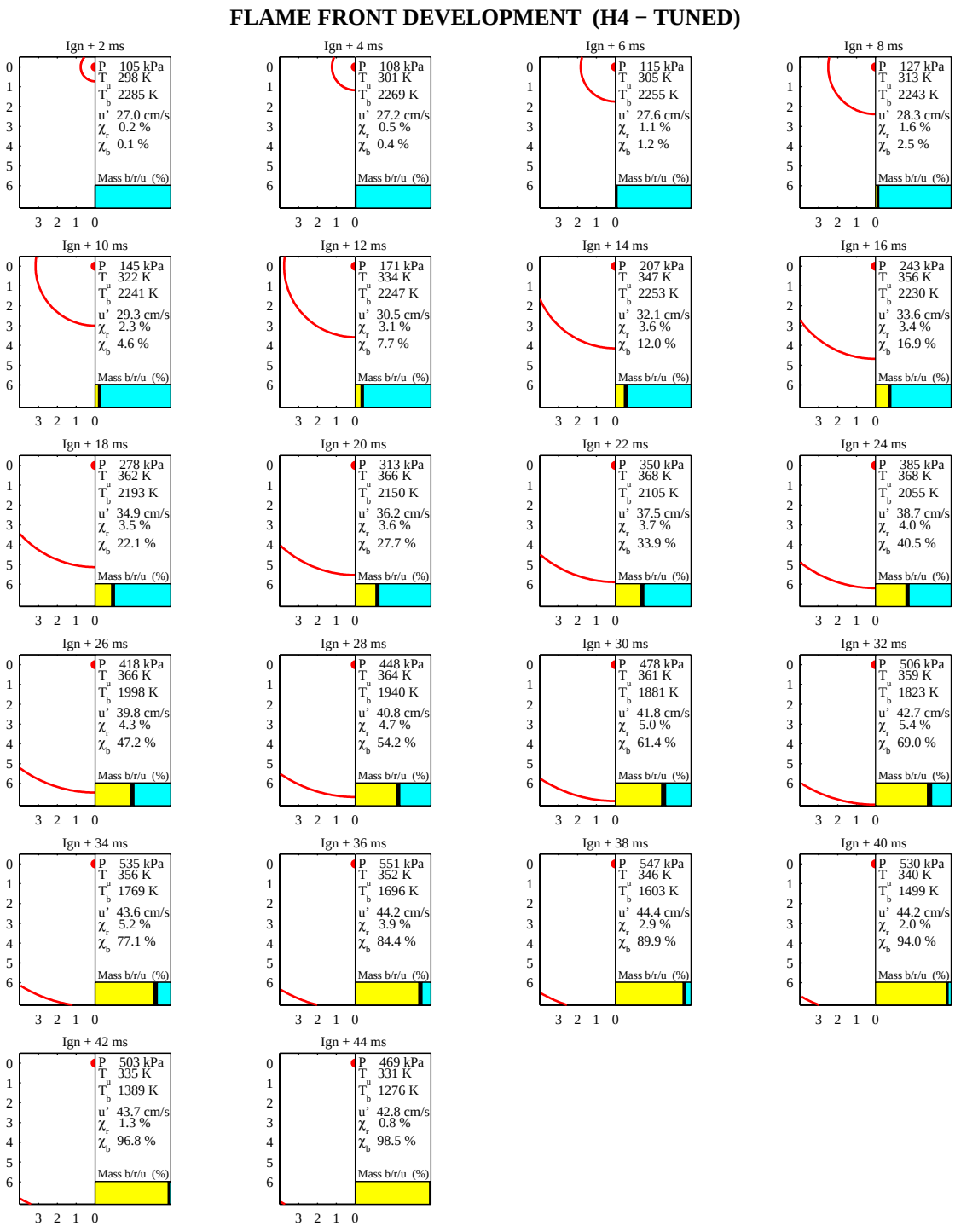

Figure 6.27: Tuned Homogeneous Simulation, Flame Development (Case H4)

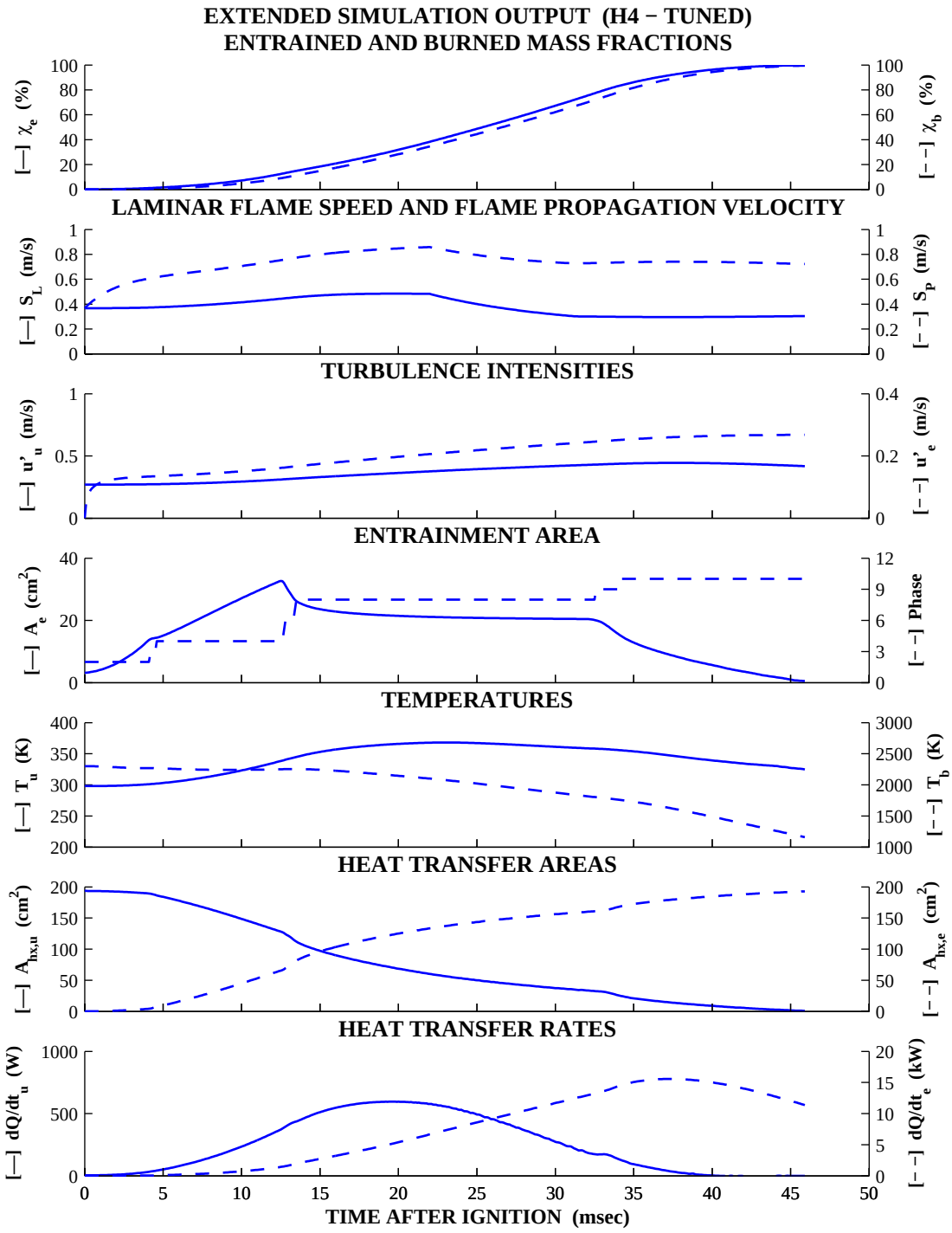

Figure 6.28: Tuned Homogeneous Simulation, Extended Output (Case H4)

The improvement after tuning is considerable. With parameter values optimized for the homogeneous matrix instead of a single case, errors in any particular case are acceptable through the entire burn. The model does not break down in any case examined and as currently developed, predicts pressure with reasonable accuracy to an indicated burned mass fraction of greater than 95 percent. There are however two periods to note where errors are most significant.

Predicted flame radius growth is consistently low in the 10 to 20 millisecond range. This is explained by the difference in this period between the simplified model and actual flame front geometries. The model assumes that mass in the clearance between the flame front and the windows and side walls, flows forward as the clearance decreases to join the bulk unburned volume. In reality, mass entrainment continues as the clearance narrows but at a different rate than along the freely expanding front. Any unaccounted for mass leads to increased growth of the entrained volume and flame radius. Changes in the radius are more accurately predicted after the entrained zone is in solid contact with the windows and side walls and the flame geometry is stable (defined as Phase 8 in Section 3.2.2.1). This explanation is supported by observed flame behavior where flattening is clearly evident at the side walls and there is an associated increase in the flame radius growth. The second period of increased error, late in the burn has already been addressed. A simple modification for terminal burning in the near-wall regime is implemented to reduce the pressure divergence.

At this point, the homogeneous model's performance is a known quantity. Stratified results can now be analyzed with this knowledge to separate behaviors resulting from model additions and modifications and those carrying through with the base homogeneous structure.

CHAPTER 7

STRATIFIED-CHARGE RESULTS

The stratified-charge model is evaluated using a method similar to that employed in the previous chapter. Output from a baseline case is examined and parameter sweeps are made to verify reasonable trends result from changes to the diffusion rate constant and degree of stratification (*DOS*). Stratified test cases from Table 5.1 are first simulated with the initial parameter values and compared against experimental data. The reverse model is then employed to obtain optimal parameter values and the improvement in model performance from the base case is evaluated.

7.1 Verification of Model Functionality

The standard case for the initial stratified model runs is defined in Table 7.1. Tuned values from the homogeneous case are included for turbulence and heat transfer scaling.

Mixture Equivalence	1.0 (Overall) 1.1 Rich / 0.9 Lean
Degree of Stratification	0.1
Initial Pressure	100 kPa (ambient)
Turbulence	0.29 m/s
H-X Scaling Constant	1.49
Time Step	0.1 msec
Diffusion Rate Constant	1.0

Table 7.1: Parameters for Base Stratified Case

The initial enflamed mass fraction is omitted since the lookup table is now available. Values obtained from the lookup are valid for a chamber at uniform equivalence and must be modified for ignition on the rich side of a stratified chamber. Rich side equivalence is used for the lookup and the returned value is scaled using the ratio of mass fractions.

$$\chi_{e,i}(\phi) = \chi_{e,i}(\phi_r) \cdot \frac{\chi_{ini,r} + \chi_{ini,l}}{2 \cdot \chi_{ini,r}} = \frac{\chi_{e,i}(\phi_r)}{2 \cdot \chi_{ini,r}} \tag{7.1}$$

Results for the initial simulation run are presented in the following two figures. Primary variables of pressure and flame radius are again provided in detail [Figure 7.1]. A subset of additional tracked variables is shown in Figure 7.2.

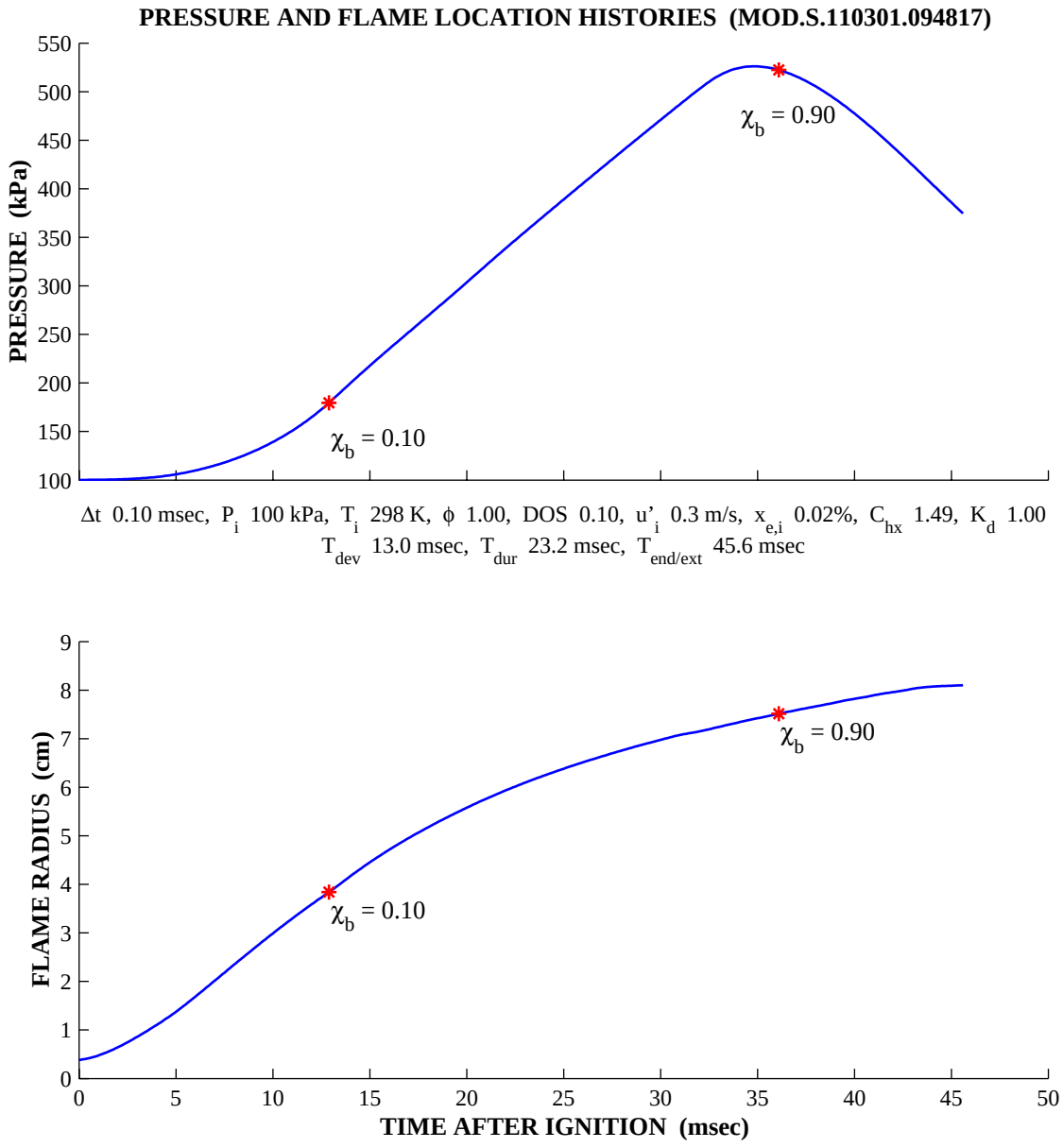

Figure 7.1: Baseline Stratified Case – Time Histories of Primary Variables

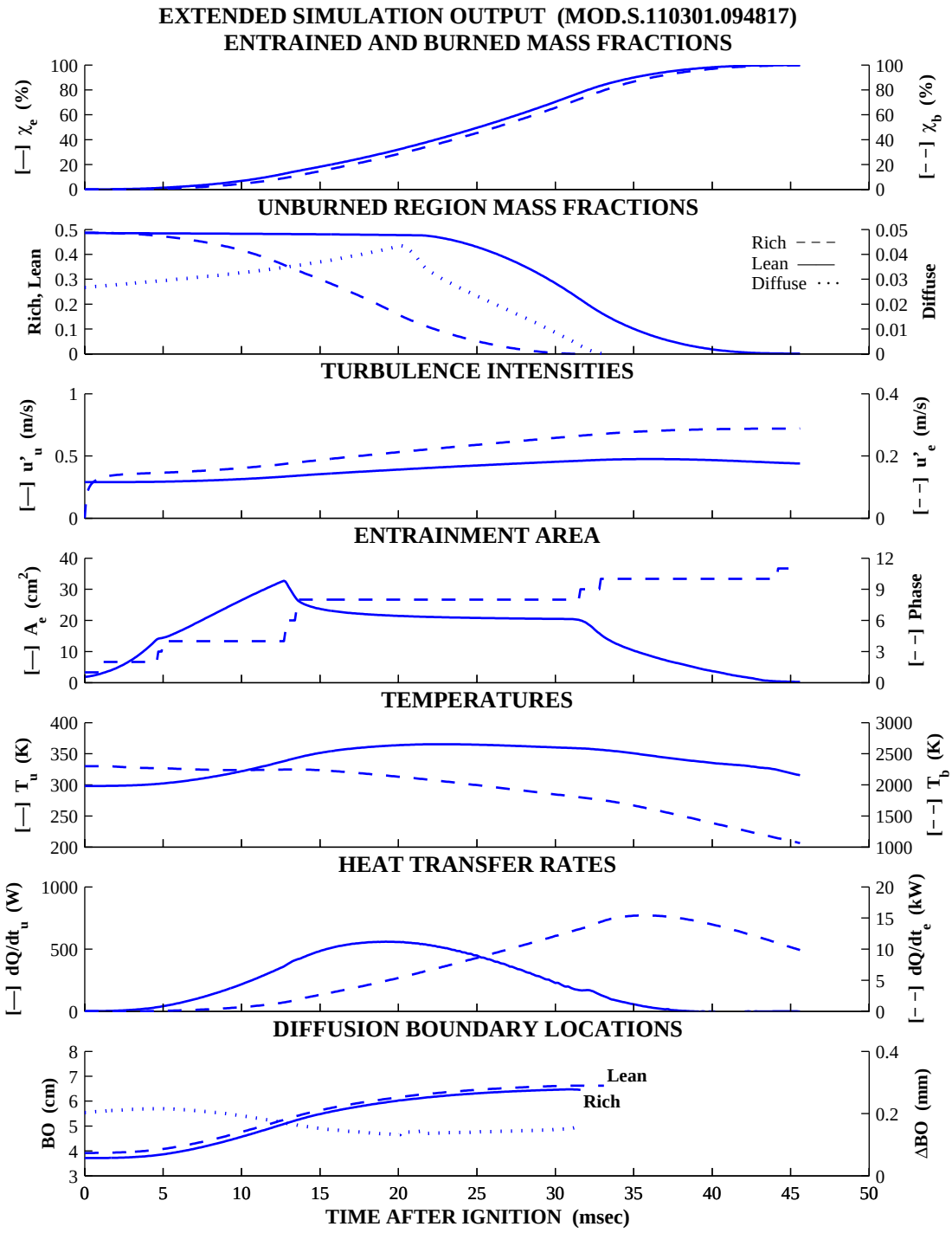

Δt 0.10 msec, P_i 100 kPa, T_i 298 K, ϕ 1.00, DOS 0.10, u'_i 0.3 m/s, $x_{e,i}$ 0.02%, C_{hx} 1.49, K_d 1.00
T_{dev} 13.0 msec, T_{dur} 23.2 msec, $T_{end/ext}$ 45.6 msec

Figure 7.2: Baseline Stratified Case – Time Histories of Additional Variables

The baseline result is similar to the homogeneous case in common tracked variables and behavior of region mass fractions and diffusion boundary displacements seems reasonable. The diffuse region thickness (measured normal to the diffusion boundaries) is nearly constant beyond the 15 millisecond marker. This can be explained during the period of net region mass loss by noting that the region thickness is a function of several processes. Mass is entrained from the diffuse region while diffusion (mass inflow) continues from the lean and possibly rich regions. Compression of the entire unburned zone is taking place continually and the net result in this base is apparently a stagnation of the distance between the diffuse boundaries.

7.1.1 Fundamental Consistency Test

Adherence to the conservative energy constraint is examined for the baseline run in Figure 7.3. The error is acceptable as in the homogeneous case. Volume error is also checked and found to be negligible (much less than one percent).

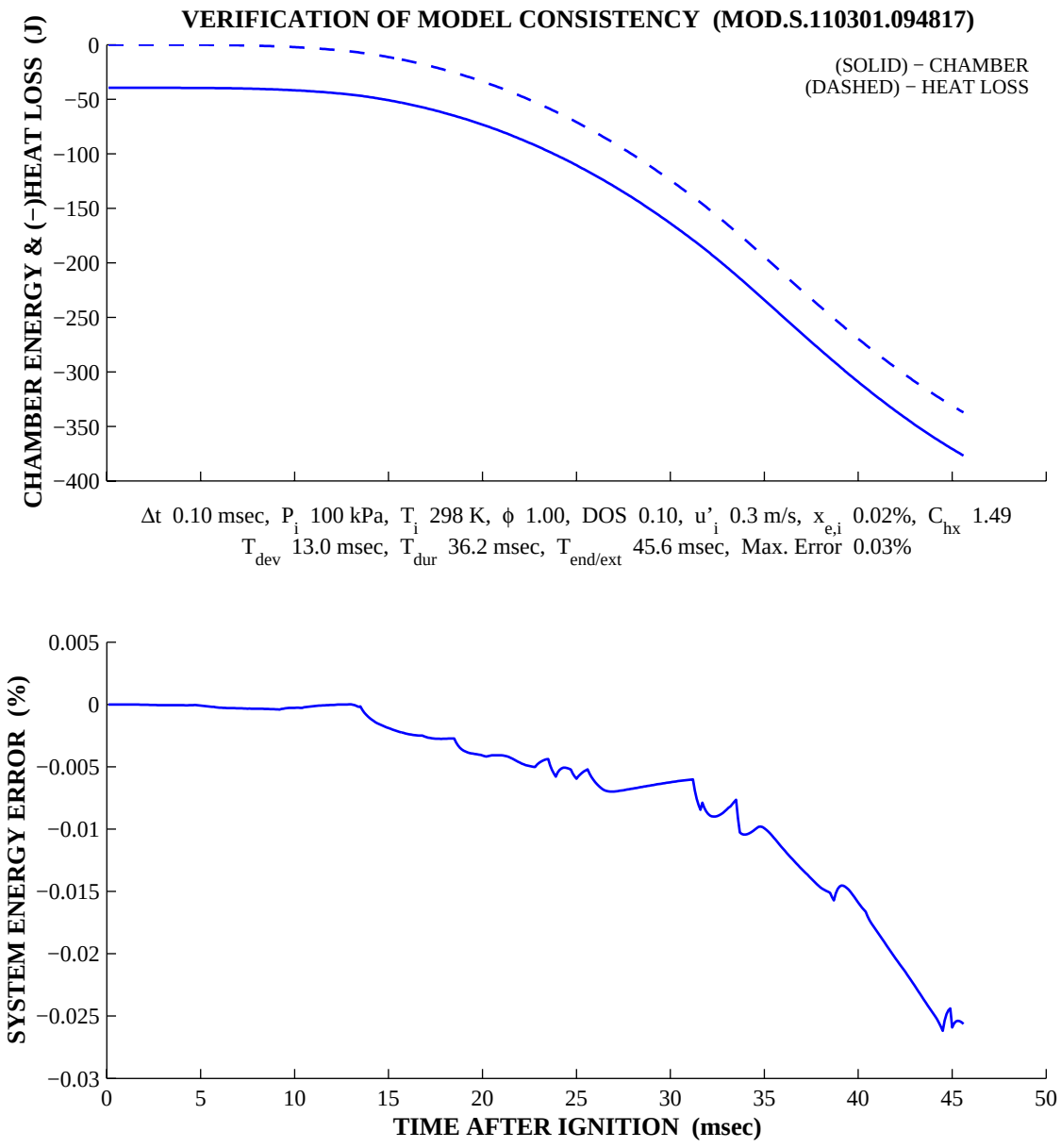

Figure 7.3: Deviation from Initial Internal Energy Through Burn Period

7.1.2 Homogeneous Equivalent Case Comparison

Parameters for the baseline homogeneous case [Table 6.1] are used with a *DOS* of zero for a second stratified case. The result is an identical equivalence in both initial mixture regions for a chamber that should burn as did the homogeneous case. Pressure and flame radius for both runs are compared in Figure 7.4 along with several key times. The close match indicates geometry approximations and other additions to the base homogeneous model function properly.

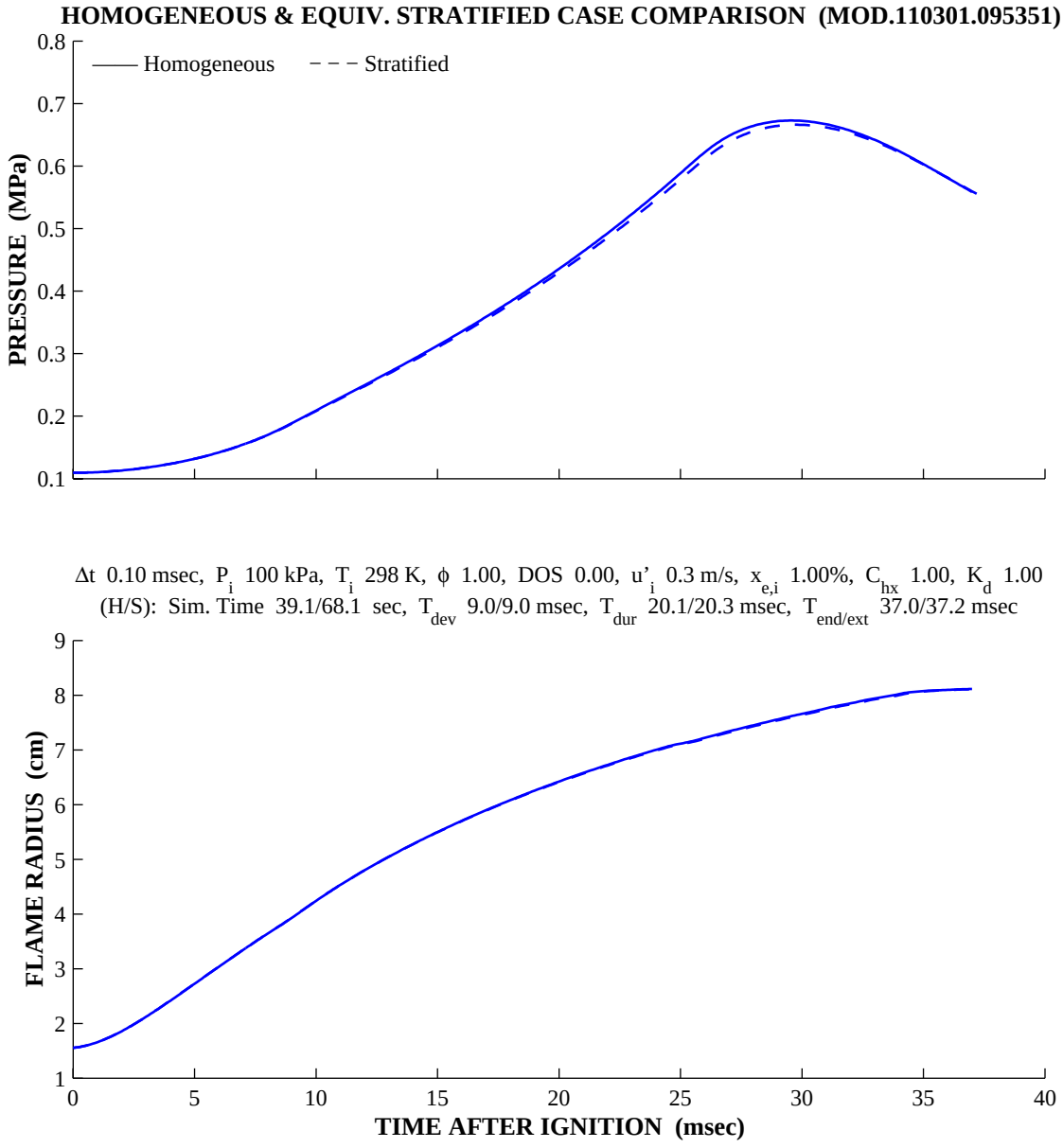

Figure 7.4: Comparison of Baseline Homogeneous and Stratified Cases (*DOS*=0.0)

7.1.3 Equivalence Tracking Test

The final test of basic functionality uses time-varying equivalence in the diffuse region and reaction and burned zones as a means to verify proper accounting for mass by the split-mass tracking method. Expected changes in equivalences may be predicted from the model definitions in Chapter 4. Diffuse region and overall equivalences are equal until the flame crosses the rich diffusion boundary. After this time the equivalence decreases with the ratio of rich and lean diffusion areas. With a low *DOS*, equivalence will continue to drop at an increasing rate until the diffuse region is consumed (entrained). Reaction zone and rich side equivalences are initially equal since ignition takes place in the rich mixture. The value begins to fall after the flame crosses the rich diffusion boundary and entrains mixture from both the rich and diffuse regions. The rate of decrease becomes more steep after the flame crosses the lean boundary and finally approaches the lean side equivalence. Burned zone equivalence is initially equal to the reaction zone value. The final value must be equal to the overall equivalence if masses are conserved and one hundred percent of the mass is burned.

The three equivalences of the baseline case are shown in Figure 7.5. All of the predicted behaviors are observed and no problems are noted.

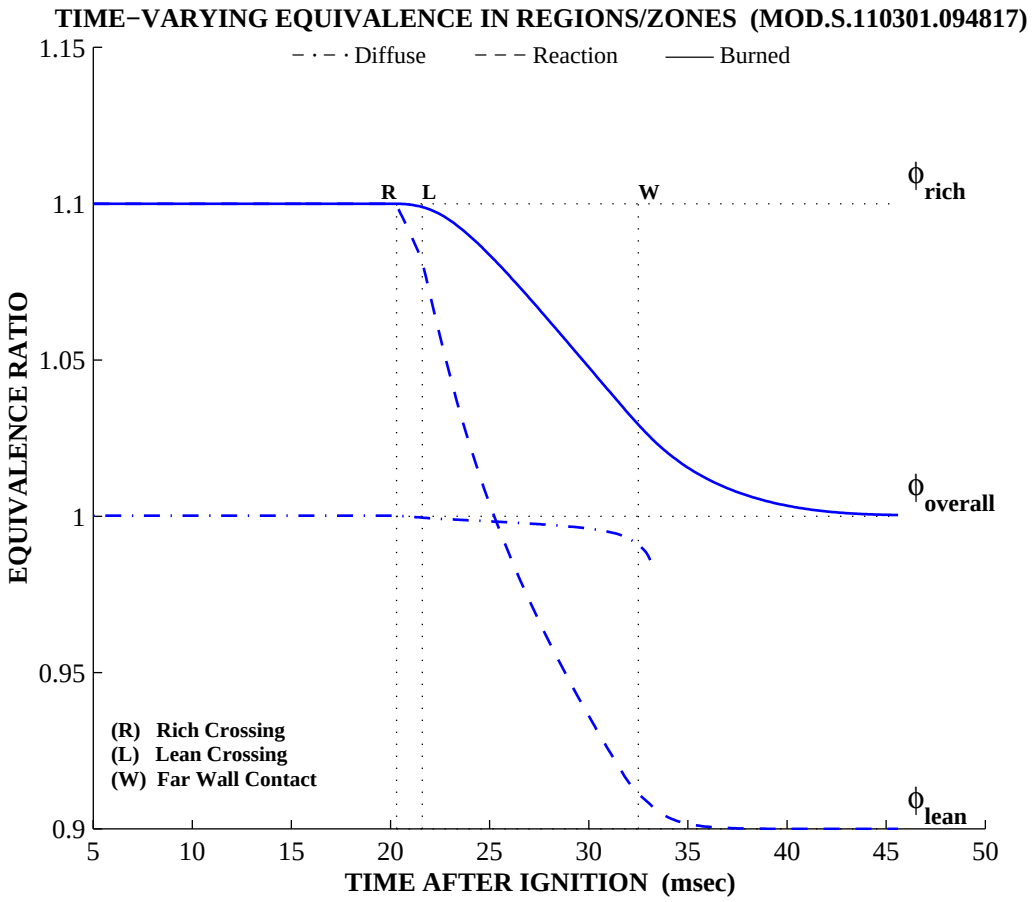

Figure 7.5: Time-Varying Equivalence Through Pre-Burn & Burn Periods

7.1.4 Parameter Sweeps & Sensitivity Analysis

Two sweeps are made to examine the effect of the degree of stratification and diffusion rate constant. Early flame development time and burn duration are again compiled as each parameter is varied. A slightly lean overall equivalence is defined for the base case [Table 7.2] to allow a larger range of *DO*S values while not exceeding the maximum rich side equivalence. The rich and lean base equivalences as specified are 1.08 and 0.72 respectively.

Mixture Equivalence	0.9
Degree of Stratification	0.2
Initial Pressure	100 kPa (ambient)
Initial Enflamed Mass	1.0 % of total chamber mass
Turbulence	0.29 m/s
H-X Scaling Constant	1.49
Diffusion Rate Constant	1.0

Table 7.2: Base Case Values for Parameter Sweeps

DOS is swept from 0.0 (homogeneous charge) to 0.4 [Figure 7.6]. The minimum flame development time occurs at a rich-side equivalence equal to the value at the minimum time of the homogeneous equivalence sweep [Figure 6.5].

Burn duration increases drastically at higher *DOS* values as the lean-side equivalence nears the lean limit for combustion. The last two runs are too lean in the lean-side and fail to reach the 90 percent burned mass fraction mark.

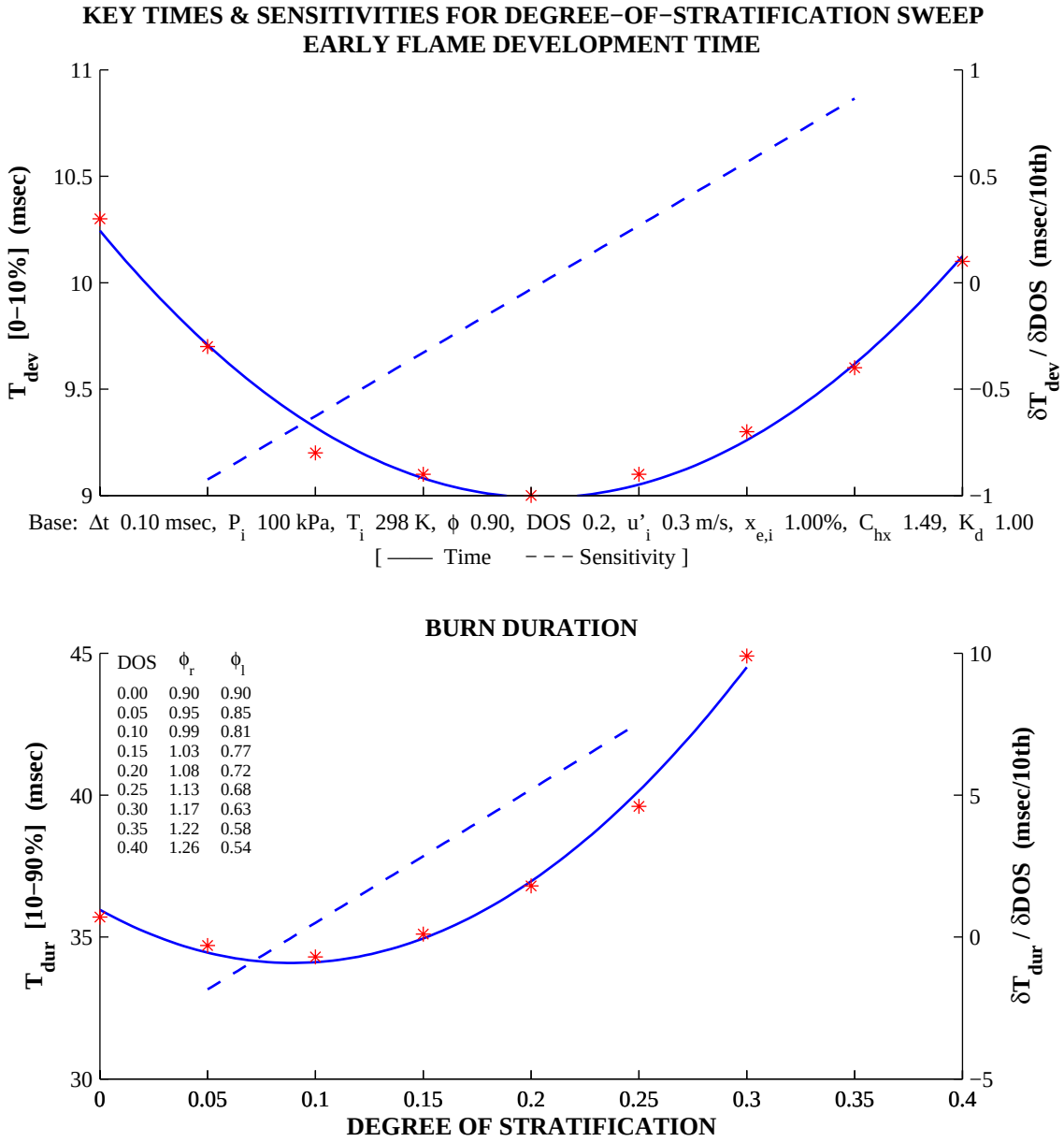

Figure 7.6: Parameter Sweep – Degree of Stratification (*DOS*)

The diffusion rate constant is swept from 0.3 to 2.0 [Figure 7.7]. Development time is unaffected since it depends only on the rich region equivalence. Burn durations are relatively flat for this particular combination of equivalence and *DOS*.

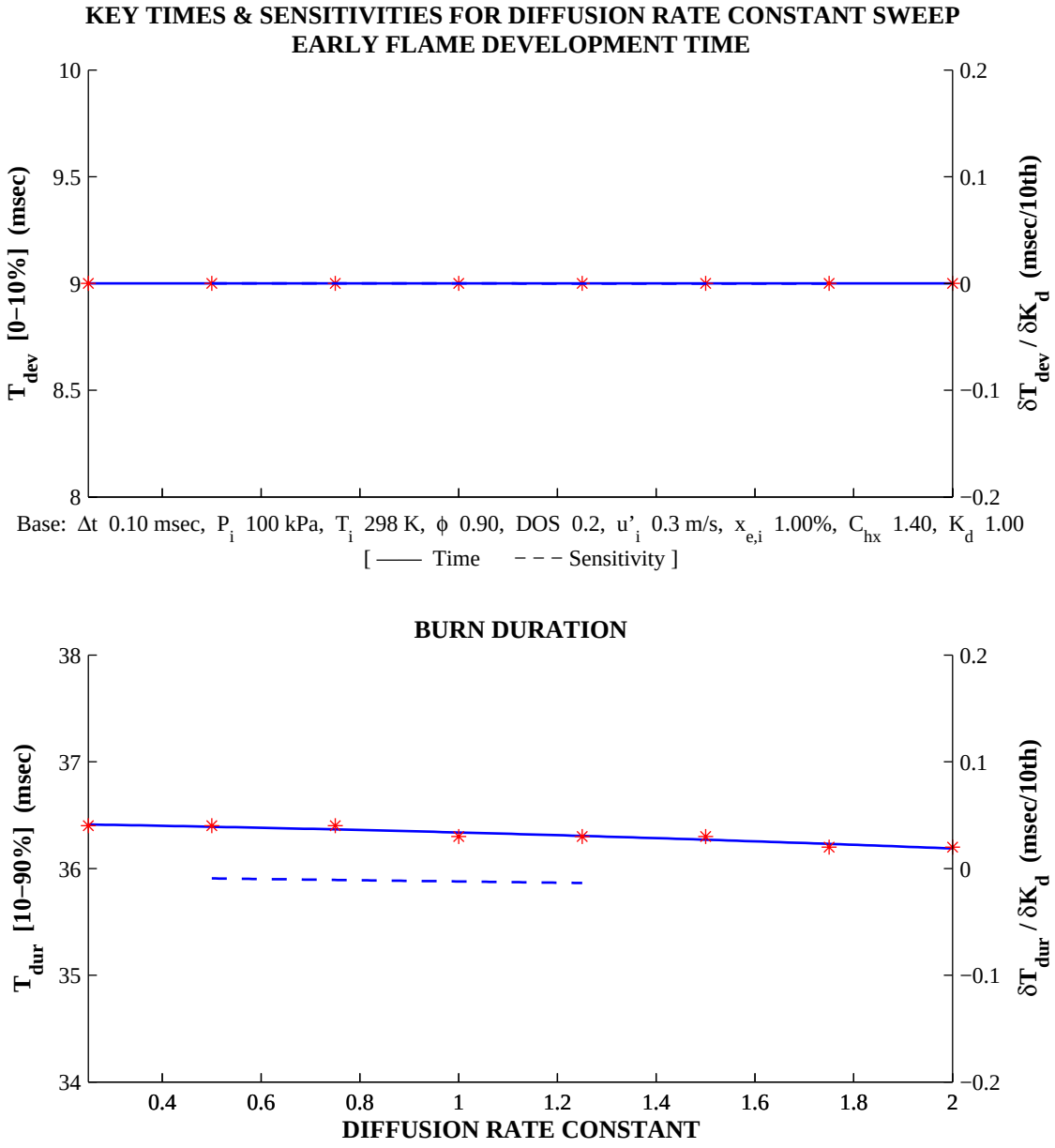

Figure 7.7: Parameter Sweep – Diffusion Rate Constant (K_d)

The diffusion rate constant does not significantly affect the characteristic times in the initial sweep. An increased rate of growth of the diffuse region is predicted as the constant is increased. The characteristic times do not give a clear indication of the change in diffuse region growth and any impact late in the burn. The greatest impact should be in cases where overall equivalence and *DOS* lead to diffuse region equivalences that approach the lean limit. In these fringe cases, diffusion is one factor that determines how much mass burns before conditions no longer support flame propagation. Ultimate progress of the flame is a function of the entrainment rates from each of the three unburned regions and the associated local flame speeds [Section 4.3.4.8].

A new case is defined with overall equivalence 0.9 and *DOS* 0.4 for an overly rich rich-side (1.26) and incombustible lean-side (0.54) equivalence. Other parameters are unchanged from the base case [Table 7.1]. Simulation runs are made with four diffusion rate constants. Histories for pressure, flame radius and diffuse region equivalence are extracted for the period after the pressure traces diverge [Figure 7.8]. Boundary crossing times are also marked to separate periods of rich, rich-diffuse and rich-diffuse-lean entrainment.

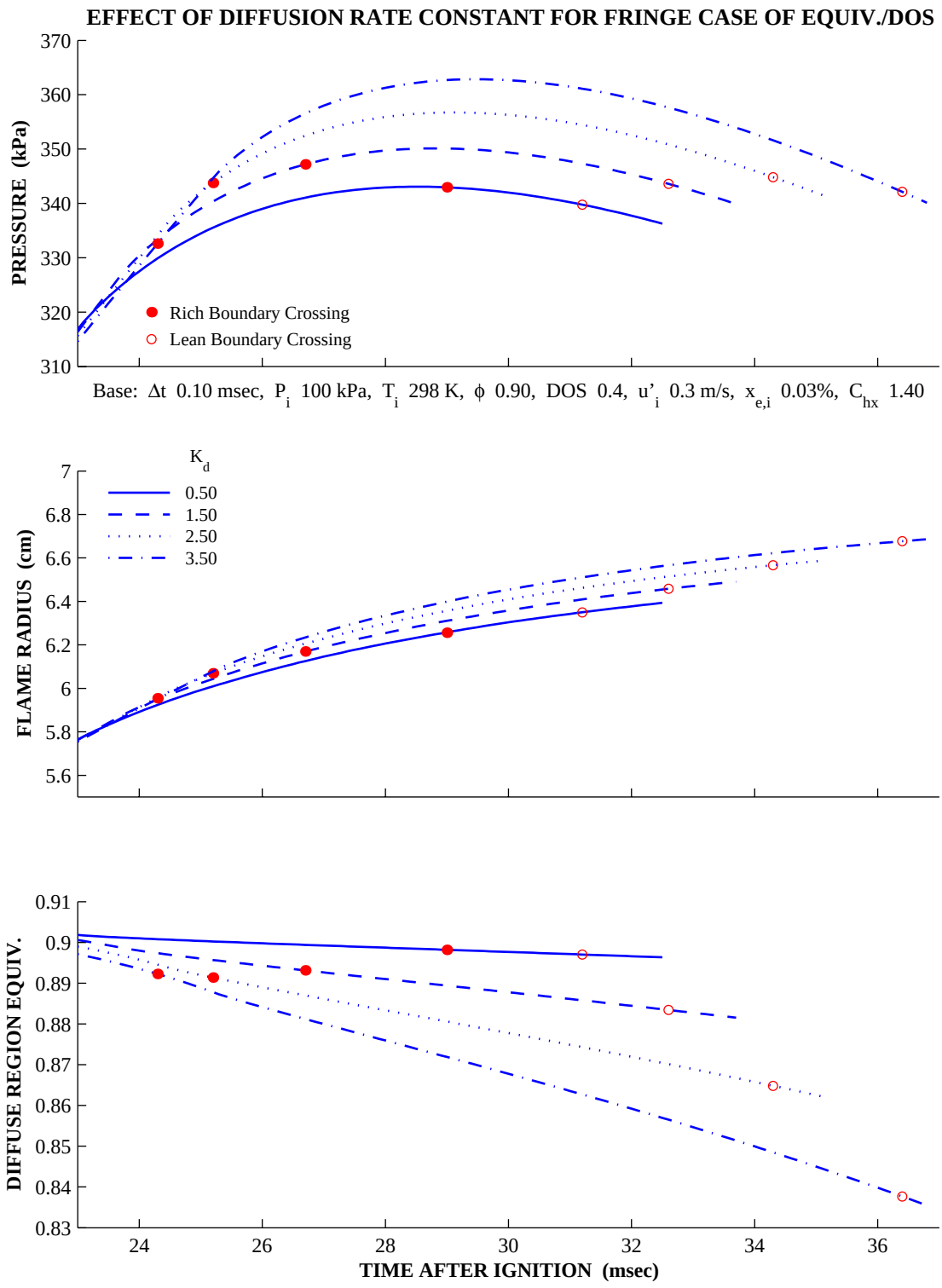

Figure 7.8: Impact of Diffusion Rate Constant in Special Case

The impact of increased diffusion is clear in these four cases. In no case does the chamber mass burn completely but as diffusion is increased, the flame's progress moves in locked step. Diffuse equivalences remain combustible and the flame stalls after the lean boundary crossing, when the entrained mixture is no longer combustible (at the current pressure and temperature). Increased growth (thickness) of the diffuse region is responsible for the delayed extinction as additional incombustible lean mixture is diffused into the combustible diffuse region and burned.

7.2 Baseline Simulation Results

Each stratified test case of Table 5.1 is simulated and the output compared against reduced experimental data. An initial diffusion rate constant of 2.0 is specified for the baseline simulation runs. Tuned parameters from the homogeneous tuning are used for initial turbulence and the heat transfer scaling constant. The experimentally derived function for initial enflamed mass fraction is also used [Section 6.3.1].

Average instantaneous errors are compiled and tabulated [Table 7.3] using the definitions from the homogeneous analysis [Section 6.2].

Case	Average Instantaneous Difference	
	Pressure (kPa)	Flame Radius (mm)
S1	4.60	2.30
S3	5.67	2.63
S4	4.21	2.54
S5	6.30	2.62
S6	8.18	2.74
S7	9.85	2.70
S8	7.18	1.80

Table 7.3: Comparison of Stratified Simulation and Experimental Results

Simulation and experimental results are also compared graphically for each case [Figure 7.9 through Figure 7.29]. The output format of the homogeneous analysis is continued with the addition of several parameters to the set of displayed parameters.

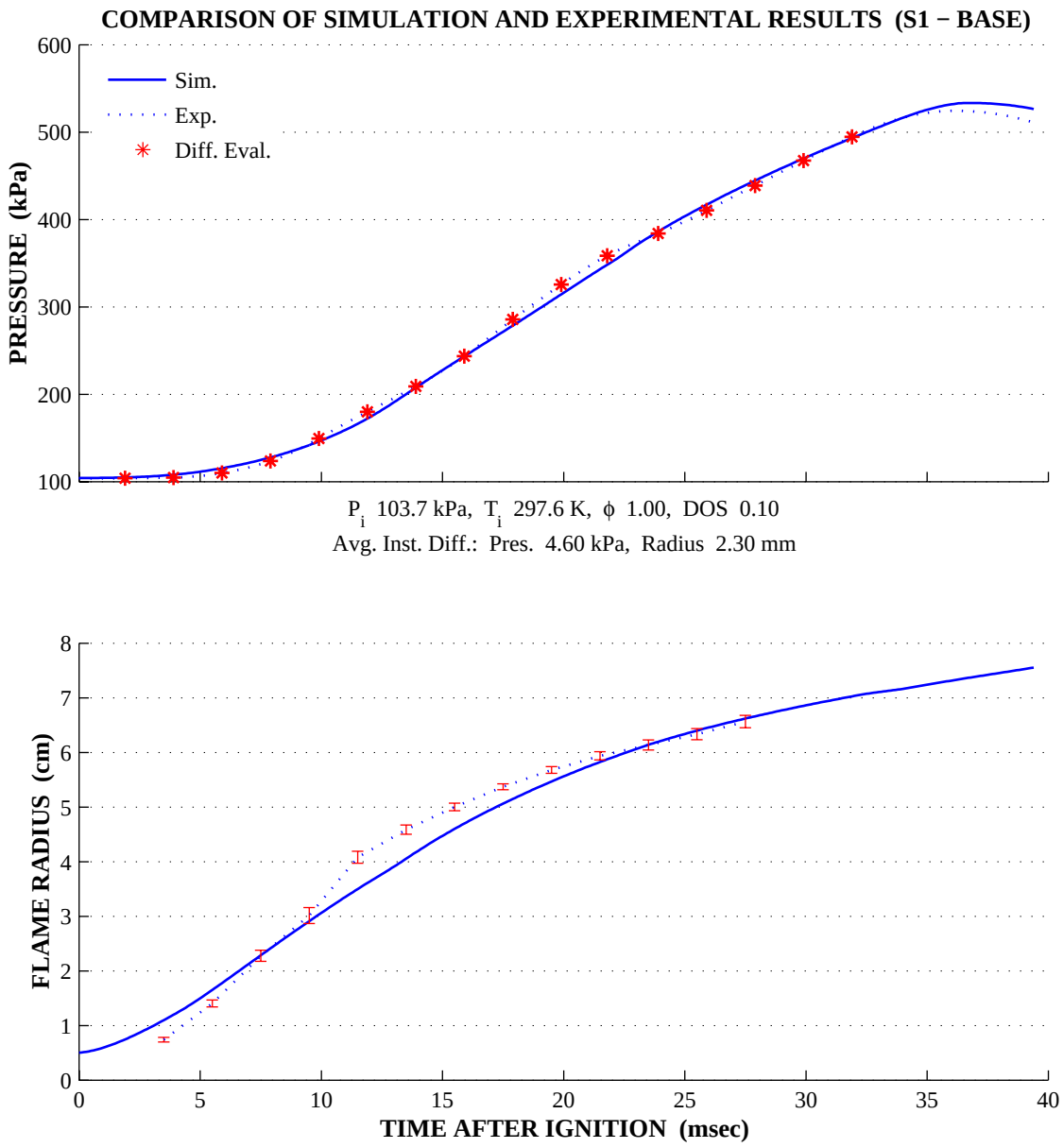

Figure 7.9: Base Stratified Simulation Results (Case S1)

FLAME FRONT AND DIFFUSE REGION DEVELOPMENT (S1 − BASE)

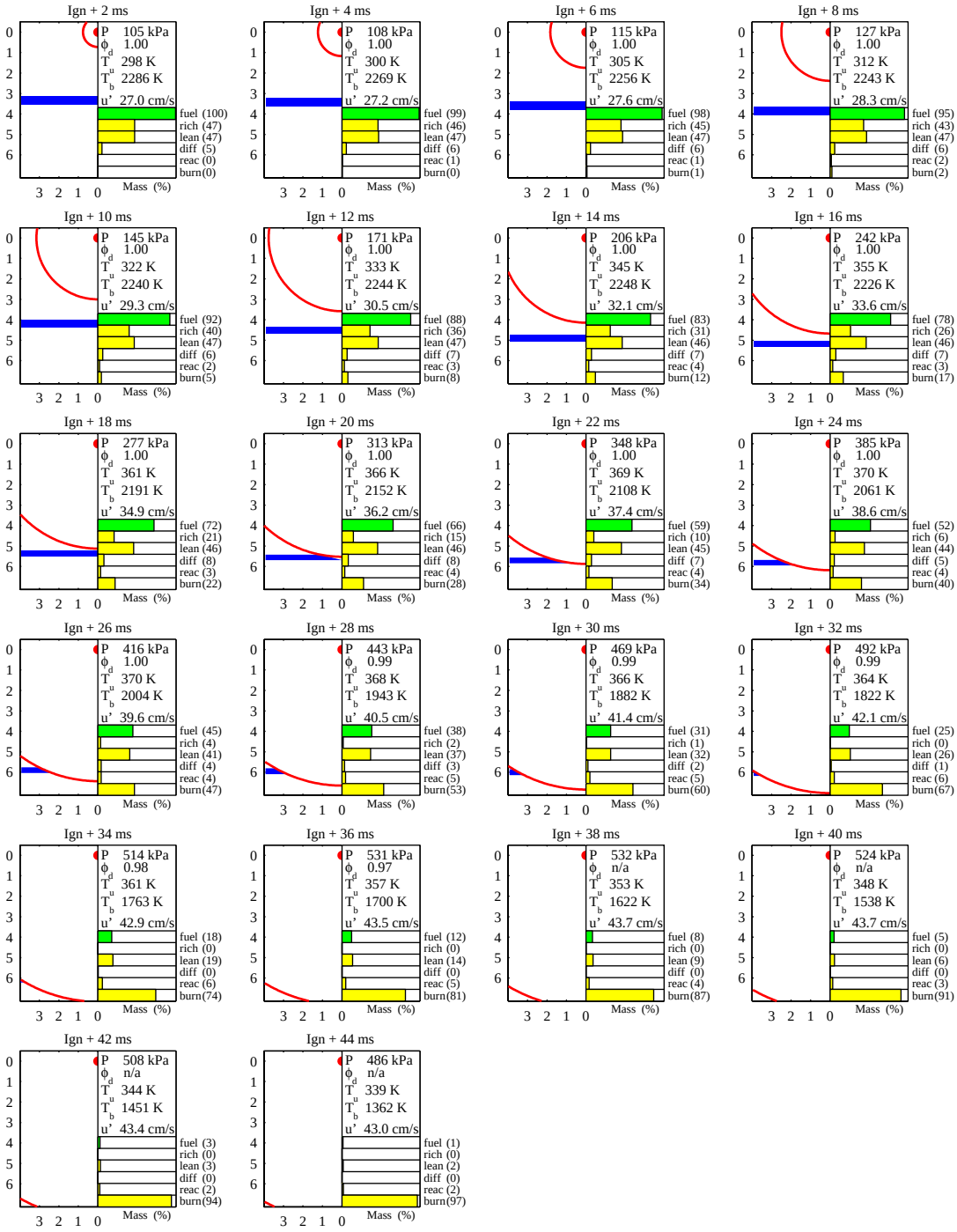

Δt 0.10 msec, P_i 104 kPa, T_i 298 K, ϕ 1.00, DOS 0.10, u'_i 0.27 m/s, $x_{e,i}$ 0.046%, C_{hx} 1.54, K_d 2.00
T_{dev} 12.9 msec, T_{dur} 26.4 msec, $T_{end/ext}$ 45.9 msec

Figure 7.10: Base Stratified Simulation, Flame Development (Case S1)

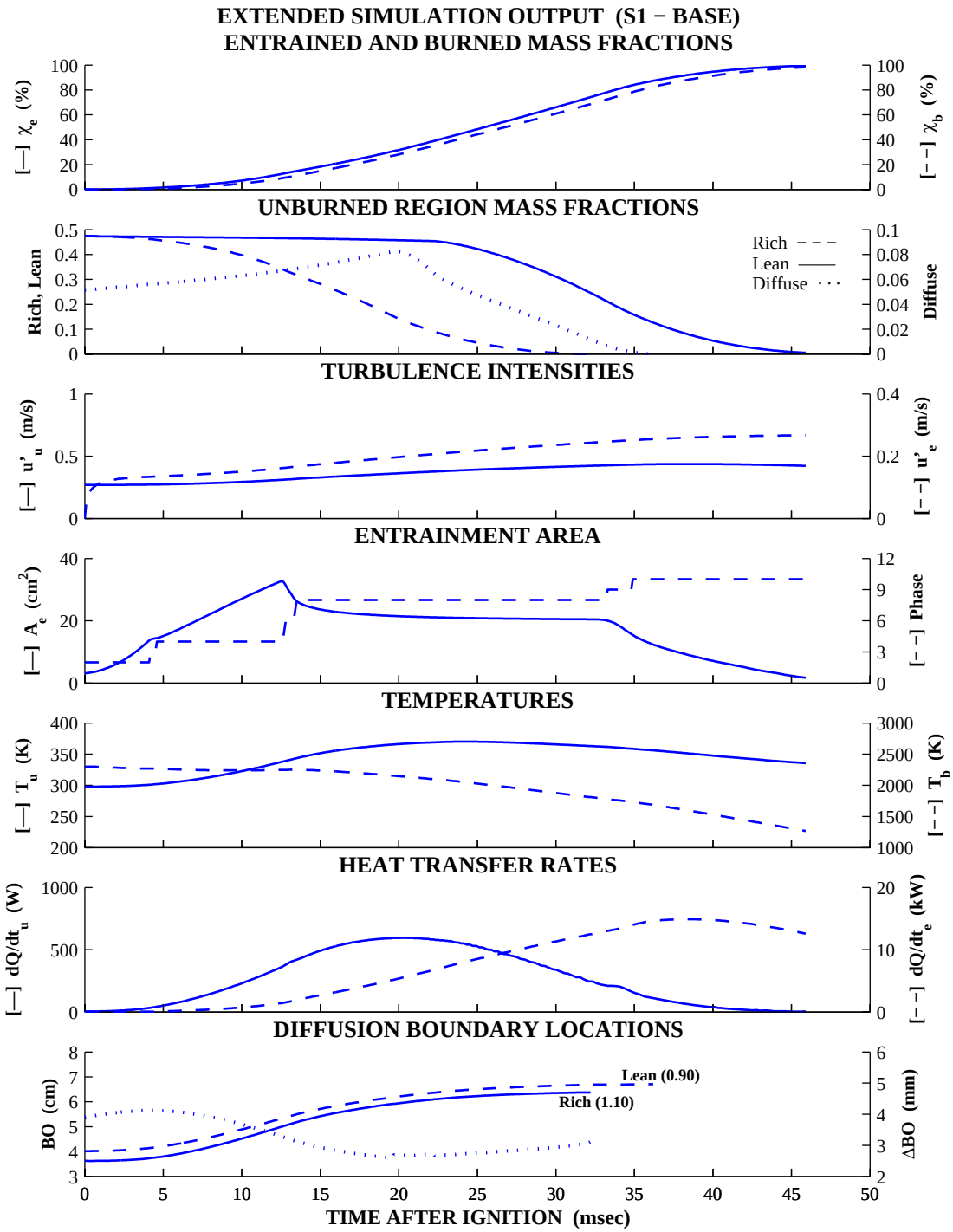

Δt 0.10 msec, P_i 104 kPa, T_i 298 K, ϕ 1.00, DOS 0.10, u'_i 0.27 m/s, $x_{e,i}$ 0.046%, C_{hx} 1.54, K_d 2.00
T_{dev} 12.9 msec, T_{dur} 26.4 msec, $T_{end/ext}$ 45.9 msec

Figure 7.11: Base Stratified Simulation, Extended Output (Case S1)

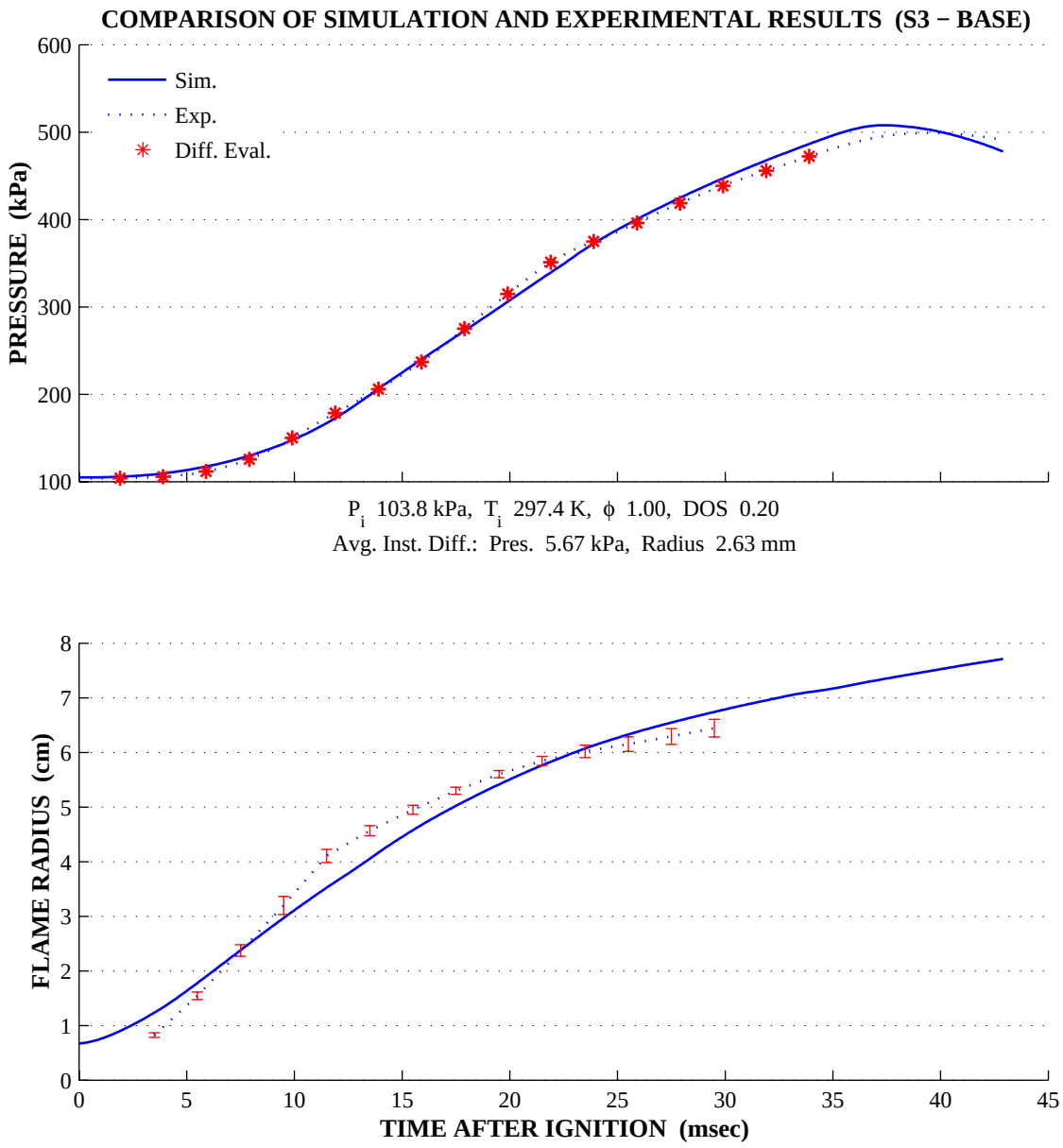

Figure 7.12: Base Stratified Simulation Results (Case S3)

FLAME FRONT AND DIFFUSE REGION DEVELOPMENT (S3 − BASE)

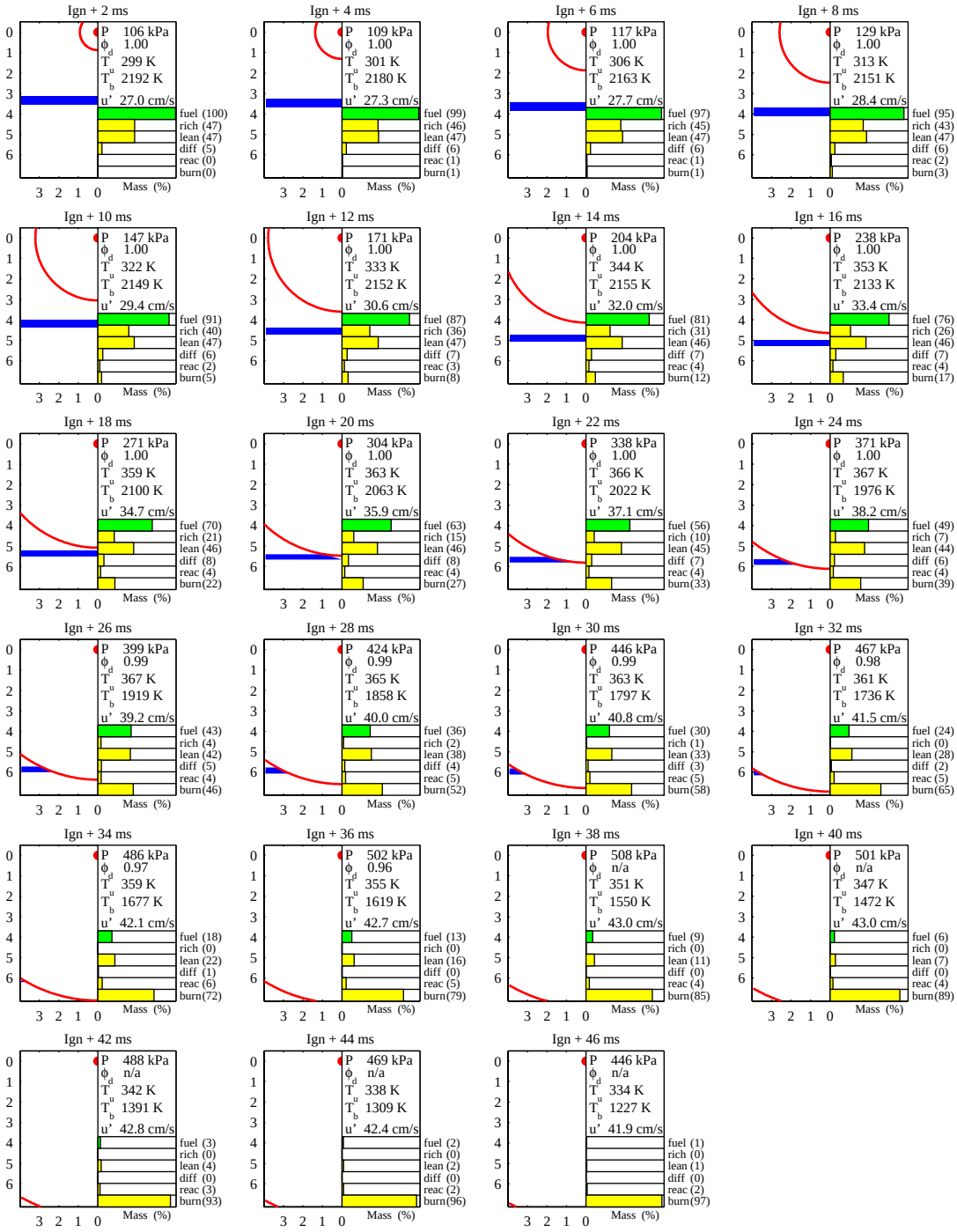

Δt 0.10 msec, P_i 104 kPa, T_i 297 K, ϕ 1.00, DOS 0.20, u'_i 0.27 m/s, $x_{e,i}$ 0.107%, C_{hx} 1.54, K_d 2.00

T_{dev} 12.8 msec, T_{dur} 27.3 msec, $T_{end/ext}$ 46.9 msec

Figure 7.13: Base Stratified Simulation, Flame Development (Case S3)

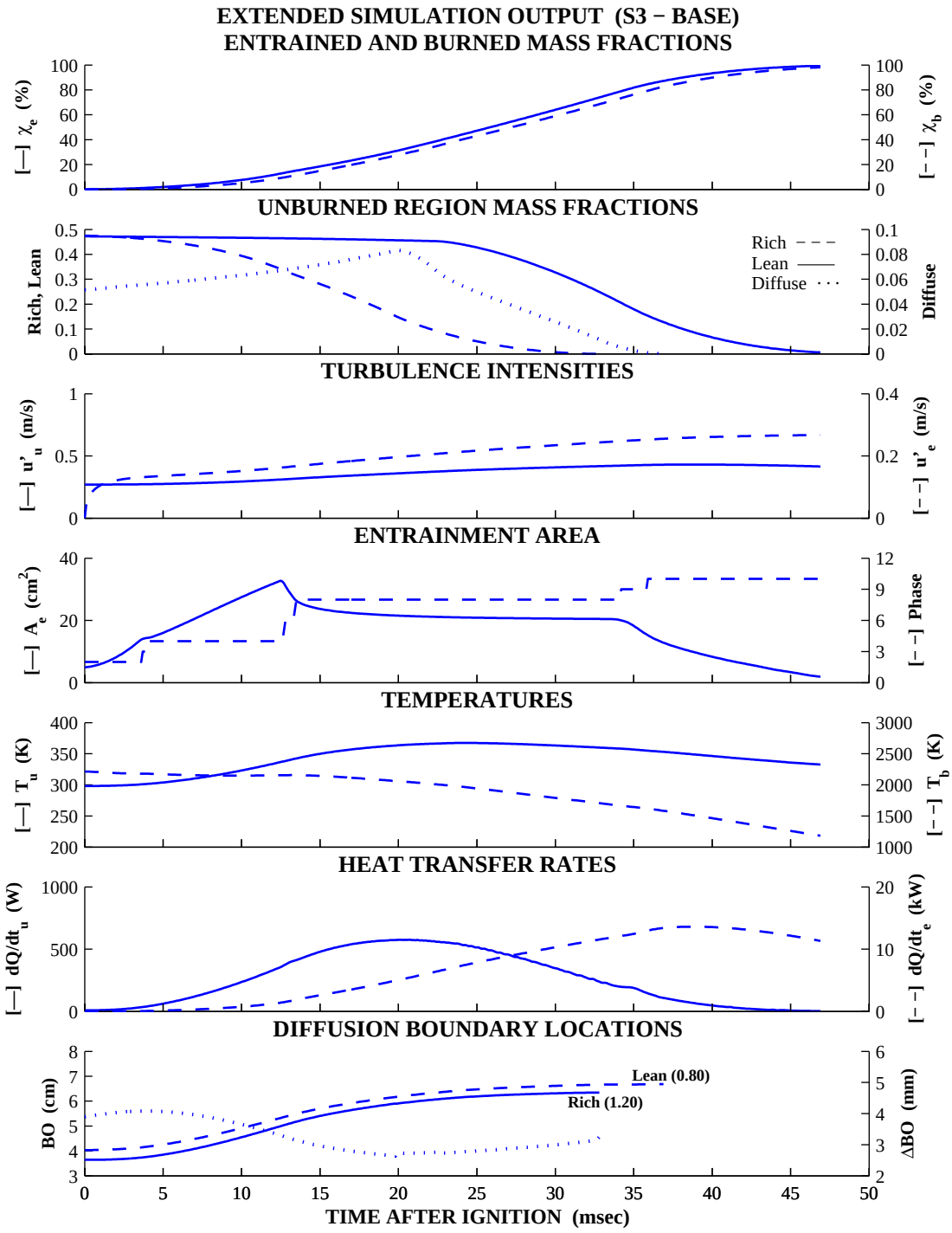

Δt 0.10 msec, P_i 104 kPa, T_i 297 K, ϕ 1.00, DOS 0.20, u'_i 0.27 m/s, $x_{e,i}$ 0.107%, C_{hx} 1.54, K_d 2.00
T_{dev} 12.8 msec, T_{dur} 27.3 msec, $T_{end/ext}$ 46.9 msec

Figure 7.14: Base Stratified Simulation, Extended Output (Case S3)

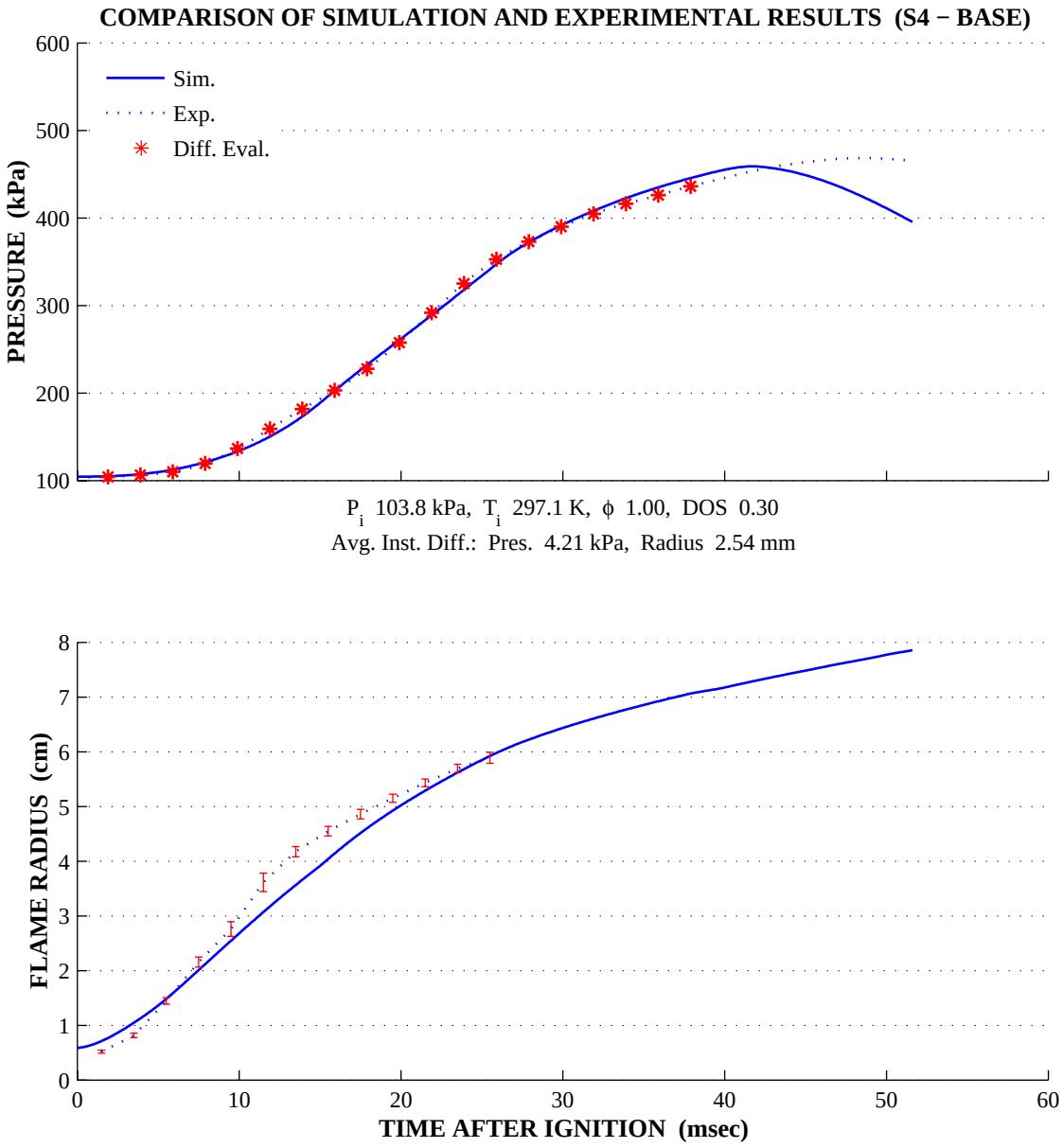

Figure 7.15: Base Stratified Simulation Results (Case S4)

FLAME FRONT AND DIFFUSE REGION DEVELOPMENT (S4 − BASE)

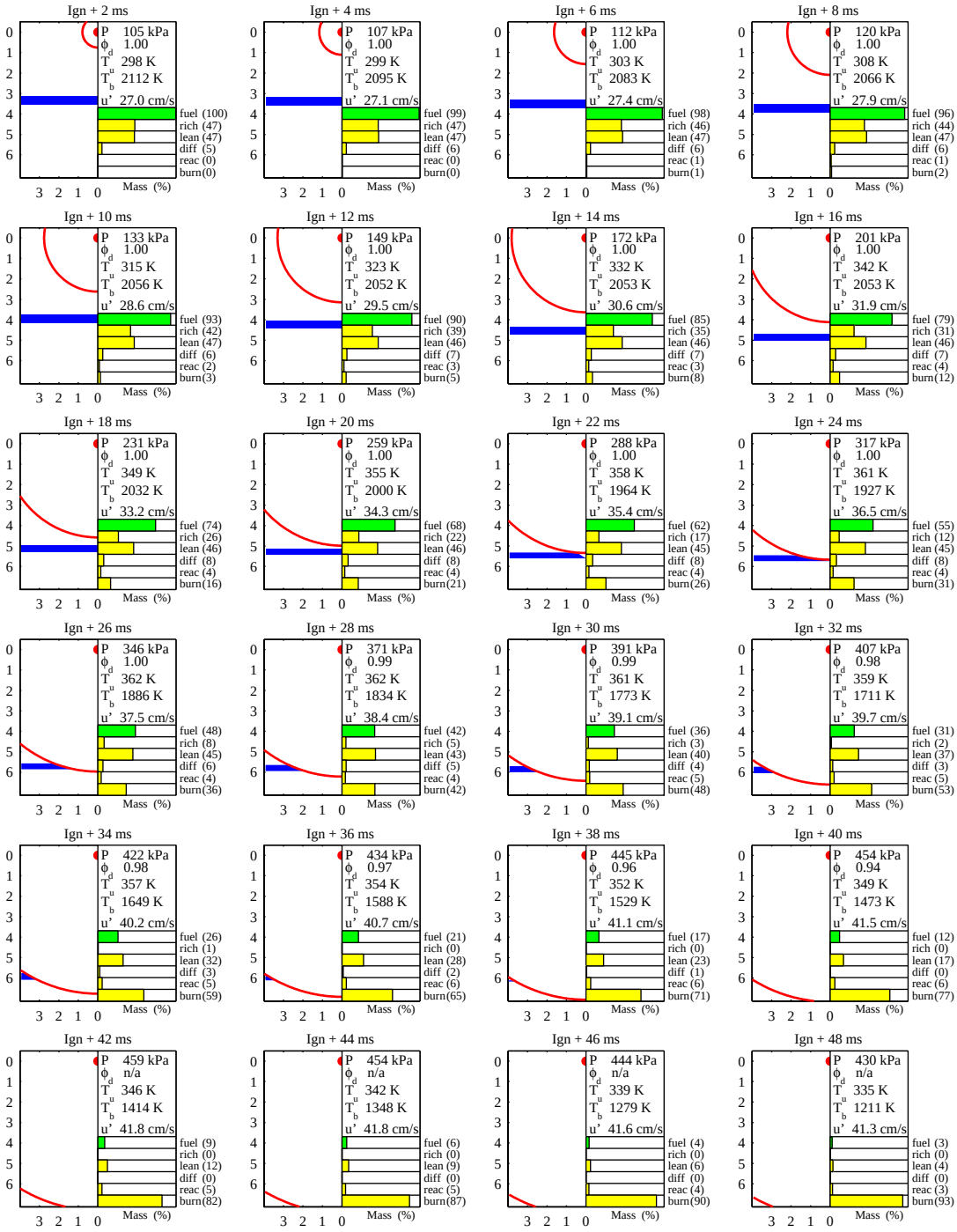

Δt 0.10 msec, P_i 104 kPa, T_i 297 K, ϕ 1.00, DOS 0.30, u'_i 0.27 m/s, $x_{e,i}$ 0.075%, C_{hx} 1.54, K_d 2.00

T_{dev} 14.7 msec, T_{dur} 31.0 msec, $T_{end/ext}$ 52.9 msec

Figure 7.16: Base Stratified Simulation, Flame Development (Case S4)

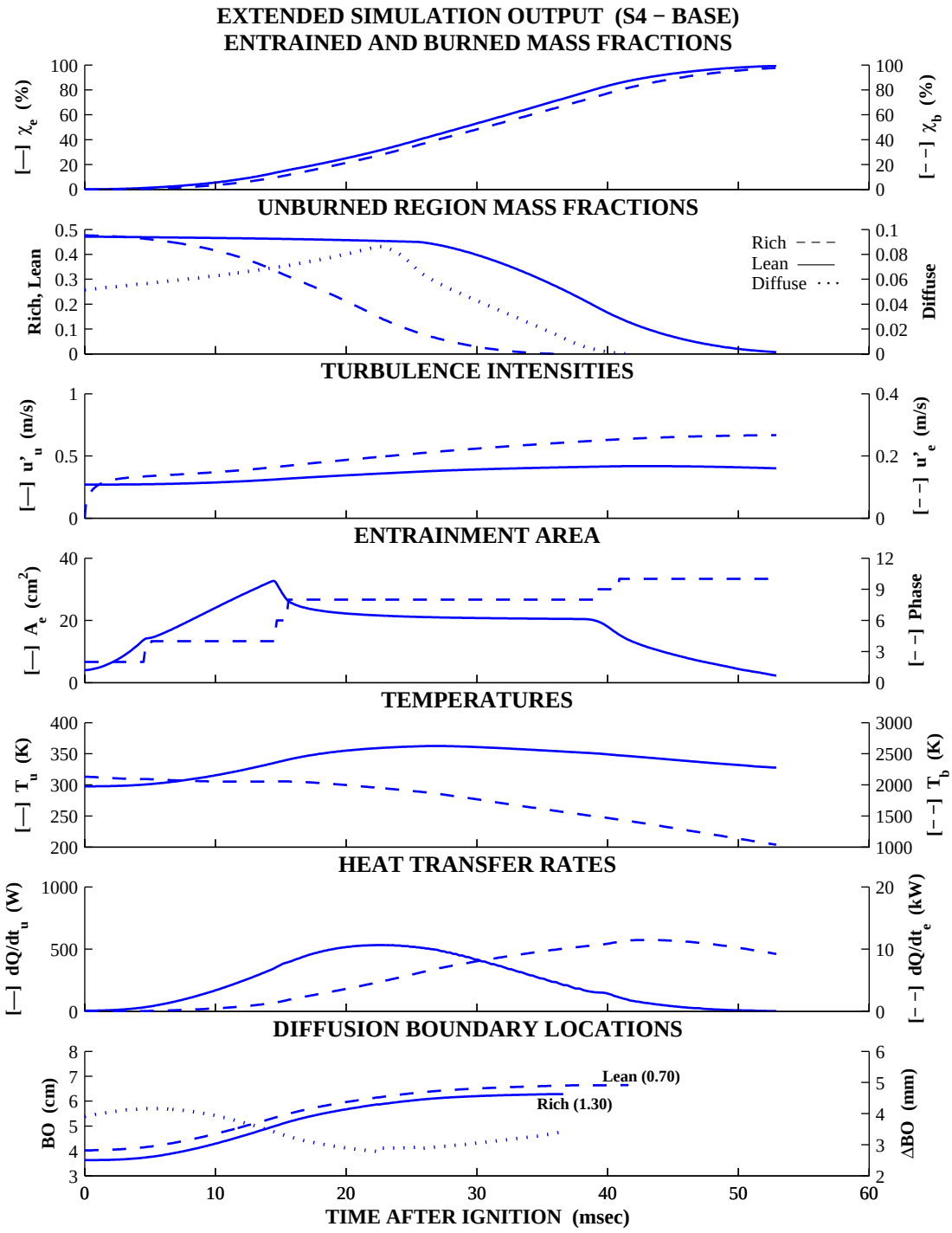

Δt 0.10 msec, P_i 104 kPa, T_i 297 K, ϕ 1.00, DOS 0.30, u'_i 0.27 m/s, $x_{e,i}$ 0.075%, C_{hx} 1.54, K_d 2.00
T_{dev} 14.7 msec, T_{dur} 31.0 msec, $T_{end/ext}$ 52.9 msec

Figure 7.17: Base Stratified Simulation, Extended Output (Case S4)

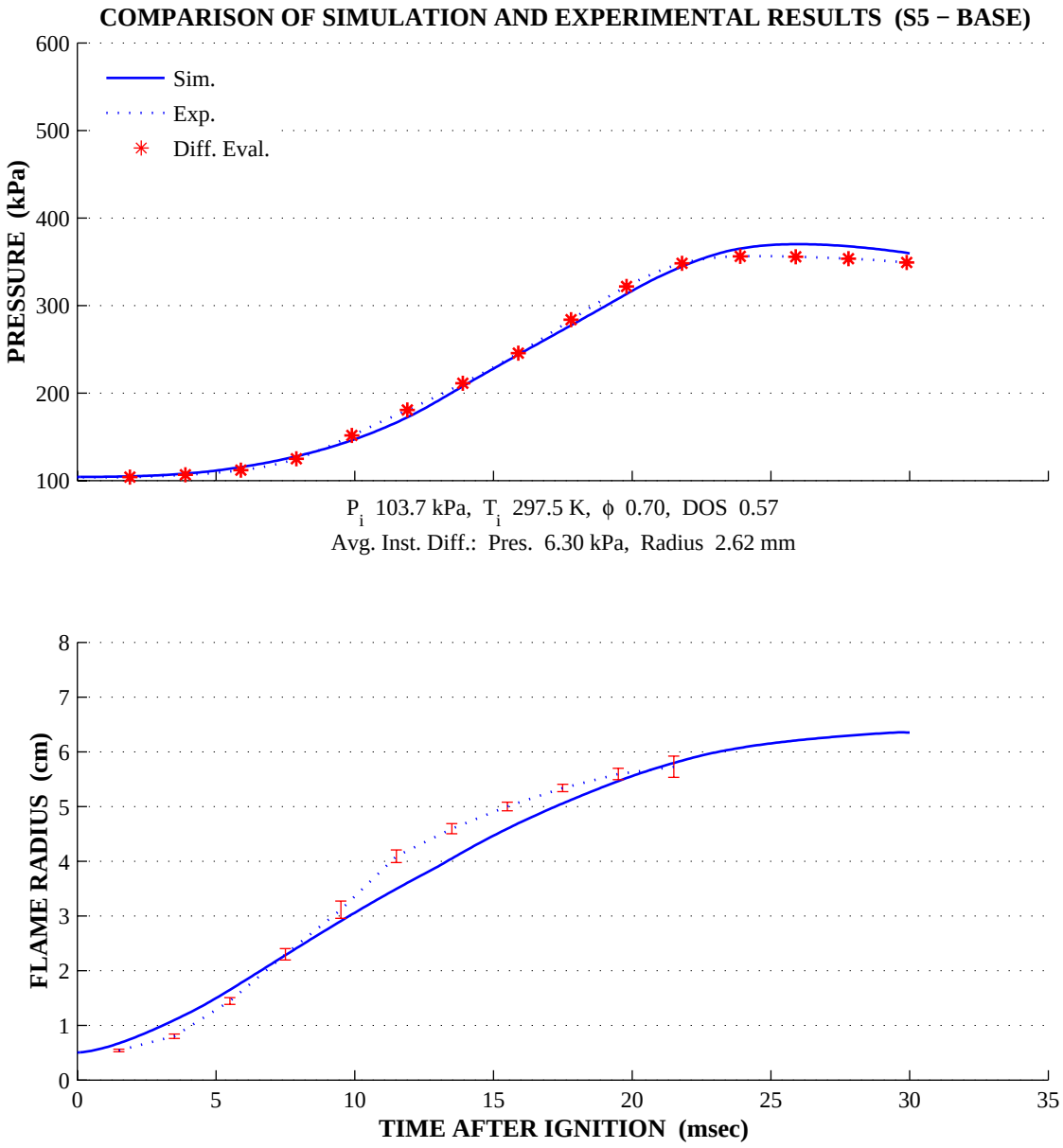

Figure 7.18: Base Stratified Simulation Results (Case S5)

FLAME FRONT AND DIFFUSE REGION DEVELOPMENT (S5 − BASE)

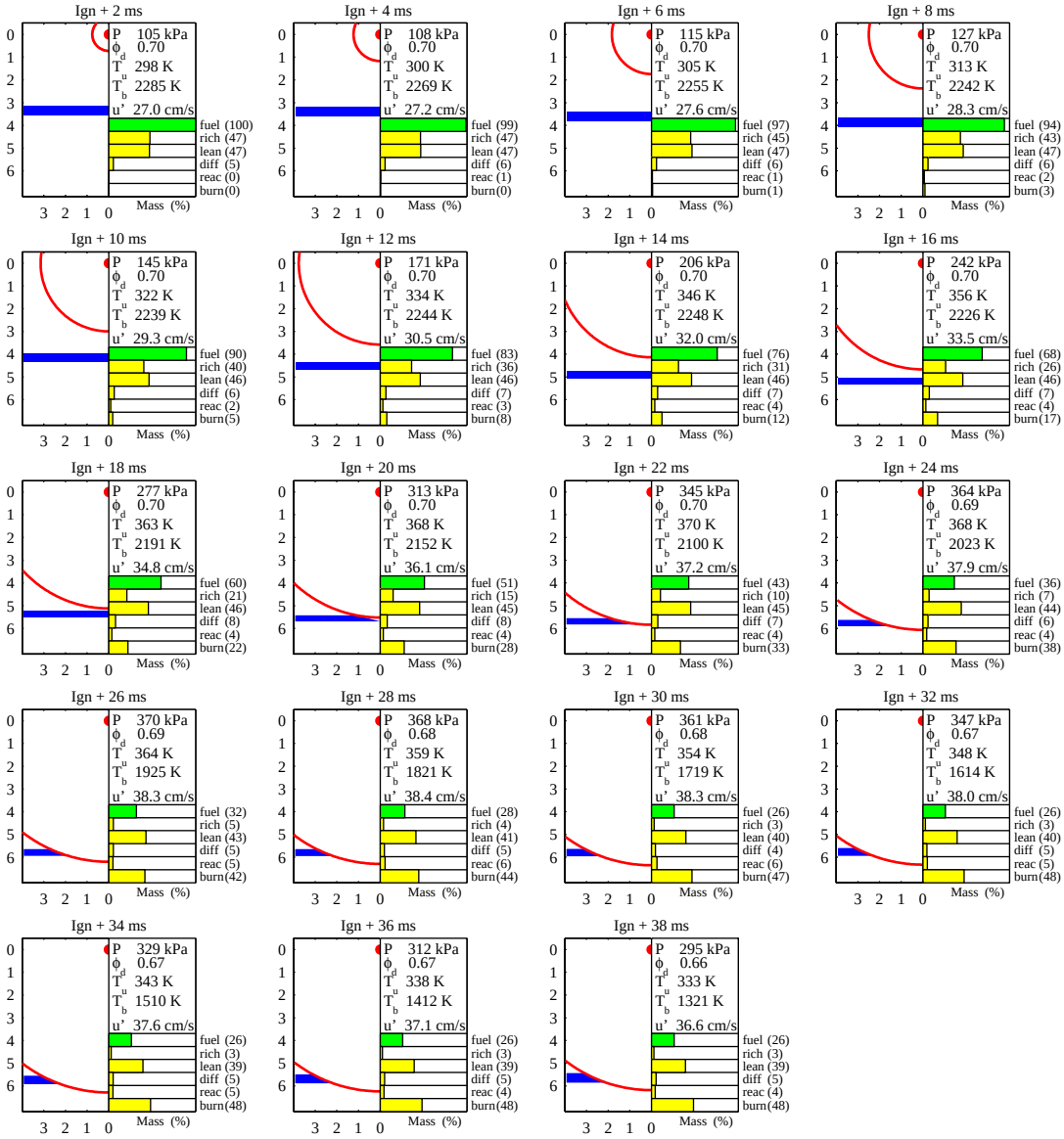

Δt 0.10 msec, P_i 104 kPa, T_i 297 K, ϕ 0.70, DOS 0.57, u'_i 0.27 m/s, $x_{e,i}$ 0.047%, C_{hx} 1.54, K_d 2.00
T_{dev} 12.9 msec, T_{dur} n/a, $T_{end/ext}$ 38.5 msec (Early burn termination due to mixture lean−out.)

Figure 7.19: Base Stratified Simulation, Flame Development (Case S5)

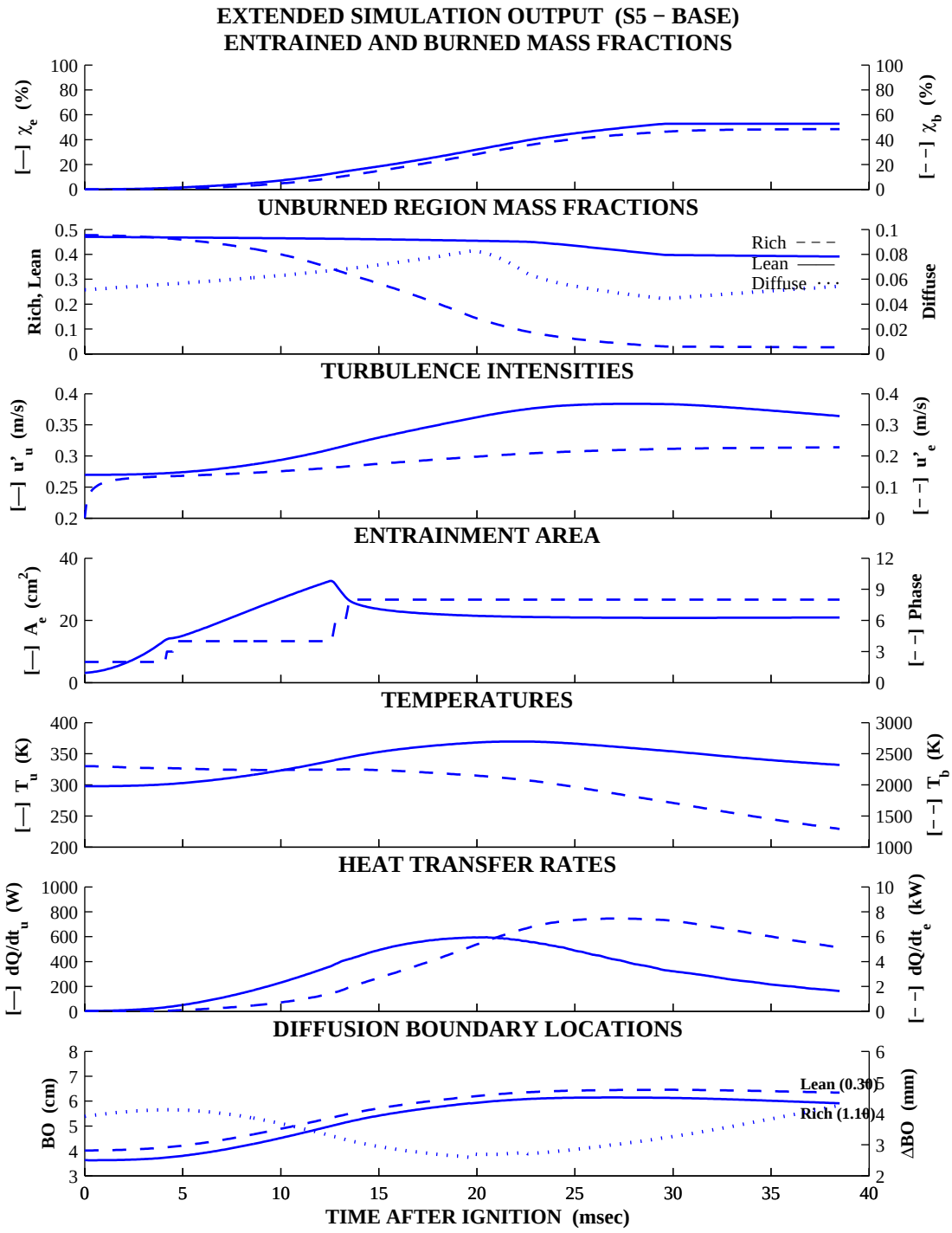

Δt 0.10 msec, P_i 104 kPa, T_i 297 K, ϕ 0.70, DOS 0.57, u'_i 0.27 m/s, $x_{e,i}$ 0.047%, C_{hx} 1.54, K_d 2.00
T_{dev} 12.9 msec, T_{dur} n/a, $T_{end/ext}$ 38.5 msec

Figure 7.20: Base Stratified Simulation, Extended Output (Case S5)

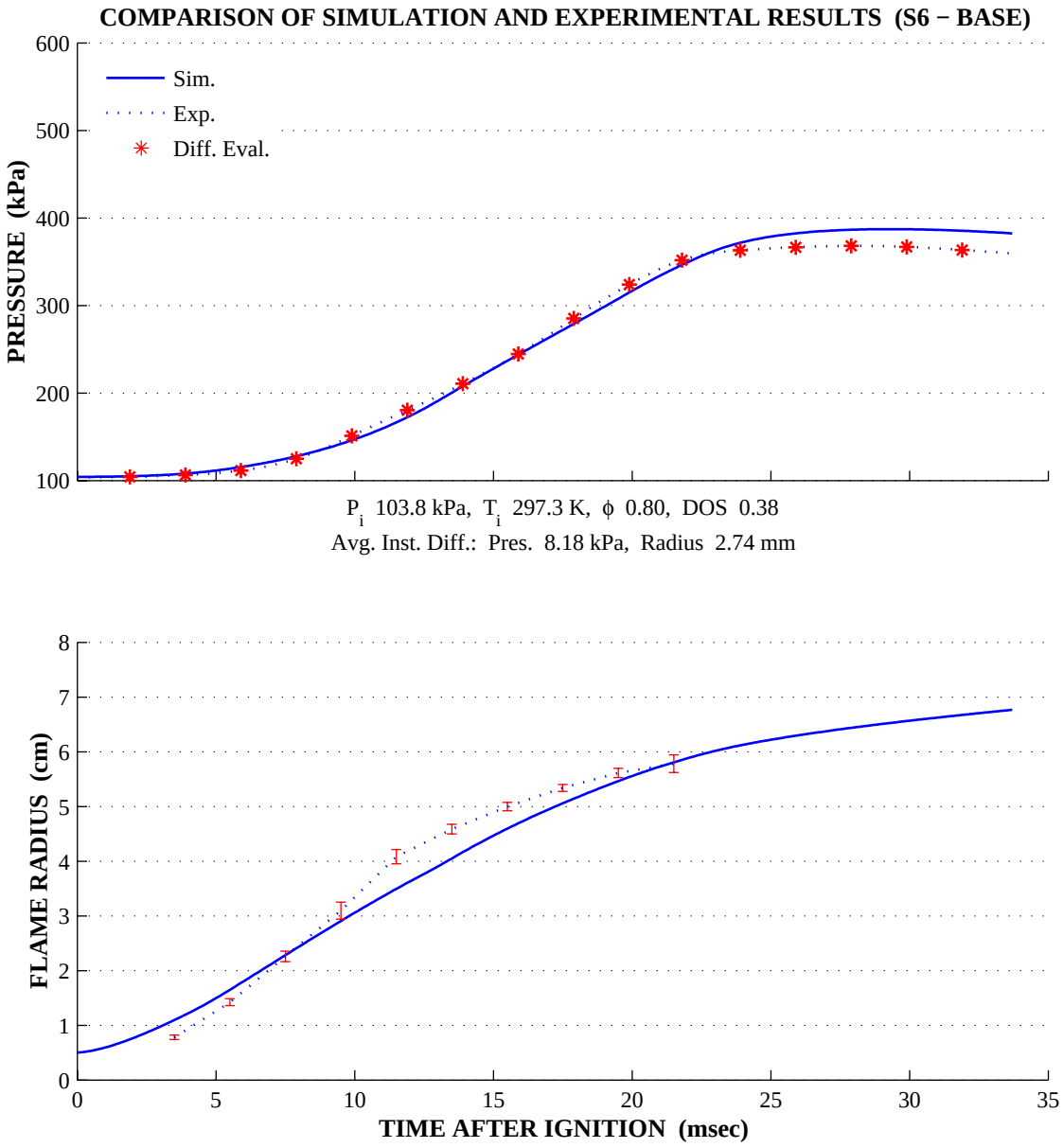

Figure 7.21: Base Stratified Simulation Results (Case S6)

FLAME FRONT AND DIFFUSE REGION DEVELOPMENT (S6 − BASE)

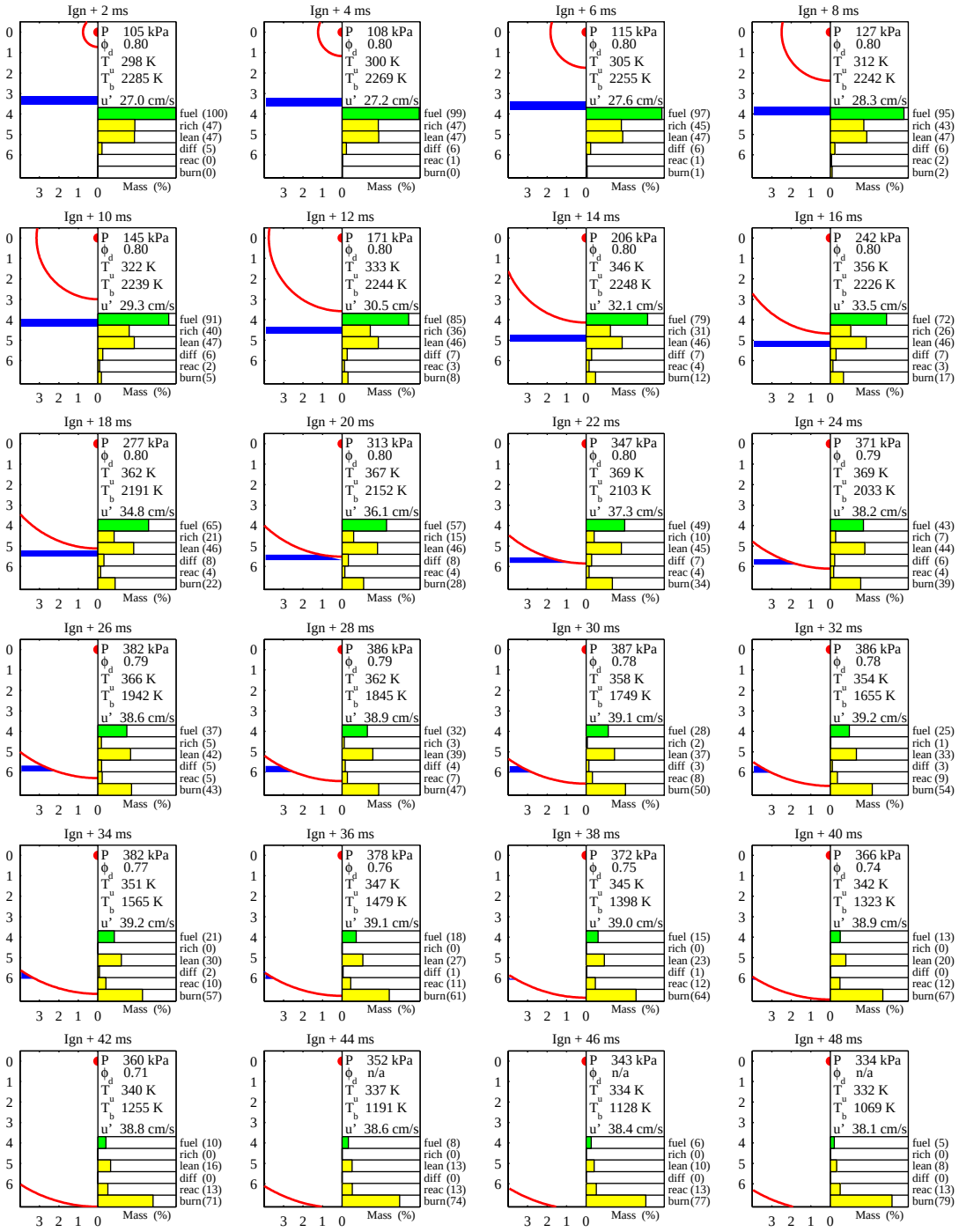

Δt 0.10 msec, P_i 104 kPa, T_i 297 K, ϕ 0.80, DOS 0.38, u'_i 0.27 m/s, $x_{e,i}$ 0.046%, C_{hx} 1.54, K_d 2.00
T_{dev} 12.9 msec, T_{dur} 46.3 msec, $T_{end/ext}$ 60.0 msec

Figure 7.22: Base Stratified Simulation, Flame Development (Case S6)

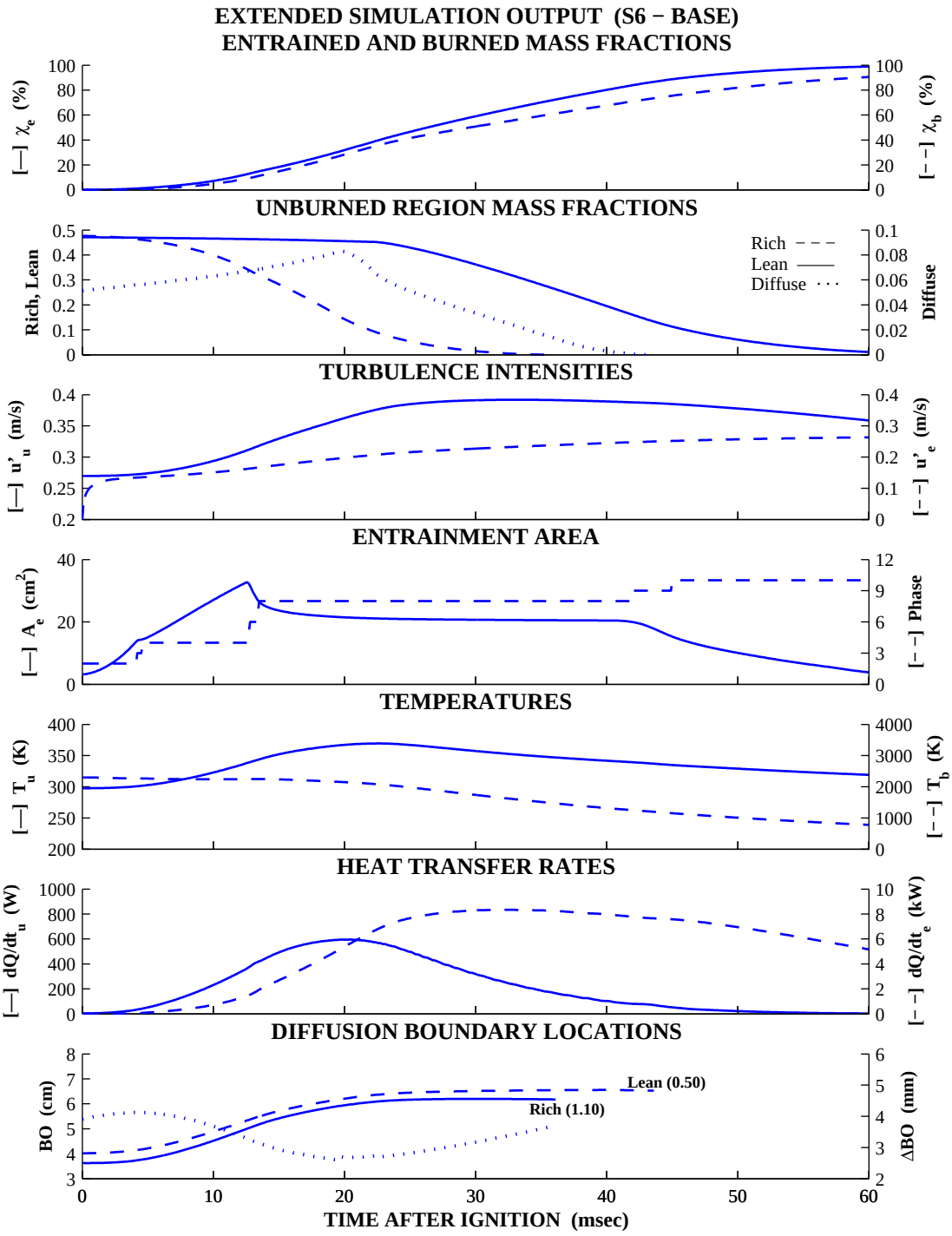

Δt 0.10 msec, P_i 104 kPa, T_i 297 K, ϕ 0.80, DOS 0.38, u'_i 0.27 m/s, $x_{e,i}$ 0.046%, C_{hx} 1.54, K_d 2.00
T_{dev} 12.9 msec, T_{dur} 46.3 msec, $T_{end/ext}$ 60.0 msec

Figure 7.23: Base Stratified Simulation, Extended Output (Case S6)

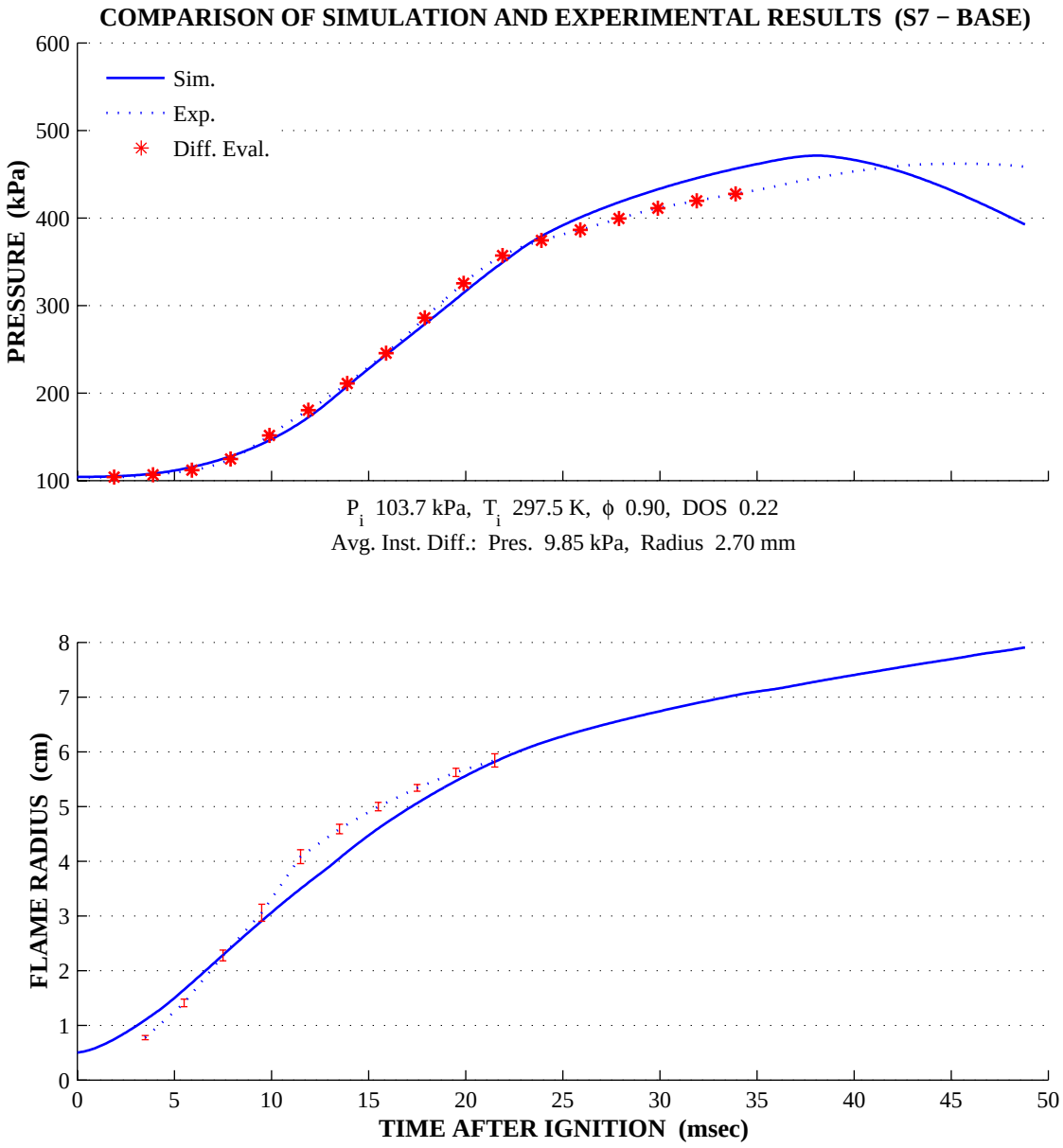

Figure 7.24: Base Stratified Simulation Results (Case S7)

FLAME FRONT AND DIFFUSE REGION DEVELOPMENT (S7 − BASE)

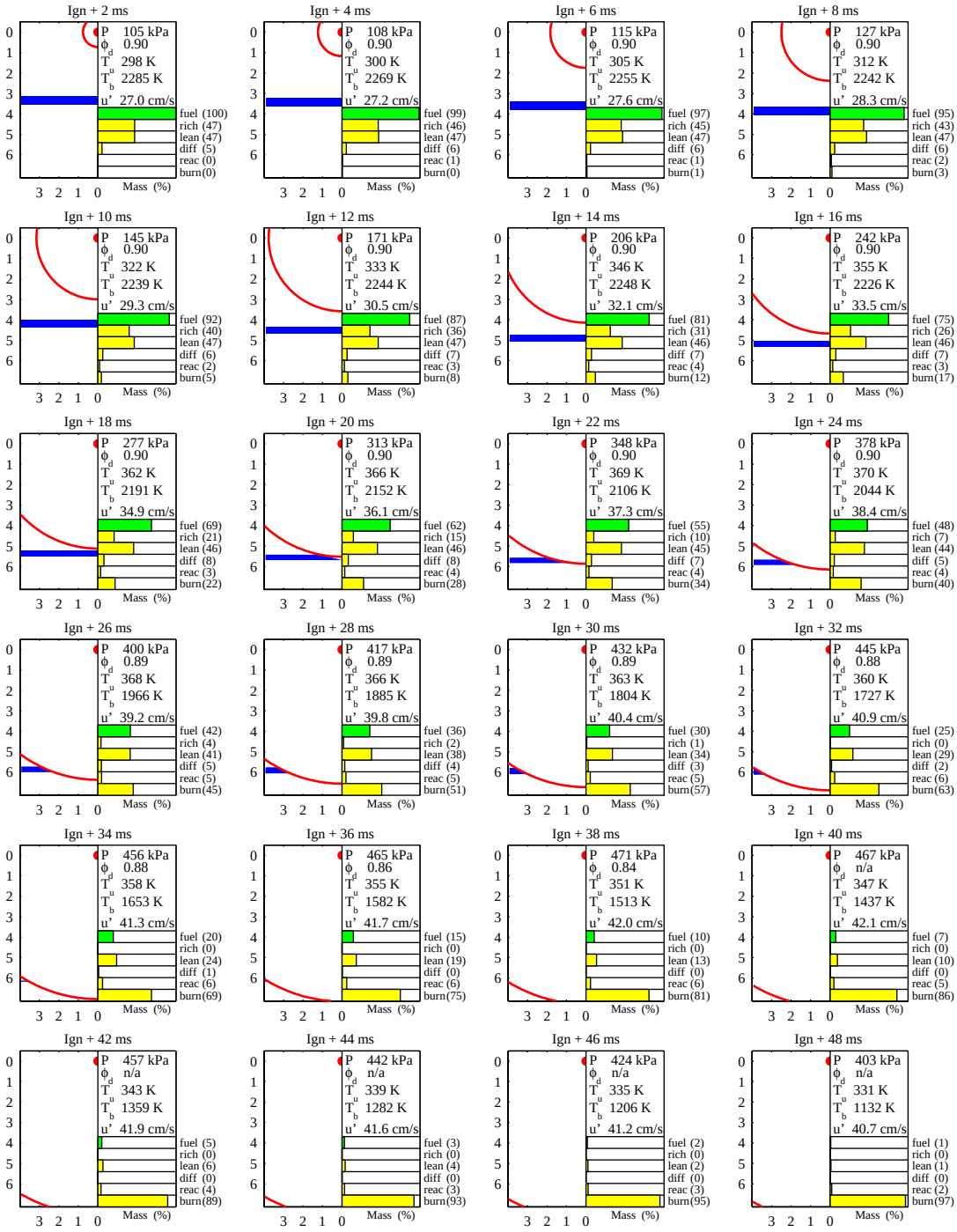

Δt 0.10 msec, P_i 104 kPa, T_i 297 K, ϕ 0.90, DOS 0.22, u'_i 0.27 m/s, $x_{e,i}$ 0.047%, C_{hx} 1.54, K_d 2.00
T_{dev} 12.9 msec, T_{dur} 29.3 msec, $T_{end/ext}$ 49.5 msec

Figure 7.25: Base Stratified Simulation, Flame Development (Case S7)

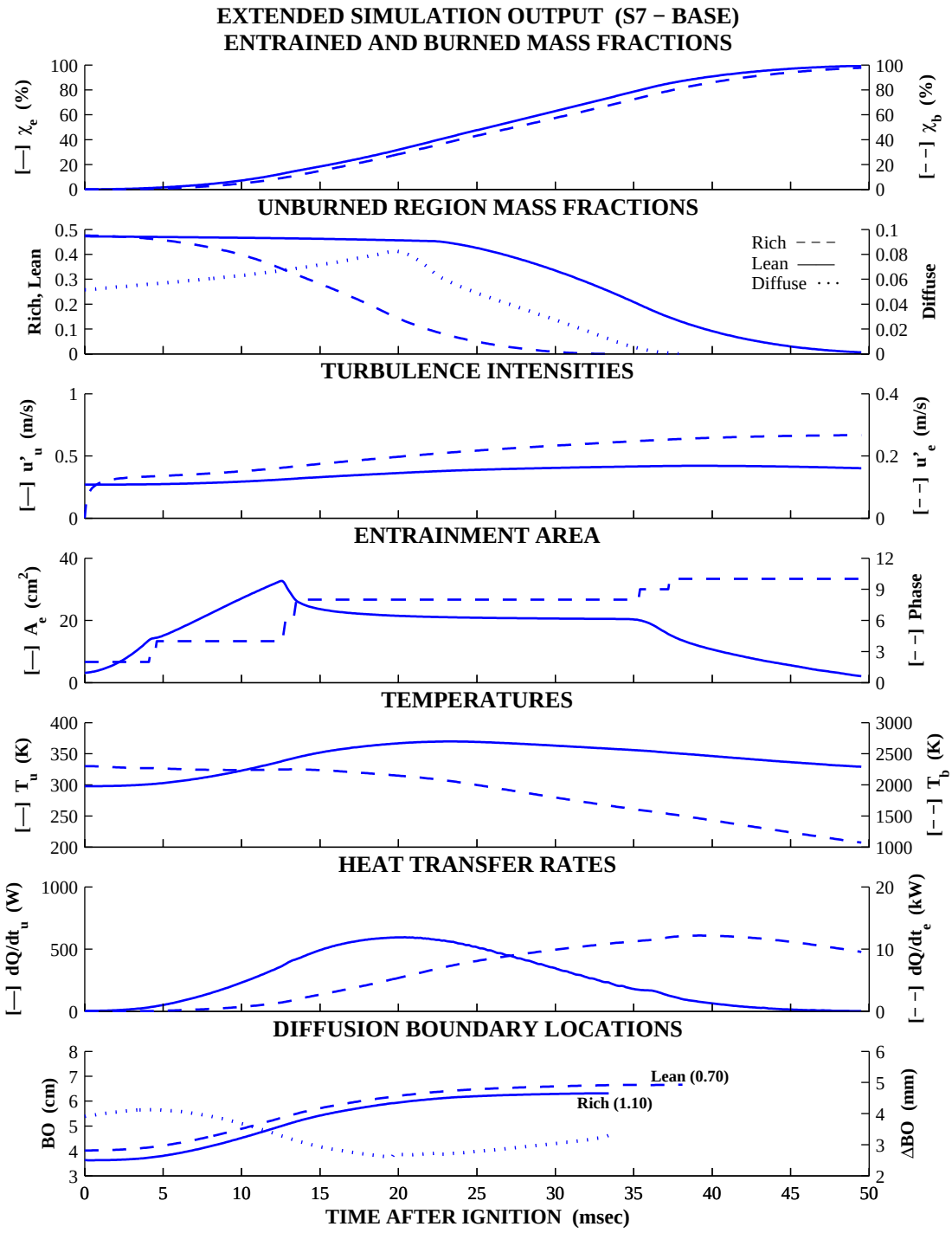

Δt 0.10 msec, P_i 104 kPa, T_i 297 K, ϕ 0.90, DOS 0.22, u'_i 0.27 m/s, $x_{e,i}$ 0.047%, C_{hx} 1.54, K_d 2.00
T_{dev} 12.9 msec, T_{dur} 29.3 msec, $T_{end/ext}$ 49.5 msec

Figure 7.26: Base Stratified Simulation, Extended Output (Case S7)

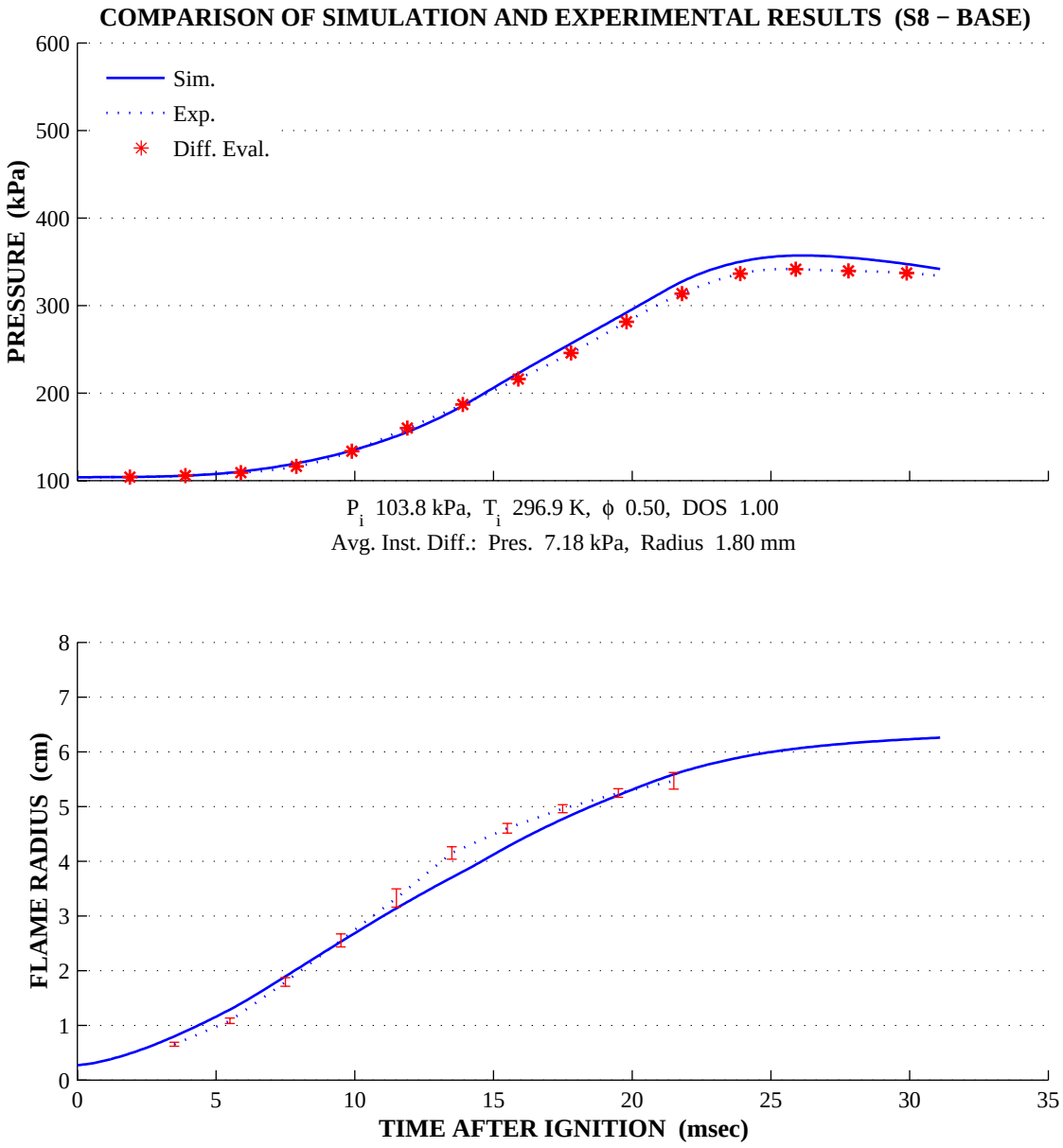

Figure 7.27: Base Stratified Simulation Results (Case S8)

FLAME FRONT AND DIFFUSE REGION DEVELOPMENT (S8 − BASE)

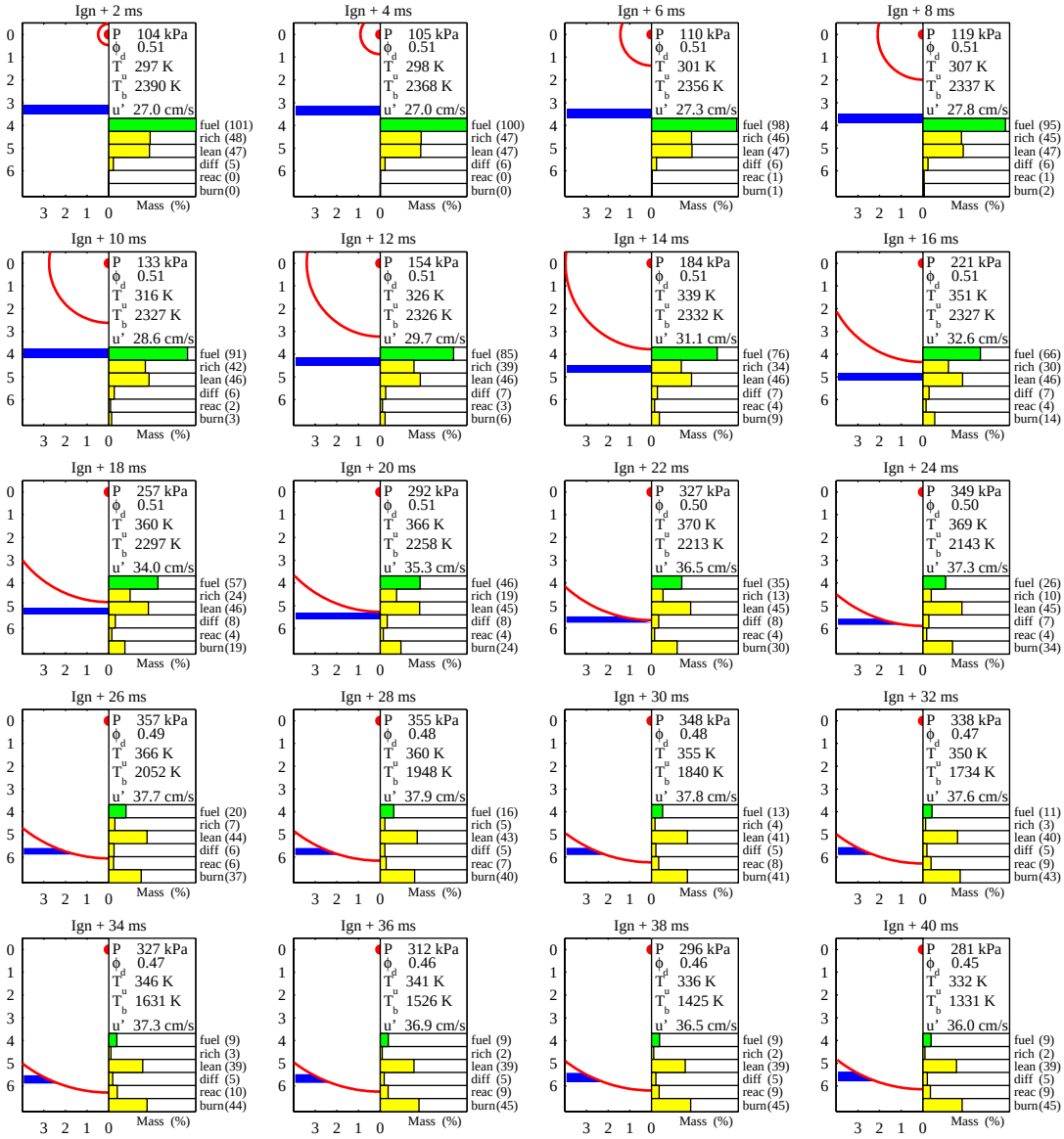

Δt 0.10 msec, P_i 104 kPa, T_i 297 K, ϕ 0.50, DOS 1.00, u'_i 0.27 m/s, $x_{e,i}$ 0.007%, C_{hx} 1.54, K_d 2.00
T_{dev} 14.2 msec, T_{dur} n/a, $T_{end/ext}$ 40.5 msec (Early burn termination due to mixture lean−out.)

Figure 7.28: Base Stratified Simulation, Flame Development (Case S8)

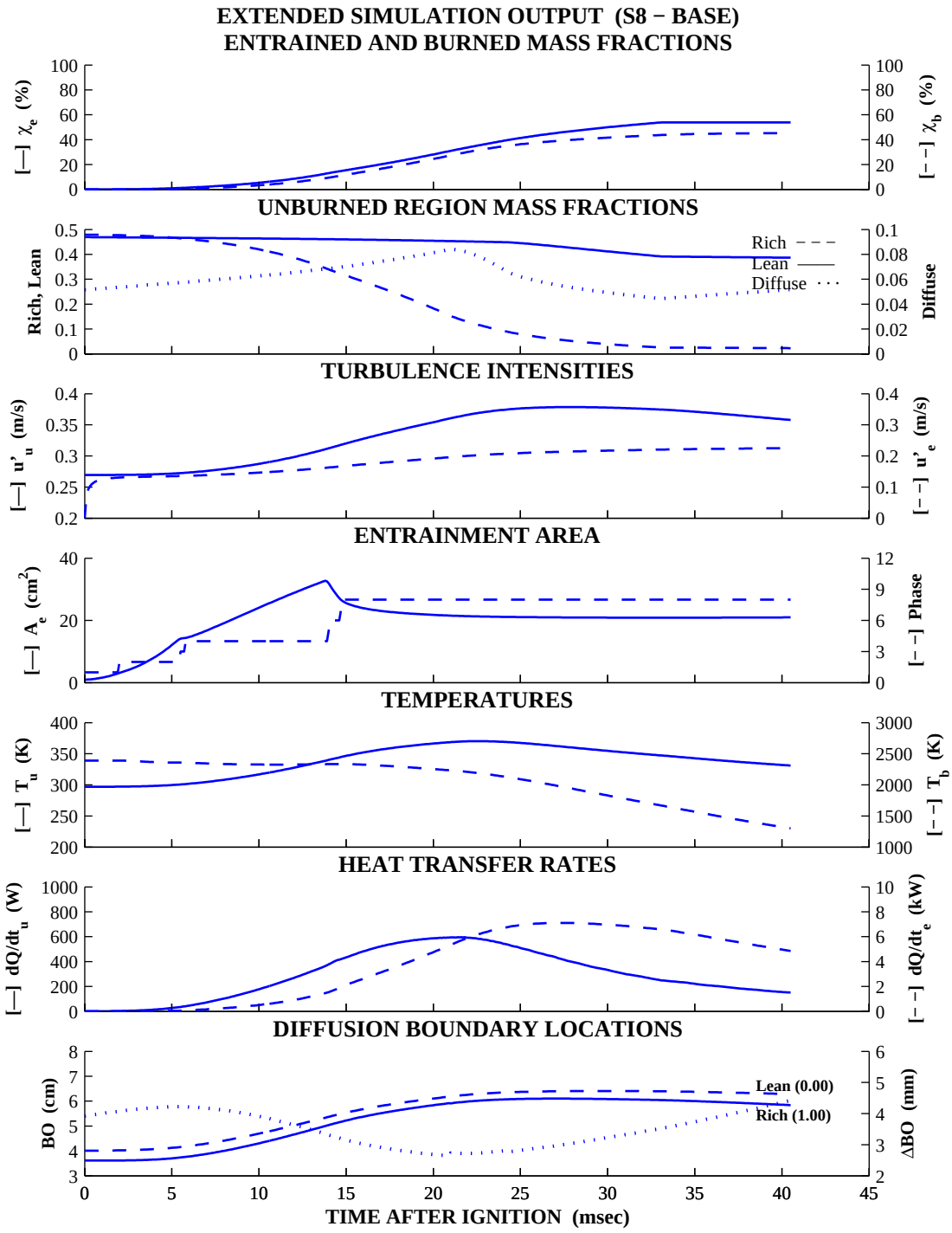

Δt 0.10 msec, P_i 104 kPa, T_i 297 K, ϕ 0.50, DOS 1.00, u'_i 0.27 m/s, $x_{e,i}$ 0.007%, C_{hx} 1.54, K_d 2.00
T_{dev} 14.2 msec, T_{dur} n/a, $T_{end/ext}$ 40.5 msec

Figure 7.29: Base Stratified Simulation, Extended Output (Case S8)

The general matrix result is positive with changes in the simulation pressure and flame radius histories closely following those observed in the experimental data as parameters are varied. With few exceptions the model predicts major transitions in experimental pressure histories and peak pressures attained with only minor errors. The choice of an upper limit for the pressure error is appropriate. At the end of flame geometry Phase 8 where wall effects begin to dominate, the simulation errors increase considerably. The model is valid until this point for all but the unique cases S4 and S7. Prediction of flame radius is not as accurate as pressure and the flame location is slightly underpredicted in the 10 to 20 millisecond range for all cases. This is explained by noting that during this period, the flame front makes the transition from expansion in two directions to only one. In reality the flame nears the side walls and slows locally while entrainment and burning continue. The model assumes that the flame simply contacts the wall and all unburned mixture is displaced. This *missing* mass entrainment/burn accounts for the greater than predicted growth of the burned zone in this period.

The mildly stratified case S1 (ϕ 1.1/0.9) pressure history can be divided into rich and lean burn periods in which there is little difference from a homogeneous case. This is expected with the small change in flame speed as the flame moves through the rich, diffuse and lean regions and the equivalence transition is from 1.1 to ~1.0 and finally 0.9. The difference in the rich and lean periods for case S3 (ϕ 1.2/0.8) is more distinct with a clear break in the pressure rate at flame contact with the diffuse region boundary. Results for cases where complete mixture reaction is unlikely are also handled well. The lean region equivalences for cases S5, S6 and S8 are 0.3, 0.5 and 0.0 respectively. In each of these cases, the simulated peak pressure and time of flame extinction gives a pressure history that closely follows the experimental data. The two exceptions to the general closeness of simulation and experimental results are cases S4 and S7.

In the mid-late burn period of cases S4 and S7, simulation and experimental pressure histories diverge. These two cases have a common lean side equivalence of 0.7 (rich side 1.3 and 1.1 respectively). Also consistent is the flame position at the start of the pressure underprediction at ~1.5 cm from the chamber's vertical centerline. There may be a single sub-model deficiency to explain the common error or it may a combination of several effects. One possibility of the first type is the laminar flame speed correlation. The correlation is used below the minimum equivalence of 0.8 and very lean flame speeds may not be accurate in the simulation. An example of the second type is the simple flame geometry sub-model. Images in Chapter 5 show the experimental and simulated shapes deviate significantly as the flame nears the far wall. The flame geometry sub-model affects both the mass entrainment and heat transfer sub-models since it feeds forward the values of heat transfer and entrainment areas (this also impacts the weighted propagation speed). It is reasonable to attribute the error to the simple flame geometry and/or heat transfer sub-models which are expected to beak down in the near-wall regime. It is also possible that the difference is a result of physical phenomena that are not modeled.

The initial results show that the basic physical characteristics of stratified combustion are captured in this first iteration of the model. There remain details without which the valid range of prediction is less than required for the model to be valuable as a research tool.

7.3 Tuned Simulation Results

The homogeneous model tuning process is repeated for the stratified case. A single parameter (diffusion rate constant) is optimized for general improvement across all stratified cases. One simple structural modification is also considered in order to evaluate the modeling of the burned zone as a non-mixing mixture of rich and lean products.

7.3.1 Tuning – Unburned Mixture Diffusion

The reverse model described in Section 3.3 is used with a single optimization stage since there is only one parameter to optimize. A degree of subjective judgment is employed to obtain a tuned value that yields the best improvement for the complete set of stratified cases. Base and tuned values of the diffusion rate constant are reported in Table 7.4.

Initial Value	Tuned Value
2.00	1.10

Table 7.4: Initial and Tuned Values for Diffusion Constant (K_d)

Each of the seven stratified test cases is simulated again using the tuned value. Average instantaneous errors and the change in each are presented in Table 7.5.

Case	Average Instantaneous Diff.					
	Pressure (kPa)			Flame Radius (cm)		
	Base	Opt.	Chg.	Base	Opt.	Chg.
S1	4.60	4.50	-2.2%	2.30	2.30	0.0%
S3	5.67	5.42	-4.4%	2.63	2.61	-0.7%
S4	4.21	3.69	-12.4%	2.54	2.54	0.0%
S5	6.30	5.47	-13.2%	2.62	2.63	0.4%
S6	8.18	7.14	-12.7%	2.74	2.75	0.4%
S7	9.85	9.37	-4.9%	2.70	2.70	0.0%
S8	7.18	9.07	26.3%	1.80	1.80	0.0%
Avg.	5.75	5.58	-2.9%	2.17	2.17	0.0%

Table 7.5: Comparison of Stratified Simulation Error Before and After Tuning

The results are expected to show that diffusion has little impact since none of the cases have lean mixture near the lean limit. The increased impact in these particular cases was shown in examined in Figure 7.8. Small base errors give percent changes that do not reflect the subtle changes in the pressure and flame radius histories. This is made clear in the graphical presentation of the results [Figure 7.30 through Figure 7.50] where simulation histories before and after tuning are displayed using the established format.

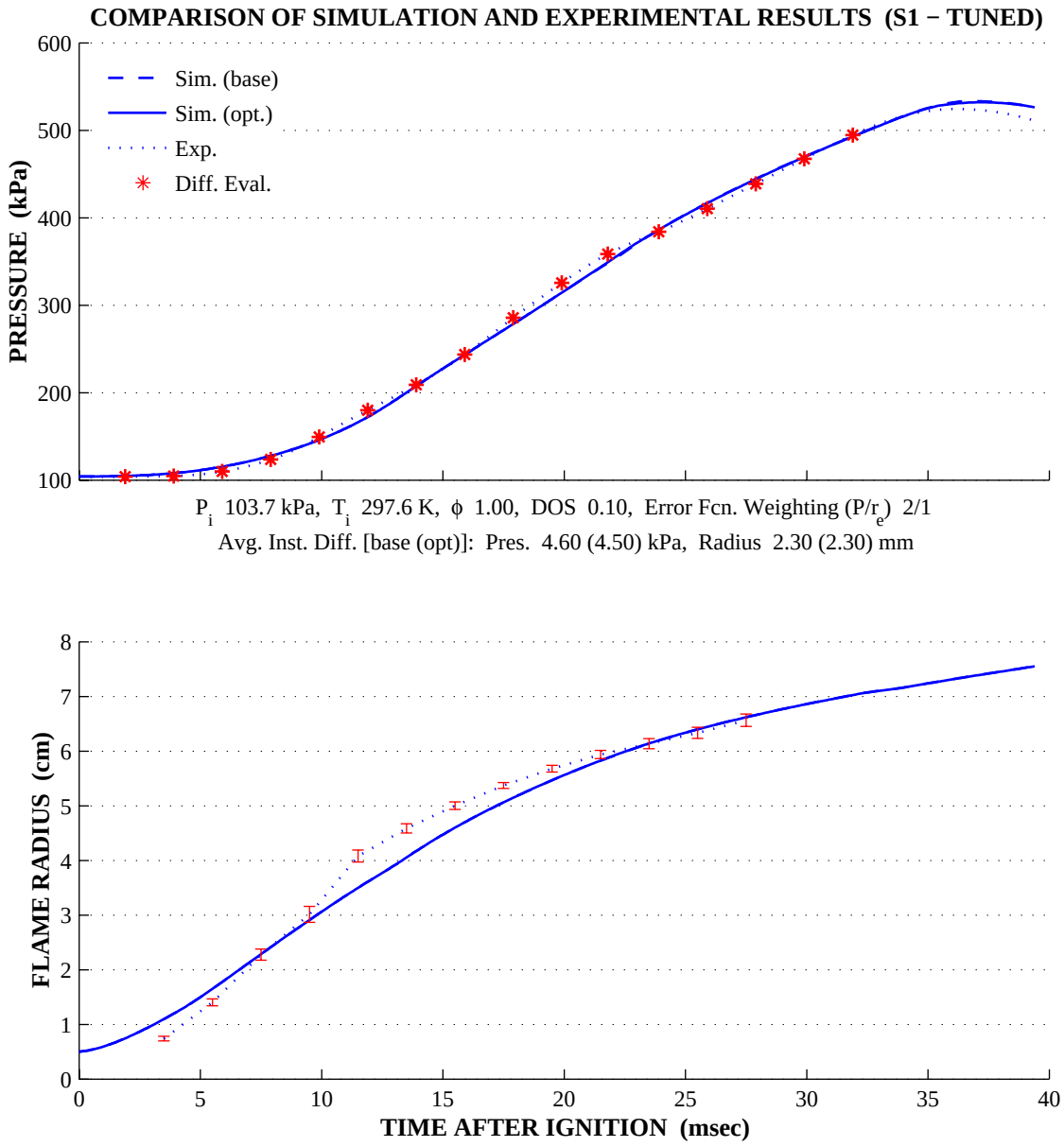

Figure 7.30: Tuned Stratified Simulation Results (Case S1)

FLAME FRONT AND DIFFUSE REGION DEVELOPMENT (S1 − TUNED)

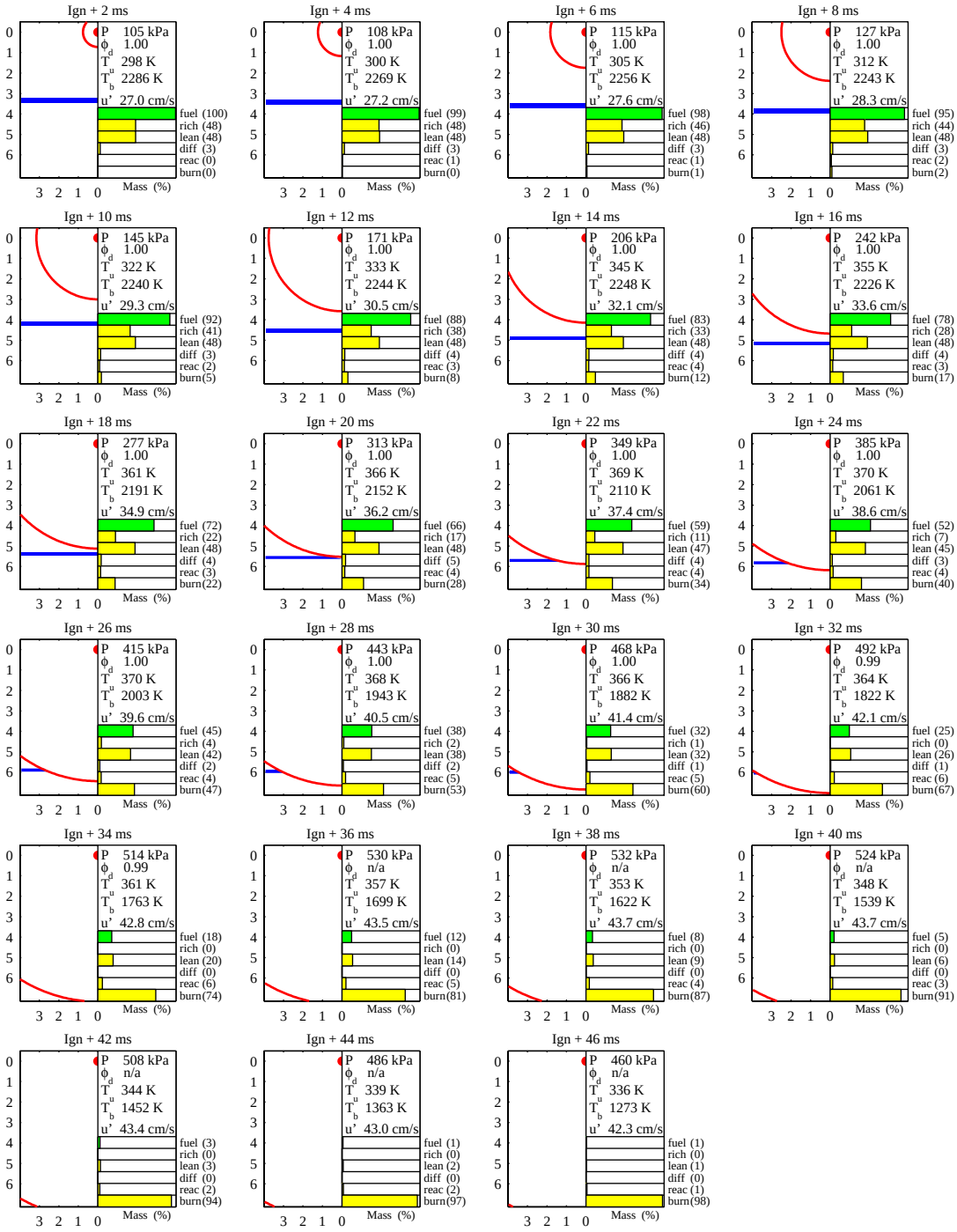

Δt 0.10 msec, P_i 104 kPa, T_i 298 K, ϕ 1.00, DOS 0.10, u'_i 0.27 m/s, $x_{e,i}$ 0.046%, C_{hx} 1.54, K_d 1.10
T_{dev} 12.9 msec, T_{dur} 26.4 msec, $T_{end/ext}$ 46.0 msec

Figure 7.31: Tuned Stratified Simulation, Flame Development (Case S1)

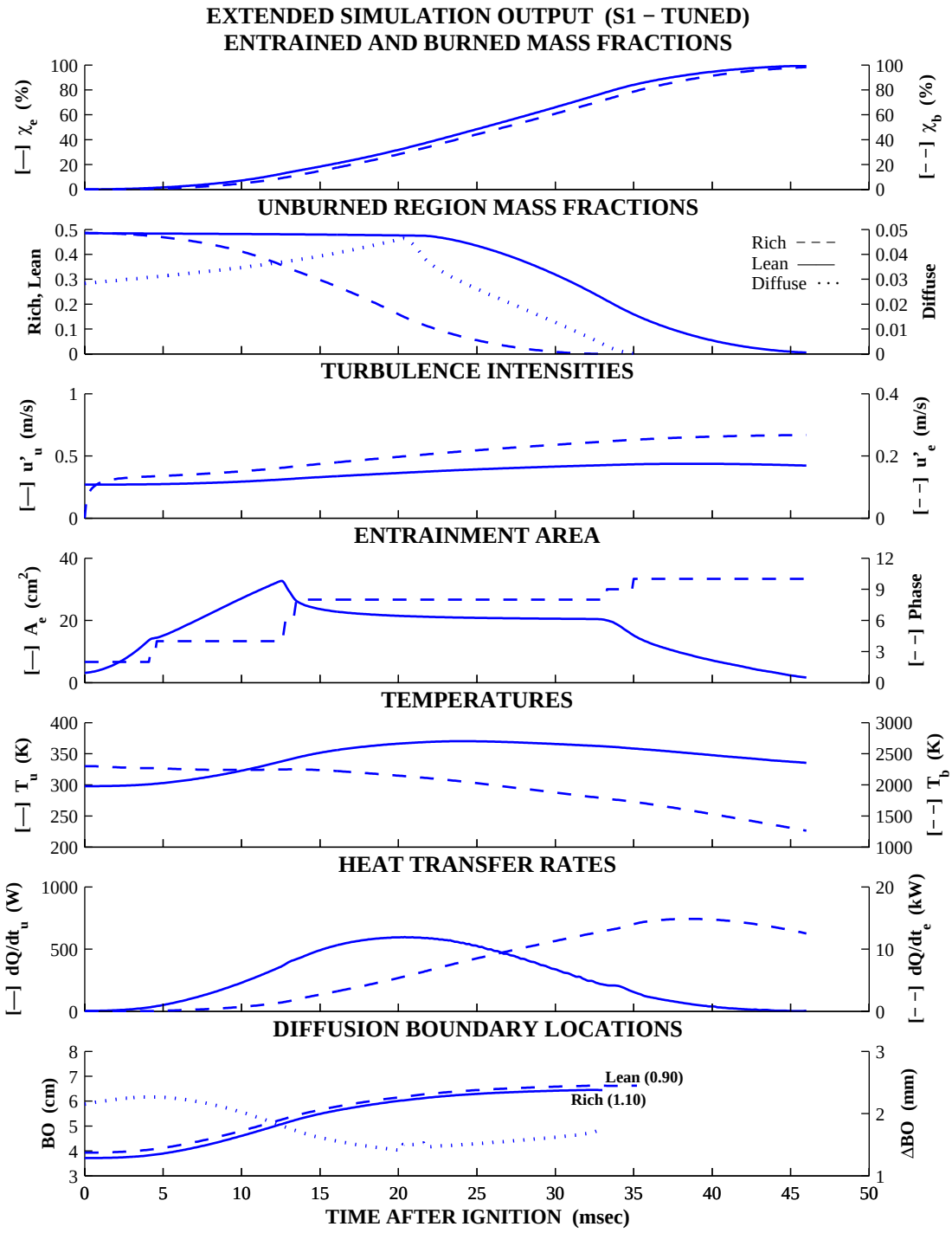

Δt 0.10 msec, P_i 104 kPa, T_i 298 K, ϕ 1.00, DOS 0.10, u'_i 0.27 m/s, $x_{e,i}$ 0.046%, C_{hx} 1.54, K_d 1.10
T_{dev} 12.9 msec, T_{dur} 26.4 msec, $T_{end/ext}$ 46.0 msec

Figure 7.32: Tuned Stratified Simulation, Extended Output (Case S1)

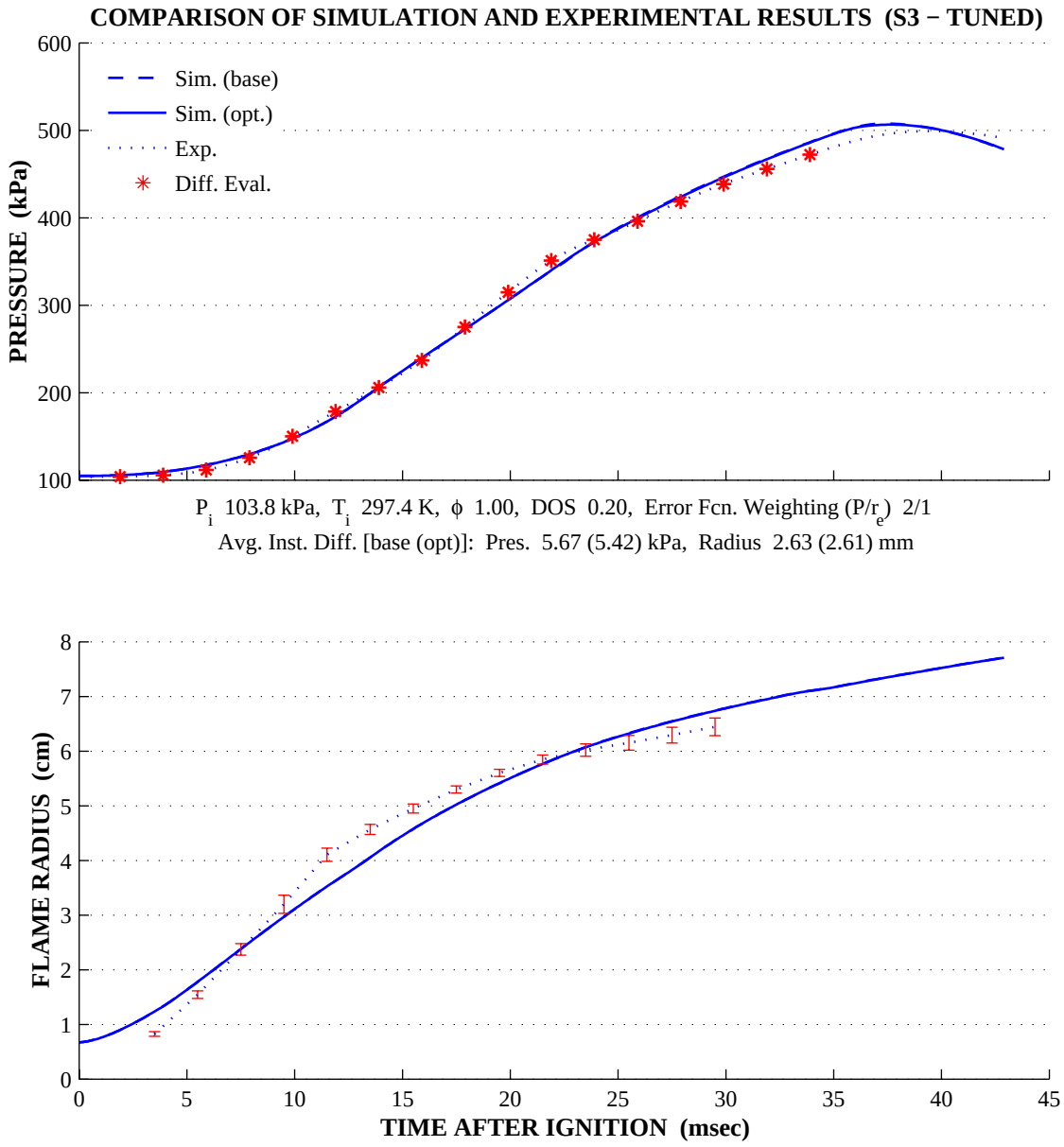

Figure 7.33: Tuned Stratified Simulation Results (Case S3)

FLAME FRONT AND DIFFUSE REGION DEVELOPMENT (S3 − TUNED)

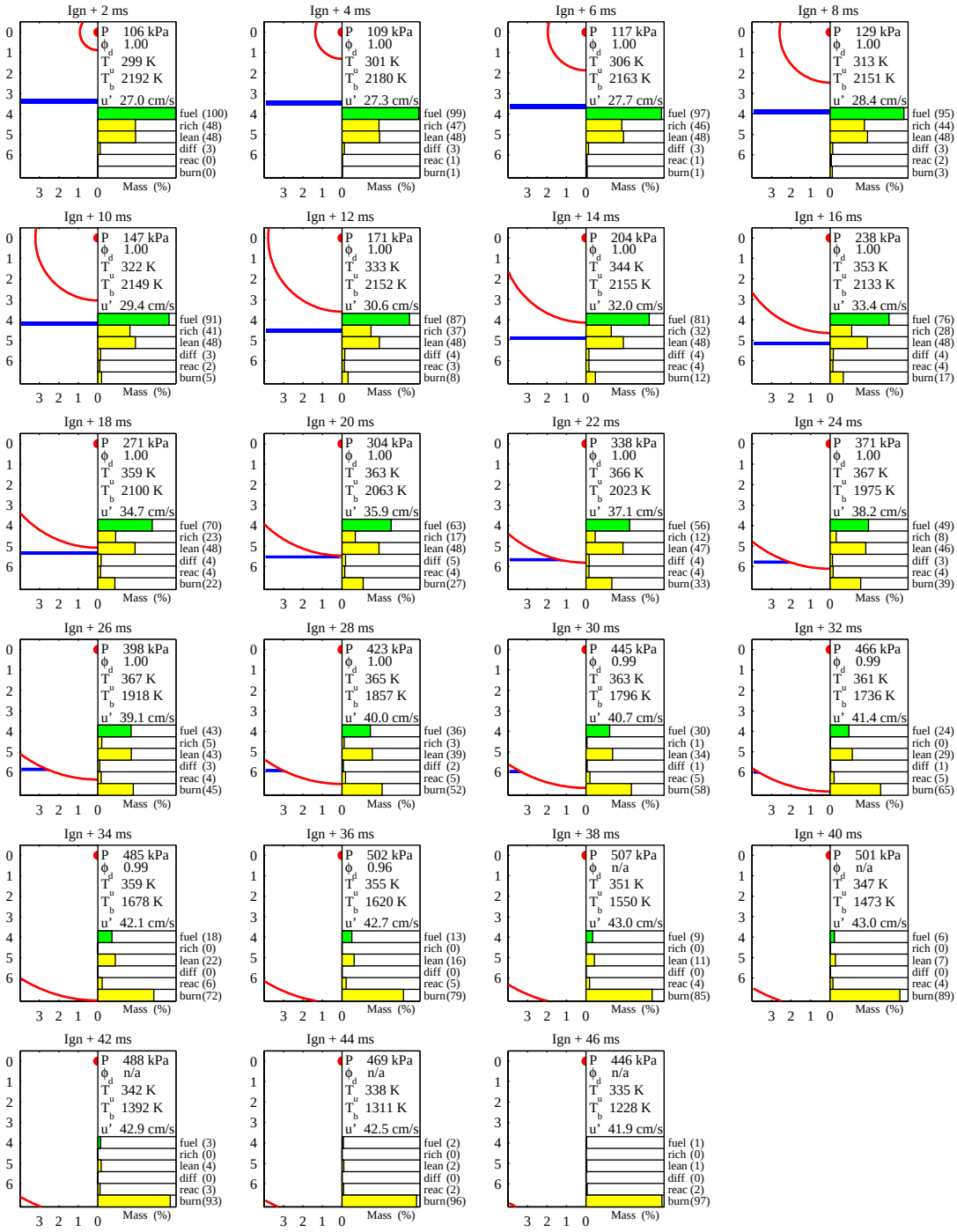

Δt 0.10 msec, P_i 104 kPa, T_i 297 K, ϕ 1.00, DOS 0.20, u'_i 0.27 m/s, $x_{e,i}$ 0.107%, C_{hx} 1.54, K_d 1.10
T_{dev} 12.8 msec, T_{dur} 27.4 msec, $T_{end/ext}$ 46.9 msec

Figure 7.34: Tuned Stratified Simulation, Flame Development (Case S3)

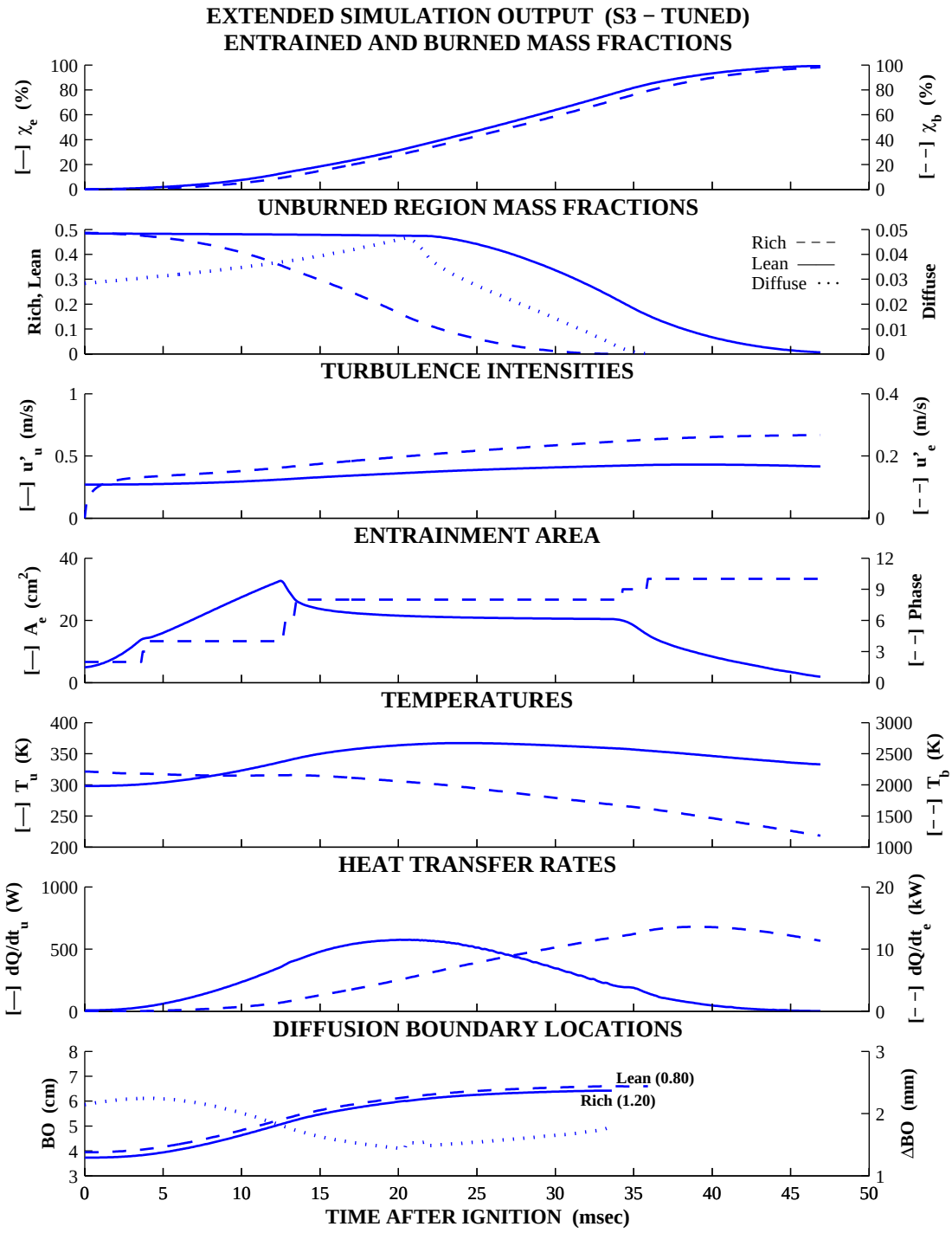

Δt 0.10 msec, P_i 104 kPa, T_i 297 K, ϕ 1.00, DOS 0.20, u'_i 0.27 m/s, $x_{e,i}$ 0.107%, C_{hx} 1.54, K_d 1.10
T_{dev} 12.8 msec, T_{dur} 27.4 msec, $T_{end/ext}$ 46.9 msec

Figure 7.35: Tuned Stratified Simulation, Extended Output (Case S3)

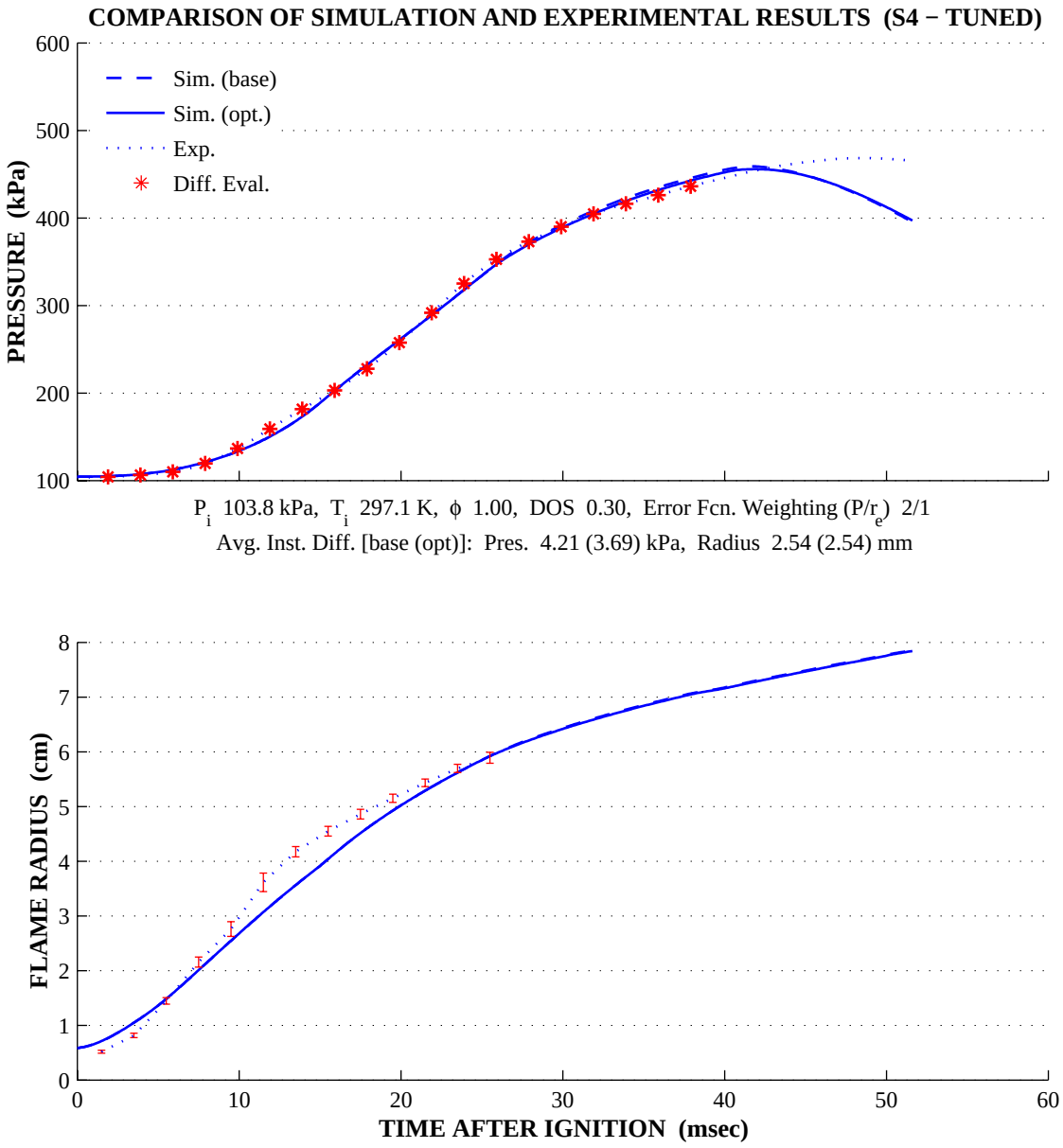

Figure 7.36: Tuned Stratified Simulation Results (Case S4)

FLAME FRONT AND DIFFUSE REGION DEVELOPMENT (S4 − TUNED)

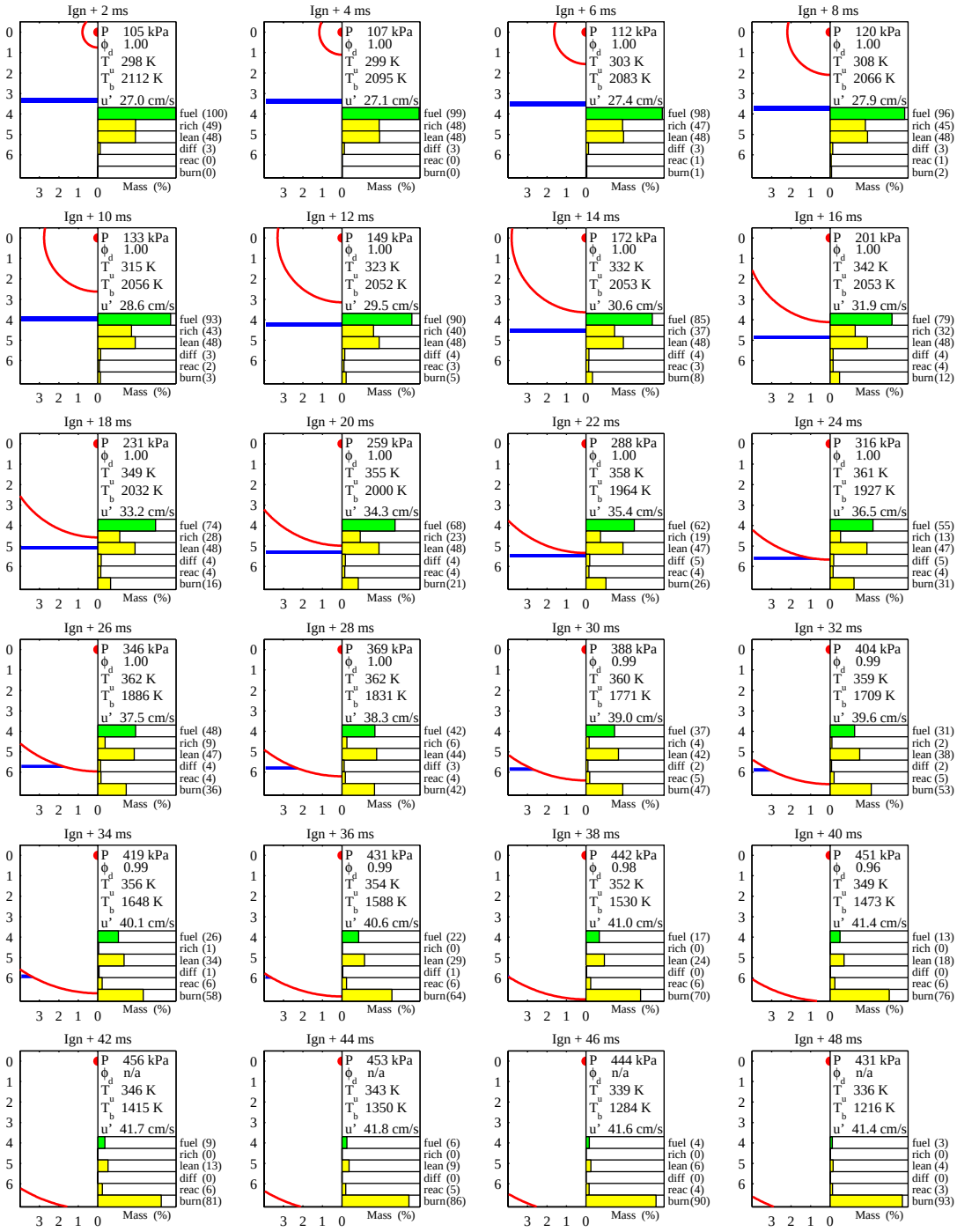

Δt 0.10 msec, P_i 104 kPa, T_i 297 K, ϕ 1.00, DOS 0.30, u'_i 0.27 m/s, $x_{e,i}$ 0.075%, C_{hx} 1.54, K_d 1.10
T_{dev} 14.7 msec, T_{dur} 31.3 msec, $T_{end/ext}$ 53.2 msec

Figure 7.37: Tuned Stratified Simulation, Flame Development (Case S4)

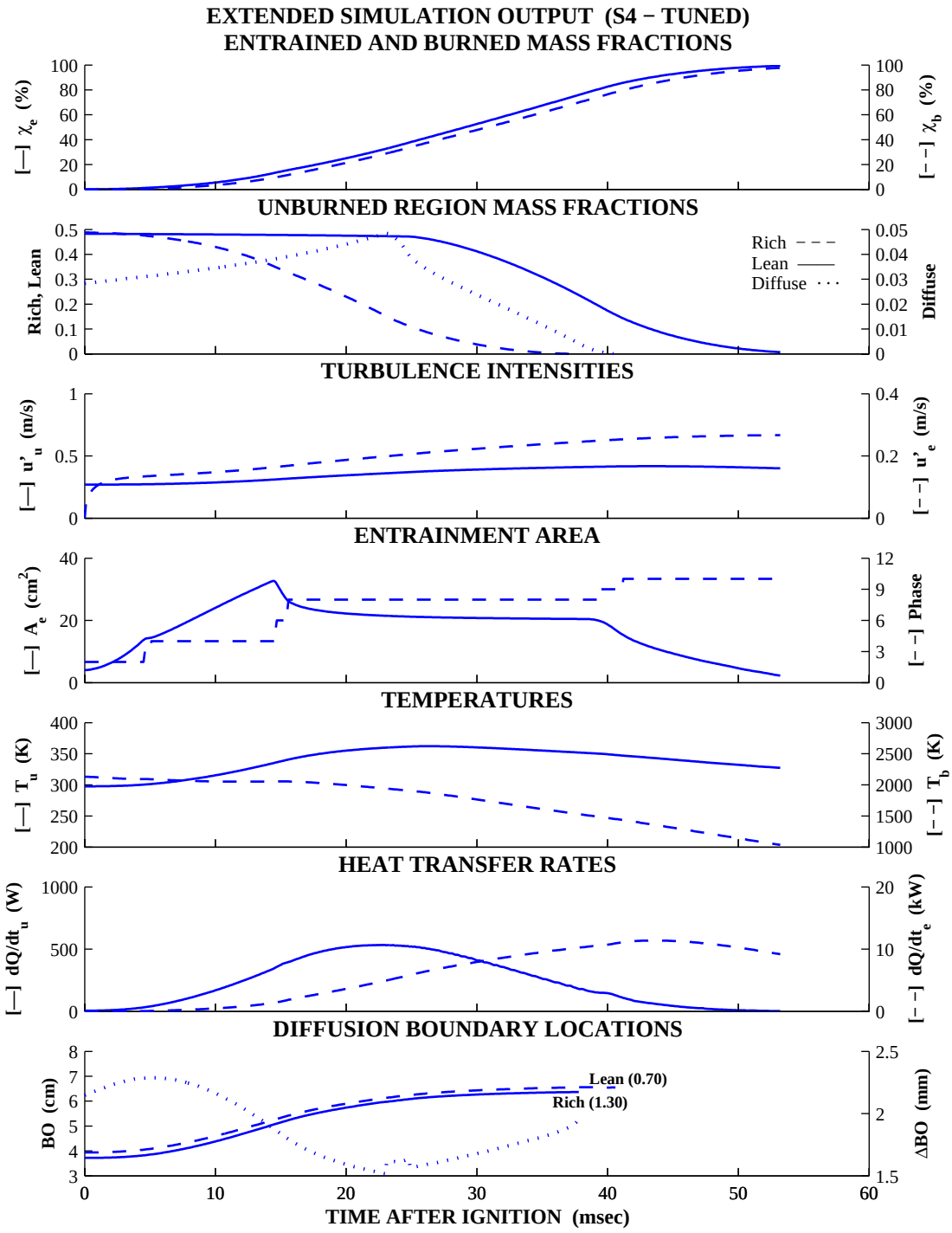

Δt 0.10 msec, P_i 104 kPa, T_i 297 K, ϕ 1.00, DOS 0.30, u'_i 0.27 m/s, $x_{e,i}$ 0.075%, C_{hx} 1.54, K_d 1.10
T_{dev} 14.7 msec, T_{dur} 31.3 msec, $T_{end/ext}$ 53.2 msec

Figure 7.38: Tuned Stratified Simulation, Extended Output (Case S4)

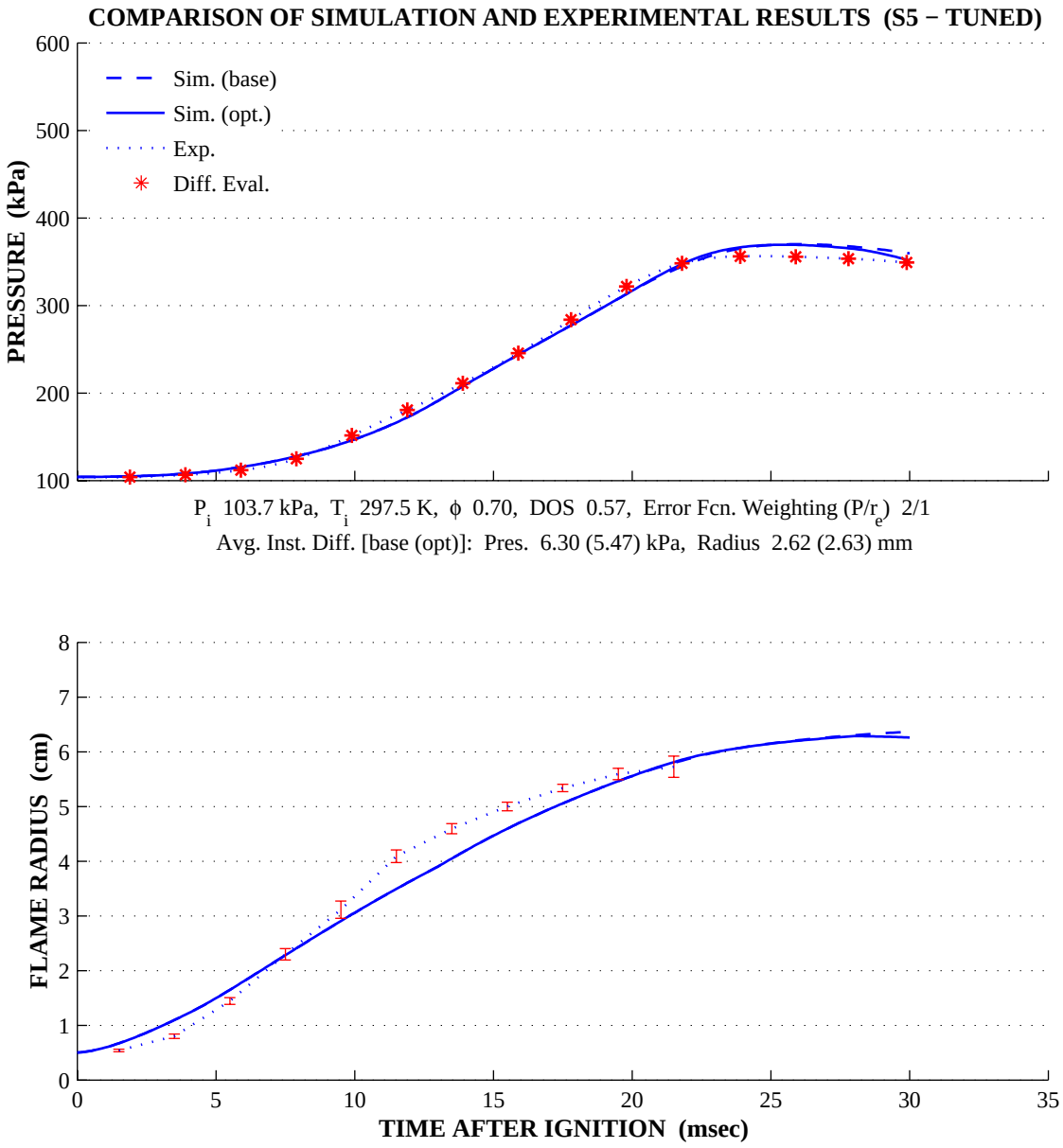

Figure 7.39: Tuned Stratified Simulation Results (Case S5)

FLAME FRONT AND DIFFUSE REGION DEVELOPMENT (S5 − TUNED)

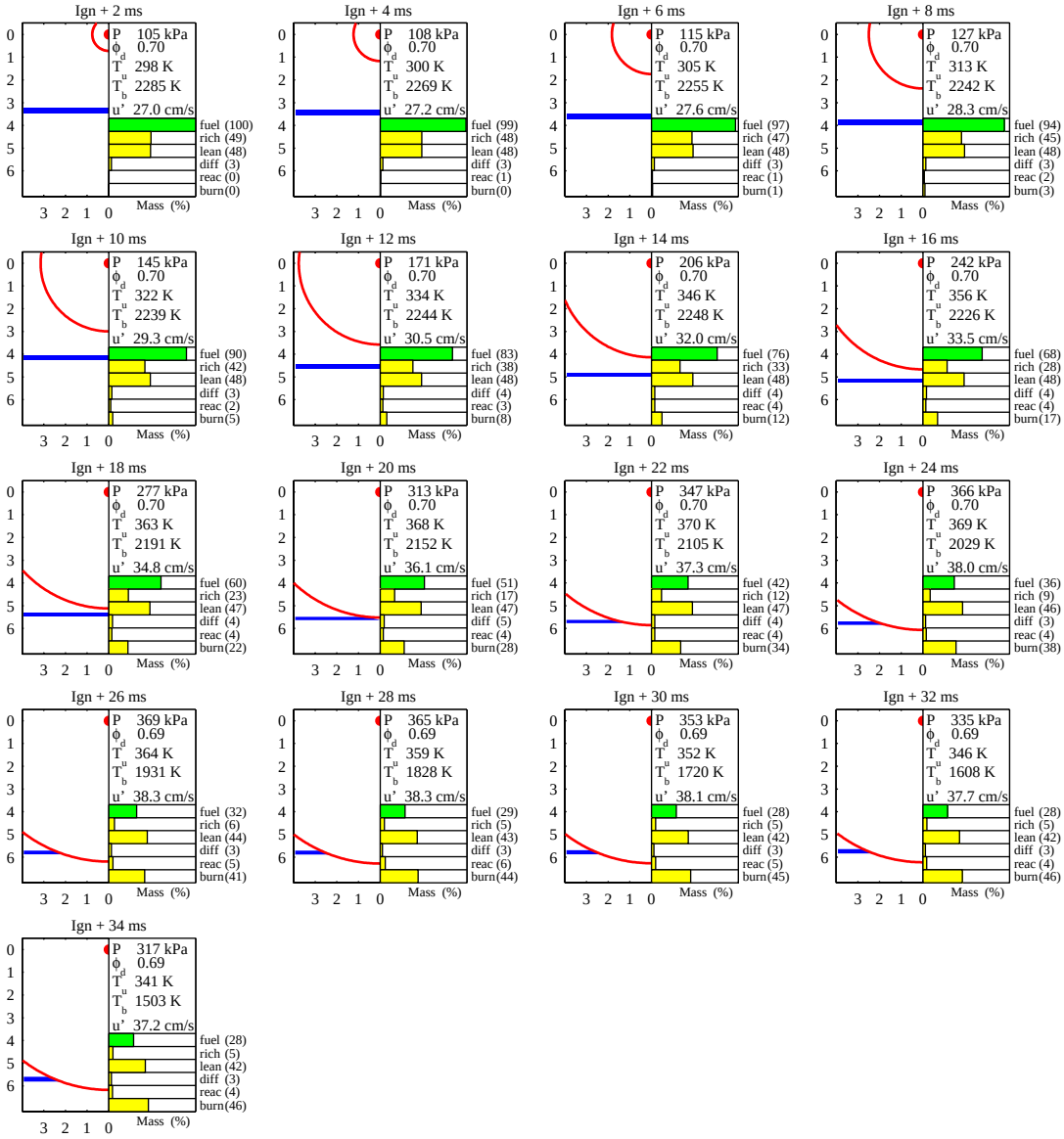

Δt 0.10 msec, P_i 104 kPa, T_i 297 K, φ 0.70, DOS 0.57, u'_i 0.27 m/s, $x_{e,i}$ 0.047%, C_{hx} 1.54, K_d 1.10
T_{dev} 12.9 msec, T_{dur} n/a, $T_{end/ext}$ 35.1 msec (Early burn termination due to mixture lean−out.)

Figure 7.40: Tuned Stratified Simulation, Flame Development (Case S5)

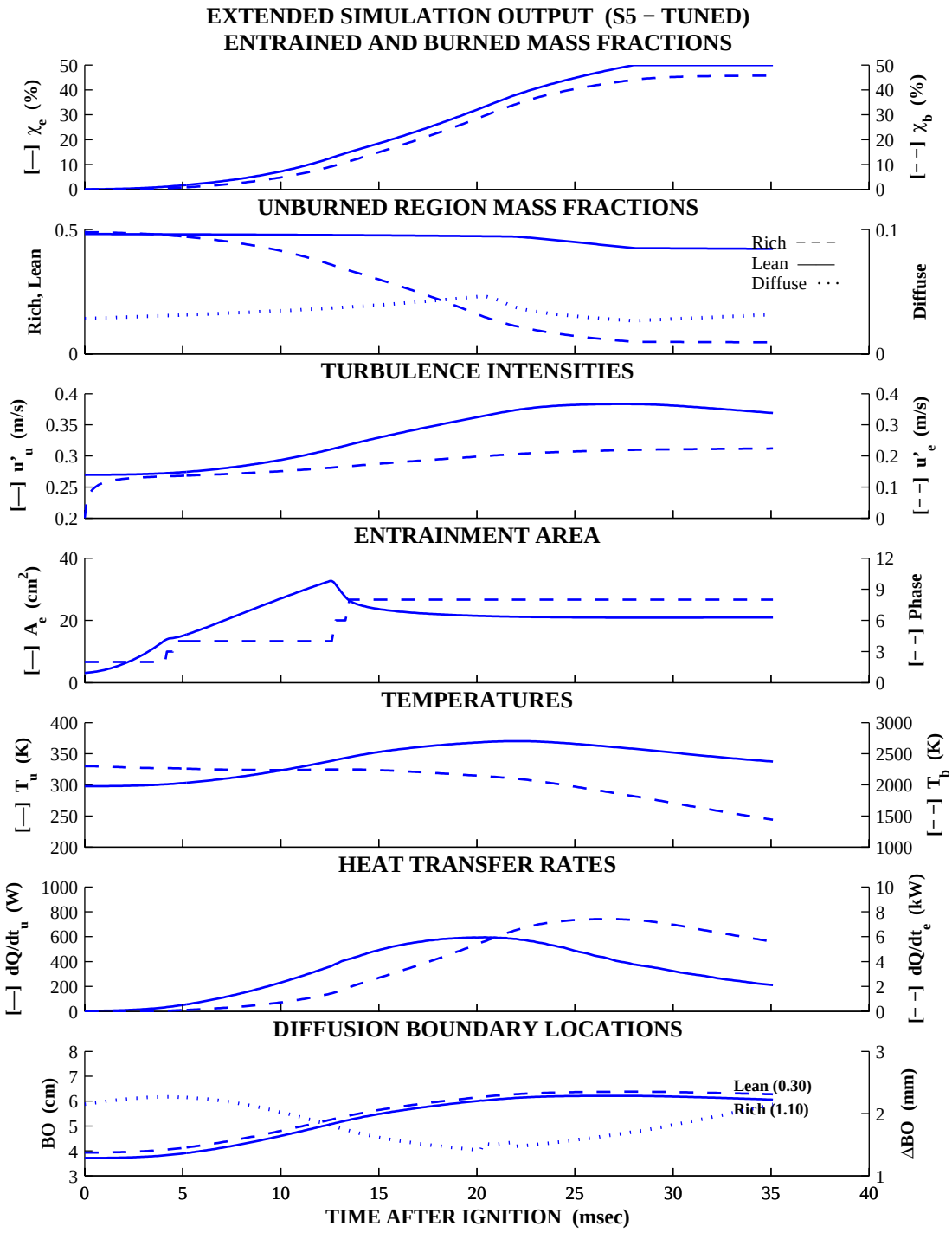

Δt 0.10 msec, P_i 104 kPa, T_i 297 K, ϕ 0.70, DOS 0.57, u'_i 0.27 m/s, $x_{e,i}$ 0.047%, C_{hx} 1.54, K_d 1.10
T_{dev} 12.9 msec, T_{dur} n/a, $T_{end/ext}$ 35.1 msec

Figure 7.41: Tuned Stratified Simulation, Extended Output (Case S5)

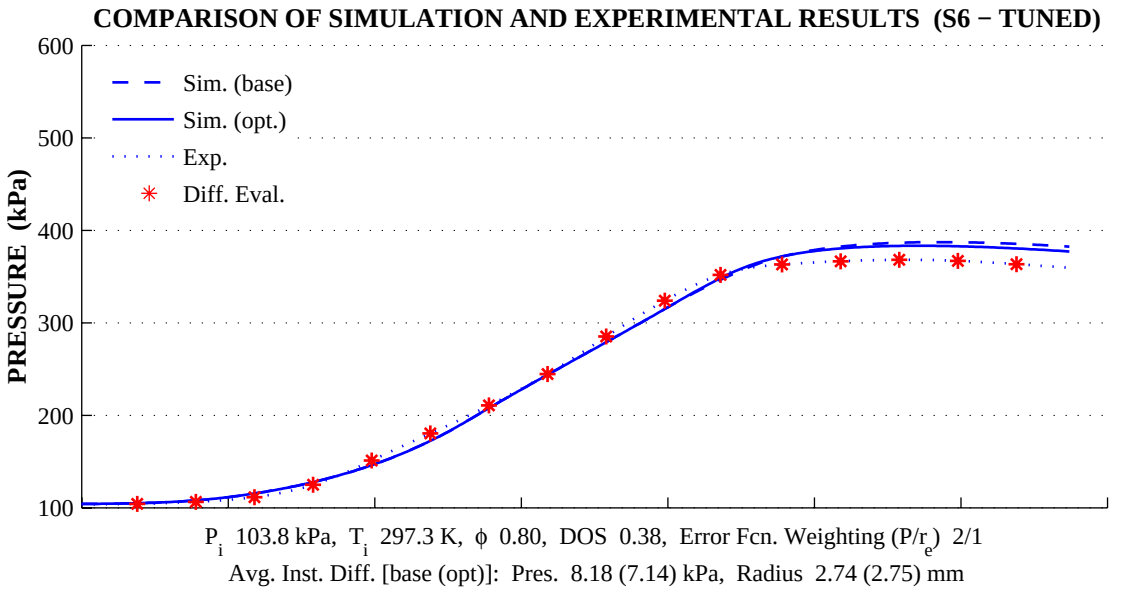

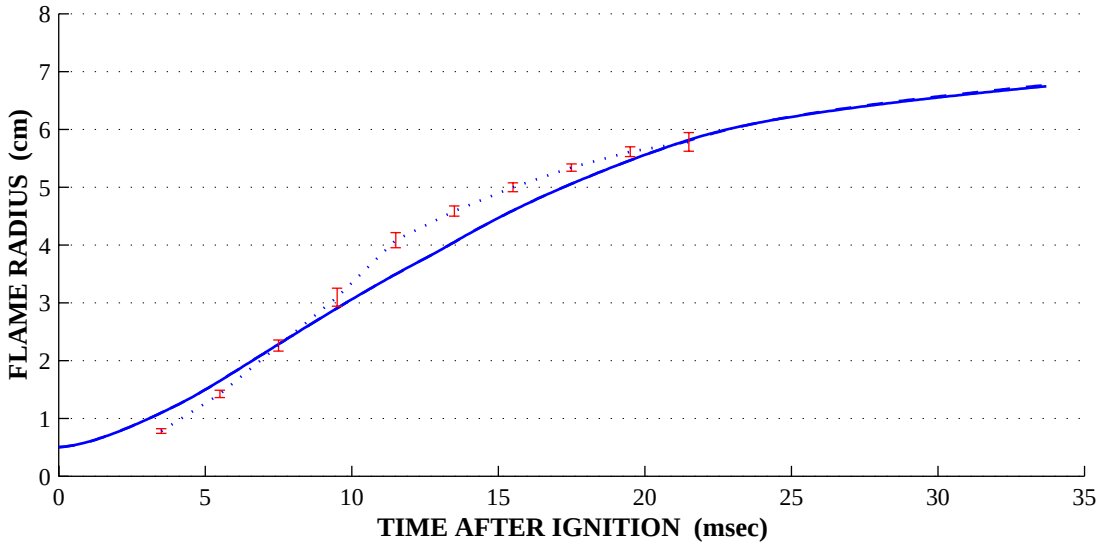

Figure 7.42: Tuned Stratified Simulation Results (Case S6)

FLAME FRONT AND DIFFUSE REGION DEVELOPMENT (S6 − TUNED)

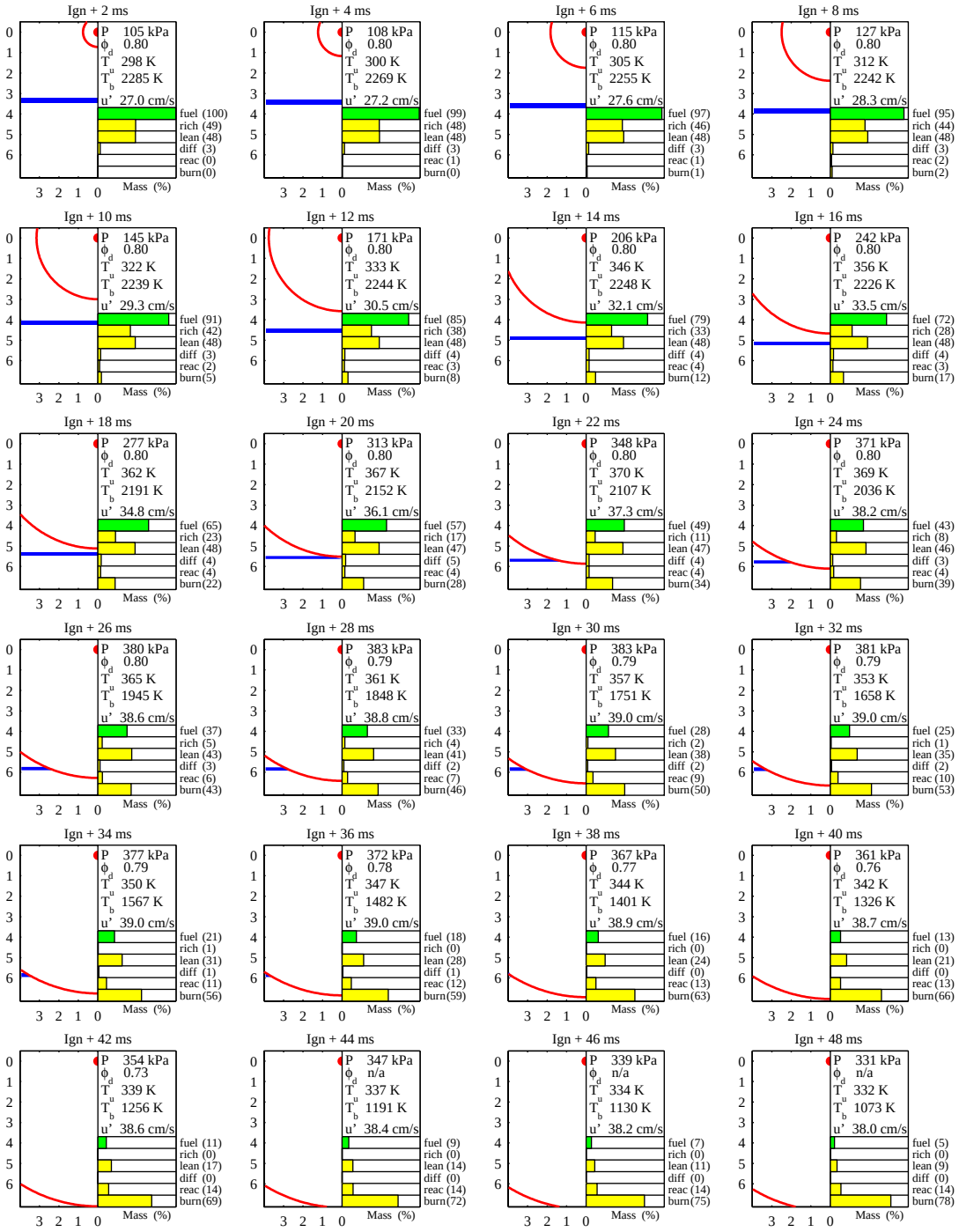

Δt 0.10 msec, P_i 104 kPa, T_i 297 K, ϕ 0.80, DOS 0.38, u'_i 0.27 m/s, $x_{e,i}$ 0.046%, C_{hx} 1.54, K_d 1.10
T_{dev} 12.9 msec, T_{dur} n/a, $T_{end/ext}$ 60.0 msec (Early burn termination due to mixture lean−out.)

Figure 7.43: Tuned Stratified Simulation, Flame Development (Case S6)

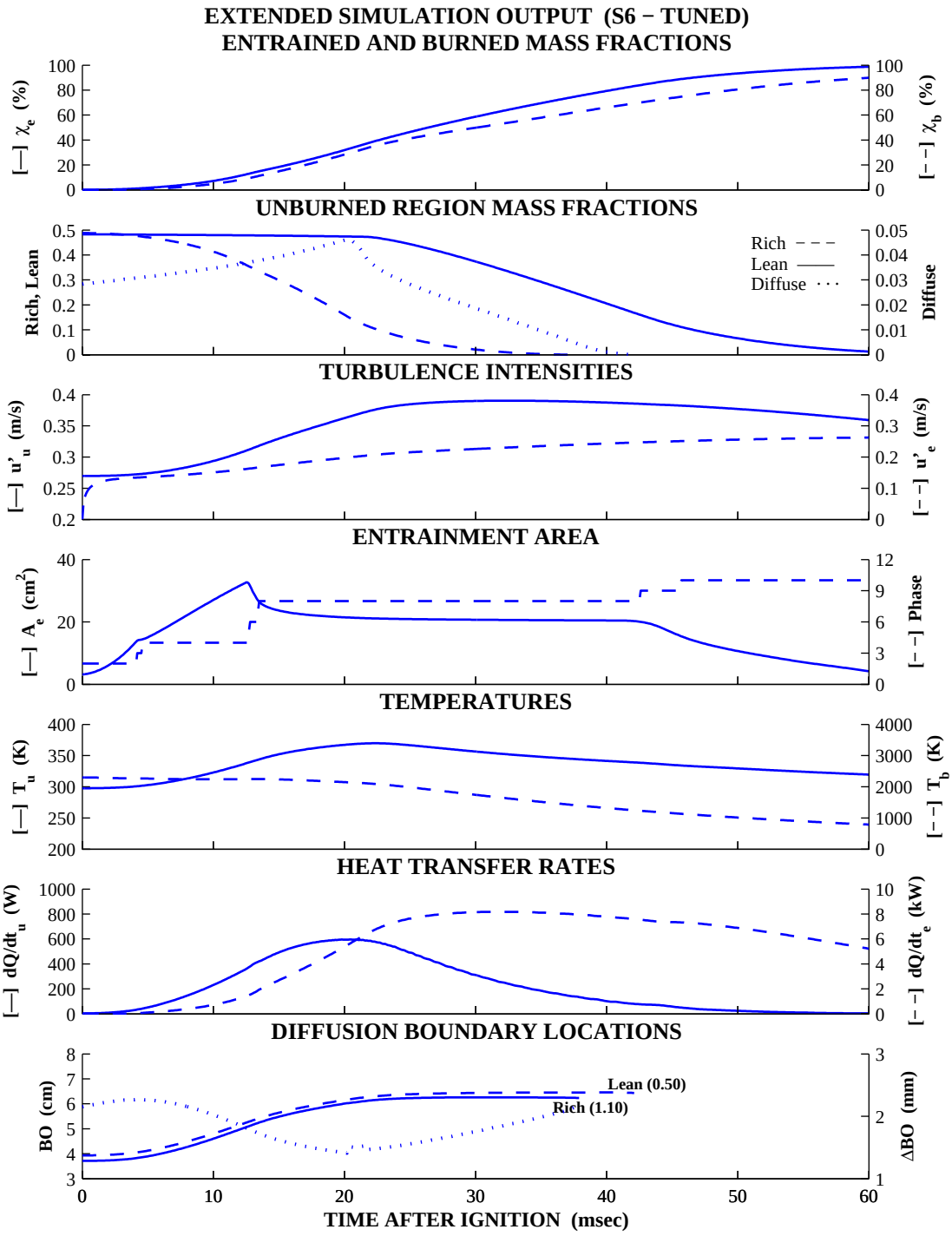

Δt 0.10 msec, P_i 104 kPa, T_i 297 K, ϕ 0.80, DOS 0.38, u'_i 0.27 m/s, $x_{e,i}$ 0.046%, C_{hx} 1.54, K_d 1.10
T_{dev} 12.9 msec, T_{dur} n/a, $T_{end/ext}$ 60.0 msec

Figure 7.44: Tuned Stratified Simulation, Extended Output (Case S6)

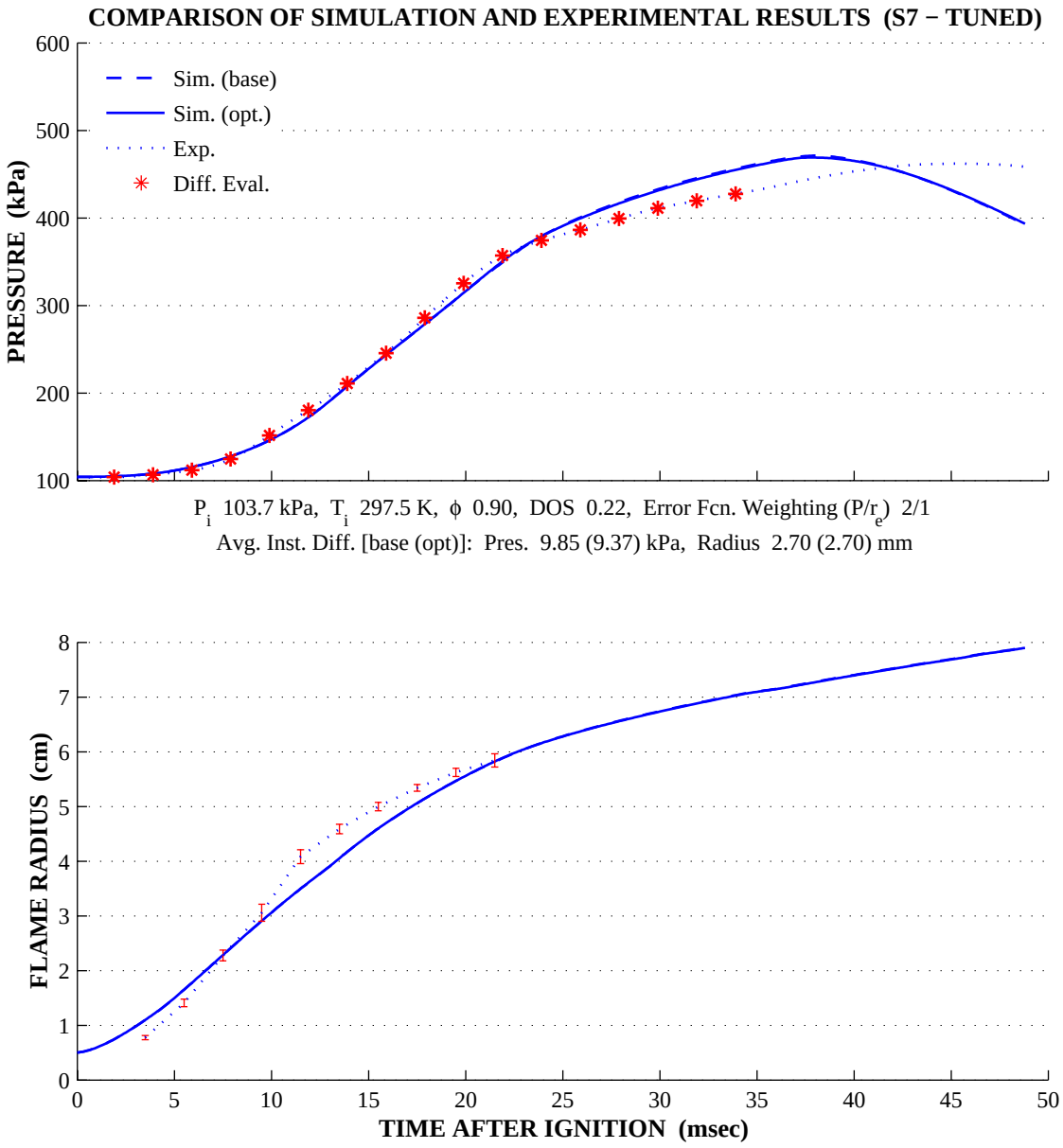

Figure 7.45: Tuned Stratified Simulation Results (Case S7)

FLAME FRONT AND DIFFUSE REGION DEVELOPMENT (S7 − TUNED)

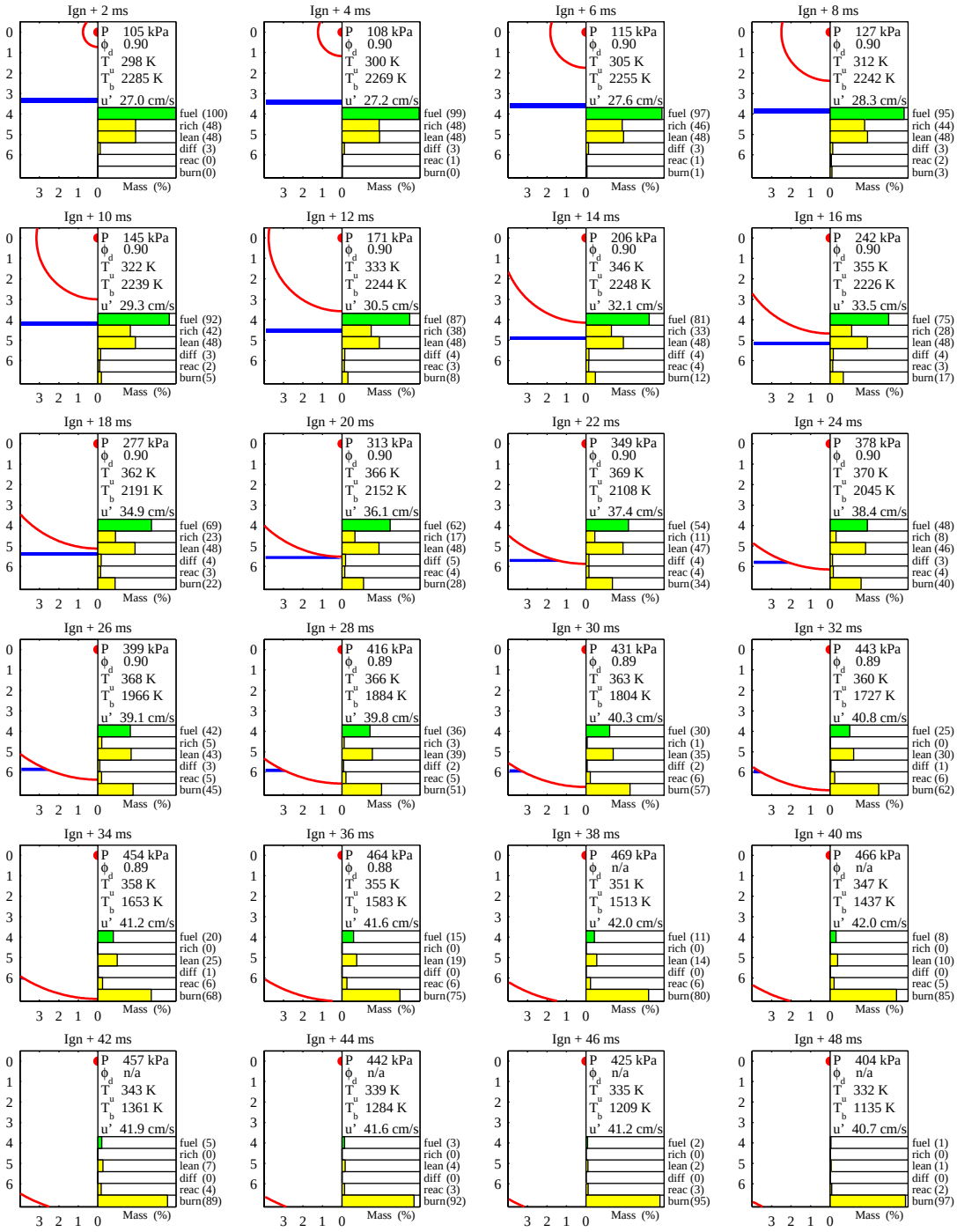

Δt 0.10 msec, P_i 104 kPa, T_i 297 K, ϕ 0.90, DOS 0.22, u'_i 0.27 m/s, $x_{e,i}$ 0.047%, C_{hx} 1.54, K_d 1.10
T_{dev} 12.9 msec, T_{dur} 29.4 msec, $T_{end/ext}$ 49.6 msec

Figure 7.46: Tuned Stratified Simulation, Flame Development (Case S7)

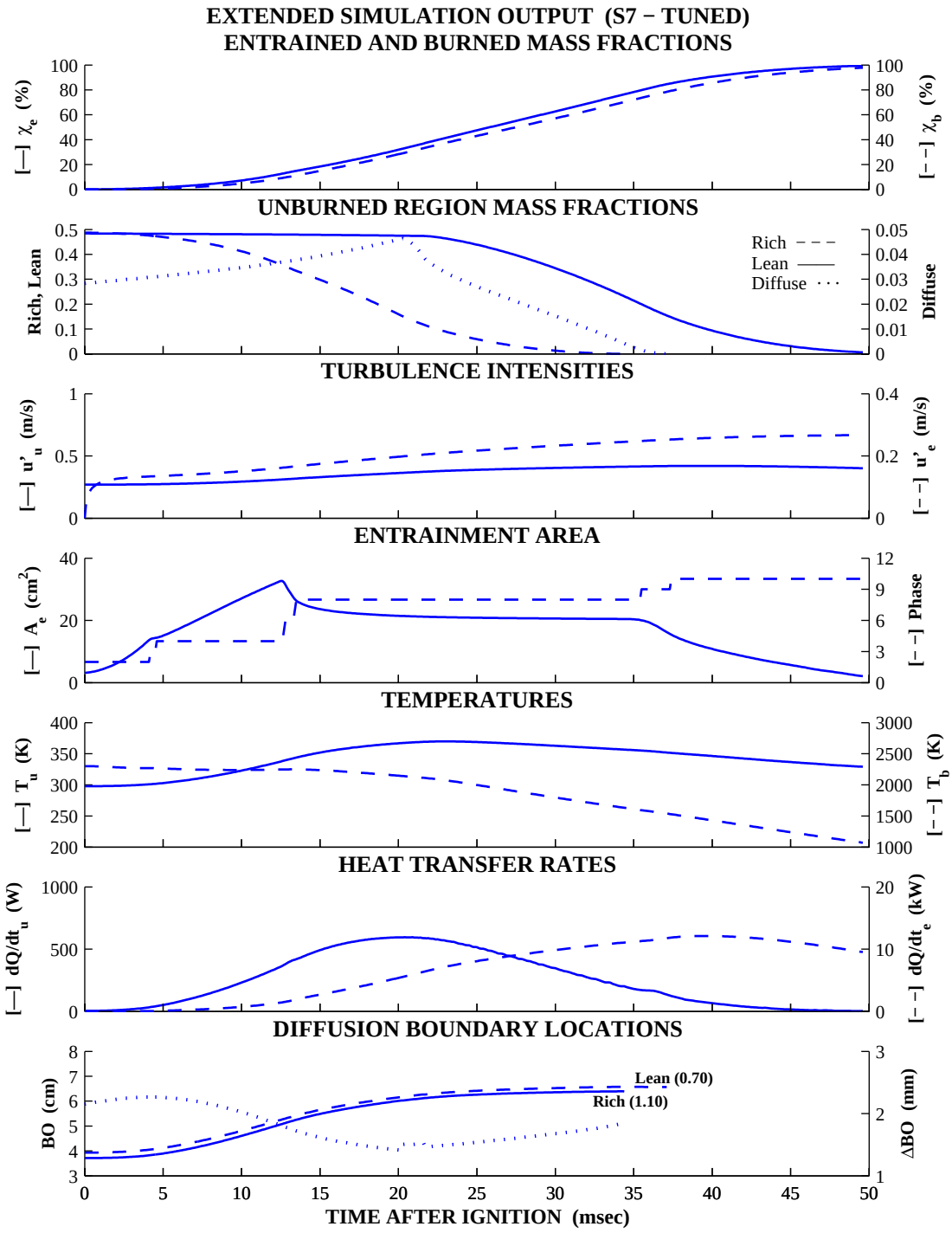

Δt 0.10 msec, P_i 104 kPa, T_i 297 K, ϕ 0.90, DOS 0.22, u'_i 0.27 m/s, $x_{e,i}$ 0.047%, C_{hx} 1.54, K_d 1.10
T_{dev} 12.9 msec, T_{dur} 29.4 msec, $T_{end/ext}$ 49.6 msec

Figure 7.47: Tuned Stratified Simulation, Extended Output (Case S7)

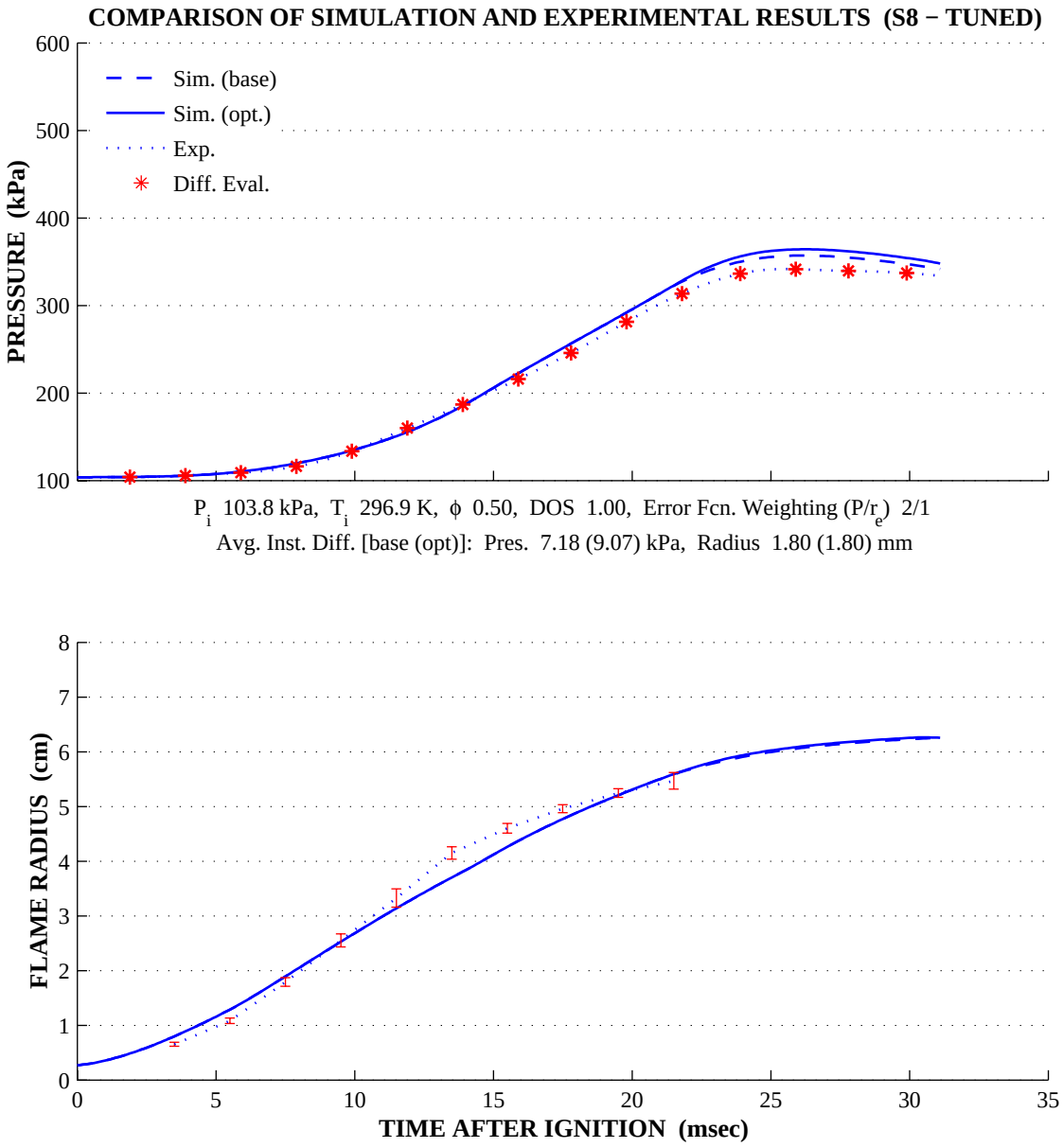

Figure 7.48: Tuned Stratified Simulation Results (Case S8)

FLAME FRONT AND DIFFUSE REGION DEVELOPMENT (S8 − TUNED)

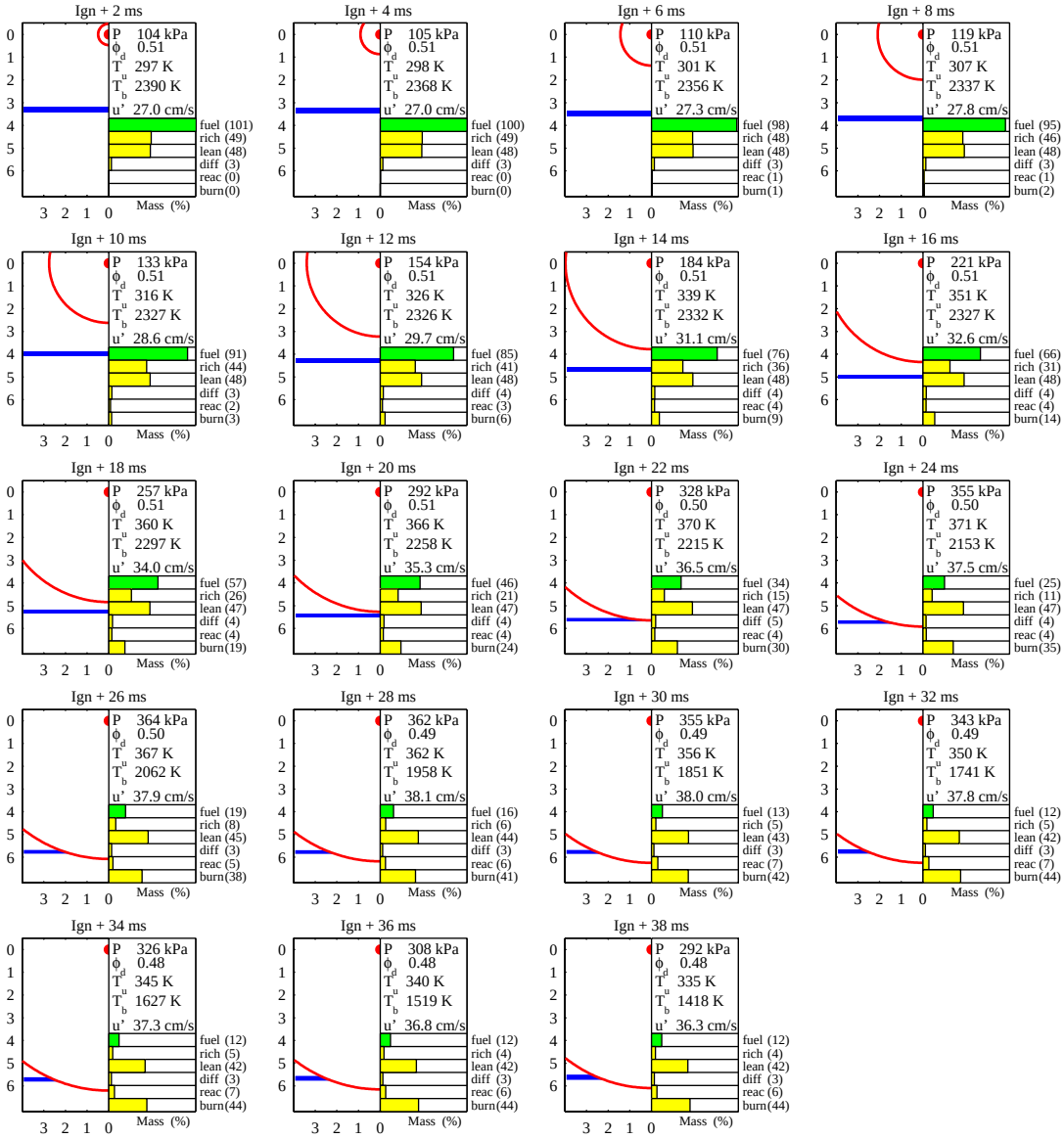

Δt 0.10 msec, P_i 104 kPa, T_i 297 K, ϕ 0.50, DOS 1.00, u'_i 0.27 m/s, $x_{e,i}$ 0.007%, C_{hx} 1.54, K_d 1.10
T_{dev} 14.2 msec, T_{dur} n/a, $T_{end/ext}$ 39.8 msec (Early burn termination due to mixture lean−out.)

Figure 7.49: Tuned Stratified Simulation, Flame Development (Case S8)

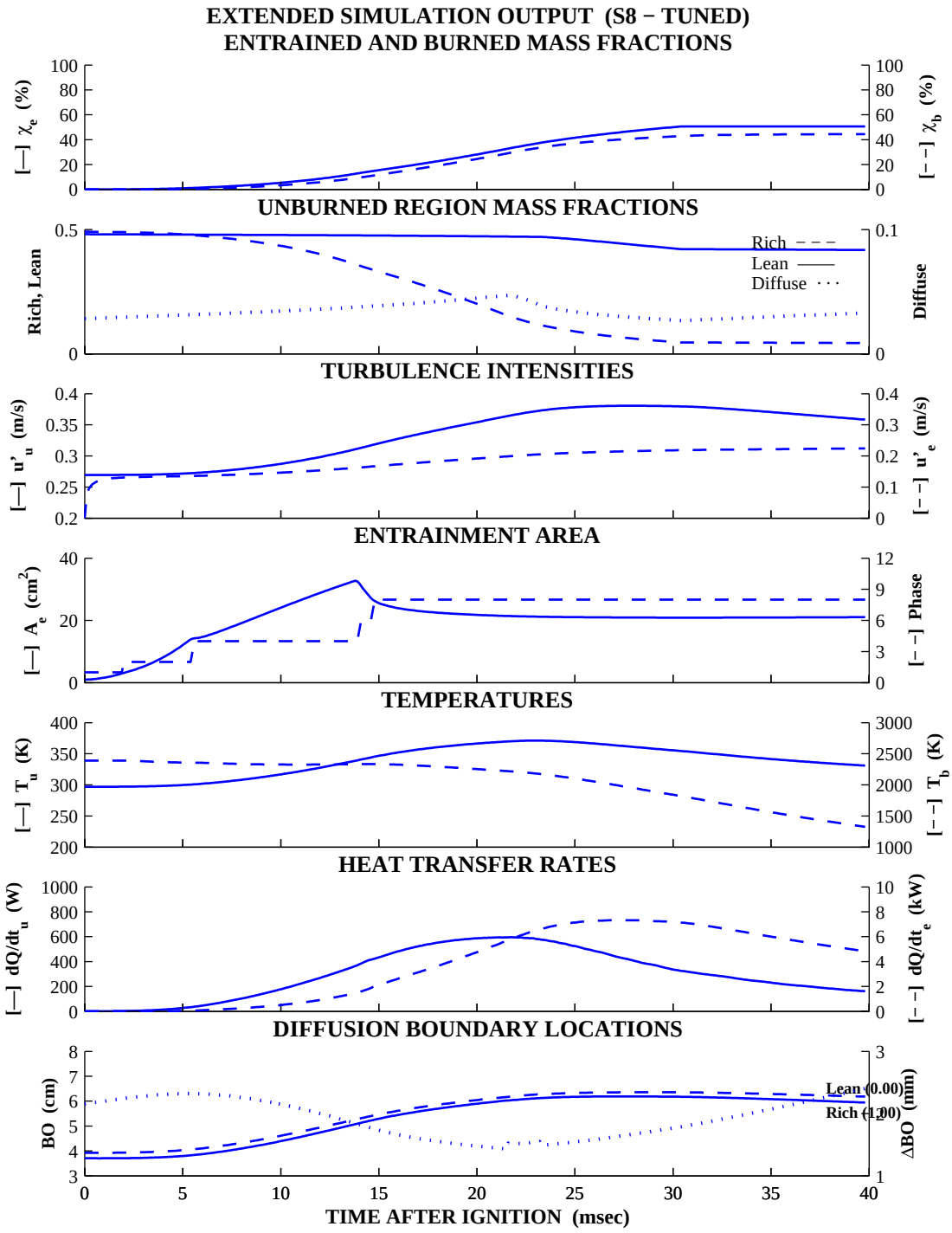

Δt 0.10 msec, P_i 104 kPa, T_i 297 K, ϕ 0.50, DOS 1.00, u'_i 0.27 m/s, $x_{e,i}$ 0.007%, C_{hx} 1.54, K_d 1.10
T_{dev} 14.2 msec, T_{dur} n/a, $T_{end/ext}$ 39.8 msec

Figure 7.50: Tuned Stratified Simulation, Extended Output (Case S8)

7.3.2 Tuning – Structural Modification

One modification is made to evaluate the treatment of the burned zone as a mixture of rich and lean products. A trial run with modified code, allowing the rich and lean products to mix and the rich products (CO and H_2) to oxidize more completely, shows increased error in all cases. The result must be labeled as inconclusive since the proper amount of mixing and degree of the secondary reaction (target equivalence of the mixed products) to allow are not clear.

7.4 Assessing the Initial Level of Model Detail

Based on the results presented in this chapter, the stratified model is clearly a success. This first iteration of this simplified approach succeeds in capturing in large part, the essential nature of the physical processes. This is accomplished with straightforward additions to the well-established homogeneous "*turbulent entrainment and laminar burnout model*." The downside of simplification is illustrated in cases S4 and S7 where the current level of detail is shown insufficient to accurately predict behavior in all cases. Additional complexity can be added to improve performance but for an initial attempt at simplified modeling of this combustion process, the level of complexity appears to be well chosen.

CHAPTER 8

EXTENSIONS AND CONCLUSION

This chapter opens with a discussion of the possible extension of the work accomplished thus far and concludes by judging the overall success of the exercise. Issues affecting the accuracy of experimental data from the CVCC test stand are addressed first. Suggestions are made that may improve the quality of data from any additional test cases run in follow-up studies. Recommendations are made for changes to the fixed chamber geometry model that might be wise to implement and evaluate before moving to the more general case. Several issues are considered that might arise as the model is extended to the more involved case of the IC engine. The chapter closes with an evaluation of the overall modeling effort success in satisfying the goals put forth in Chapter 1.

8.1 Improvements for CVCC Test Stand Data

The CVCC test stand may be used to obtain data for additional test cases in follow-up studies. Several hardware issues may be addressed if time permits in order to improve data quality and qualify experimental errors.

8.1.1 Equivalence Measurement

Mixture equivalences at present are computed from pressure readings taken as the sub-tanks are filled with fuel and oxidizer. A direct measurement is suggested to verify the accuracy

of the reported values and quantify the magnitude of the error. Theoretical measurement error is a function of the pressure transducer full-scale error and drift and any signal noise present at the time readings are made through the data acquisition system. An analysis of five samples each at two different equivalence settings (minimum and maximum of the test matrix) would establish the range of error in mixture consistency. In the case that the error is judged excessive it is possible to adjust hardware settings and provide a higher degree of control at the expense of increased delay.

8.1.2 Turbulence Measurement

The initial turbulence is estimated from a measurement of the mixing paddle speed but no direct measurement of turbulence or integral length scale has been made. The turbulence intensity was one parameter extracted from the experimental data during homogeneous model tuning and this is not as desirable as a direct measurement. It is strongly recommended that the mixing control system be calibrated against direct turbulence measurements and that the assumption of isotropic turbulence be validated. LDV measurements at three of four points on one side of the partition should be sufficient to establish the spatial uniformity of the turbulence. The decay might also be measured at one point until ignition if a suitable seeding material is available. This will allow tuning of the turbulence sub-model and also allow simulation of cases where the mixture regions are allowed to mingle for a period before ignition.

8.1.3 Imaging Sensitivity

The noted absence of a visible flame in late in cases S4 and S7 complicates the analysis. If this is simply a matter of camera sensitivity then modification of the current system or replacement with an alternate system is in order.

8.2 Suggestions for Continued Model Development

Suggestions for continued model development are put forth in this section. The current fixed geometry CVCC model is discussed first. Some recommendations apply only to fixed geometry chambers and others are more general, for application to any chamber geometry. Several major challenges to address in extending the model for IC engine use are also identified and discussed.

8.2.1 Additional Experimental Cases

Test cases may be run for a more telling test of the diffusion region treatment. In the cases here, the diffuse region does not attain a significant size. Experimental cases can be run with a range of delay periods after the mixtures are conjoined and before the spark is delivered. The reason for this test is to evaluate whether it is reasonable to treat the diffuse region as having a uniform equivalence. It should be possible to determine if there is a need to include the effect of the equivalence gradient or if the simple treatment is satisfactory for the particular experimental chamber.

8.2.2 Fixed Geometry Improvements

It is possible that further development of the current model for the fixed geometry case may reduce the total effort required to produce a model for general application. Adding detail to improve performance and working out any bugs that are introduced in the process will be easier before adding the further complexities of variable geometry, etc. for the IC engine. A dominant concern in the initial formulation was simplicity. The goal in any change should be to increase the level of complexity only as much as is absolutely necessary to achieve the desired effect. The goal may be improved predictive accuracy or added versatility such as the ability to model other simple chamber geometries.

The noted shortcomings of the heat transfer model and too simplistic flame geometry sub-models are two likely targets for improvement. Changes to these components in addition to explicit accounting for mass burning in the near-wall regime may allow the model to predict behavior after significant flame contact with the walls. This is essential before the model can be extended to the IC engine where one of the possibilities is a study of combustion efficiency for a of piston and chamber geometry combinations. The noted errors in cases S4 and S7 may be eliminated if these changes are made. If late errors in all cases are not reduced to an acceptable level then the next suggested step is to consider the effects of secondary reaction in the burned zone (rich and lean mixing and CO or H_2 oxidation).

8.2.3 Extension to the IC Engine

It is not possible to address in detail the application of the current model structure to an IC engine. The discussion is limited to several major challenges that must be overcome in order to apply the simple model concept to the more complicated case.

The method described in Section 3.2.2 for building flame geometry lookup tables cannot be used. The ignition center may be displaced over time. Even if fixed, it would still be necessary to build a table for the valid range of flame radii at each piston position. A similar method can be used on the fly although the code must be streamlined. Inputs to the function are then zone volume, piston position, ignition center location and rich mixture core boundary information. Outputs are flame radius, entrainment area and heat transfer areas. Two such calls to the proposed function are required since the ignition center is free to move. The first call updates information on the rich mixture core center and radius (assuming the region is modeled as a simple sphere). The second call does the same for the enflamed volume. This method allows the entrained volume and rich core volumes to have different centers and is more advanced than

the use of two concentric cylinders to represent the growing entrained volume within an also expanding (with diffusion) rich mixture core.

A second major issue is that of the change in fuel type from gaseous to liquid. Direct injection of liquid fuel can lead to a burning mode that is similar to the diffusion flame of a diesel engine [26]. The same geometry model may be employed in these cases but a multi-mode burning model may be required with options of turbulent entrainment and laminar burnout, diffusion burning and possibly a mixture of the two.

8.3 Conclusion

The modest goals outlined in Chapter 1 are satisfied in the following body of work. A new formulation for a simplified stratified-charge combustion model is developed. Well-established modeling techniques are applied to reduce the complexities to a manageable level by using a simplifying logic similar to that observed in the reduction of the homogeneous case by past researchers. The model is structured to allow those familiar with existing homogeneous models to quickly grasp the nature of the new formulation. The model is validated against experimental data from simple geometry CVCC. Simulation results for pressure and flame radius match well with the experimental data. The timing of key events is also predicted with relative accuracy. Significant errors are observed only in the period where the model is predicted to break down. The positive results show that it should be possible to capture the essential characteristics of stratified-charge combustion in a simple model, given adequate development time. It is clear at least that the promise exists.

BIBLIOGRAPHY

1. Agarwal, A., Filipi, Z. S., Assanis, D. N. and Baker, D. M. (1998). "Assessment of Single- and Two-Zone Turbulence Formation for Quasi-Dimensional Modeling of Spark-Ignition Engine Combustion," *Combustion Science and Technology*, Vol. 136, issue 1-6, pp. 13-39.

2. Anbarasu, M., Abata, D. L. and Moilanen, P. C. (1994). "Modeling of Early Pressure Rise and Flame Growth in a Spark Ignition Engine," *SAE Paper* 941930.

3. Arcoumanis, D.R. and Bae, C.S. (1993). "Visualization of Flow/Flame Interaction in a Constant-Volume Combustion Chamber," *SAE Paper* 930868.

4. Baritaud, T. A., Duclos, J. M. and Fusco, A. (1996). "Modeling Turbulent Combustion and Pollutant Formation in Stratified Charge SI Engines," *Twenty-Sixth Symposium. (Intl.) on Combustion*, pp. 2627-2635, The Combustion Institute.

5. Beretta, G. P., Rashidi, M. and Keck, J. C. (1983). "Turbulent Flame Propagation and Combustion in Spark Ignition Engines," *Combustion and Flame*, Vol. 52, pp. 217-245.

6. Blizard, N. C. and Keck, J. C. (1974). "Experimental and Theoretical Investigation of Turbulent Burning Model for Internal Combustion Engines," *SAE Paper* 740191.

7. Blumberg, P. N., Lavoie, G. A. and Tabaczynski, R. J. (1979). "Phenomenological Models for Reciprocating Internal Combustion Engines," *Progress in Energy and Combustion Science*, Vol. 5, pp. 123-167.

8. Borgnakke, C., Arpaci, V. S. and Tabaczynski, R. J. (1980). "A Model for the Instantaneous Heat Transfer and Turbulence in a Spark Ignition Engine," *SAE Paper* 800027.

9. Butler, T. D., Cloutman, L. D., Dukowicz, J. K. and Ramshaw, J. D. (1980). "Toward a Comprehensive Model for Combustion in a Direct Injection Stratified Charge Engine," in J.N. Mattavi and C. A. Amann (eds.), Combustion Modeling in Reciprocating Engines, pp. 231-260, Plenum Press.

10. Chen, C. and Veshagh A. (1992). "A Refinement of Flame Propagation Combustion Model for Spark-Ignition Engines," *SAE Paper* 920679.

11. Dai, W., Davis, G. C., Hall, M. J. and Matthews, R. D. (1995). "Diluents and Lean Mixture Combustion Modeling for SI Engines with a Quasi-Dimensional Model," *SAE Paper* 952382.

12. Fan, L. Li, G., Han, Z. and Reitz, R. D. (1999). "Modeling Fuel Preparation and Stratified Combustion in a Gasoline Direct Injection Engine," *SAE Paper* 1999-01-0175.

13. Fujimoto, M., Nishida, K., Hiroyasu, H. and Tabata, M. (1995). "Influence of Mixture Stratification Pattern on Combustion Characteristics in a Constant-Volume Combustion Chamber," *SAE Paper* 952412.

14. Furuno, S., Iguchi, S. and Inoue, T. (1995). "Lean Combustion Characteristics of Locally Stratified Charge Mixture: Basic Studies of In-Vessel Combustion Ignited by Laser," *JSAE Paper* 9537925.

15. Hara, H., Komoriya, H., Ikebe, H. and Iwamiya, Y. (1996). "Lean-Burn Fuel Development Using the Correlation of CVCC and Test Data," *SAE Paper* 961158.

16. Harada, J., Tomita, T., Mitzuno, H., Mashiki, Z. and Ito, Y. (1997). "Development of Direct Injection Gasoline Engine," *SAE Paper* 970540.

17. Herweg, R. and Maly, R. R. (1992). "A Fundamental Model for Flame Kernel Formation in S.I. Engines," *SAE Paper* 922243.

18. Heywood, J.B. (1988). Internal Combustion Engine Fundamentals, McGraw-Hill, New York.

19. Incropera & Dewitt (1990). Introduction to Heat Transfer, Wiley, New York.

20. Iwamoto, Y., Noma, K., Nakayama, O.,Yamauchi, T. and Ando, H. (1997). "Development of Gasoline Direct Injection Engine," *SAE Paper* 970541.

21. Janes, N. (1998). "Design, Construction and Evaluation of a New High-Pressure Stratified Combustion Research Tool," MS Thesis, The Ohio State University.

22. Jennings, M. J. (1992). "Multi-Dimensional Modeling of Turbulent Pre-Mixed Charge Combustion," *SAE Paper* 920589.

23. Keck, J. C. (1982). "Turbulent Flame Structure and Speed in Spark Ignition Engines," *Nineteenth Symposium (Intl.) on Combustion*, pp. 1451-1466, The Combustion Institute.

24. Keck, J. C., Heywood, J. B. and Noske, G. (1987). "Early Flame Development and Burning Rates in Spark Ignition Engines," *SAE Paper* 870164.

25. Kume, T., Iwamoto, Y., Lida, K., Murakami, M., Akishino K. and Ando, H. (1996). "Combustion Control Technologies of Mitsubishi Direct SI Engine," *SAE Paper* 960600.

26. Kuwahara, K., Ueda, K. and Ando, H. (1998). "Mixing Control Strategy for Engine Performance Improvement in a Gasoline Direct Injection Engine," *SAE Paper* 980158.

27. Lumley, J.L. (1999). Engines, An Introduction, Cambridge University Press, Cambridge, UK.

28. Maly, R. (1981). "Ignition Model for Spark Discharges and Early Phase of Flame Front Growth," *Eighteenth Symposium (Intl.) on Combustion*, pp. 1747-1754, The Combustion Institute.

29. Mathews, R. D., Hall, M. J., Dai, W. and Davis, G. C. (1996). "Combustion Modeling in SI Engines with a Peninsula-Fractal Combustion Model," *SAE Paper* 960072.

30. Matsuki, M., Nakano, K., Amemiya, T., Tanabe, Y., Shimizu, D. and Ohmura, I. (1996). "Development of a Lean-Burn Engine with a Variable Valve Timing Mechanism," *SAE Paper* 960583.

31. Metghalchi, M. and Keck, J. C. (1980). "Laminar Burning Velocity of Propane-Air Mixtures at High Temperature and Pressure," *Combustion and Flame*, Vol. 38, pp. 143-154.

32. Moryoshi, Y, Morikawa, H., Kamimoto, T. and Hayashi, T. (1996). "Combustion Enhancement of Very Lean Premixture Part in Stratified Charge Conditions," *SAE Paper* 962087.

33. Plackmann, J.D., Kim, T. and Ghandhi, J.B. (1998). "The Effects of Mixture Stratification on Combustion in a Constant-Volume Combustion Vessel," *SAE Paper* 980159.

34. Robeck, C. M. and Ellzey, J. L. (1998). "Simulation of Stratified Combustion," *SAE Paper* 981454.

35. Shen, H., Hinze. P. C. and Heywood, J. B. (1994). "A Model for Flame Initiation and Early Development in SI Engine and its Application to Cycle-to-Cycle Variations," *SAE Paper* 942049.

36. Stone, R. (1995). Internal Combustion Engines, SAE, Warrendale, PA.

37. Tabaczynski, R. J., Ferguson, C. R. and Radhakrishnan, K. (1977). "A Turbulent Entrainment Model for Spark Ignition Engine Combustion," *SAE Paper* 770647.

38. Tabaczynski, R. J., Trinker, F. H. and Shannon, B. A. S. (1980). "Further Refinement and Validation of a Turbulent Entrainment Model for Spark Ignition Engine Combustion," *Combustion and Flame*, Vol. 39, pp. 111-121.

39. Tatschl, R. and Riediger, H. (1998). "PDF Modelling of Stratified SI Engine Combustion," *SAE Paper* 981464.

40. Ting, D. S-K, Checkel, M. D., Haley, R. and Smy, P. R. (1994). "Early Flame Acceleration Measurements in a Turbulent Spark-Ignited Mixture," *SAE Paper* 940687.

41. Woschni, G. and Anisits, F. (1974). "Experimental Investigation and Mathematical Presentation of Rate of Heat Release in Diesel Engines Dependent Upon Engine Operating Conditions," *SAE Paper* 720086.

42. Yossefi, D., Belmont, M. R., Thurley, R., Thomas, J. C. and Hacohen, J. (1993). "A Coupled Experimental-Theoretical Model of Flame Kernel Development in a Spark Ignition Engine," *SAE Paper* 932716.

43. Zhao, F-Q, Lai, M-C and Harrington, D.L. (1999). "Automotive Spark-Ignited Direct-Injection Gasoline Engines," *Progress in Energy and Combustion Science*, Vol. 25, pp. 437-562.

44. Zhao, X., Matthews, R. D. and Ellzey, J. L. (1993). "Three-Dimensional Numerical Simulation of Flame Propagation in Spark Ignition Engines," *SAE Paper* 932713.

APPENDIX A

THERMODYNAMIC PROPERTY DATA

Original data and simplified curve-fits used in the model for evaluation of thermodynamic properties are included in this appendix. Included is stainless steel (ignition electrode) specific heat [Figure A.1 and Table A.1] and kinematic viscosity of air data from Incropera and Dewitt [19] [Figure A.2 and Table A.2]. Also included is reduced JANAF table data from Heywood [18] for typical fuel types and the six species of the combustions products model [Table A.3 and Table A.4].

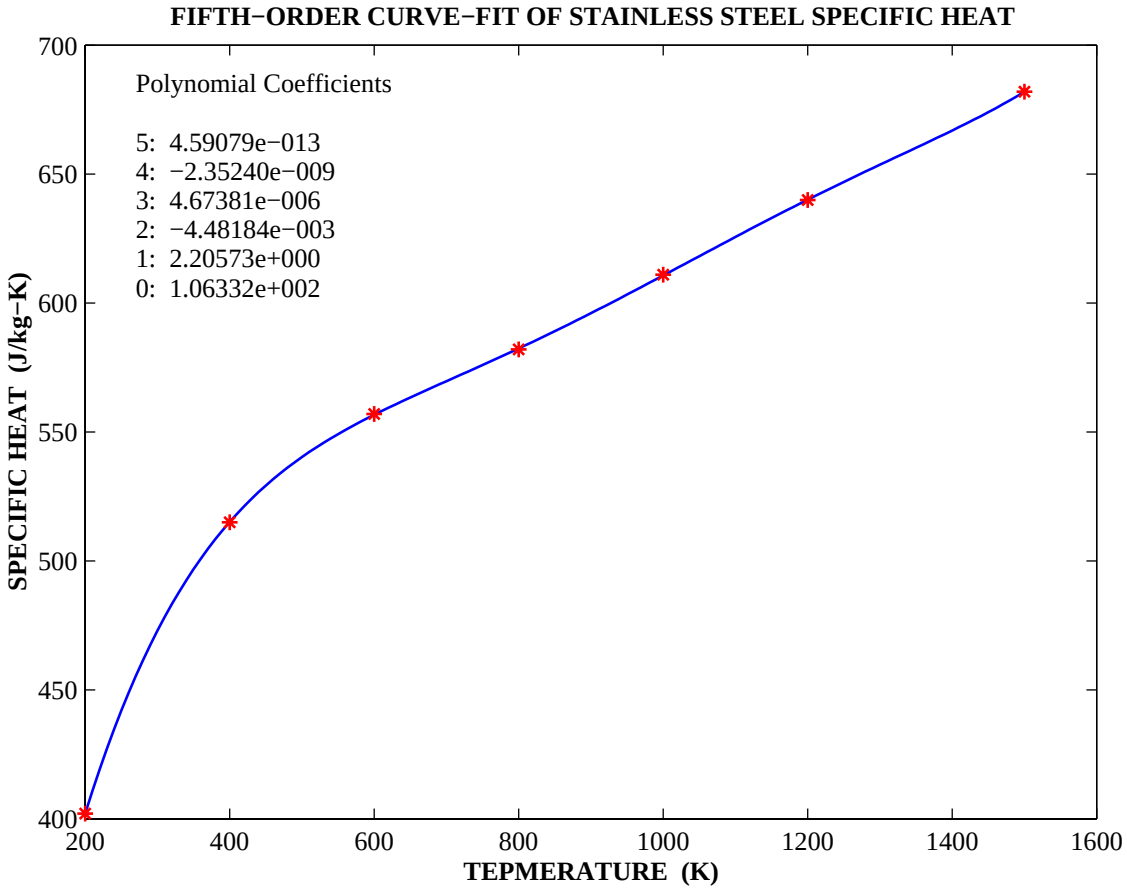

Figure A.1: Curve-Fit of Ignition Electrode Specific Heat Data

Temperature (K)	200	400	600	800	1000	1200	1500
Specific Heat (J/kg-K)	402	515	557	582	611	640	682

Table A.1: Ignition Electrode Specific Heat (Incropera & Dewitt)

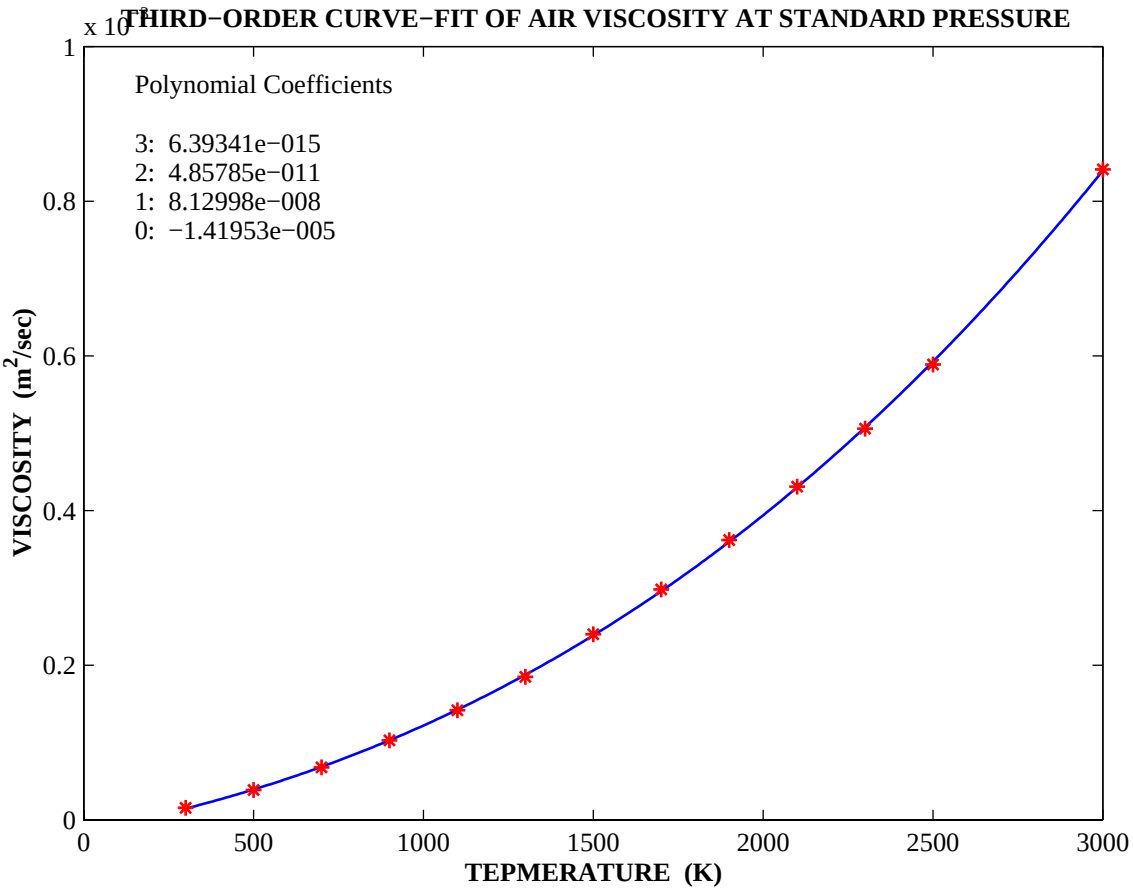

Figure A.2: Curve-Fit of Kinematic Viscosity Data for Air at Ambient Pressure

Temperature (K)	300	500	700	900	1100	1300	1500
Viscosity (m^2/sec)	15.89	38.79	68.10	102.9	141.8	185.1	240
Temperature (K)	1700	1900	2100	2300	2500	3000	
Viscosity (m^2/sec)	298	362	431	506	589	841	

Table A.2: Kinematic Viscosity of Air at Ambient Pressure (Incropera & Dewitt)

Thermodynamic properties are evaluated for a particular species at any temperature using curve fits of JANAF table data given in Heywood [18]. Enthalpies and specific heats for each mixture species and various fuel types are given by the following equations.

$$\frac{\tilde{h}_i}{\tilde{R}\cdot T} = a_{i1} + \frac{a_{i2}\cdot T}{2} + \frac{a_{i3}\cdot T^2}{3} + \frac{a_{i4}\cdot T^3}{4} + \frac{a_{i5}\cdot T^4}{5} + \frac{a_{i6}}{T} \tag{A.1}$$

$$\frac{\tilde{c}_{p,i}}{\tilde{R}} = a_{i1} + a_{i2}\cdot T + a_{i3}\cdot T^2 + a_{i4}\cdot T^3 + a_{i5}\cdot T^4 \tag{A.2}$$

$$\tilde{h}_{fuel} = A_{f1}\cdot t + \frac{A_{f2}\cdot t^2}{2} + \frac{A_{f3}\cdot t^3}{3} + \frac{A_{f4}\cdot t^4}{4} - \frac{A_{f5}}{t} + A_{f6} + A_{f8} \tag{A.3}$$

$$\tilde{c}_{p,\,fuel} = A_{f1} + A_{f2}\cdot t + A_{f3}\cdot t^2 + A_{f4}\cdot t^3 + \frac{A_{f5}}{t^2} \tag{A.4}$$

$$t = \frac{T}{1000}$$

Units for exhaust species are cal/gmol·K and kcal/gmol (tilde in this section indicates molar basis) for specific heat and enthalpy respectively. Temperature input in all cases is in degrees Kelvin and as indicated the value is scaled by a factor of one thousand for the fuel expressions. The fuel enthalpy expression is based on a 0K datum. Dropping the eighth term gives the value based on a 298K datum.

Table A.3: Coefficients for Species Thermodynamic Property Evaluation (Heywood)

Species	Temp., K	a_{f1}	a_{f2}	a_{f3}	a_{f4}	a_{f5}	a_{f6}	a_{f7}
$C0_2$	300-1000	0.44608(+1)	0.30982(-2)	-0.12393(-5)	0.22741(-9)	-0.15526(-13)	-0.48961(+5)	-0.98636(0)
	1000-5000	0.24008(+1)	0.87351(-2)	-0.66071(-5)	0.20022(-8)	0.63274(-15)	-0.48378(+5)	0.96951(+1)
H_2O	300-1000	0.27168(+1)	0.29451(-2)	-0.80224(-6)	0.10227(-9)	-0.48472(-14)	-0.29906(+5)	0.66306(+1)
	1000-5000	0.40701(+l)	-0.11084(-2)	0.41521(-5)	-0.29637(-8)	0.80702(-12)	-0.30280(+5)	-0.32270(0)
CO	300-1000	0.29841(+1)	0.14891(-2)	-0.57900(-6)	0.10365(-9)	-0.69354(-14)	-0.14245(+5)	0.63479(+1)
	1000-5000	0.37101(+1)	-0.16191(-2)	0.36924(-5)	-0.20320(-8)	0.23953(-12)	-0.14356(+5)	0.29555(+1)
H_2	300-1000	0.31002(+1)	0.51119(-3)	0.52644(-7)	-0.34910(-10)	0.36945(-14)	-0.87738(+3)	-0.19629(+1)
	1000-5000	0.30574(+1)	0.26765(-2)	-0.58099(-5)	0.55210(-8)	-0.18123(-11)	-0.98890(+3)	-0.22997(+1)
0_2	300-1000	0.36220(+1)	0.73618(-3)	-0.19652(-6)	0.36202(-10)	-0.28946(-14)	-0.12020(+4)	0.36151(+1)
	1000-5000	0.36256(+1)	-0.18782(-2)	0.70555(-5)	-0.67635(- 8)	0.21556(-11)	-0.10475(+4)	0.43053(+1)
N_2	300-1000	0.28963(+1)	0.15155(-2)	-0.57235(-6)	0.99807(-10)	-0.65224(-14)	-0.90586(+3)	0.61615(+1)
	1000-5000	0.36748(+1)	-0.12082(-2)	0.23240(-5)	-0.63218(-9)	-0.22577(-12)	-0.10612(+4)	0.23580(+1)
OH	1000-5000	0.29106(+1)	0.95932(-3)	-0.19442(-6)	0.13757(-10)	0.14225(-15)	0.39354(+4)	0.54423(+1)
NO	1000-5000	0.31890(+1)	0.13382(-2)	-0.52899(-6)	0.95919(-10)	-0.64848(-14)	0.98283(+4)	0.67458(+1)
O	1000-5000	0.25421(+1)	-0.27551(-4)	-0.31028(-8)	0.45511(-11)	-0.43681(-15)	0.29231(+5)	0.49203(+1)
H	1000-5000	0.25(+1)	0.0	0.0	0.0	0.0	0.25472(+5)	-0.46012(0)

Table A.4: Coefficients for Fuel Thermodynamic Property Evaluation (Heywood)

Fuel	Formula	Molecular Weight	$(A/F)_s$	$(F/A)_s$	A_{f1}	A_{f2}	A_{f3}	A_{f4}	A_{f5}	A_{f6}	A_{f8}
Methane	CH_4	16.04	17.23	0.0580	-0.29149	26.327	-10.610	1.5656	0.16573	-18.331	4.3000
Propane	C_3H_8	44.10	15.67	0.0638	-1.4867	74.339	-39.065	8.0543	0.01219	-27.313	8.852
Hexane	C_6H_{14}	86.18	15.24	0.0656	-20.777	210.48	-164.125	52.832	0.56635	-39.836	15.611
Isooctane	C_8H_{18}	114.2	15.14	0.0661	-0.55313	181.62	-97.787	20.402	-0.03095	-60.751	20.232
Methanol	CH_30H	32.04	6.47	0.1546	-2.7059	44.168	-27.501	7.2193	0.20299	-48.288	5.3375
Ethanol	C_2H_5OH	46.07	9.00	0.1111	6.990	39.741	-11.926	0	0	-60.214	7.6135
Gasoline	$C_{8.26}H_{15.5}$	114.8	14.64	0.0683	-24.078	256.63	-201.68	64.750	0.5808	-27.562	17.792
	$C_{7.76}H_{13.1}$	106.4	14.37	0.0696	-22.501	227.99	-177.26	56.048	0.4845	-17.578	15.235
Diesel	$C_{10.8}H_{18.7}$	148.6	14.4	0.0694	-9.1063	246.97	-143.74	32.329	0.0518	-50.128	23.514

APPENDIX B

EXPERIMENTAL DATA VALIDATION

Data validation figures for homogeneous cases H3, H4 and all stratified cases are included in this appendix (case H1 is included in Section 5.2.2) in Figure B.1through Figure B.9. As noted in the text, data is consistent in all cases with measured pressure rise deviations of less than two percent.

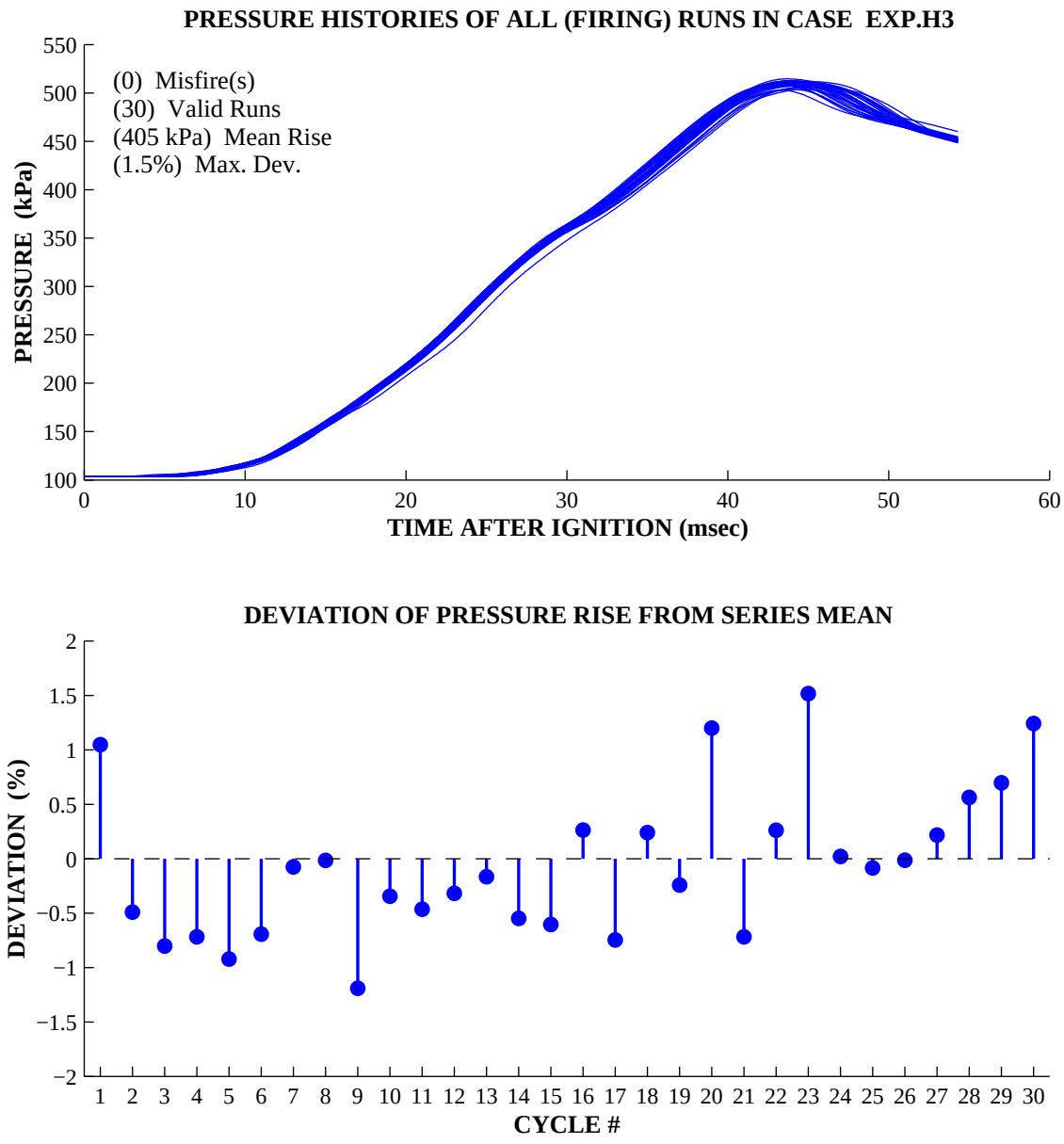

Figure B.1: Series Statistics for Experimental Case H3

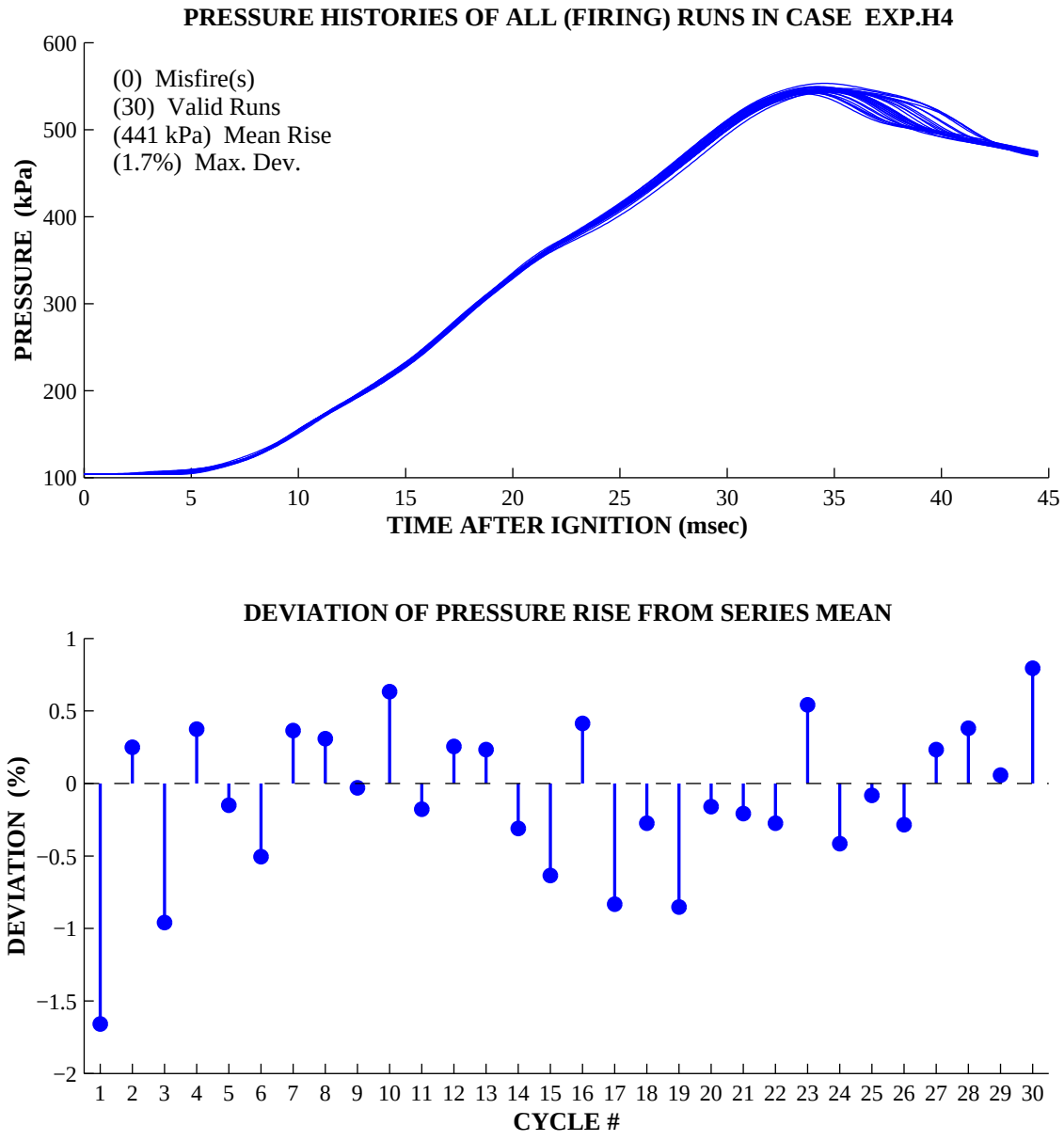

Figure B.2: Series Statistics for Experimental Case H4

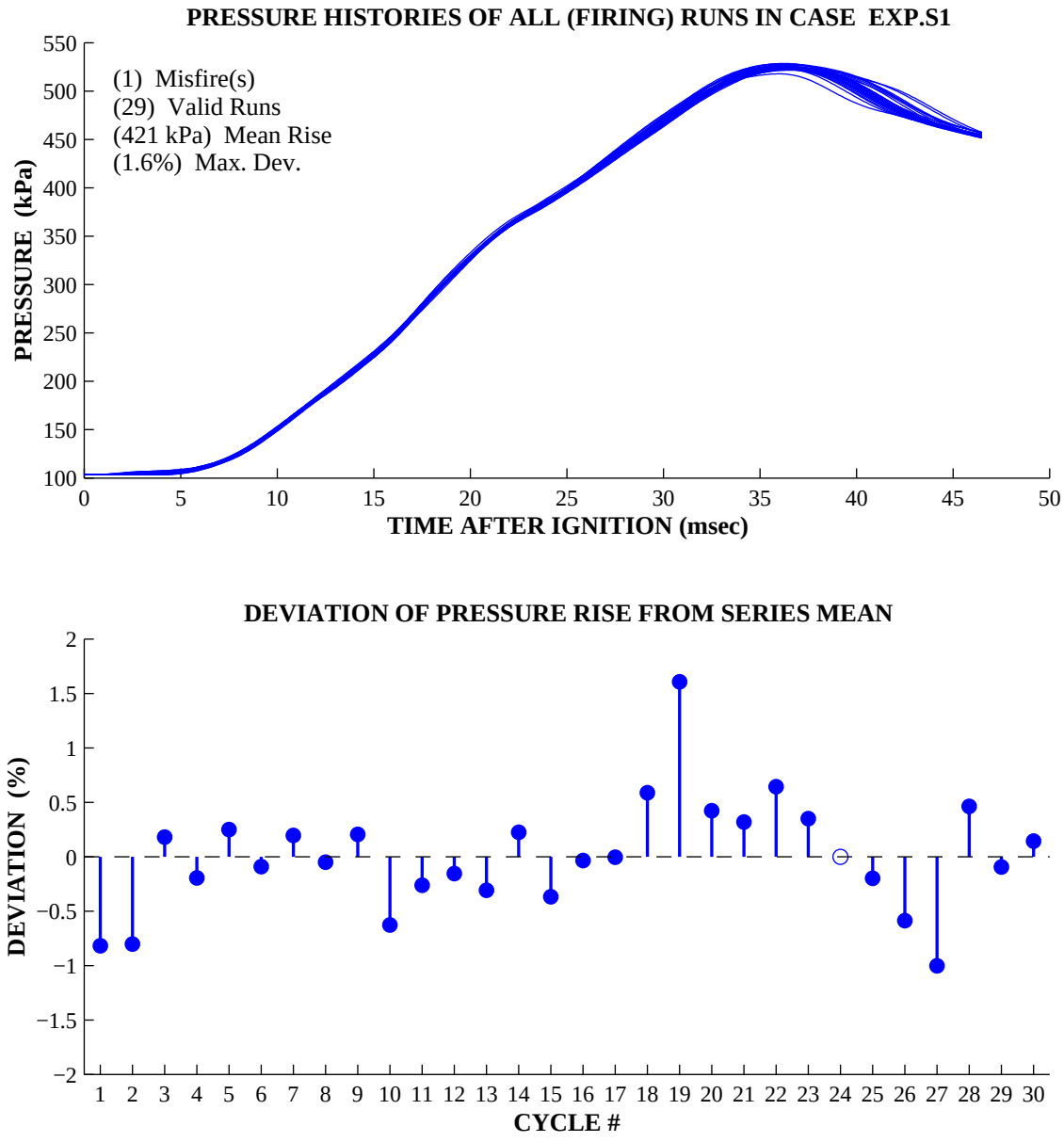

Figure B.3: Series Statistics for Experimental Case S1

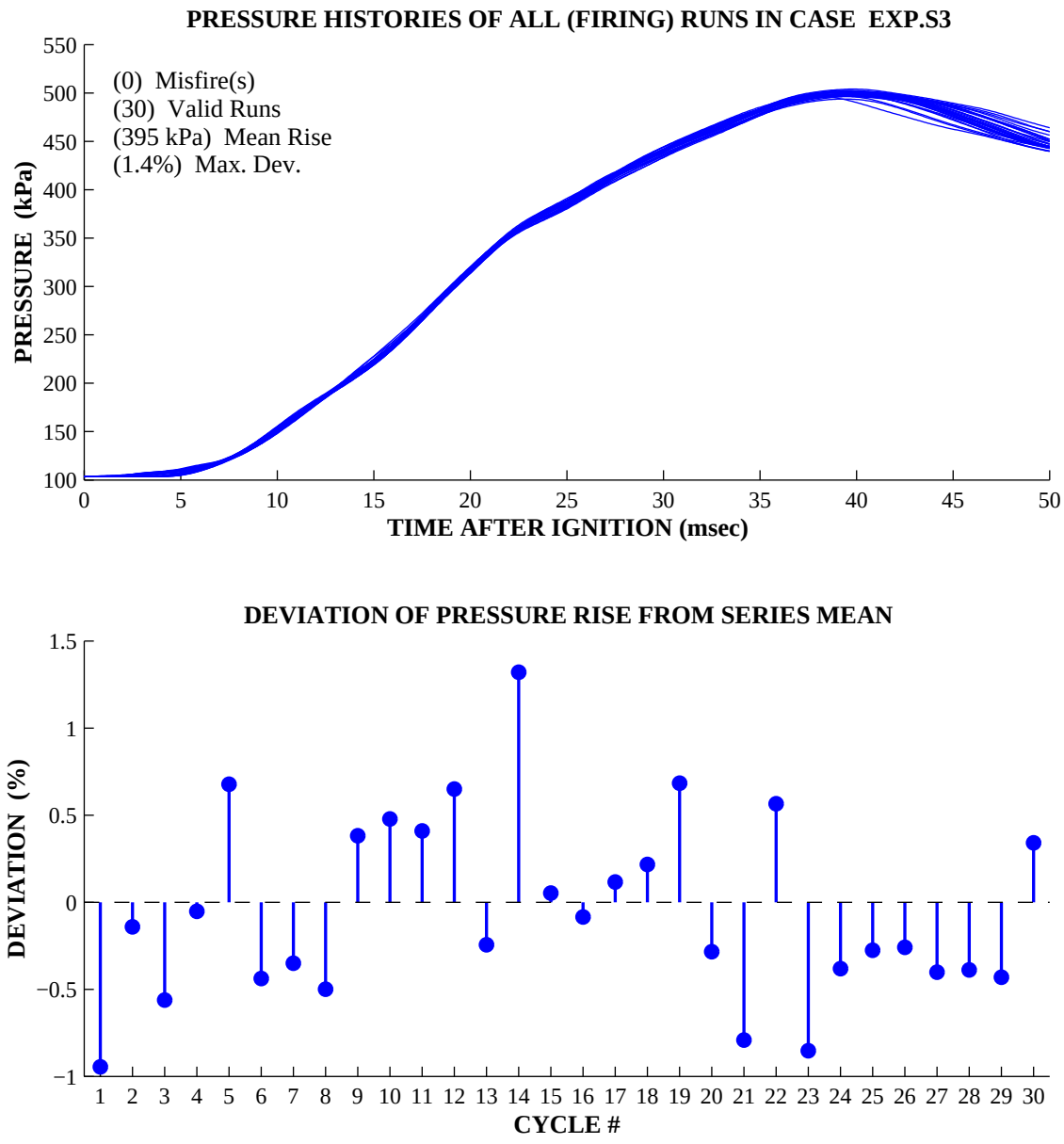

Figure B.4: Series Statistics for Experimental Case S3

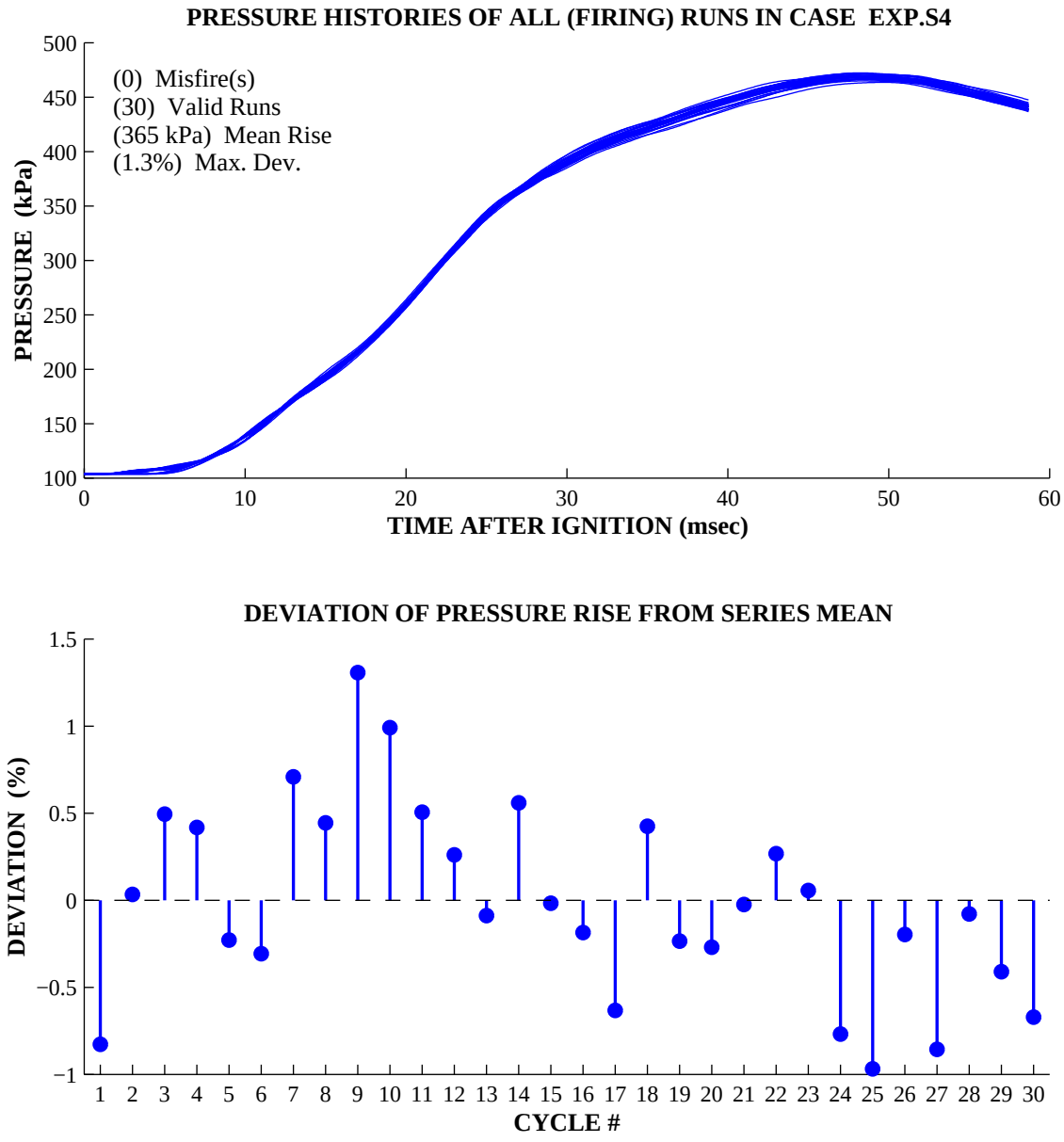

Figure B.5: Series Statistics for Experimental Case S4

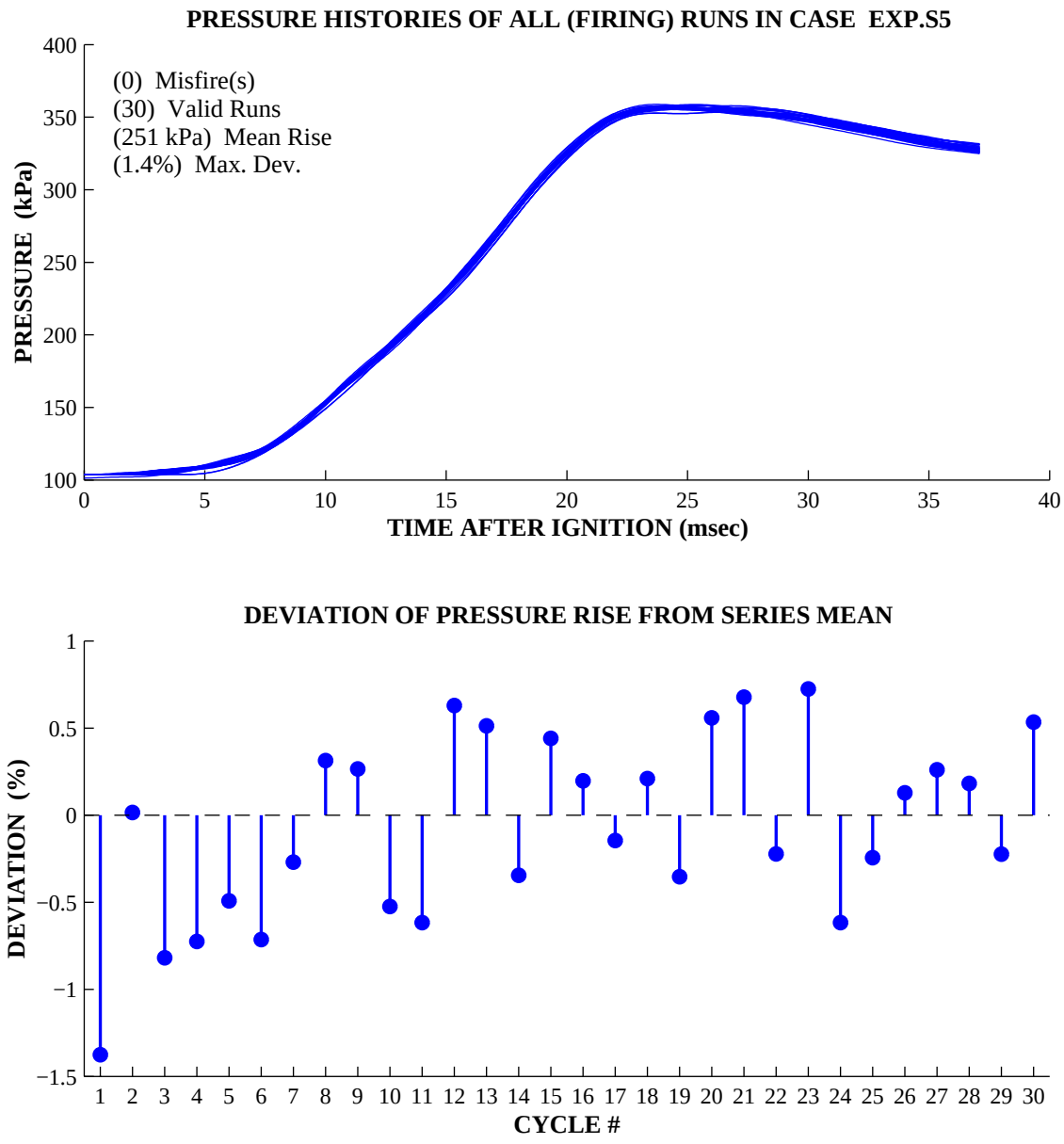

Figure B.6: Series Statistics for Experimental Case S5

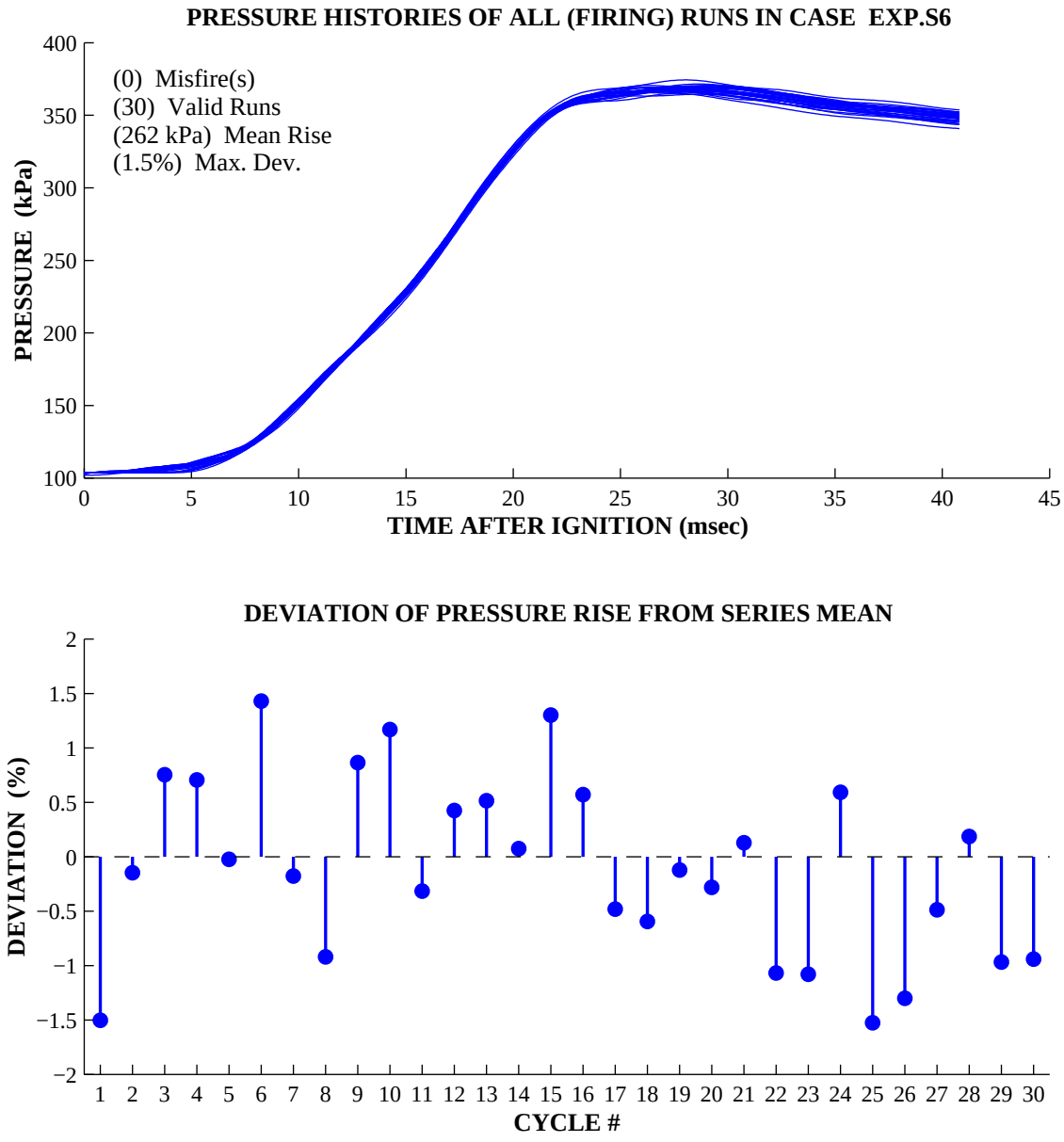

Figure B.7: Series Statistics for Experimental Case S6

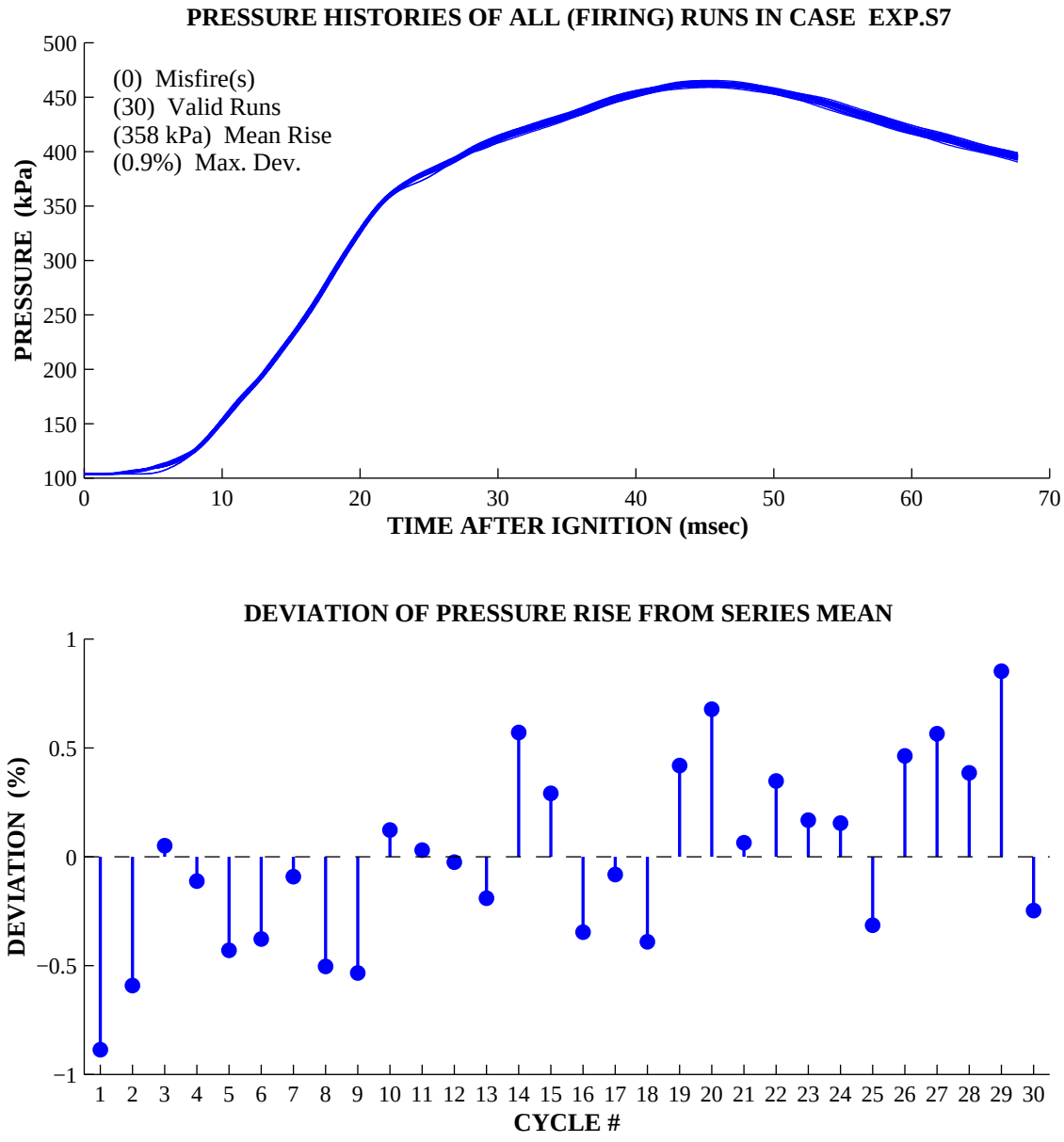

Figure B.8: Series Statistics for Experimental Case S7

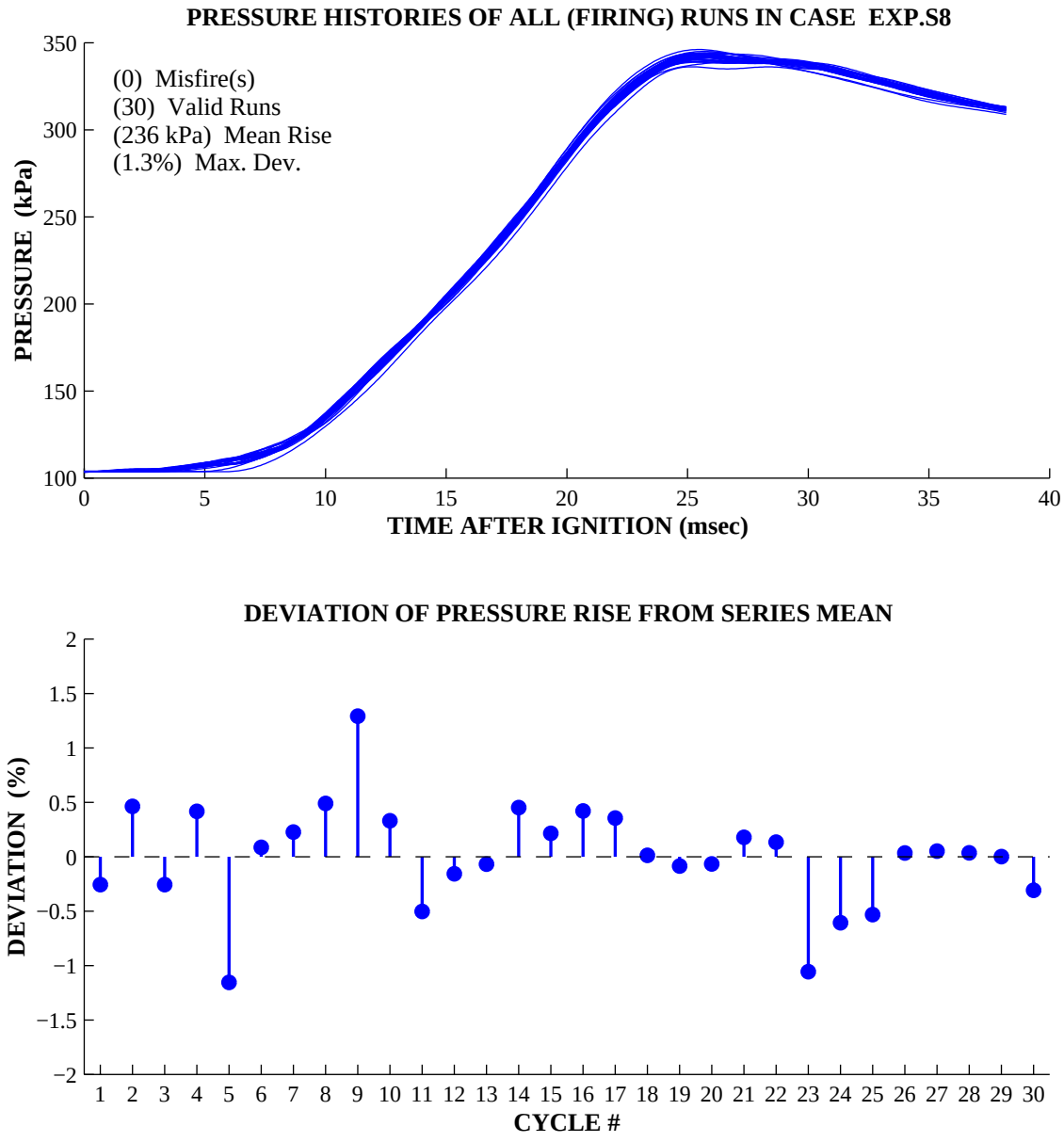

Figure B.9: Series Statistics for Experimental Case S8